

## ABSTRACT

Title of Dissertation:     MODELING AND EXPERIMENTAL INVESTIGATIONS OF  
                                  THE SHOCK RESPONSE OF VISCOELASTIC FOAMS

Richard J Deigan, Doctor of Philosophy, 2007

Dissertation directed by: Professor Amr Baz

Department of Mechanical Engineering

This dissertation presents a new constitutive model for closed-cell foams tailored for compressive shock loads and an experimental investigation of two commercial foam products. The new model requires just two characterization experiments to find material parameters, making it far more convenient than other approaches. A specific form of the hyperelastic free energy function is developed that permits an extension of a three-phase composite theory to finite strain hyperelasticity providing the following advantages: 1) identification of the hyperelastic free energy contributions associated with the gas and material phases, 2) elimination of deviatoric experiments for parameter determination, and 3) proper behavior at the densification limit. A viscoelastic model of the matrix shear modulus is used to introduce rate effects and plasticity. A time-incremental formulation of the constitutive model is developed and implemented using a finite element approach. Model results are compared with data obtained in high strain-rate experiments.

MODELING AND EXPERIMENTAL INVESTIGATIONS OF THE SHOCK  
RESPONSE OF VISCOELASTIC FOAMS

by

Richard J. Deigan

Dissertation submitted to the Faculty of the Graduate School of the  
University of Maryland, College Park, in partial fulfillment  
of the requirements for the degree of  
Doctorate of Philosophy  
2007

Advisory Committee:

Professor Amr Baz, Chair  
Professor Balakumar Balachandran  
Professor Alison Flatau  
Professor Darryll Pines  
Professor Norm Wereley

## **Acknowledgements**

I wish to express my deep gratitude to my dissertation advisor, Professor Amr Baz, for his encouragement, his technical guidance, and his excellent advice throughout all stages of my doctoral pursuit. I consider myself very fortunate to have had the opportunity to study with such a renowned expert in the fields of vibration control and damping materials.

I owe special thanks to Dr. Adel El Sabbagh for his expert advice and kind support with the Split Hopkinson Pressure Bar experiments at UMD. It was a great help to have the assistance of someone who still knew his way around a bridge amplifier.

I want to acknowledge several of my colleagues at NSWCCD. Mr. Patrick Klippel for his assistance with the Conical Shock Tube experiment and also for his keen interest in my defense date; Dr. Kin Ng and Dr. Ryan Braun for their encouragement and discussions; Dr. Steven O'Regan for his consultations on tensorial mathematics. Finally, I owe a special thanks to Dr. Anna Diperna for her assistance with the ABAQUS modeling and for her many consultations regarding finite element analysis, which more than once served to pull me out of the mud and put me back on the road.

I wish to thank my management at NSWCCD, especially Mr. Samuel McKeon and Dr. Paul Shang, who afforded me this excellent opportunity to continue my education at UMD. The editorial comments of Mr. Garth Jensen were greatly appreciated. Also, I wish to acknowledge the Extended Term Training program at NSWCCD and to thank them for their financial assistance.

The sponsorship of the Office of Naval Research was greatly appreciated. I especially wish thank Mr. William J. Martin for his interest in this research and for the financial support of his office.

Finally, I want to thank my terrific family for their support and patience –my wife Federica, and my sons, Thomas and James.

# Table of Contents

List of Figures .....	viii
List of Tables .....	xvi
List of Symbols .....	xvii
1. Introduction.....	1
1.1. Linear Viscoelasticity and Creep .....	5
1.1.1. Viscoelastic Phenomenon in Polymers.....	5
1.1.2. 1-Dimensional Linear Viscoelasticity .....	6
1.1.3. Viscoelastic Models.....	7
1.1.4. 3-D Linear Viscoelasticity .....	10
1.2. Hyperelasticity .....	12
1.2.1. Specific Forms of the Hyperelastic Potential .....	17
1.2.2. Hyperviscoelasticity.....	20
1.3. Hypoelasticity .....	21
1.4. Strain/Strain-Rate Reparability.....	23
1.5. Plasticity.....	24
1.6. High Strain – High Strain-rate Experiments.....	25
1.6.1. Split Hopkinson Pressure Bar .....	25
1.6.2. Conical Shock Tube.....	28

1.7.	Objectives of Current Research .....	29
1.8.	Summary .....	31
2.	Constitutive Theory .....	33
2.1.	Three-phase Composite Theory .....	33
2.2.	Cell-Wall Bending Softening Factor .....	41
2.3.	Consistent Hyperelastic Form.....	45
2.4.	Stress and Tangent Moduli .....	46
2.4.1.	A Note on Stability .....	49
2.5.	Relationship between the Hyperelastic Form and Hydrostatic Moduli.....	49
2.5.1.	Nonlinear Strain Functions .....	53
2.6.	Incorporation of Viscoelastic Relaxation and Plasticity.....	55
2.7.	Time Incremental formulation .....	57
2.8.	The Incremental Stress Jacobian and Partial Time Derivative .....	60
2.9.	Summary .....	61
3.	Characterization of Commercial Closed Cell Foams.....	63
3.1.	Foam Samples.....	63
3.2.	Characterization Experiments.....	67
3.2.1.	Dynamic Mechanical Thermal Analysis.....	68
3.2.2.	APP Dilatometer 1000 Compression Test.....	84

3.3.	Summary .....	96
4.	Shock Experiments .....	98
4.1.	Split Hopkinson Pressure Bar Experiments .....	98
4.1.1.	SHPB Results for RUBATEX R451 .....	101
4.1.2.	SHPB Results for RUBATEX R8702 .....	109
4.2.	Conical Shock Tube Experiments.....	117
4.2.1.	CST Results for RUBATEX R451 .....	123
4.2.2.	CST Results for RUBATEX R8702 .....	129
4.3.	Summary.....	135
5.	Finite Element Implementation.....	137
5.1.	Dedicated MATLAB Model.....	137
5.1.1.	Axisymmetric Element Derivation .....	137
5.1.2.	The Equation of Motion.....	145
5.1.3.	Mesh Transition.....	146
5.2.	ABAQUS/EXPLICIT User Defined Material Subroutine (VUMAT).....	147
5.3.	Summary.....	148
6.	Comparisons of FE Simulations and Experimental Data .....	150
6.1.	MATLAB SHPB Model Compared with Experimental Data .....	150
6.1.1.	Still Images from SHPB Simulations of R8702 .....	151

6.1.2.SHPB Simulations for R8702 Compared with Measurements .....	164
6.1.3.SHPB Simulations for R451 Compared with Measurements .....	172
6.2. Comparison of ABAQUS and MATLAB Models for SHPB Cases .....	181
6.3. ABAQUS CST Model Compared with Experimental Data .....	186
6.3.1.CST Simulations for R8702 Compared with Measurements .....	191
6.3.2.CST Simulations for R451 Compared with Measurements.....	195
6.4. Summary .....	199
7. Summary and Conclusions .....	201
Appendix A: VUMAT .....	207
Bibliography .....	217

## List of Figures

Figure 1-1 Prony series representation for the complex modulus of a VEM .....	8
Figure 2-1 Three-Phase model.....	34
Figure 2-2 Exact and approximate Kerner equations for the effective bulk modulus of a voided rubber.....	40
Figure 2-3 Nonlinear strain function, Q, acting on the linear Prony representation of the neat shear modulus .....	57
Figure 3-1 Foam Specimens. Rubatex R451 (right). Rubatex R8702 (left). DMTA Specimens shown in the foreground . SHPB specimens of ½” and 1” heights shown in back. ....	67
Figure 3-2 DMTA V with FTS Temperature Controller .....	69
Figure 3-3 Single Cantilever Specimen Loaded in the DMTA V .....	70
Figure 3-4 Mastercurve for the dynamic shear modulus and loss factor for RUBATEX R8702 at 20 C.....	73
Figure 3-5 Relaxation shear modulus of RUBATEX R8702 at 20 C.....	74
Figure 3-6 Mastercurve for the real part of the shear modulus – RUBATEX R451.....	78
Figure 3-7 Relaxation shear modulus of RUBATEX R451 at 20 C.....	79

Figure 3-8 Mastercurve for the real part of the shear modulus – RUBATEX R451 – [High Loss Factor Weighting for Prony Coefficients] .....	81
Figure 3-9 Relaxation shear modulus of RUBATEX R451 at 20 C R451 – [High Loss Factor Weighting for Prony Coefficients] .....	82
Figure 3-10 Schematic of APP Dilatometer 1000 with Pressure Vessel .....	85
Figure 3-11 APP Dilatometer 1000 with Level Meter for Volume Metering - Exterior .....	86
Figure 3-12 APP Dilatometer 1000 with Level Meter for Volume Metering - Interior .....	87
Figure 3-13 R451 Hyperbaric chamber test data and model optimization results – (fixed relaxation spectrum) .....	90
Figure 3-14 Optimized Static Hydrostatic Moduli for R451 versus Volumetric Stretch.....	92
Figure 3-15 R8702 Hyperbaric chamber test data and model optimization results – (fixed relaxation spectrum) .....	94
Figure 3-16 Optimized Static Hydrostatic Moduli for R8702 versus Volumetric Stretch.....	96
Figure 4-1 Photo of UMD SHPB with Polycarbonate Pressure Bar .....	100
Figure 4-2 Schematic of the UMD SHPB with Polycarbonate Pressure Bar .....	100
Figure 4-3 SHPB Strain Gauge Data - 1” RUBATEX R451 specimen with 7psi charge.....	103

Figure 4-4 SHPB Strain Gauge Data - 1" RUBATEX R451 specimen	
with 10 psi charge.....	104
Figure 4-5 SHPB Strain Gauge Data - 1" RUBATEX R451 specimen	
with 13 psi charge.....	105
Figure 4-6 SHPB Strain Gauge Data - 1/2" RUBATEX R451 specimen	
with 7psi charge.....	106
Figure 4-7 SHPB Strain Gauge Data - 1/2" RUBATEX R451 specimen	
with 10 psi charge.....	107
Figure 4-8 SHPB Strain Gauge Data - 1/2" RUBATEX R451 specimen	
with 13 psi charge.....	108
Figure 4-9 SHPB Strain Gauge Data - 1" RUBATEX R8702 specimen	
with 7psi charge.....	111
Figure 4-10 SHPB Strain Gauge Data - 1" RUBATEX R8702 specimen	
with 10psi charge.....	112
Figure 4-11 SHPB Strain Gauge Data - 1" RUBATEX R8702 specimen	
with 13psi charge.....	113
Figure 4-12 SHPB Strain Gauge Data - 1/2" RUBATEX R8702 specimen	
with 7psi charge.....	114
Figure 4-13 SHPB Strain Gauge Data - 1/2" RUBATEX R8702 specimen	
with 10 psi charge.....	115
Figure 4-14 SHPB Strain Gauge Data - 1/2" RUBATEX R8702 specimen	
with 13 psi charge.....	116

Figure 4-15 Conical Shock Tube Schematic (top). Photo of rigged test specimen (bottom).....	118
Figure 4-16 Test specimen setup in the CST.....	121
Figure 4-17 Frequency Response of Endevco Model 2255B Shock Accelerometer (Type –01 Used in CST).....	122
Figure 4-18 RUBATEX R451 sample ready for Conical Shock Tube Testing.....	123
Figure 4-19 CST Pressure Sensors Data - 1.875” RUBATEX R451 specimen – no booster.....	125
Figure 4-20 CST Accelerometer Data - 1.875” RUBATEX R451 specimen – no booster.....	126
Figure 4-21 CST Pressure Sensors Data - 1.875” RUBATEX R451 specimen – with booster.....	127
Figure 4-22 CST Accelerometer Data - 1.875” RUBATEX R451 specimen – with booster.....	128
Figure 4-23 CST Pressure Sensors Data - 1.00” RUBATEX R8702 specimen – no booster.....	131
Figure 4-24 CST Accelerometer Data - 1.00” RUBATEX R8702 specimen – no booster.....	132
Figure 4-25 CST Pressure Sensors Data - 1.00” RUBATEX R8702 specimen – with booster.....	133
Figure 4-26 CST Accelerometer Sensors Data - 1.00” RUBATEX R8702 specimen – with booster.....	134

Figure 5-1 Quad Element.....	138
Figure 5-2 Hour Glassing Mode in an Element with a Single Energy Evaluation Point .....	143
Figure 5-3 Multiple Energy Evaluation Points to Suppress Hour Glassing .....	144
Figure 5-4 Interface between dissimilar mesh densities .....	147
Figure 6-1 SHPB geometry and MATLAB model configuration .....	151
Figure 6-2 SHPB Simulation at 0.10 ms– ½” R8702 Specimen with 13 psi charge. Overall view (left). Specimen area (right).....	153
Figure 6-3 SHPB Simulation at 0.30 ms– ½” R8702 Specimen with 13 psi charge. Overall view (left). Specimen area (right).....	154
Figure 6-4 SHPB Simulation at 1.00 ms– ½” R8702 Specimen with 13 psi charge. Overall view (left). Specimen area (right).....	155
Figure 6-5 SHPB Simulation at 1.20 ms– ½” R8702 Specimen with 13 psi charge. Overall view (left). Specimen area (right).....	156
Figure 6-6 SHPB Simulation at 1.40 ms– ½” R8702 Specimen with 13 psi charge. Overall view (left). Specimen area (right).....	157
Figure 6-7 SHPB Simulation at 1.60 ms– ½” R8702 Specimen with 13 psi charge. Overall view (left). Specimen area (right).....	158
Figure 6-8 SHPB Simulation at 1.80 ms– ½” R8702 Specimen with 13 psi charge. Overall view (left). Specimen area (right).....	159
Figure 6-9 SHPB Simulation at 2.00 ms– ½” R8702 Specimen with 13 psi charge. Overall view (left). Specimen area (right).....	160

Figure 6-10 SHPB Simulation at 2.20 ms– ½” R8702 Specimen with 13 psi charge. Overall view (left). Specimen area (right). .....	161
Figure 6-11 SHPB Simulation at 2.50 ms– ½” R8702 Specimen with 13 psi charge. Overall view (left). Specimen area (right). .....	162
Figure 6-12 SHPB Simulation at 3.50 ms– ½” R8702 Specimen with 13 psi charge. Overall view (left). Specimen area (right). .....	163
Figure 6-13 SHPB Data Theory Comparison - MATLAB model – 1.00” R8702 Specimen with 7 psi charge .....	166
Figure 6-14 SHPB Data Theory Comparison - MATLAB model – 1.00” R8702 Specimen with 10 psi charge .....	167
Figure 6-15 SHPB Data Theory Comparison - MATLAB model – 1.00” R8702 Specimen with 13 psi charge .....	168
Figure 6-16 SHPB Data Theory Comparison - MATLAB model – 0.50” R8702 Specimen with 7 psi charge .....	169
Figure 6-17 SHPB Data Theory Comparison - MATLAB model – 0.50” R8702 Specimen with 10 psi charge .....	170
Figure 6-18 SHPB Data Theory Comparison - MATLAB model – 0.50” R8702 Specimen with 13 psi charge .....	171
Figure 6-19 Effect of Christensen’s Shear Equation – 0.5” R8702 Specimen with 13 psi charge .....	172
Figure 6-20 SHPB Data Theory Comparison - MATLAB model – 1.00” R451 Specimen with 7 psi charge .....	174

Figure 6-21 SHPB Data Theory Comparison - MATLAB model – 1.00”	
R451 Specimen with 10 psi charge .....	175
Figure 6-22 SHPB Data Theory Comparison - MATLAB model – 1.00”	
R451 Specimen with 13 psi charge .....	176
Figure 6-23 SHPB Data Theory Comparison - MATLAB model – 0.50”	
R451 Specimen with 7 psi charge .....	177
Figure 6-24 SHPB Data Theory Comparison - MATLAB model – 0.50”	
R451 Specimen with 10 psi charge .....	178
Figure 6-25 SHPB Data Theory Comparison - MATLAB model – 0.50”	
R451 Specimen with 13 psi charge .....	179
Figure 6-26 SHPB Data Theory Comparison - MATLAB model – 0.50”	
R451 Specimen with 13 psi charge – [High Loss Factor	
Weighting for Prony Coefficients] .....	180
Figure 6-27 ABAQUS Mesh of the SHPB experiment near the specimen .....	183
Figure 6-28 A comparison of ABAQUS and MATLAB simulations of the	
SHPB experiment for ½” R451 with a 13 psi striker charge.....	184
Figure 6-29 A comparison of ABAQUS and MATLAB simulations of the	
SHPB experiment for ½” R8702 with a 13 psi striker charge.....	185
Figure 6-30 ABAQUS Mesh for the CST experiment.....	188
Figure 6-31 Incident Shock Pressure Profile used for CST model – with	
booster .....	189
Figure 6-32 Comparison of data with ABAQUS simulation of the CST	
experiment for 1.0” R8702. No booster used. ....	193

Figure 6-33 Comparison of data with ABAQUS simulation of the CST experiment for 1.0" R8702. Booster used. ....	194
Figure 6-34 Comparison of data with ABAQUS simulation of the CST experiment for 1.0" R8702. No booster used. ....	197
Figure 6-35 Comparison of data with ABAQUS simulation of the CST experiment for 1.0" R8702. Booster used. ....	198

## List of Tables

Table 2-1. Summary of Three-Phase Parameters .....	44
Table 2-2 Matrix Identities of Symmetric Matrix C.....	47
Table 3-1 Measured Physical Properties of RUBATEX Foam Samples.....	64
Table 3-2 Manufacturer’s Physical Properties for R451 .....	65
Table 3-3 Manufacturer’s Physical Properties for R8702 .....	66
Table 3-4 Optimized Prony Coefficients for RUBATEX R8702.....	75
Table 3-5 Optimized Prony Coefficients for RUBATEX R451 .....	80
Table 3-6 Optimized Prony Coefficients for RUBATEX R451 [High Loss Factor Weighting].....	83
Table 3-7. Optimized Three-Phase and Plastic Parameters for R451.....	91
Table 3-8. Optimized Three-Phase and Plastic Parameters for R8702.....	95

## List of Symbols

<b>B</b>	left-Cauchy-Green strain tensor
$C_1, C_{10}, C_{20}, C_{30}$	constitutive material parameters relating to deviatoric stress
$C_1, C_2$	constitutive parameters relating to cell wall bending
<b>C</b>	right Cauchy-Green strain tensor
$\bar{\mathbf{C}}$	volume preserving Cauchy-Green strain tensor
$c$	wave speed
<b>c</b>	shape coefficient matrix for radial displacements
$D_1, D_{10}, D_{20}, D_{30}$	constitutive material parameters relating to volumetric stress
$D_1, D_2$	constitutive parameters relating to host shear modulus
<b>D</b>	deformation tensor
<b>d</b>	shape coefficient matrix for axial displacements
$E$	Young's modulus
$E^{(0)}$	Prony equilibrium modulus – Young's
$E^{(k)}$	relaxation modulus of the $k^{\text{th}}$ Prony element – Young's
<b>E</b>	Green-Lagrange strain tensor
$f$	Blatz-Ko material parameter
$f$	force

<b>F</b>	deformation gradient
$\bar{\mathbf{F}}$	volume preserving deformation gradient
<b>I</b>	identity tensor
$I_{\bar{\mathbf{C}}}$	First invariant of the volume preserving Cauchy-Green strain tensor
$II_{\bar{\mathbf{C}}}$	second invariant of the volume preserving Cauchy-Green strain tensor
$J$	volumetric stretch
$k$	elastic tensor
<b>K</b>	elastic tensor
$K$	bulk modulus
$K_{\text{eff}}$	effective bulk modulus
$\hat{K}_{\text{eff}}$	effective bulk modulus with cell wall bending modification
$k_{ijkl}$	elastic tangent matrix
<b>L</b>	velocity gradient
$l$	length
$m$	mass
<b>N</b>	shape matrix
$P$	pressure

$p$	plastic parameter
$Q$	nonlinear strain function
$R$	rotation tensor
$S$	second Piola-Kirchhoff stress tensor
$S$	solidity
$s$	Laplace variable
$s^{(k)}$	internal stress variable for the $k^{\text{th}}$ Maxwell element
$t$	time
$u$	displacement
$U$	right stretch tensor
$v$	velocity
$V$	left stretch tensor
$V$	volume
$W$	spin tensor
$W$	strain energy density function (per unit reference volume)
$\bar{W}$	strain energy density function (per unit current volume)
$x$	position vector in current configuration
$X$	position vector in reference configuration
$Y$	yield stress

$\alpha_i$	Ogden material parameter
$\beta$	matrix of first order terms relating energy to shape coefficients
$\beta$	Blatz-Ko material parameter
$\chi$	vector of zero order terms relating energy to shape coefficients
$\varepsilon$	Hencky (true) strain tensor
$\delta$	Kronecker's delta
$\phi$	volume fraction
$\Lambda$	stress Jacobian
$\lambda$	1 <sup>st</sup> Lamé constant
$\lambda_i$	principal stretches
$\bar{\lambda}_i$	modified principal stretches
$\nu$	Poisson's ratio
$\rho$	mass density
$\Theta$	partial time derivative of stress
$\sigma$	Cauchy (true) stress tensor
$\hat{\sigma}$	Corotated Cauchy stress tensor

$\tau$	convolution time variable
$\tau^{(k)}$	relaxation time
$\mu$	shear modulus
$\mu_i$	Ogden material parameter
$\mu_{eff}$	effective shear modulus
$\hat{\mu}_{eff}$	effective shear modulus with cell wall bending modification
$\nu$	Poisson ratio
$\omega$	radial frequency
$\xi^{(k)}$	internal displacement variable of the $k^{th}$ Maxwell element

# CHAPTER 1

## 1. Introduction

Elastomeric foams are increasingly used in crash and shock mitigation applications. Examples include protective helmets, automotive bumpers, packaging, and advanced wall systems for blast damping and containment in ordnance storage facilities and other structures. In addition to their effectiveness in shock mitigation applications, they are desirable for their low weight and their relatively low cost. Foams vary widely in their composition and density. Depending on the manufacturing process and density, elastomeric foams can be open cell, closed cell, or a combination of both. Many types of polymeric resins can be used to create elastomeric foam such as rubbers, polyurethanes, and polystyrenes. In impact mitigation applications, soft flexible foams can be effective by blocking the transmission of shock energy. However, densification hardening of the foam limits the level and duration of shock loading that can be blocked and a sudden loss of shock isolation can occur when over stressed. Medium to hard foams can be used to improve effectiveness at higher levels of shock loading by absorbing energy via viscoelastic, viscoplastic-damage mechanisms, but due to their greater stiffness they allow partial transmission of energy at all shock levels. The development of a general constitutive description of elastomeric foams requires that all of the aforementioned mechanisms be incorporated. Furthermore, this must be done in the context of a finite strain formulation where a concurrence of high strain and high strain-rates is expected.

In recent years numerous constitutive models for polymeric materials have been developed for use in finite element analyses of their use in high strain and high strain-rate applications. The development of formulations for compressible elastomers has been the topic of even more recent interest. Several commercial finite element packages such as ABAQUS and LS-DYNA provide their users with some modeling capability of rate-dependent elastomeric foams [12][13]. In most cases, standard models of polymer viscoelasticity are used in combination with hyperelastic energy density functions, which are commonly called *hyperviscoelastic* models. These models can be effective for shock loading scenarios, but can require a high number of material parameters, and associated material tests, to track detailed constitutive behavior over the entire range of load, especially if the foam is to be modeled near its densification limit. Furthermore, there are few constitutive models available that include plastic effects within the hyperviscoelastic framework.

In this dissertation, a constitutive model for closed-cell foams is developed which combines the descriptions of nonlinearity, viscoelasticity, and plastic effects. The model is motivated by a need for a practical modeling tool for the accurate predictions of shock isolation effectiveness in loading scenarios that are predominantly compressive in nature. A material characterization plan is provided for model parameter determination. Implementation is made in a MATLAB finite element program and a VUMAT is developed for use with commercial the software, ABAQUS. The restriction to loading scenarios that are primarily compressive is exploited to develop a constitutive theory that

is far more practical to implement than most hyperviscoelastic formulations while providing a detailed and relatively stable description of nonlinearities associated with the collapse of the foam microstructure. This simplification involves the use of composite theory to help define the hyperelastic free energy function. Specifically, we investigate the use of three-phase composite theory to supply a complete description of the deviatoric constitutive behavior, thereby eliminating the need for specimen characterization under deviatoric strain conditions. The resulting hyperelastic form is fully isotropic. Since the three-phase composite theory does not track strong nonlinear behavior in foams associated with elastic instabilities under compressive strains [32], a phenomenological modification to the composite theory is made to incorporate this behavior. Viscoelastic behavior is described with a generalized Maxwell model, also known as the Prony Series. Internal variables are used to track the hereditary response. Finally, a plastic model for polymeric materials motivated by the model of Bardenhagen [35] is incorporated within the viscohyperelastic framework using an approach described by Nedjar [23]. The resulting approach offers a model for foams with a unique combination of the following features:

- 1) An isotropic constitutive description formulated directly in terms of strain-dependent tangent moduli.
- 2) Separation of the gas phase contribution to the constitutive response.
- 3) Viscoelastic behavior of the matrix polymer.
- 4) A rate-dependent plasticity model integrated within viscoelastic framework.

- 5) Unification of the constitutive description over a large region of the strain/strain-rate space.

The validity of the latter feature is a hypothesis tested in this dissertation. Model parameters of the constitutive theory are developed using characterization experiments that lie far outside the region in strain/strain-rate space normally characterized as “shock”. The ability of the constitutive model to predict the results of shock experiments is then investigated using finite element analysis.

This dissertation includes experimental results for two commercially available closed-cell foam specimens. These experiments are the Split Hopkinson Pressure Bar (SHPB) and a Conical Shock Tube (CST), which both measure material behavior at a combination of high strain and high strain-rate. The subject foams are RUBATEX<sup>®</sup> #R451 Neoprene Foam, and RUBATEX<sup>®</sup> #R8702 SBR Foam. These foams are made from different base elastomers and possess markedly different moduli and relaxation behaviors. Split Hopkinson Pressure Bar experiments are used to characterize small cylindrical specimens. Conical Shock Tube experiments are also used to characterize the response to underwater shock of larger specimens.

Shock experiments are simulated with finite element models that incorporate the constitutive theory. Two modeling approaches are employed. The first is a dedicated model of the SHPB experiment that is written in MATLAB. This model uses an implicit solution technique. Simulations are also made using the commercial software ABAQUS using its explicit solution option. In this case, the constitutive theory is implemented via

user defined material subroutine known as a VUMAT. Material parameters needed for the constitutive theory are established for the foams using hydrostatic dilatometer experiments and with master curves of the dynamic complex shear modulus, which are developed from experiments in a Dynamic Mechanical Thermal Analyzer (DMTA).

The remainder of this chapter provides a brief background on the theoretical aspects of the constitutive model development and provides a description and some background of the high strain rate experiments conducted on the foam specimens.

## **1.1. Linear Viscoelasticity and Creep**

### ***1.1.1. Viscoelastic Phenomenon in Polymers***

Viscoelasticity is the manifestation of relaxation phenomena associated with spatial molecular rearrangements that occur within a stressed polymer structure [1][3]. This behavior is readily evident in dynamic mechanical thermal experiments in which the magnitude of the complex Young's or shear modulus can change orders of magnitude over the glass transition region. In the rubbery region (high temperatures) the polymer chains are highly mobile and fast to react to an applied stress, whereas in the glassy region (cold temperatures) the polymer chains are inactive and slow to react. This underlying relaxation phenomenon also gives rise to the well-known time-temperature superposition principle, which postulates a correspondence between temperature and time dependence of the viscoelastic moduli. An increase in temperature at a fixed time-scale corresponds to an increased time-scale (or a reduced dynamic frequency) at fixed

temperature and vice versa. This principle is used to create dynamic modulus mastercurves over a wide range of frequency from dynamic mechanical experiments conducted over a narrow frequency range and repeated at many temperatures. Rubbery creep relaxation seen in most polymers is also part of the same viscoelastic phenomenon, but is usually associated with relaxation phenomenon occurring over large time scales much larger than those associated with a polymer's glass-transition frequency [1][2][3][3].

### ***1.1.2. 1-Dimensional Linear Viscoelasticity***

Viscoelastic materials exhibit a time-dependent stress in response to the application of fixed strain. Accordingly, constitutive relationships via constant elastic moduli are not sufficient to describe their behavior. For a viscoelastic solid subjected to a step in strain, a time-dependent *relaxation modulus* is the analog to the constant modulus value of an elastic solid

$$E = \frac{\sigma}{\varepsilon} \qquad \text{elastic modulus} \qquad (1-1)$$

$$E(t) = \frac{\sigma(t)}{\varepsilon} \qquad \text{viscoelastic relaxation modulus} \qquad (1-2)$$

By virtue of the Boltzmann's linear superposition principle, the stress response to an arbitrary strain history can be derived at any time,  $t$ , from the relaxation modulus by a hereditary convolution integral over the entire strain history. The hereditary integral for a material that has no strain history prior to  $t=0$  is given by

$$\sigma(t) = \int_0^t E(t-\tau) \frac{\partial \varepsilon}{\partial \tau} d\tau \quad (1-3)$$

The Laplace transform of the hereditary integral gives us the following constitutive relationship in the Laplace domain:

$$\sigma = E\varepsilon \quad (\text{elastic stress}) \quad (1-4)$$

$$\tilde{\sigma}(s) = [s\tilde{E}(s)]\tilde{\varepsilon}(s) \quad (\text{viscoelastic stress}) \quad (1-5)$$

From (1-4) and (1-5) we see that in the Laplace domain the constitutive relationship of a viscoelastic material is analogous to an elastic material, where the *Laplace modulus*, which we define as  $s\tilde{E}(s)$ , takes the role of the elastic modulus. This similarity between the elastic form and the viscoelastic form in the Laplace domain is known as the Elastic-Viscoelastic Correspondence Principle [4].

### 1.1.3. Viscoelastic Models

Viscoelastic behavior is often modeled with mechanical analogs consisting of springs and dashpots in various configurations commonly referred to as Viscoelastic Models (VEMs). The stress-strain relationship developed by these mechanical systems can emulate the behavior of real viscoelastic materials as given by the hereditary integral. In some VEMs like the Gollah, Hughs and McTavish (GHM) model, which is widely used in viscoelastic damping problems, masses are also used to facilitate the mathematical treatment the finite element approach, but the masses have no tangible physical meaning.

In this work, a generalized Maxwell model, also known as a Prony series, is used to describe viscoelastic behavior. The Prony series represents a discretization of the continuous relaxation spectrum within the polymer chains [1]. The model is well suited to describe the macroscopic behavior of the material to almost any degree of accuracy, provided that sufficient number of Maxwell elements is used. A desirable feature of the Prony series model is that it is particularly well suited for the inter-conversion between modulus and compliance functions in time, frequency, and Laplace transform domains [6].

The Prony series is shown Figure 1-1. It consists of a lone spring element in parallel with  $N$  Maxwell elements. Each Maxwell element introduces an internal degree of freedom, which is the displacement between the spring and dashpot components. Subscripts ‘e’ and ‘v’ refer to the elastic and viscous components of the Maxwell elements.

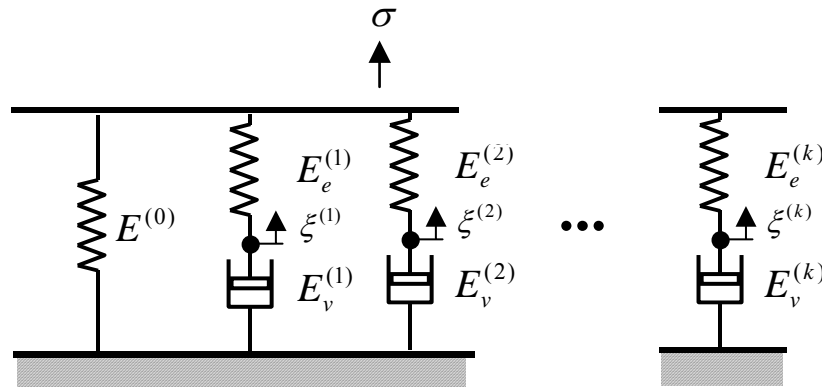


**Figure 1-1 Prony series representation for the complex modulus of a VEM**

In the Laplace domain, the Prony system shown above has the following stress strain relationship:

$$\tilde{\sigma}(s) = \left( E^{(0)} + \sum_{k=1}^N E_e^{(k)} \frac{s\tau^{(k)}}{1 + s\tau^{(k)}} \right) \tilde{\varepsilon}(s), \quad (1-6)$$

where,

$$\tau^{(k)} \equiv \text{Relaxation time of the } k^{\text{th}} \text{ element} = \frac{E_v^{(k)}}{E_e^{(k)}}$$

$s \equiv$  Laplace variable.

Relaxation modulus (time-domain) and dynamic modulus (frequency-domain) are readily obtained from the Laplace domain, allowing Prony coefficients to be established with either relaxation or dynamic experiments.

Relaxation modulus,  $E(t)$ , is defined by the ratio of stress to strain after imposing a step strain to the system. The Laplace transform of the step strain is given by:

$$\tilde{\varepsilon}(s) = 1/s. \quad (1-7)$$

Substituting equation (1-7) into equation (1-6) gives the relaxation modulus in the Laplace domain:

$$\tilde{E}(s) = \frac{1}{s} E^{(0)} + \sum_{k=1}^N E_e^{(k)} \frac{1}{s + 1/\tau^{(k)}} \quad (1-8)$$

As expected equations (1-6) and (1-8) lead to the same constitutive relation in the Laplace domain as was developed from general convolution integral,  $\tilde{\sigma}(s) = s\tilde{E}(s)\tilde{\varepsilon}(s)$ .

The inverse transform of equation (1-8) gives the relaxation modulus in the time domain:

$$E(t) = E^{(0)} + \sum_{k=1}^N E_e^{(k)} \exp\left(-\frac{t}{\tau^{(k)}}\right). \quad (1-9)$$

Dynamic modulus can be obtained directly from the Laplace domain by replacing the Laplace variable with  $-i\omega$  where  $\omega$  is the radial frequency, and separating the real and imaginary components:

$$E'(\omega) = E^{(0)} + \sum_{k=1}^N E_e^{(k)} \frac{(\omega\tau^{(k)})^2}{1 + (\omega\tau^{(k)})^2}, \quad (1-10)$$

$$E''(\omega) = \sum_{k=1}^N E_e^{(k)} \frac{\omega\tau^{(k)}}{1 + (\omega\tau^{(k)})^2}, \quad (1-11)$$

such that the complex dynamic modulus is given by:

$$E^*(\omega) = E'(\omega) + iE''(\omega). \quad (1-12)$$

#### 1.1.4. 3-D Linear Viscoelasticity

This section provides a brief review of three-dimensional linear viscoelasticity. We begin with generalized Hooke's law for linear elastic solids:

$$\sigma_{ij} = k_{ijkl} \varepsilon_{kl}. \quad (1-13)$$

The elastic tensor relating stress and strain is 4<sup>th</sup> order and has 81 elements. In view of the symmetry of the stress and strain tensors ( $\sigma_{ij} = \sigma_{ji}$  and  $\varepsilon_{kl} = \varepsilon_{lk}$ ) the elastic tensor

has at most 36 independent elements [3]. For a completely isotropic solid, additional symmetries, and the requirement that the properties are invariant with rotation reduces the number of independent constants to just two and the constitutive relation is given by,

$$\sigma_{ij} = \lambda \varepsilon_{kk} \delta_{ij} + 2\mu \varepsilon_{ij}, \quad (1-14)$$

where  $\lambda$  and  $\mu$  are the first and second Lamé constants, respectively. The second Lamé constant is more commonly referred to as the shear modulus. The constitutive relation can also be written in terms of the bulk and shear moduli, which is a more meaningful form in the context of the model development in Chapter 2:

$$\sigma_{ij} = \left( K - \frac{2}{3} \mu \right) \varepsilon_{kk} \delta_{ij} + 2\mu \varepsilon_{ij}. \quad (1-15)$$

The bulk modulus is of particular interest because it provides the constitutive response to isotropic normal stress, which is a stress state that is readily achievable in dilatometer experiments. In nearly all hyperelastic formulations, a portion of the energy potential dependent only on volumetric strain is additively split from a remaining energy potential containing the deviatoric behavior.

In the Laplace domain, the viscoelastic problem has a form that is similar to the elastic problem. Consider the 3-D generalization of equation 2-2 by replacing the modulus with the elastic matrix:

$$\tilde{\sigma}_{ij}(s) = s\tilde{K}(s)\tilde{\varepsilon}_{kk}(s)\delta_{ij} + 2s\tilde{\mu}(s)\left(\tilde{\varepsilon}_{ij}(s) - \frac{1}{3}\tilde{\varepsilon}_{kk}(s)\delta_{ij}\right). \quad (1-16)$$

Equation (1-16) provides the 3-D linear viscoelastic response of an isotropic material in the Laplace domain. It can be seen in this equation that there is one independent hereditary integral associated with the bulk modulus,  $s\tilde{K}(s)\tilde{\varepsilon}_{kk}(s)$ , and 9 associated with the shear modulus,  $s\tilde{\mu}(s)\tilde{\varepsilon}_{ij}(s)$ . Symmetry of the strain tensor eliminates 3 of the shear integrals making for a total of 7 hereditary integrals.

## 1.2. Hyperelasticity

Hyperelasticity is used to describe rubber-like materials undergoing finite deformations. The underlying assumption of hyperelastic theory is the existence of a strain energy density function, that is dependent only on the current state of strain and serves as the free energy potential from which the stresses are obtained. Hyperelastic forms most often express the energy density function in terms of the invariants of the finite strain tensor. What is often cited as an advantage of the hyperelastic description is that it ensures path independent behavior since the stored elastic energy at any point in the material is determined by its current state of deformation. This also ensures a fixed point of equilibrium, which is typically the undeformed state.

A Lagrangian framework is used in the following development. The deformation gradient is given by:

$$\mathbf{F} = \frac{\partial \mathbf{x}}{\partial \mathbf{X}},$$

or

$$F_{ij} = \frac{\partial x_i}{\partial X_j}, \quad (1-17)$$

where  $\mathbf{x}$  represents the current position of a material particle, and  $\mathbf{X}$  represents its reference position. To indicate vector components, lower case letters are used for the current configuration and upper case is used for the reference configuration. The deformation gradient is a poor measure of deformation since it contains rigid body rotation. By the polar decomposition principle, the finite strain deformation gradient can be multiplicatively decomposed into an orthogonal matrix,  $\mathbf{R}$ , representing rigid body rotation, and either a right or left symmetric stretch matrix representing pure deformation

$$\mathbf{F} = \mathbf{R} \cdot \mathbf{U}, \quad \mathbf{F} = \mathbf{V} \cdot \mathbf{R}. \quad (1-18)$$

A right and left Cauchy-Green deformation tensor is formed as follows:

$$\mathbf{C} = \mathbf{F}^T \mathbf{F} = (\mathbf{U}^T \cdot \mathbf{R}^T) \mathbf{R} \cdot \mathbf{U} \quad (\text{right Cauchy Tensor}) \quad (1-19)$$

$$\mathbf{B} = \mathbf{F} \mathbf{F}^T = \mathbf{V} \cdot \mathbf{R} (\mathbf{R}^T \cdot \mathbf{V}^T) \quad (\text{left Cauchy Tensor}) \quad (1-20)$$

The rotation matrix,  $\mathbf{R}$ , is orthogonal so  $\mathbf{R}^T \mathbf{R} = \mathbf{I}$ . The stretch matrix,  $\mathbf{U}$ , is symmetric so  $\mathbf{U}^T \mathbf{U} = \mathbf{U}^2$ . Using these properties becomes

$$\mathbf{C} = \mathbf{U}^2, \quad \mathbf{B} = \mathbf{V}^2 \quad (1-21)$$

The right Cauchy-Green tensor maps the dot product of infinitesimal material fiber (vector joining two neighboring particles) with itself at the reference configuration to the same fiber at the current location.

$$d\mathbf{x} \cdot d\mathbf{x} = d\mathbf{X} \cdot \mathbf{C} \cdot d\mathbf{X}. \quad (1-22)$$

The Green-Lagrange finite strain tensor is closely related to  $\mathbf{C}$  but maps the change in the dot products:

$$\mathbf{E} = \frac{1}{2}(\mathbf{C} - \mathbf{I}), \quad (1-23)$$

$$d\mathbf{x} \cdot d\mathbf{x} - d\mathbf{X} \cdot d\mathbf{X} = d\mathbf{X} \cdot 2\mathbf{E} \cdot d\mathbf{X}. \quad (1-24)$$

The Green finite strain is energy conjugate with the second Piola-Kirchhoff stress. Hence, an incremental change in internal energy density is given by;

$$dW = \mathbf{S} : d\mathbf{E}, \quad (1-25)$$

where  $dW$  represents the change in strain energy density with respect to the reference volume. The volumetric stretch,  $J = \det(\mathbf{F})$ , is a strain invariant always used for hyperelastic descriptions of compressible materials. The deviatoric strain invariants are usually derived from a form of the deformation gradient and deformation matrix that is independent of volumetric strain,

$$\bar{\mathbf{F}} = J^{-1/3} \mathbf{F}, \quad (1-26)$$

$$\bar{\mathbf{C}} = \bar{\mathbf{F}}^T \bar{\mathbf{F}} = J^{-2/3} \mathbf{C}. \quad (1-27)$$

Such tensors are sometimes referred to as *volume preserving* since they change only with deviatoric deformation. The invariants of the volume preserving right-Cauchy deformation tensor are given by the coefficients of the characteristic eigenvalue equation:

$$\det[\bar{C}_{IJ} - \lambda \delta_{IJ}] = 0, \quad (1-28)$$

$$\lambda^3 + I_{\bar{C}} \lambda^2 + II_{\bar{C}} \lambda + 1 = 0. \quad (1-29)$$

From which we have for the first invariant,

$$I_{\bar{C}} = \bar{\lambda}_1^2 + \bar{\lambda}_2^2 + \bar{\lambda}_3^2, \quad (1-30)$$

and for the second invariant,

$$II_{\bar{C}} = \bar{\lambda}_1^{-2} + \bar{\lambda}_2^{-2} + \bar{\lambda}_3^{-2}. \quad (1-31)$$

where  $\lambda_i$  are the principal stretches and  $\bar{\lambda}_i = J^{-1/3} \lambda_i$ . The eigenvectors of  $\mathbf{C}$  provide the principal directions.

The hyperelastic strain energy density equation has the general form,

$$W = W(I_{\bar{C}}, II_{\bar{C}}, J), \quad (1-32)$$

and the second Piola-Kirchhoff stress tensor is derived from the potential as follows:

$$\mathbf{S} = \frac{\partial \mathbf{W}}{\partial \mathbf{E}} = 2 \frac{\partial \mathbf{W}}{\partial \mathbf{C}}, \quad (1-33)$$

or

$$S_{IJ} = \frac{\partial W}{\partial E_{IJ}} = 2 \frac{\partial W}{\partial C_{IJ}}. \quad (1-34)$$

In most cases, the hyperelastic energy density is written in terms of the strain invariants and the chain rule is used to develop the stresses,

$$\mathbf{S} = 2 \left( \frac{\partial \mathbf{W}}{\partial I_{\bar{c}}} \frac{\partial I_{\bar{c}}}{\partial \mathbf{C}} + \frac{\partial \mathbf{W}}{\partial II_{\bar{c}}} \frac{\partial II_{\bar{c}}}{\partial \mathbf{C}} + \frac{\partial \mathbf{W}}{\partial J} \frac{\partial J}{\partial \mathbf{C}} \right). \quad (1-35)$$

The second Piola-Kirchhoff stress tensor is related to the Cauchy stress tensor as follows:

$$\mathbf{S} = J \mathbf{F}^{-1} \cdot \boldsymbol{\sigma} \cdot \mathbf{F}^{-T}. \quad (1-36)$$

Using the polar decomposition theorem, we can express the second Piola-Kirchhoff stress in terms of the co-rotational Cauchy stress,

$$\mathbf{S} = J \mathbf{U}^{-1} \cdot \hat{\boldsymbol{\sigma}} \cdot \mathbf{U}^{-T} \quad (1-37)$$

where  $\hat{\boldsymbol{\sigma}}$  represents the corotational Cauchy stress given by,

$$\hat{\boldsymbol{\sigma}} = \mathbf{R}^T \cdot \boldsymbol{\sigma} \cdot \mathbf{R}, \quad (1-38)$$

The co-rotational Cauchy stress is the Cauchy stress tensor pulled-back to reference configuration by the material rotation tensor,  $\mathbf{R}$ . The second Piola-Kirchhoff stress represents the co-rotated stress scaled from the deformed to undeformed configuration.

Linearization of the hyperelastic relation is used in the finite element method. A first order Taylor expansion of the stress tensor at strain  $\mathbf{E}$  gives the perturbed stress in terms of this gradient:

$$\mathbf{S}(\mathbf{E} + d\mathbf{E}) = \mathbf{S}(\mathbf{E}) + \frac{\partial \mathbf{S}}{\partial \mathbf{E}} d\mathbf{E}. \quad (1-39)$$

Rearranging we can write,

$$d\mathbf{S} = \left( \frac{\partial \mathbf{S}}{\partial \mathbf{E}} \right) d\mathbf{E} = \mathbf{K} d\mathbf{E}, \quad (1-40)$$

where  $\mathbf{K} = \left( \frac{\partial \mathbf{S}}{\partial \mathbf{E}} \right)$  is the Lagrangian tangent modulus. Finally, the true Cauchy stress,

which is the more useful form for engineering computations, is related to  $\mathbf{S}$  via:

$$\boldsymbol{\sigma} = \frac{1}{J} \mathbf{F} \cdot \mathbf{S} \cdot \mathbf{F}^T, \quad (1-41)$$

or

$$\sigma_{ij} = \frac{1}{J} F_{iI} S_{IJ} F_{jJ}. \quad (1-42)$$

### ***1.2.1. Specific Forms of the Hyperelastic Potential***

Many forms of the hyperelastic energy potential have been proposed. Below is a brief review of several common models that include to compressible materials.

*Neo-Hookean.*

Neo-Hookean form is the most basic form of the hyperelastic potential. In its general form, the Neo-Hookean model is the expression of the strain energy density derived from integration of the stress and strain in the case where the tangent moduli remain isotropic and constant. The form below is a first order expansion of general form often available in commercial FEA material libraries:

$$W = C_1(I_{\bar{c}} - 3) + \frac{1}{D_1}(J - 1)^2 \quad (1-43)$$

Neo-Hookean form is suitable for slightly compressible materials at low strains. The coefficient  $C_1$  represents the initial shear modulus of the material. Coefficient  $D_1$  represents the inverse of the initial bulk modulus.

### *Moony- Rivlin*

Moony-Rivlin (MR) form is motivated by the fact that the free energy of any homogeneous, isotropic material can be expressed as an infinite series of the three strain invariants [58]. For a first-order expansion, Mooney-Rivlin form is given by:

$$W = C_1(\bar{I}_1 - 3) + C_2(\bar{I}_2 - 3) + \frac{1}{D_1}(J - 1)^2 \quad (1-44)$$

It is evident in comparing Moony-Rivlin to Neo-Hookean form it is seen that Neo-Hookean is a reduced form of the first order MR form with  $C_2=0$ .

### *Ogden form.*

Ogden form, shown here for slightly compressible materials, describes the deviatoric portion of the hyperelastic potential in terms of the principal stretches rather than the invariants. Hence, implementation of Ogden form requires use of the eigenvectors in addition to the eigenvalues. Anisotropic behavior can develop along the principle directions, but the model is still “isotropic” in the sense that the elastic response can be derived from the deformation tensor without regard to reference coordinates. The non-

integer exponential coefficients also provide greater flexibility than polynomial forms in describing nonlinear deviatoric behavior at lower order expansions. The use of higher order expansions allows for detailed descriptions of polymeric behavior at high deviatoric strains.

$$W = \sum_{i=1}^N \frac{2\mu_i}{\alpha_i^2} (\bar{\lambda}_1^{\alpha_i} + \bar{\lambda}_2^{\alpha_i} + \bar{\lambda}_3^{\alpha_i}) + \frac{1}{D_1} (J-1)^2 \quad (1-45)$$

A hyperfoam version of the Ogden is similar to the expression above, except the volumetric term is expanded in similar fashion.

#### *Yeoh form*

The Yeoh form (also known as Reduced Polynomial Form) is a versatile polynomial form that can handle moderate material compressibility and moderate levels of deviatoric strain. It provides an even balance between the description deviatoric and volumetric behavior making it a good choice for an overall description of moderately compressible polymers. Yeoh form is given by:

$$W = C_{10}(\bar{I}_1 - 3) + C_{20}(\bar{I}_1 - 3)^2 + C_{30}(\bar{I}_1 - 3)^3 + \frac{1}{D_1}(J-1)^2 + \frac{1}{D_2}(J-1)^2 + \frac{1}{D_3}(J-1)^2 \quad (1-46)$$

where  $C_{10}$  and  $1/D_1$  represent the initial bulk and shear moduli, respectively.

### *Blatz-Ko*

Blatz-Ko form is of particular research in the context of this dissertation since it was developed for the express reason of describing the behavior of polyurethane foams. They derived a hyperelastic free energy function that describes the high compressibility of foams, which was lacking in most hyperelastic formulations at the time of its development. An interesting property of the Blatz-Ko form, not obvious from inspection, is that the elastic response depends only on the third invariant [37].

Blatz-Ko form is given by,

$$W = f \frac{\mu}{2} \left[ (I_1 - 3) + \frac{1}{\beta} (I_3^{-\beta} - 1) \right] + (1 - f) \frac{\mu}{2} \left[ \left( \frac{I_2}{I_3} - 3 \right) + \frac{1}{\beta} (I_3^\beta - 1) \right] \quad (1-47)$$

where,

$$\beta = \frac{\nu}{1 - 2\nu}$$

and  $f$  is an interpolation parameter that can vary between 0 and 1.

### ***1.2.2. Hyperviscoelasticity***

In recent years, there has been a considerable amount of development in hyperviscoelastic models. In 1985 Lubliner [18] introduced the general approach of incorporating viscoelasticity in which the free energy is additively separated into equilibrium and non-equilibrium parts. Lubliner considered the use of a Kelvin element and a Maxwell element to model relaxation and concluded that the Maxwell element is

advantageous since it is readily expanded for multiple relaxations. Since Lubliner, Holzapfel [19] and Nedjar [23], among others, have developed specific viscoelastic models using this approach.

### 1.3. Hypoelasticity

Hypoelasticity generally refers to the constitutive relationship between stress and strain in rate form [49]. It differs from the hyperelastic approach in that a unique, governing strain energy potential is not identified and often does not exist. Hence, unlike the hyperelastic form, the hypoelastic description can be path dependent. In this sense, the hypoelastic form is a more general description of constitutive behavior.

The velocity gradient,  $\mathbf{L}$ , can be additively split into a symmetric rate of deformation tensor,  $\mathbf{D}$  and an asymmetric spin tensor,  $\mathbf{W}$ :

$$\mathbf{L} = \mathbf{D} + \mathbf{W}, \quad (1-48)$$

where,

$$\mathbf{D} = \frac{1}{2}(\mathbf{L} + \mathbf{L}^T) \quad (1-49)$$

$$\mathbf{W} = \frac{1}{2}(\mathbf{L} - \mathbf{L}^T). \quad (1-50)$$

The velocity gradient is related to the deformation tensor as;

$$\mathbf{L} = \dot{\mathbf{F}} \cdot \mathbf{F}^{-1}. \quad (1-51)$$

For small strain, small displacement hypoelasticity the constitutive relationship is simply

$$\dot{\boldsymbol{\sigma}} = \mathbf{C}(p_1, p_2 \dots) : \mathbf{D} \quad (1-52)$$

For finite strain and displacements, the rotational portion of the velocity gradient must be accounted for to ensure objectivity of the stress rate. Objective stress rates can be developed by considering the polar decomposition of the deformation tensor. The rotation tensor may be used to rotate the Cauchy stress tensor back to the undeformed configuration.

$$\hat{\boldsymbol{\sigma}} = \mathbf{R}^T \cdot \boldsymbol{\sigma} \cdot \mathbf{R}. \quad (1-38)$$

Taking the time derivative gives the rate of Cauchy stress in the material's corotational reference frame,

$$\dot{\boldsymbol{\sigma}}^* = \dot{\mathbf{R}}^T \cdot \boldsymbol{\sigma} \cdot \mathbf{R} + \mathbf{R}^T \cdot \dot{\boldsymbol{\sigma}} \cdot \mathbf{R} + \mathbf{R}^T \cdot \boldsymbol{\sigma} \cdot \dot{\mathbf{R}}. \quad (1-53)$$

Rotating this rate forward to the spatial coordinates gives the Green-Naghdi rate;

$$\boldsymbol{\sigma}^{\nabla GN} = \mathbf{R} \cdot \dot{\boldsymbol{\sigma}}^* \cdot \mathbf{R}^T = \dot{\boldsymbol{\sigma}} - \boldsymbol{\Omega} \cdot \boldsymbol{\sigma} - \boldsymbol{\sigma} \cdot \boldsymbol{\Omega}^T, \quad (1-54)$$

where,

$$\boldsymbol{\Omega} = \dot{\mathbf{R}} \cdot \mathbf{R}^T. \quad (1-55)$$

If the spatial coordinate system coincides with the material coordinates we have:

$$\mathbf{R} = \mathbf{I}. \quad (1-56)$$

It can be also shown through consideration of the polar decomposition theorem (1-18) and equations (1-50) and (1-51) that in the absence of deformation,

$$\boldsymbol{\Omega} = \mathbf{W} \quad (1-57)$$

Making these substitutions into (1-54) we find that the Green-Naghdi rate coincides with the Jaumann rate:

$$\boldsymbol{\sigma}^{\nabla GN} = \boldsymbol{\sigma}^{\nabla J} = \dot{\boldsymbol{\sigma}} - \mathbf{W} \cdot \boldsymbol{\sigma} - \boldsymbol{\sigma} \cdot \mathbf{W} \quad (1-58)$$

Because the Jaumann form is written in terms of the corotational coordinate system it is often referred to as the corotational rate of Cauchy stress.

#### 1.4. Strain/Strain-Rate Reparability

In general, the Boltzmann superposition principle is invalid for nonlinear problems, and hence the viscoelastic response cannot be represented via Laplace transforms. However, linearity can be preserved under the assumption that nonlinear behavior is separable from linear viscoelastic rate dependence by factorization. Separability of the foam's rate dependence from its strain nonlinearity has been a key assumption, which sometimes goes unstated, in the development of hyperviscoelastic constitutive models. This is also true of the constitutive model developed in this dissertation. In these cases, and in the model developed in this dissertation, polymer stretching is assumed to not affect the relaxation spectra to a significant degree. Very little is found on this topic in the literature, but it should be expected that the validity of this assumption will depend greatly on the magnitude of strain and will surely vary among different polymer formulations.

Some authors have retained coupled strain and strain-effects in foam constitutive models. In the development of a one-dimensional compressive constitutive model for

automotive polyurethane foam (Sherwood [7]) strain is allowed to effect modify the exponential term in a power law description of rate-dependence. Compressive stress in the foam is given as the product of a “shape function” depending on the strain and a strain and strain-rate dependent modulus such that:

$$\sigma_c = f(\varepsilon)M(\varepsilon, \dot{\varepsilon}) \quad (1-59)$$

where,

$$f(\varepsilon) = \sum_{n=1}^{10} A_n \varepsilon^n \quad (1-60)$$

and

$$M(\varepsilon, \dot{\varepsilon}) = \left( \frac{\dot{\varepsilon}}{\dot{\varepsilon}_0} \right)^{(b_1 + b_2 \varepsilon)}. \quad (1-61)$$

Function  $M(\varepsilon, \dot{\varepsilon})$  gives the power-law stiffening effect of the polymer where  $\dot{\varepsilon}_0$  is the reference strain rate. The coupling term is the coefficient  $b$ , which was shown from experiments on polyurethane foam to be small but significant. However, Sherwood states that the motivation for the coupling term  $b_2$  in his model is pneumatic damping, presumably due to an open cell structure in the foam.

## 1.5. Plasticity

A permanent deformation develops in the VEM when strained beyond its elastic limit. Plasticity in polymers is often treated as a flow phenomenon that occurs when

stress exceeds the boundaries of an elastic space. In some cases, plasticity is assumed to occur at all strains and a loan dashpot is used to allow accumulation of simulate plastic set. This treatment essentially makes plasticity mathematically equivalent to a viscous creep phenomenon. Many rate independent plasticity models have also been developed, mostly for metals, and are attractive due to their simplicity and their ability to simulate experimentally observed plastic effects. However, such treatment is inappropriate for shock analysis since plasticity is an inherently rate dependent phenomenon.

## **1.6. High Strain – High Strain-rate Experiments**

### ***1.6.1. Split Hopkinson Pressure Bar***

The SHPB consists of a horizontally suspended, slender rod that is split at its center to accommodate test specimens. A striker rod is used to launch a compressive strain pulse that interacts with the specimen. The origins of the SHPB experiment date back more than a century. Development of the original Hopkinson Pressure Bar is credited to the work of British physicist John Hopkinson (1872) and his son Bertram Hopkinson. The development of the Split Hopkinson Pressure Bar in its present day form is credited to the work of Kolsky (1949) and Volterra (1948) who were the first to use the split configuration with a sandwiched specimen.

The use of strain gauges to monitor the pulse started to be used in SHPBs in the mid 1950s to early 1960s. Strain gauges are still widely used today, but recent investigators have begun making use of new developments in measurement techniques such as

piezoelectric velocimeters and laser Doppler vibrometry. Ramesh and Narasimhan (1996) [52] published some earliest results using laser vibrometry. Casem (2003) [44] has published results for low-density foams tested in a polymeric SHPB using electromagnetic velocimeters placed at the specimen interfaces.

The common approach to the SHPB developed with D'Alembert's classical solution to the 1-dimensional wave equation:

$$u(x,t) = f(x - ct) + g(x + ct) \quad (1-62)$$

Functions  $f$  and  $g$  represent waves propagating in the positive and negative  $x$ -direction, respectively. The shapes of the waves remain constant. The wave speed of a long slender rod is controlled by Young's modulus,

$$c = \sqrt{\frac{E}{\rho}} \quad (1-63)$$

Consider the wave traveling in the positive  $x$ -direction. The particle velocity is given by:

$$v_+ = -c \frac{\partial u}{\partial x} = -c\varepsilon. \quad (1-64)$$

Using the elastic relationship,  $\varepsilon = \sigma / E$ , and the wave speed equation we have,

$$v_+ = -\frac{\sigma}{\rho c}. \quad (1-65)$$

When compressive stress is taken to be positive we have,

$$v_+ = \frac{\sigma_c}{\rho c} \quad (1-66)$$

It follows that the particle velocity associated with the traveling in the negative x-direction is given by,

$$v_- = -\frac{\sigma_c}{\rho c}. \quad (1-67)$$

At the interface of the incident bar and the specimen there must be a continuity of stress and velocity. Continuity of stress at the interfaces provides:

$$\sigma_s |_{\text{int}1} = \sigma_i |_{\text{int}1} + \sigma_r |_{\text{int}1} \quad (1-68)$$

$$\sigma_s |_{\text{int}2} = \sigma_t |_{\text{int}1}. \quad (1-69)$$

It is commonly assumed that the specimen is sufficiently short such that the stress in the specimen is nearly uniform. With this assumption the average of the interface stresses are reported as the sample stress:

$$\bar{\sigma}_s = \sigma_i |_{\text{int}1} + \sigma_r |_{\text{int}1} + \sigma_t |_{\text{int}2} \quad (1-70)$$

$$\bar{\sigma}_s = \sigma_i |_{\text{int}1} + \sigma_r |_{\text{int}1} + \sigma_t |_{\text{int}2} \quad (1-71)$$

$$\bar{\sigma}_s = \frac{1}{2} \rho c^2 (\varepsilon_i + \varepsilon_r + \varepsilon_t). \quad (1-72)$$

The average specimen strain is given by:

$$\bar{\varepsilon}_s = \frac{1}{2} \frac{u_1 - u_2}{l} = \frac{c}{l} \int_0^t (\varepsilon_i - \varepsilon_r - \varepsilon_t) dt, \quad (1-73)$$

where  $t=0$  refers to the arrival time at the first interface. Hence, the strain rate of the specimen is given by:

$$\dot{\varepsilon}_s = \frac{c}{l}(\varepsilon_i - \varepsilon_r - \varepsilon_t). \quad (1-74)$$

Numeric integration of equation (1-74) with strain gauge data, using the appropriate time offsets to locate the data at the interfaces, gives the specimen strain. The above equations for the sample stress and strain are valid for short specimens that are closely matched to the bar's wave speed characteristics. Also, the dimensional change of the specimen is assumed negligible. For polymeric materials with relatively low wave speeds, the above relationships are invalid and a different analytical approach must be used. A number of investigators have pursued analytic approaches that account for wave propagation and deformation of the specimen. More recent investigations have utilized finite element modeling for data analysis.

### ***1.6.2. Conical Shock Tube***

Underwater shock experiments were conducted on the RUBATEX foam in the Navy's Conical Shock Tube (CST) facility operated by the Naval Underwater Warfare Center in Newport, Rhode Island. The CST is a 20-ft. long thick-walled steel waveguide with a conical bore. A blast cap is fired at the small diameter end and the wave is guided to the cylindrical test specimen, which is typically 9 1/2" in diameter. The CST simulates a small sector of a spherical blast. The device is used by the Navy to evaluate vessel components in at shock levels similar to underwater explosions. More recently the Office

of Naval Research (ONR) has sponsored material investigations using the CST similar to the present work, which motivated the choice of this experimental approach.

### **1.7. Objectives of Current Research**

The primary objective of this work is to develop and validate a constitutive model that can serve as a useful engineering tool for the numerical characterization of viscoelastic foams under conditions of compressive shock. The goals for achieving this objective are,

- 1) To minimize the characterization experiments needed for establishing the material model.
- 2) To minimize the number of coupled material parameters.
- 3) To implement the constitutive model in commercially available software package.

The term “coupled material parameters” in goal #2 refers to those parameters that cannot be isolated for characterization. For example, the Prony representation of the host shear modulus can require tens of parameters to cover the relaxation spectrum. These parameters are uncoupled in the sense that they can be characterized independently without ambiguous influence from the other material parameters.

We are particularly interested in developing an accurate description of the loss of shock isolation that may occur during the densification process. This is critical for the proper design of shock isolation treatments. For shock isolation, material designers are often concerned about the level of shock isolation provided and at what level of shock the

treatment ceases to function. We also seek a constitutive formulation that is compatible with most implicit and explicit finite element approaches.

A secondary objective is to gain insight into the material physics of closed-cell foams. Understanding the fundamental mechanisms of shock isolation and energy absorption is important for the efficient development of specialized material treatments. To this end, an attempt is made to retain tangible meaning to the material parameters that describe the constitutive behavior.

Of course, experimental validation of the proposed constitutive model is an objective of this work. Two experiments are used for this purpose - a Split Hopkinson Pressure Bar (SHPB) and a Conical Shock Tube (CST). These two experiments have different advantages and disadvantages. The SHPB experiment is relatively fast and simple allowing for the investigation of multiple shock levels and specimen thicknesses. A limitation of the SHPB is the achievable sample aspect ratio. The bar is only  $\frac{3}{4}$ " diameter, so large diameter-to-thickness aspect ratios would require specimens of undesirably small thickness. The Conical Shock Tube is a more complicated experiment to conduct as it requires specimen rigging in a water-filled tube and the use of real explosives to generate a fluid-borne shock wave. Its key advantage for the present study is the larger specimen size it can accommodate, which is about  $9\frac{1}{2}$ " in diameter. This permits much larger aspect ratios.

## 1.8. Summary

From the Elastic-Viscoelastic Correspondence Principle, the basic concepts of 3-dimensional linear elasticity and one-dimensional viscoelasticity can be extended to form a 3-dimensional viscoelastic theory for small deformations. Multiplication of the viscoelastic matrix with the strain tensor forms a stress tensor whose components are given by the sum of hereditary integrals. This provides a general approach to solving 3-dimensional viscoelasticity problems.

Viscoelastic models such as the Prony series provide a means of describing viscoelastic behavior with a mechanical system of springs and dashpots. In a time-incremental analysis, monitoring of the internal strain (or stress) variables within the viscoelastic model allows the hereditary integrals to be computed throughout the analysis.

Two possible approaches for describing constitutive behavior under finite deformation and displacement are the hyperelastic and hypoelastic formulations. The hyperelastic approach is attractive because it ensures path-independence, which is a reasonable assumption for rubber-like materials. Inelastic behaviors like plasticity and damage can be incorporated, and such hyperelastic models have been developed. This is often accomplished by introducing additional free energy functions potential to the hyperelastic potential as is done in models developed by Bickard [38] and Simo [20]. A drawback to the hyperelastic approach is that common forms are limited in their descriptive power for nonlinear behavior. For example, when using a polynomial form of the hyperelastic energy function, the polynomial order of the tangent moduli derived

from the potential function is reduced by two. This deficiency can be overcome by extending the polynomial order, but this comes at the risk of stability problems of the type described by Drucker [50]. Drucker stability requires that the tangential material stiffness be positive definite at all times [12].

A key advantage of hypoelastic form is the ease at which strain dependent behavior can be introduced. It can describe both path-dependent and path independent materials, whereas a hyperelastic model can only describe the latter. This makes hypoelastic formulations the clear choice for describing materials like soil where effects like packing can alter the equilibrium-state of the material and hence the governing potential. Likewise, they are also widely used to describe large strain plasticity in metals, especially for simulating metal forming operations. The major drawback to hypoelastic formulations is that they are typically limited to small strains.

There are few experimental devices that test materials at a combination of high strains and high rates of strain. The SHPB is one of the oldest and best known of these devices. It is widely used by researchers due to its simplicity, ease of use and adaptability. The Conical Shock Tube facility at the Naval Surface Underwater Warfare Center is a unique facility that is used to subject samples to a waterborne shock wave.

## **CHAPTER 2**

### **2. Constitutive Theory**

In this section we will develop a hyperviscoelastic constitutive model for highly deformable elastomeric foams suitable to describe behavior under compressive shock conditions. The model is constructed from parameterized functions describing the static tangent moduli of foams under hydrostatic conditions. The tangent moduli expressions are related to a hyperelastic energy function whose form is judiciously selected such that it is uniquely defined by these moduli. A modified version of a three-phase composite theory is used to describe the tangent moduli. Use of the three-phase formulae for the effective bulk and shear moduli permit the multiplicative separation of the host shear modulus from a nonlinear strain function in the stress equation. Also, it permits an additive separation of the gaseous and viscoelastic phases. A phenomenological correction to the composite theory is included to account for stress-induced collapse of the foam's microstructure. A plasticity model is introduced to the first element in the Prony series based motivated by the approaches used by Bardenhagen [35] and Nedjar [23].

#### **2.1. Three-phase Composite Theory**

An effective properties model by Kerner will be used to help formulate the constitutive behavior. The Kerner model is based on a three-phase analysis consisting of a unit cell surrounded by the effective medium as shown in Figure 2-1.

Since the three-phase problem is posed in terms of a spherical inclusion, it is incapable of describing geometric softening effects that occur due to cell wall bending and distributed elastic instabilities. To correct this deficiency, a phenomenological cell-wall bending factor will be introduced to modify the effective moduli equations.

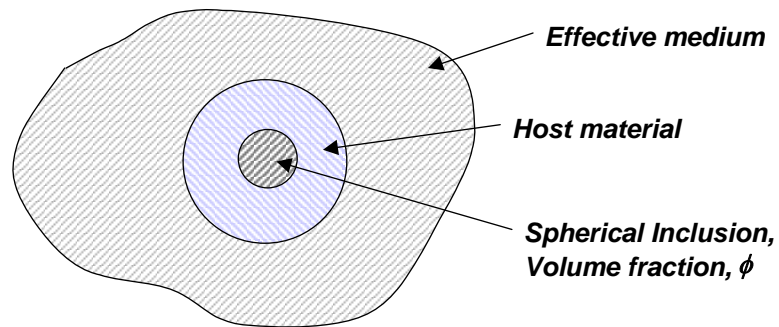


**Figure 2-1 Three-Phase model**

Kerner developed relationships of the effective moduli for composites consisting of a matrix material containing spherical inclusions of one or more different materials. The analysis is sufficiently general such that it can be used to estimate the effective moduli of closed-cell foams given the assumption that the voids are reasonably spherical. The Kerner relationships provide expressions for the effective moduli of the composite in terms of the matrix moduli, and the moduli and volume fractions of the inclusions.

Kerner's equations for the effective bulk and shear moduli of a composite containing just one filler are given by:

$$K = \frac{\frac{(1-\phi)K_H}{3K_H + 4\mu_H} + \frac{\phi K_{inc}}{3K_{inc} + 4\mu_H}}{\frac{(1-\phi)}{3K_H + 4\mu_H} + \frac{\phi}{3K_{inc} + 4\mu_H}} \quad (2-1)$$

$$\mu = \mu_H \left( \frac{\frac{\phi \mu_{inc}}{(7-5\nu_H)\mu_H + (8-10\nu_H)\mu_{inc}} + \frac{1-\phi}{15(1-\nu_H)}}{\frac{\phi \mu_H}{(7-5\nu_H)\mu_H + (8-10\nu_H)\mu_{inc}} + \frac{1-\phi}{15(1-\nu_H)}} \right), \quad (2-2)$$

where  $\phi$  is the void fraction,  $K$  and  $\mu$  are the bulk and shear moduli of the host polymer and  $K_{inc}$  and  $\mu_{inc}$  are the bulk and shear moduli of the inclusion. Subscript “ $H$ ” to specifies the host polymer. For a foam, we use the above equations with inclusion properties of an ideal gas. Hence, the shear moduli of the inclusion are set to zero. This leads to a simplified form of the Kerner equations as follows:

$$K = \frac{\frac{(1-\phi)K_H}{3K_H + 4\mu_H} + \frac{\phi K_{inc}}{3K_{inc} + 4\mu_H}}{\frac{(1-\phi)}{3K_H + 4\mu_H} + \frac{\phi}{3K_{inc} + 4\mu_H}} \quad (2-3)$$

$$\mu = \mu_H \left( \frac{\frac{1-\phi}{15(1-\nu_H)}}{\frac{\phi}{(7-5\nu_H)} + \frac{1-\phi}{15(1-\nu_H)}} \right) \quad (2-4)$$

Polymer incompressibility is also assumed, ( $K \rightarrow \infty, \nu \rightarrow 1/2$ ), so equations (2-3) and (2-4) can be further simplified:

$$K = \mu_H \left( \frac{4(1-\phi)}{3\phi} \right) + \frac{K_{air}}{\phi} \quad (2-5)$$

$$\mu = \mu_H \left( \frac{1-\phi}{1+\frac{2}{3}\phi} \right) \quad (2-6)$$

Christensen also analyzed the three-phase model but arrived at a different equation for the shear modulus. He attributes his discrepancy with Kerner's shear modulus equation to the latter's assumption of a uniform shear state, although he could not demonstrate this conclusively due to the brevity of Kerner's paper. Since Christensen makes no such assumption, his equation presumably represents the exact solution for the three-phase problem as posed in Figure 2-1<sup>1</sup>. In consideration of Christensen's assertion, Kerner's shear modulus equation should be considered only as an approximate solution to the three-phase problem. Christensen's "exact" three-phase solution for the effective shear modulus, reduced for the case of an incompressible matrix containing spherical gaseous inclusions, reduces to the following expression,

$$\mu = \mu_H \left( \frac{-19\phi^{10/3} + 450\phi^{7/3} - 672\phi^{5/3} + 250\phi - 9 + 5\sqrt{361\phi^{20/3} + 76\phi^{13/3} - 5502\phi^{10/3} + 9408\phi^{8/3} - 4700\phi^2 - 84\phi + 441}}{76\phi^{10/3} + 450\phi^{7/3} - 672\phi^{5/3} + 400\phi + 96} \right) \quad (2-7)$$

Clearly, Christensen's shear modulus equation (2-7) is more cumbersome than the Kerner's shear equation (2-6) and for this reason we would prefer to proceed using Kerner's equation. Convenience alone is not a compelling motivation to choose Kerner's equation over Christensen's, hence the impact this choice is evaluated in the numerical simulations of the SHPB experiment in chapter 6 for a specific case. This exercise also provides the opportunity to gauge the significance of deviatoric response in the SHPB experiment, testing the assumption that deviatoric experiments are unnecessary to characterize foams for compressive shock loads.

The reduced three-phase equations contain just one geometric parameter - the void fraction. Hence, these formulas can also be used to describe the dependence of the effective moduli under pure volumetric strain since, given the assumption that the microstructure remains reasonably spherical, the effect of volumetric strain on the microstructure is to change the effective void fraction and the internal gas pressure.

---

<sup>1</sup> The three-phase shear modulus expression in Christensen's book [4] contains two small errors. A corrected derivation can be found in [59].

The gas bulk modulus term that appears in equation (2-5) is readily developed. Given a volume of gas,  $V_{gas}$ , trapped within a unit volume of the foam material the bulk modulus of the gas is related to the pressure and volume as follows:

$$K_{gas} = -V_{gas} \frac{\partial P}{\partial V_{gas}} \quad (2-8)$$

From Boyle's law the pressure can be written as,

$$P = P_0 \frac{V_{0,gas}}{V_{gas}} \quad (2-9)$$

Substituting (2-9) into (2-8) we have:

$$K_{gas} = P_0 \frac{V_{0,gas}}{V_{gas}} = P_0 \frac{V_{0,gas}}{(V_{0,gas} + \Delta V_{gas})} \quad (2-10)$$

The initial gas volume is given by,

$$V_{0,gas} = (1 - S_0) \quad (2-11)$$

Incompressibility of the host polymer requires that the change in gas volume is the same as the change in the total volume such that:

$$\Delta V_{gas} = \Delta V = (J - 1) \quad (2-12)$$

Substituting (2-11) and (2-12) into (2-10) gives the bulk modulus of the entrapped gas in terms of the initial solidity, initial gas pressure and volumetric stretch we find:

$$K_{gas} = P_0 \frac{(1 - S_0)}{(J - S_0)} \quad (2-13)$$

Again using the assumption of polymer incompressibility, the void fraction term that appears in the effective moduli expressions of is related to the volume stretch as follows:

$$\phi = \frac{(J - S_0)}{J} \quad (2-14)$$

Substituting (2-14) and (2-13) into equations (2-5) and (2-6) gives the effective moduli in terms of the volumetric stretch,

$$K = \mu_H \left( \frac{4S_0}{3(J - S_0)} \right) + P_0 \frac{J(1 - S_0)}{(J - S_0)^2} \quad (2-15)$$

$$\mu = \mu_H \left( \frac{3S_0}{5J - 2S_0} \right) \quad (2-16)$$

It is evident from (2-15) and (2-16) that the Kerner formulas are consistent with expected limit at full densification,

$$\mu|_{J \rightarrow S_0} = \mu_H \quad (2-17)$$

$$K|_{J \rightarrow S_0} = \infty. \quad (2-18)$$

Figure 2-2 examines the agreement of the approximate formula for bulk modulus with the exact formula. The plot compares the effective bulk modulus from each formula as a function of void fraction and for different values of host shear modulus. The figure shows that the approximation breaks down at low void fractions and for high shear

modulus values, but provides a good estimate over a fairly wide range of conditions. For the low modulus rubbers under investigation, the approximation is quite good even near the limit of densification.

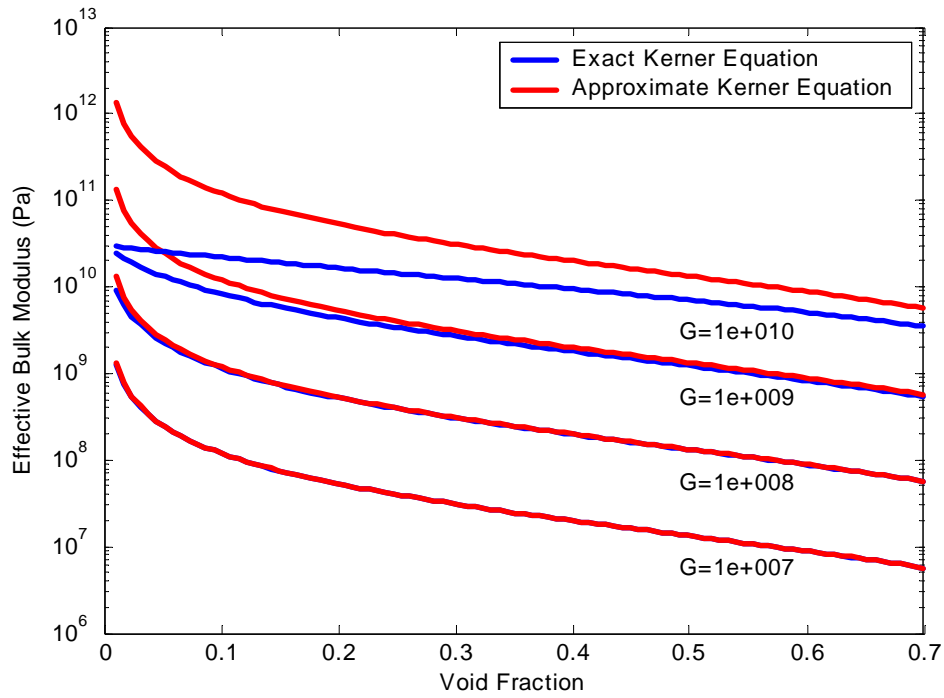


**Figure 2-2 Exact and approximate Kerner equations for the effective bulk modulus of a voided rubber**

## 2.2. Cell-Wall Bending Softening Factor

Low-density foams often exhibit a large cell-wall bending effect under compressive load. In this bending region the effective tangent moduli drop significantly. This behavior is often seen in load deflection tests on foams where a stress-plateau region over some span of compressive strain. The three-phase model as posed in Figure 2-1 provides no description of this important transition, but the effect can be simulated by a modulus reduction in the bending region. Numerous phenomenological models have been proposed to describe foam behavior over the entire range of compression and tension [45]. We propose a phenomenological correction based on the following assumptions:

- 1) The transition from compressive strain to bending strain within the cell walls is distributed over a span of compressive strain.
- 2) The bending transition affects both the deviatoric and volumetric portion of the constitutive relation equally.
- 3) The hydrostatic bulk modulus can approach zero values, but cannot become negative

The second assumption is highly important. It means that a softening effect is to be applied equally to both the hydrostatic shear modulus and the bulk modulus. We base this assumption on Ashby's equations for low-density foams. Bending within the microstructure largely controls their effective moduli and Ashby's equations provide the

same behavior of the bulk and Young's moduli. Accordingly, the Poisson's ratio, which is related to the ratio of moduli, is unaffected.

A softening factor is developed by considering the material as being comprised of a mix of pre-bending and post-bending regions. Three parameters are introduced to incorporate the softening behavior. The first two parameters,  $C_1$  and  $C_2$ , are used in a hyperbolic tangent function that is intended to describe the cumulative distribution, based on volume, of the material that has passed into the bending mode. The fraction of cells that have transitioned to a bending mode being given by:

$$f_b = \frac{\tanh(C_2 * (C_1 - J)) + 1}{2} \quad (2-19)$$

The third parameter,  $D_2$ , is a coefficient to modify the strength of the strain-induced softening effect. The homogenized softening factor is then given by:

$$SF = 1 - D_2 f_b. \quad (2-20)$$

This softening factor is applied to the viscoelastic term of the hydrostatic bulk modulus as follows:

$$\hat{K}(J) = D_1 \left( \frac{4S_0}{3(J - S_0)} \right) SF + P_0 \frac{J(1 - S_0)}{(J - S_0)^2} \quad (2-21)$$

The final forms for the tangent moduli as function of model parameters and the volumetric stretch are then given by:

$$\hat{K}(J) = D_1 \left( \frac{4S_0}{3(J - S_0)} \right) \left( 1 - \frac{1}{2} D_2 (\tanh(C_2 * (C_1 - J)) + 1) \right) + P_0 \frac{J(1 - S_0)}{(J - S_0)^2} \quad (2-22)$$

$$\hat{\mu}(J) = D_1 \left( \frac{3S_0}{5J - 2S_0} \right) \left( 1 - \frac{1}{2} D_2 (\tanh(C_2 * (C_1 - J)) + 1) \right) \quad (2-23)$$

With the introduction of the bending correction, the resulting moduli equations must be classified as phenomenological in a strict sense. But the parameters do bear tangible significance and can provide some insight to the material physics. The significance of the material parameters is summarized in Table 2-1.

In the next two sections, the Kerner moduli will be incorporated into finite strain constitutive formulations.

**Table 2-1. Summary of Three-Phase Parameters**

Parameter	Constraints	Physical Significance
$D_1$	Real, positive	Quasi-static shear modulus of the host polymer
$D_2$	Real, positive $0 < D_2 < 1$	Softening coefficient.  Complete softening in bending region as $D_2 \rightarrow 1$ .  No softening in bending region as $D_2 \rightarrow 0$
$C_1$	Real, positive $S_0 < C_1 < 1$	Center point of the bending transition given in terms of volumetric stretch.
$C_2$	Real, positive	Sharpness of the bending transition.  Broadening distribution as $C_2 \rightarrow 0$  Narrowing distribution as $C_2 \rightarrow \infty$
$P_0$	Real, positive	Initial gas pressure within the closed cells
$S_0$	Real, positive $0 < S_0 < 1$	Initial foam solidity

### 2.3. Consistent Hyperelastic Form

In this section the general form of the hyperelastic free energy is developed. The selection of this form is guided by the desire of having the associated tangent moduli coincide with the composite theory in the case of infinitesimal deviatoric strain.

We begin with a judicious selection of a consistent form of the free energy function. By consistent, we mean that equality with the Kerner moduli is enforceable for all values of pure hydrostatic strain. We begin with an additive decomposition of the hyperelastic free energy into two energy functions:

$$W = W^{(1)}(J) + W^{(2)}(J, I_{\bar{c}}). \quad (2-24)$$

This choice of form provides one function that depends only on volumetric stretch,  $J$ , and a “mixed” function that depends both on volumetric stretch and a deviatoric strain invariant,  $I_{\bar{c}}$ . The second term is further split multiplicatively to separate volumetric and deviatoric strain dependence:

$$W^{(2)} = \Phi(J)\Gamma(I_{\bar{c}}). \quad (2-25)$$

This second term contains the deviatoric dependence of the energy density function. Since a major thesis is that deviatoric experiments can be forgone, no experimental data will be used to help establish the second term. Rather, we will rely entirely on three-phase composite theory to establish  $\Phi(J)$ . Moreover, there will no basis whatsoever to

establish  $\Gamma(I_{\bar{c}})$  making the only reasonable choice for deviatoric strain dependence first order. This leads to the general hyperelastic form,

$$W = \Psi(J) + \Phi(J)(I_{\bar{c}} - 3) \quad (2-26)$$

In section 2.4 the stress and tangent moduli are derived from the general form. In Section 2.5 we will show that the functions  $\Psi(J)$  and  $\Phi(J)$  can be identified in terms of the hydrostatic bulk and shear moduli, respectively.

## 2.4. Stress and Tangent Moduli

With the proposed hyperelastic form defined, the stress and tangent moduli can be derived. First, the second Piola-Kirchhoff stress is developed. The stress tensor is given by:

$$\mathbf{S} = 2 \frac{\partial W}{\partial \mathbf{C}}. \quad (2-27)$$

By the chain rule we have,

$$\mathbf{S} = 2 \frac{\partial W}{\partial \mathbf{C}} = 2 \left[ \left( \frac{\partial W}{\partial J} \right) \frac{\partial J}{\partial \mathbf{C}} + \left( \frac{\partial W}{\partial I_c} \right) \frac{\partial I_c}{\partial \mathbf{C}} \right]. \quad (2-28)$$

The following three matrix identities are useful for the following development:

**Table 2-2 Matrix Identities of Symmetric Matrix C**

<b>X</b>	<b>MATRIX FORM</b>	<b>TENSOR FORM</b>
$\frac{\partial I_c}{\partial \mathbf{C}}$	$\mathbf{X} = \mathbf{I}$	$X_{IJ} = \delta_{IJ}$
$\frac{\partial J}{\partial \mathbf{C}}$	$\mathbf{X} = \frac{J}{2} (2\mathbf{C}^{-1} - \mathbf{C}^{-1} \circ \mathbf{I})$	$X_{IJ} = \frac{J}{2} (2C_{IJ}^{-1} - C_{IJ}^{-1} \delta_{IJ})$
$\frac{\partial I_{\bar{c}}}{\partial \mathbf{C}}$	$\mathbf{X} = J^{-2/3} \mathbf{I} - \frac{1}{3} I_{\bar{c}} (2\mathbf{C}^{-1} - \mathbf{C}^{-1} \circ \mathbf{I})$	$X_{IJ} = J^{-2/3} \delta_{IJ} - \frac{1}{3} I_{\bar{c}} (2C_{IJ}^{-1} - C_{IJ}^{-1} \delta_{IJ})$
$\frac{\partial \mathbf{C}^{-1}}{\partial \mathbf{C}}$	$\mathbf{X} = -\mathbf{C}^{-1} \frac{\partial \mathbf{C}}{\partial \mathbf{C}} \mathbf{C}^{-1}$	$X_{IJKL} = (C_{IK}^{-1} C_{LJ}^{-1} + C_{IL}^{-1} C_{KJ}^{-1}) (1 - \delta_{KL}/2)$
$\frac{\partial (\mathbf{C}^{-1} \circ \mathbf{I})}{\partial \mathbf{C}}$	$\mathbf{X} = \left( -\mathbf{C}^{-1} \frac{\partial \mathbf{C}}{\partial \mathbf{C}} \mathbf{C}^{-1} \right) \circ \mathbf{I}$	$X_{IJKL} = (C_{IK}^{-1} C_{LJ}^{-1} + C_{IL}^{-1} C_{KJ}^{-1} - \delta_{KL} C_{IK}^{-1} C_{LJ}^{-1}) \delta_{IJ}$

Making use of the above identities, the stress tensor derived from the hyperelastic free energy is then given by:

$$\mathbf{S} = 2 \left[ (\Psi_{,J} + \Phi_{,J} (I_{\bar{c}} - 3)) \frac{J}{2} (2\mathbf{C}^{-1} - \mathbf{C}^{-1} \circ \mathbf{I}) + \Phi \left( J^{-2/3} \mathbf{I} - \frac{1}{3} I_{\bar{c}} (2\mathbf{C}^{-1} - \mathbf{C}^{-1} \circ \mathbf{I}) \right) \right]$$

$$\mathbf{S} = \left[ (J\Psi_{,J} + J\Phi_{,J} (I_{\bar{c}} - 3)) (2\mathbf{C}^{-1} - \mathbf{C}^{-1} \circ \mathbf{I}) + 2\Phi J^{-2/3} \mathbf{I} - 2\Phi \frac{1}{3} I_{\bar{c}} (2\mathbf{C}^{-1} - \mathbf{C}^{-1} \circ \mathbf{I}) \right]$$

$$\mathbf{S} = \left[ \left( J\Psi_{,J} + J\Phi_{,J}(I_{\bar{C}} - 3) - \frac{2}{3}\Phi I_{\bar{C}} \right) (2\mathbf{C}^{-1} - \mathbf{C}^{-1} \circ \mathbf{I}) + 2\Phi J^{-2/3} \mathbf{I} \right]. \quad (2-29)$$

The Lagrangian tangent moduli can be formed using:

$$\mathbf{K} = 2 \frac{\partial \mathbf{S}}{\partial \mathbf{C}} \quad (2-30)$$

This gives:

$$\begin{aligned} K_{IJKL} = & \left( J^2(\Psi_{,JJ} - 3\Phi_{,JJ}) + J(\Psi_{,J} - 3\Phi_{,J}) \right) + \left( J^2\Phi_{,JJ} - \frac{1}{3}J\Phi_{,J} + \frac{4}{9}\Phi \right) I_{\bar{C}} \Big) C_{IJ}^{-1} C_{KL}^{-1} \\ & + \left( 2\Phi_{,J} J^{1/3} - \frac{4}{3}\Phi J^{-2/3} \right) (\delta_{IJ} C_{KL}^{-1} + C_{IJ}^{-1} \delta_{KL}) \\ & - 2 \left( J\Psi_{,J} + J\Phi_{,J}(I_{\bar{C}} - 3) - \frac{2}{3}\Phi I_{\bar{C}} \right) (C_{IK}^{-1} C_{LJ}^{-1} + C_{IL}^{-1} C_{KJ}^{-1} - \delta_{KL} C_{IK}^{-1} C_{LJ}^{-1}) \end{aligned} \quad (2-31)$$

The tangent moduli relating Kirchhoff stress and the rate of deformation can also be determined from the Lagrangian tangent moduli via a “push forward” transformation involving the deformation gradient:

$$K_{ijkl}^{\tau:D} = F_{iI} F_{jJ} F_{kK} F_{lL} K_{IJKL}^{S:E}.$$

### *2.4.1. A Note on Stability*

With the introduction of a bending transition we have introduced the possibility of Drucker instability under certain deformations. Consider the form of the hyperelastic free energy shown in equation (2-26). The volumetric term,  $\Psi(J)$ , is unconditionally stable, provided that the hydrostatic bulk modulus is always positive, since it is related to hydrostatic bulk modulus via double integration of equation (2-37). This is not the case for the deviatoric term,  $\Phi(J)$ , which is directly related to the hydrostatic shear modulus via equation (2-46). Hence, if there is a reduction in the hydrostatic shear modulus with an increase in volumetric deformation due to bending effects, the possibility exists that the net change in free energy will be negative. This is also evident in the elastic response given by equation (2-29). The first derivative of the hydrostatic shear modulus function with respect to  $J$  appears in the equation with the deviatoric strain. In the bending transition, this derivative can be positive and large causing negative stresses to develop in the presence of shear deformation.

If needed, Drucker instability can be controlled with the constitutive model by artificially reducing the sharpness parameter,  $C_2$ . Drucker instability was encountered in several cases for the modeling done for this dissertation.

## **2.5. Relationship between the Hyperelastic Form and Hydrostatic Moduli**

We seek to make the tangent moduli as derived from the hyperelastic formulation consistent with the modified three-phase theory for the case of pure triaxial strain. The

hyperelastic tangent moduli can be derived from the Cauchy stress following the approach used by Scott [53]. The Cauchy stress is first derived from the Second Piola-Kirchhoff stress:

$$\boldsymbol{\sigma} = J^{-1} \mathbf{F} \cdot \mathbf{S} \cdot \mathbf{F}^T \quad (2-32)$$

For our specific hyperelastic form we have for the second Piola-Kirchhoff stress,

$$\mathbf{S} = \left[ \left( J\Psi_{,J} + J\Phi_{,J}(I_{\bar{C}} - 3) - \frac{2}{3}\Phi I_{\bar{C}} \right) (2\mathbf{C}^{-1} - \mathbf{C}^{-1} \circ \mathbf{I}) + 2\Phi J^{-2/3} \mathbf{I} \right] \quad (2-33)$$

The Cauchy stress tensor is then given by,

$$\boldsymbol{\sigma} = \left( \Psi_{,J} + \Phi_{,J}(J^{-2/3}I_C - 3) - \frac{2}{3}\Phi J^{-5/3}I_C \right) \mathbf{I} + 2\Phi J^{-5/3} \mathbf{B} \quad (2-34)$$

Under pure hydrostatic strain,  $\mathbf{B} = J^{2/3} \mathbf{I}$ , and the Cauchy stress tensor simplifies to;

$$\boldsymbol{\sigma} = \Psi_{,J} \mathbf{I} \quad (2-35)$$

The tangent bulk modulus is then derived from the Cauchy stress tensor:

$$\widehat{K}(J) = \frac{J}{3} \left( \frac{\partial \sigma_{pp}}{\partial J} \right)_{\lambda_1=\lambda_2=\lambda_3=J^{1/3}} \quad (2-36)$$

This leads to the following relationship between the hydrostatic bulk modulus and the potential function,  $\Psi$ ,

$$\widehat{K}(J) = J\Psi_{,JJ} \quad (2-37)$$

We use a similar approach to develop the deviatoric potential function  $\Phi$ . In this case, the task is to relate the tangent shear modulus from composite theory the hyperelastic function. To sample the shear modulus, a perturbation shear deformation is introduced. We make the perturbation to the material already in a state of finite volumetric strain where the deformation is given by,

$$\mathbf{F} = J^{\frac{1}{3}} \begin{bmatrix} 1 & 0 & 0 \\ 0 & 1 & 0 \\ 0 & 0 & 1 \end{bmatrix}. \quad (2-38)$$

Next, an incremental deformation gradient due to a small shearing angle,

$$\Delta\mathbf{F} = \begin{bmatrix} 1 & \gamma & 0 \\ 0 & 1 & 0 \\ 0 & 0 & 1 \end{bmatrix}. \quad (2-39)$$

The perturbed right-Cauchy Green tensor is then given by:

$$\mathbf{C} = \mathbf{F}^T (\Delta\mathbf{F}^T \Delta\mathbf{F}) \mathbf{F} = J^{\frac{2}{3}} \begin{bmatrix} 1 & \gamma & 0 \\ \gamma & 1 + \gamma^2 & 0 \\ 0 & 0 & 1 \end{bmatrix}. \quad (2-40)$$

The perturbed left-Cauchy strain tensor is identical.

Recalling that  $\bar{\mathbf{C}} = J^{\frac{2}{3}} \mathbf{C}$ , the perturbed invariant is given by:

$$I_{\bar{\mathbf{C}}} - 3 = \gamma^2, \quad (2-41)$$

and the Cauchy stress tensor can be written as follows:

$$\boldsymbol{\sigma} = \left( \Psi_{,J} + \Phi_{,J} \gamma^2 - \frac{2}{3} \Phi J^{-1} (\gamma^2 + 3) \right) \mathbf{I} + 2\Phi J^{-1} \begin{bmatrix} 1 & \gamma & 0 \\ \gamma & 1 + \gamma^2 & 0 \\ 0 & 0 & 1 \end{bmatrix} \quad (2-42)$$

$$\boldsymbol{\sigma} = (\Psi_{,J} - 2\Phi J^{-1}) \mathbf{I} + 2\Phi J^{-1} \begin{bmatrix} 1 & \gamma & 0 \\ \gamma & 1 + \gamma^2 & 0 \\ 0 & 0 & 1 \end{bmatrix} \quad (2-43)$$

$$\boldsymbol{\sigma} = \begin{bmatrix} \Psi_{,J} & 2\Phi J^{-1} \gamma & 0 \\ 2\Phi J^{-1} \gamma & \Psi_{,J} + 2\Phi J^{-1} \gamma^2 & 0 \\ 0 & 0 & \Psi_{,J} \end{bmatrix}. \quad (2-44)$$

The tangent shear can now be identified:

$$\hat{\mu}(J) = \frac{\partial \sigma_{12}}{\partial \gamma} = 2\Phi J^{-1}. \quad (2-45)$$

Finally, rearranging equation (2-45) provides our expression for  $\Phi$ :

$$\Phi(J) = \frac{J \hat{\mu}(J)}{2}. \quad (2-46)$$

Equation is analogous to the relationship found in neo-Hookean form,  $C_{10} = \frac{\mu_0}{2}$ , where

the initial modulus is replaced with one that varies with the volumetric stretch.

Equations (2-37) and (2-46) provide the defining relationships between hydrostatic moduli and the hyperelastic free energy, completing the general form. A key feature of Kerner's equation for effective bulk modulus is that it also allows us to express separate a material phase and a gas phase contributions;

$$\widehat{K}(J) = \widehat{K}^g(J) + \widehat{K}^m(J) \quad (2-47)$$

Hence, it follows from equation (2-37) that an additive split of the energy potential can be made:

$$\Psi(J) = \Psi^g(J) + \Psi^m(J) \quad (2-48)$$

### 2.5.1. Nonlinear Strain Functions

With equations (2-37) and (2-46) the second Piola-Kirchhoff stress tensor can be written in terms of the hydrostatic tangent moduli derived from three-phase composite theory.

$$\mathbf{S} = \left( J\Psi_{,J}^g + J\Psi_{,J}^m + J\Phi_{,J}(I_{\bar{C}} - 3) - \frac{2}{3}\Phi I_{\bar{C}} \right) (2\mathbf{C}^{-1} - \mathbf{C}^{-1} \circ \mathbf{I}) + 2\Phi J^{-2/3} \mathbf{I} \quad (2-49)$$

where,

$$\Psi_{,J}^g = P_0(1 - S_0) \int_0^J \frac{dx}{(x - S_0)^2}, \quad (2-50)$$

$$\Psi_{,J}^m = 4D_1 S_0 \int_0^J \frac{1 - \frac{1}{2} D_2 (\tanh(C_2(C_1 - x)) + 1)}{3(x - S_0)} dx, \quad (2-51)$$

$$\Phi = D_1 \left( \frac{3JS_0}{10J - 2S_0} \right) \left( 1 - \frac{1}{2} D_2 (\tanh(C_2 * (C_1 - J)) + 1) \right), \quad (2-52)$$

$$\Phi_{,J} = \frac{\partial}{\partial J} \Phi. \quad (2-53)$$

It should be noted here that a closed form of the integral equation given in (2-51) is desirable, but unnecessary since it will be evaluated numerically in the final implementation.

The relationships developed between the hydrostatic moduli and the hyperelastic free energy given in equations (2-50), (2-51), (2-51) and (2-53) allow us to write the stress function in a form where the neat shear modulus and initial gas pressure terms are factored from remaining nonlinear strain functions such that:

$$\mathbf{S} = P_0 \mathbf{Q}^g + D_1 \mathbf{Q}^m, \quad (2-54)$$

The tensors  $\mathbf{Q}^g$  and  $\mathbf{Q}^m$  are referred to as the *nonlinear strain functions*. They are formed by normalizing the terms of the stress function by the initial gas pressure and the matrix shear modulus, respectively. These functions are given by the following expressions:

$$\mathbf{Q}^g = \left( (1 - S_0) \int_0^J \frac{dx}{(x - S_0)^2} \right) (2\mathbf{C}^{-1} - \mathbf{C}^{-1} \circ \mathbf{I}), \quad (2-55)$$

$$\begin{aligned}
\mathbf{Q}^m = & \left( \begin{array}{l} 4JS_0 \int_0^J \frac{1 - \frac{1}{2} D_2(\tanh(C_2(C_1 - x)) + 1)}{3(x - S_0)} dx \\ + J \frac{\partial}{\partial J} \left\{ \left( \frac{3JS_0}{10J - 2S_0} \right) \left( 1 - \frac{1}{2} D_2(\tanh(C_2 * (C_1 - J)) + 1) \right) \right\} (I_{\bar{c}} - 3) \\ - \frac{2}{3} \left( \frac{3JS_0}{10J - 2S_0} \right) \left( 1 - \frac{1}{2} D_2(\tanh(C_2 * (C_1 - J)) + 1) \right) I_{\bar{c}} \end{array} \right) (2\mathbf{C}^{-1} - \mathbf{C}^{-1} \circ \mathbf{I}) \\
& + 2J^{-2/3} \left( 1 - \frac{1}{2} D_2(\tanh(C_2 * (C_1 - J)) + 1) \right) \mathbf{I}
\end{aligned} \tag{2-56}$$

For an incremental change we have,

$$\Delta \mathbf{S} = P_0 \Delta \mathbf{Q}^g + D_1 \Delta \mathbf{Q}^m. \tag{2-57}$$

In this form the stress is given by the nonlinear strain functions acting on the initial bulk modulus of the air, and the linear shear modulus of the host polymer. The analogy to linear viscoelasticity should be clear. Replacement of the shear modulus term with the viscoelastic modulus forms the hyperviscoelastic response.

## 2.6. Incorporation of Viscoelastic Relaxation and Plasticity

Up to this point we have developed a hyperelastic energy potential and the associated stress and tangent moduli. Viscoelasticity is introduced to the constitutive model using a Prony model for the second Piola-Kirchhoff stress that is analogous to the linear, 1-dimensional modulus model described in chapter 1. Plasticity will also be incorporated into the Prony model by modifying the elastic spring using an approach motivated by the works of Nedjar [23] and Bardenhagen [35].

Figure 2-3 illustrates the Prony system for the viscoelastic portion of the problem. The subscript now refers to the components of the stress and nonlinear strain function in Voigt notation. Note that internal displacement variables are needed for each component of stress. Plasticity is introduced in the Prony series for each strain component. A plastic spring with a slider is introduced in series with the elastic spring as shown.

The plastic yield parameter controlling the slider is given in terms of strain. A plastic condition is developed when the elastic strain exceeds the yield strain limit,  $QLIM$ , and when the total amount of plastic set is beneath the permanent set limit,  $QSET$ .

$$\text{Plastic Condition:} \quad (Q_J^m - Q_J^{m,set}) > QLIM \text{ and } Q_J^{m,set} < QSET$$

During a plastic increment, the static spring element is softened such that its effective value is

$$\mu'_0 = \frac{\mu_0 \mu_p}{\mu_0 + \mu_p}. \quad (2-58)$$

The plastic modulus is related to the static modulus with a coefficient,  $p$ , such that,

$$\mu_p = \frac{\mu_0}{p}. \quad (2-59)$$

Substituting (2-59) into (2-58) we have:

$$\mu'_0 = \mu_0 \frac{1}{p+1} \quad (2-60)$$

Finally, the amount of set accumulated in the plastic increment can be determined by solving for the internal displacement between the elastic and plastic springs (not shown in the figure). It is given by:

$$\Delta Q_J^{m,set} = \Delta Q_J^m \frac{p_J}{p_J + 1}. \quad (2-61)$$

Implementation of these plastic rules requires additional state variables for each element and for each strain component. These include the maximum and minimum strain values seen over the strain history, and the accumulated set.

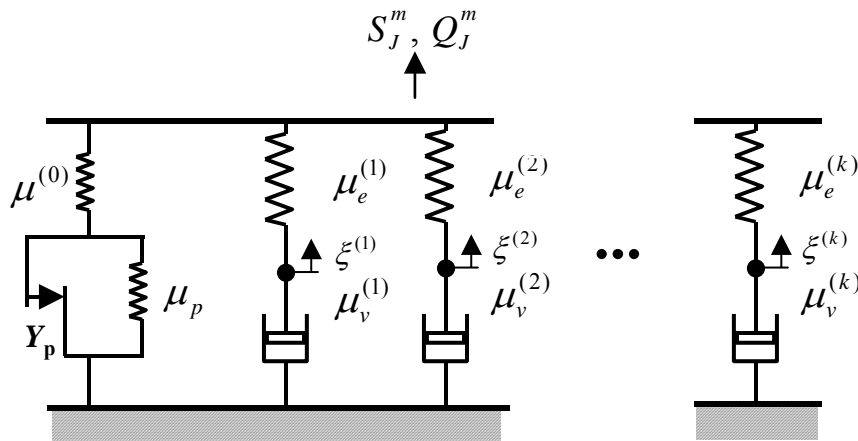


**Figure 2-3 Nonlinear strain function,  $Q$ , acting on the linear Prony representation of the neat shear modulus**

## 2.7. Time Incremental formulation

A central difference operator is used for time integration. In this scheme, the value and time derivative for a function,  $X$ , is given at the midpoint of the interval by:

$$X_{t+\Delta t/2} = X_t + \frac{\Delta X}{2}, \quad (2-62)$$

$$\dot{X}_{t+\Delta t/2} = \frac{\Delta X}{\Delta t}. \quad (2-63)$$

Referring to Figure 2-3, the stress can be written as the sum of the internal stresses within the Prony elements. Ignoring the plastic effect for the time being we have,

$$S_J^m = \mu_0 Q_J + \sum_{k=1}^N s_J^{(k)}. \quad (2-64)$$

where,

$s_J^{(k)} \equiv$  **internal stress of the  $k^{\text{th}}$  Maxwell element**

Continuity of stress across one Maxwell element allows us to write two equalities for the internal stress:

$$s_J^{(k)} = \mu_e^{(k)} (Q_J^m - \xi_J^{(k)}), \quad (2-65)$$

and

$$s_J^{(k)} = \mu_v^{(k)} \dot{\xi}_J^{(k)}. \quad (2-66)$$

Taking the time derivative of equation (2-65) and rearranging we have,

$$\dot{\xi}_J^{(k)} = \dot{Q}_J^m - \frac{\dot{s}_J^{(k)}}{\mu_e^{(k)}}. \quad (2-67)$$

Substitution of equation (2-67) into (2-66) eliminates the internal displacement variable and yields the following expression for the internal stress variable:

$$s_J^{(k)} + \tau_J^{(k)} \dot{s}_J^{(k)} = \mu_v^{(k)} \dot{Q}_J^m, \quad (2-68)$$

where,

$$\tau_J^{(k)} = \frac{\mu_v^{(k)}}{\mu_e^{(k)}}. \quad (2-69)$$

Applying the time increment scheme to equations (2-68) and (2-64) and reintroducing the plastic effect and the elastic response of the gas, we obtain the following expression for the stress change over the time increment:

$$\Delta S_J = P_0 \Delta Q_J^g + \left( \frac{\mu^{(0)}}{1 + p_J} + \sum_{k=1}^N \frac{\mu_e^{(k)}}{1 + \Delta t / 2\tau^{(k)}} \right) \Delta Q_J^m - \sum_{k=1}^N \frac{s_J^{(k)}}{1 + \tau^{(k)} / \Delta t}. \quad (2-70)$$

Written to fully identify the relation to the strain invariants and material parameters we have,

$$\Delta S_J = P_0 \Delta Q_J^g(J, s_0) + D_1 \left( \frac{1}{1 + p_J} + \sum_{k=1}^N \frac{\bar{\mu}_e^{(k)}}{1 + \Delta t / 2\tau^{(k)}} \right) \Delta Q_J^m(J, I_{\bar{C}}, s_0, c_1, c_2, D_1) - \sum_{k=1}^N \frac{s_J^{(k)}}{1 + \tau^{(k)} / \Delta t} \quad (2-71)$$

where,

$$\bar{\mu}_e = \frac{\mu_e^{(k)}}{\mu_0} \quad (2-72)$$

$$p_J = \begin{cases} 0 & \text{when } (Q_J^m - Q_J^{m,set}) < Y_p \text{ or } Q_J^{m,set} \geq PSET \\ p & \text{when } (Q_J^m - Q_J^{m,set}) \geq Y_p \text{ or } Q_J^{m,set} < PSET \end{cases} \quad (2-73)$$

Equation (2-70) provides the basis for numerical implementation. It alone is sufficient to implement an explicit analysis. However, an implicit analysis also requires that the stress Jacobian and the time derivative be available. These are developed in the next section.

## 2.8. The Incremental Stress Jacobian and Partial Time Derivative

In the implicit MATLAB model that is discussed in chapter 5, two additional tensors are needed to implement the analysis. The incremental energy change of the system is written as a first order Taylor series expansion involving the stress increment and the time increment [see section 5.1.1]. Hence, the stress Jacobian relating the incremental second Piola-Kirchhoff stress to the finite strain is and the partial time derivative of the stress are needed. The incremental stress Jacobian is given by:

$$\Lambda_{IJ} = \frac{\partial \Delta S_I}{\partial \Delta E_J} \quad (2-74)$$

Note that we are using Voigt notation. Considering equations (2-70) and (2-57) we develop the following equation for the incremental Jacobian:

$$\Lambda_{IJ} = K_{IJ}^g + \left( \frac{\mu^{(0)}}{1 + p_I} + \sum_{k=1}^N \frac{\mu_e^{(k)}}{1 + \Delta t / 2\tau^{(k)}} \right) K_{IJ}^m. \quad (2-75)$$

The material tangent tensors appearing in (2-75) are developed from equation (2-31) using the respective substitutions. For the gas phase all deviatoric terms are zero.

The partial time derivative of the stress is given by:

$$\Theta_J = \frac{\partial \Delta S_J}{\partial \Delta t}$$

Referring to equation (2-70) we find,

$$\Theta_J = - \sum_{k=1}^N \frac{s_J^{(k)} \tau_J^{(k)}}{(\Delta t + \tau_J^{(k)})^2} \quad (2-76)$$

## 2.9. Summary

A hyperviscoelastic constitutive theory for closed-cell foams has been fully developed. A particular form of the hyperelastic free energy was chosen to allow the constitutive behavior to exactly match a three-phase composite theory under hydrostatic loading. The elastic response derived from this potential [see equation (2-29)] depends on both the first and third invariants. Hence, this form cannot be classified as a Blatz-Ko model, which depends only on the third invariant.

A phenomenological correction for softening due to cell-wall bending was introduced and applied to the hydrostatic moduli that are related to the free energy function. Three parameters control the softening effect: the center of the bending transition, the modulus reduction when fully transitioned, and last, the sharpness of the

transition. The last of these parameters can lead to model Drucker instability stemming from the deviatoric terms in the stress and tangent moduli equations. If needed, Drucker instability could be controlled with a stability parameter that would reduce the sharpness of the bending transition for the hydrostatic shear modulus term.

Time-incremental equations for the stress and stress Jacobian were developed for implementation in finite analysis. Viscoelastic and plastic effects were introduced by factoring out a parameter that represents the matrix shear modulus from nonlinear strain functions. This shear modulus parameter was replaced with a Prony viscoelastic model that includes a plastic spring.

## **CHAPTER 3**

### **3. Characterization of Commercial Closed Cell Foams**

This section describes the foam specimens selected for experimental investigation, the experiments used for their characterization and the techniques used to extract the material parameters for the constitutive model.

#### **3.1. Foam Samples**

Two commercial closed-cell foams were chosen for experimental investigation. The desired characteristics were a relatively high density and stiffness, very low water absorption and significant viscoelastic behavior. Furthermore, it was desired that the two foams exhibit significantly different viscoelastic behavior. RUBATEX R451 and RUBATEX R8702 were ultimately selected. Basic physical properties measured for the foams are provided in Table 3-1. Table 3-2 and Table 3-3 provide the manufacturers specifications for these products. Densities of the two products are about the same, but the composition is different. R451 is formed from a neoprene rubber whereas R8702 is formed from styrene/butadiene rubber (SBR). The manufacturer's durometer data indicate that R451 is the more compliant of the two foams.

A photograph of some of the foam specimens tested is shown in figure. Specimens for DMTA testing are shown in the foreground. Shorter beam lengths were chosen for

the R451 specimens due to the low durometer values for the foam. This ensures that the beam is sufficiently stiff to stay above the noise floor of the DMTA system.

**Table 3-1 Measured Physical Properties of RUBATEX Foam Samples**

Property	RUBATEX R451	RUBATEX R8702
Density	0.48-0.52	0.49-0.56
Shore A	21-30	44-50
Water Absorption (24 hrs at 700 psi)	0.8%	0.7%
Set (24 hrs at 700 psi)	12%	25%



**PRESS MOLDED BUNS  
PHYSICAL PROPERTIES**

Type .....	<b>R-451-N</b>
Polymer .....	Neoprene (CR)
Color .....	Black
ASTM D-1056-67 Classification .....	SCE-45
ASTM D-1056-00 Classification .....	2C5
Suffix Requirements .....	B2, C1, F1, M
ASTM D-6576-00 Type II .....	Grade A or B Firm
25% Compression Resistance <sup>1)</sup> [psi] .....	17 - 24
50% Compression Set <sup>2)</sup> [%] .....	25
Density <sup>3)</sup> [lb/ft <sup>3</sup> ] .....	22 - 35
Water Absorption <sup>4)</sup> [lb/ft <sup>2</sup> ] .....	0.1 max.
Tensile <sup>5)</sup> [psi] .....	150 min.
Elongation <sup>6)</sup> [%] .....	175 min.
Flammability <sup>7)</sup> - FMVSS302 .....	Pass
UL 94 .....	HBF - 1/16" min.
Standard Sheet Size [in] ±3% .....	42" x 45"
Expected Yield [in] .....	1.50"
<small>From full bun thickness - based on 2 level cuts</small>	

- <sup>1)</sup> 25% Compression Resistance                      ASTM D-1056
- <sup>2)</sup> 50% Compression Set                                ASTM D-1056
- <sup>3)</sup> Density     ASTM D-1056
- <sup>4)</sup> Water Absorption                                     ASTM D-1067
- <sup>5)</sup> Tensile     ASTM D-412
- <sup>6)</sup> Elongation    ASTM D-412
- <sup>7)</sup> Flammability - This item and any corresponding data refer to typical performance in the specific test indicated and should not be construed to imply this material's behavior in other fire conditions. UL 94-test valid for specific rating and thickness only. See UL 94 listing for details. (File # E55475).

Other gauges and widths may be available. Please refer to Customer Service  
 Note: SAEJ 18 is equivalent to ASTM D-1056  
 Mil 8130 has been replaced by ASTM D-8578-00

Issued 10/01/04  
**RUBATEX INTERNATIONAL, LLC.**  
 906 ADAMS STREET, BEDFORD, VA 24523  
[www.rubatex.com](http://www.rubatex.com) 1-800-782-2839 540-586-2611

**Table 3-2 Manufacturer's Physical Properties for R451**



## PRESS MOLDED BUNS

### PHYSICAL PROPERTIES

Type .....	<b>R-8702</b>
Polymer .....	Styrene / Butadiene Rubber (SBR)
Color .....	Black
ASTM D-1056-67 Classification .....	---
ASTM D-1056-00 Classification .....	---
Shore Durometer [A] .....	40 - 60
50% Compression Set <sup>2)</sup> [%] .....	50
Density <sup>3)</sup> [lb/ft <sup>3</sup> ] .....	25 - 35
Water Absorption <sup>4)</sup> [lb/ft <sup>2</sup> ] .....	0.1 max.
Tensile <sup>5)</sup> [psi] .....	275 min.
Elongation <sup>6)</sup> [%] .....	175 min.
Standard Sheet Size [in] ±3% .....	36" x 42"
Expected Yield [in] .....	0.875"
<small>From full bun-thickness -based on 2 level cuts</small>	

<sup>1)</sup> Shore Durometer (A)	ASTM D-1056
<sup>2)</sup> 50% Compression Set	ASTM D-1056
<sup>3)</sup> Density	ASTM D-1056
<sup>4)</sup> Water Absorption	ASTM D-1687
<sup>5)</sup> Tensile	ASTM D-412
<sup>6)</sup> Elongation	ASTM D-412

Other gauges and widths may be available. Please refer to Customer Service

Note: SAEJ 18 is equivalent to ASTM D-1056

Issued 10/01/04

**RUBATEX INTERNATIONAL, LLC.**  
**906 ADAMS STREET, BEDFORD, VA 24523**  
[www.rubatex.com](http://www.rubatex.com) 1-800-782-2839 540-586-2611

**Table 3-3 Manufacturer’s Physical Properties for R8702**

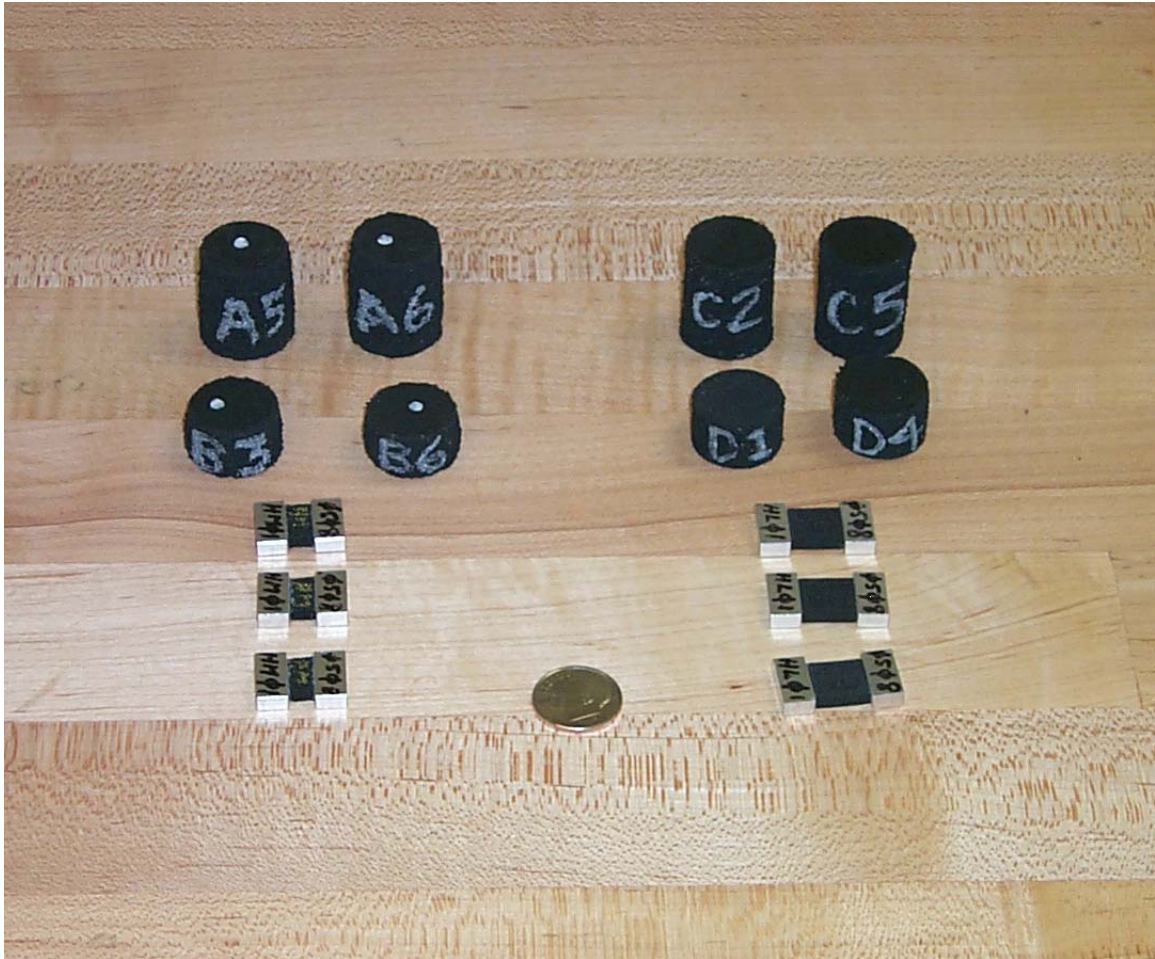


**Figure 3-1 Foam Specimens. Rubatex R451 (right). Rubatex R8702 (left). DMTA Specimens shown in the foreground . SHPB specimens of ½” and 1” heights shown in back.**

### **3.2. Characterization Experiments**

The material parameters required by the constitutive model are the Prony coefficients and plastic terms, and the modified three-phase parameters. This information is collected in two experiments. A Dynamic Mechanical Thermal Analyzer (DMTA) is used to

generate a mastercurve of the dynamic shear modulus for the foams. Fitting the mastercurve with a Prony viscoelastic model provides the moduli and relaxation times of the viscoelastic Maxwell elements. A hydrostatic dilatometer test is used to develop the three-phase parameters. This provides the volume strain of the specimen under a known hydrostatic pressure-history. Parameters are extracted through optimization of the experimental results using the constitutive model. Relaxation behavior must be established *a priori* to account for long-term relaxation behavior seen in the quasi-static experiment.

### ***3.2.1. Dynamic Mechanical Thermal Analysis***

A Dynamic Mechanical Thermal Analyzer V (DMTA V) shown in Figure 3-2 was used to measure the complex shear modulus of the foams at isothermal temperatures ranging from  $-50^{\circ}\text{C}$  to  $50^{\circ}\text{C}$ . At each isotherm the bending/shear stiffness and phase of a short sample beam is measured at dynamic frequencies ranging from 0.3 to 10 Hz. A typical test specimen in the testing fixture is shown in Figure 3-3. Specimens are bonded to metal end blocks for the test to ensure that the boundary conditions for the specimen are fixed. Geometry factors relating the modulus to the stiffness are developed with a high order beam formulation that is accurate for all DMTA sample lengths. A mastercurve of the dynamic shear modulus is developed from the isothermal frequency scans using the time-temperature superposition principle discussed in chapter 1.



**Figure 3-2 DMTA V with FTS Temperature Controller**

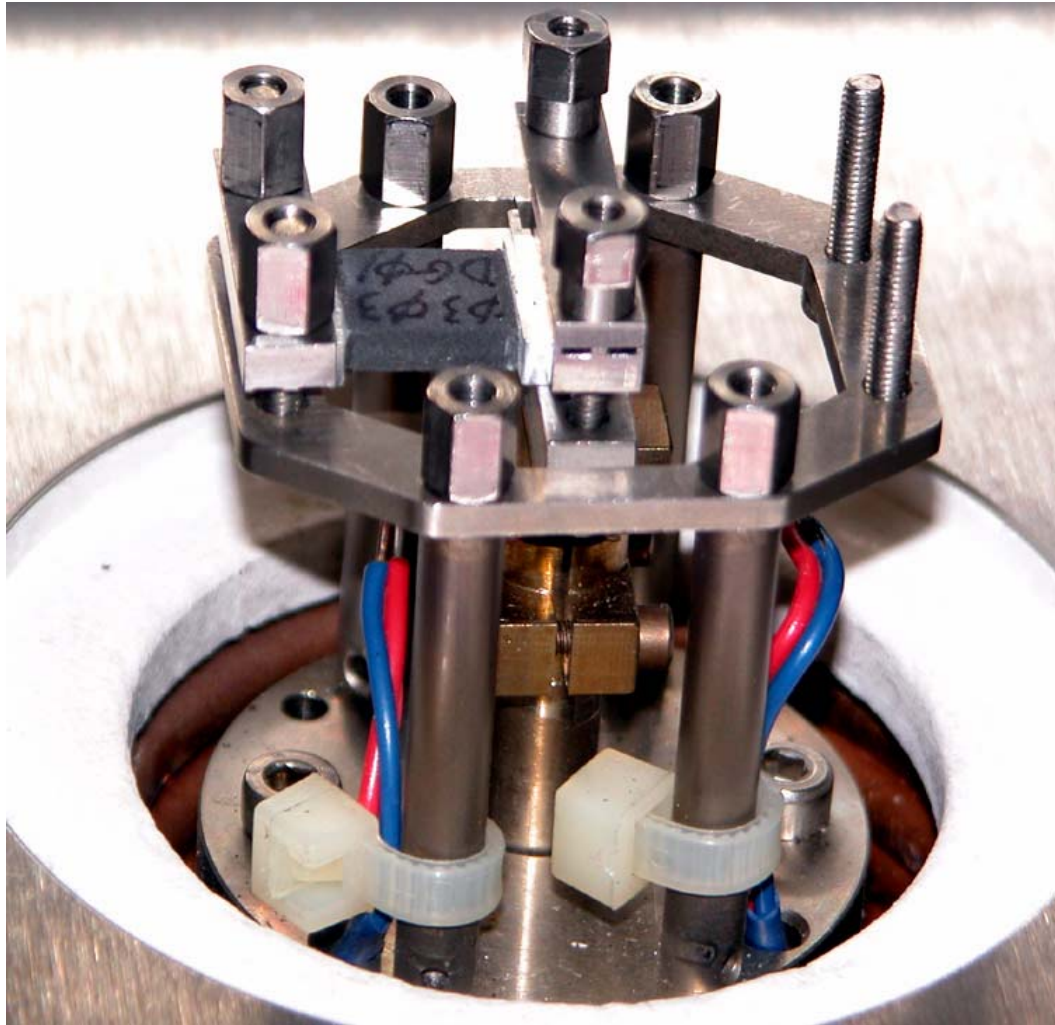


**Figure 3-3 Single Cantilever Specimen Loaded in the DMTA V**

*3.2.1.1. Determining Prony Coefficients*

The Prony coefficients are provided to the model as pairs of the normalized relaxation moduli and the corresponding relaxation time,

$$g_i = \frac{\mu_{el}^{(i)}}{\mu^{(0)}} \quad (3-1)$$

$$\tau_i = \frac{\mu_v^{(i)}}{\mu_e^{(i)}} \Rightarrow \text{relaxation time of the } i^{\text{th}} \text{ Prony element} \quad (3-2)$$

Pre-selecting the relaxation times over the time-scale of interest facilitates the least squares optimization of the Prony coefficients. The long-term elastic modulus,  $\mu_0$  is not required by the constitutive model since the initial foam moduli are established by the modified Kerner parameters.

Prony coefficients are established by utilizing a nonlinear least-square optimization routine to fit dynamic shear modulus mastercurves to the Prony expressions given in equations 2-6 and 2-7. MATLAB routine, “lsqnonlin” is used to perform the nonlinear optimization. Rather than optimizing the spring and the dashpot values simultaneously, a fixed set of element relaxation times is selected in advance. This approach greatly improves the stability of the optimization. Of course, the range of relaxation times must cover the time scales of interest.

Since the Prony series is a mechanical description of viscoelasticity, it necessarily satisfies the Kramers-Kronig’s causality relations [56],[57]. Furthermore, since the Prony series can be expanded without limit, it must also provide a convergent description of any linear viscoelastic system. Therefore curve fitting of complex modulus data with the Prony series model is a way to test the validity of frequency domain viscoelastic data. As it is shown in the next section, neither of the mastercurves developed for the RUBATEX specimens fully obeys Kramers-Kronig’s relations. The violation is particularly significant with the RUBATEX R451 mastercurve.

### 3.2.1.2. Prony Series Optimization for RUBATEX R8702

The DMTA mastercurve for RUBATEX R8702 and its Prony optimization is shown in Figure 3-4. The upper curve shows the real part of the dynamic shear modulus and the lower curve shows the dynamic loss factor. The optimization was made in MATLAB using the 'lsqnonlin' function. Optimized R8702 Prony coefficients are provided in Table 3-4. The objective function used for optimization was an equal weighting of the difference in predicted and measured  $\log_{10}(\text{Re}(G))$  and  $\log_{10}(\eta)$ . This foam turns out to be quite unusual since it exhibits two strong phase transitions, which are evident by the double peak in loss factor. The value the Prony model is evident here since it has no difficulty in describing multiple transitions. The low-frequency transition poses an additional challenge from a modeling perspective since the material has strong relaxation behavior on very long time scales. This is evident in relaxation modulus in the time domain shown in Figure 3-5, which shows that the modulus drops by about a factor of 5 over the time period of 1 second to 1 day. The popular approach of characterizing 'static' properties via quasi-static experiments will not accurately characterize this type of foam, unless one is willing to conduct his experiments over a time scale of weeks.

These problems are circumvented in the present approach since the assumption of a 'static' material response is not made. Relaxation is fully accounted for when extracting static material parameters. This is discussed in more detail in the next section.

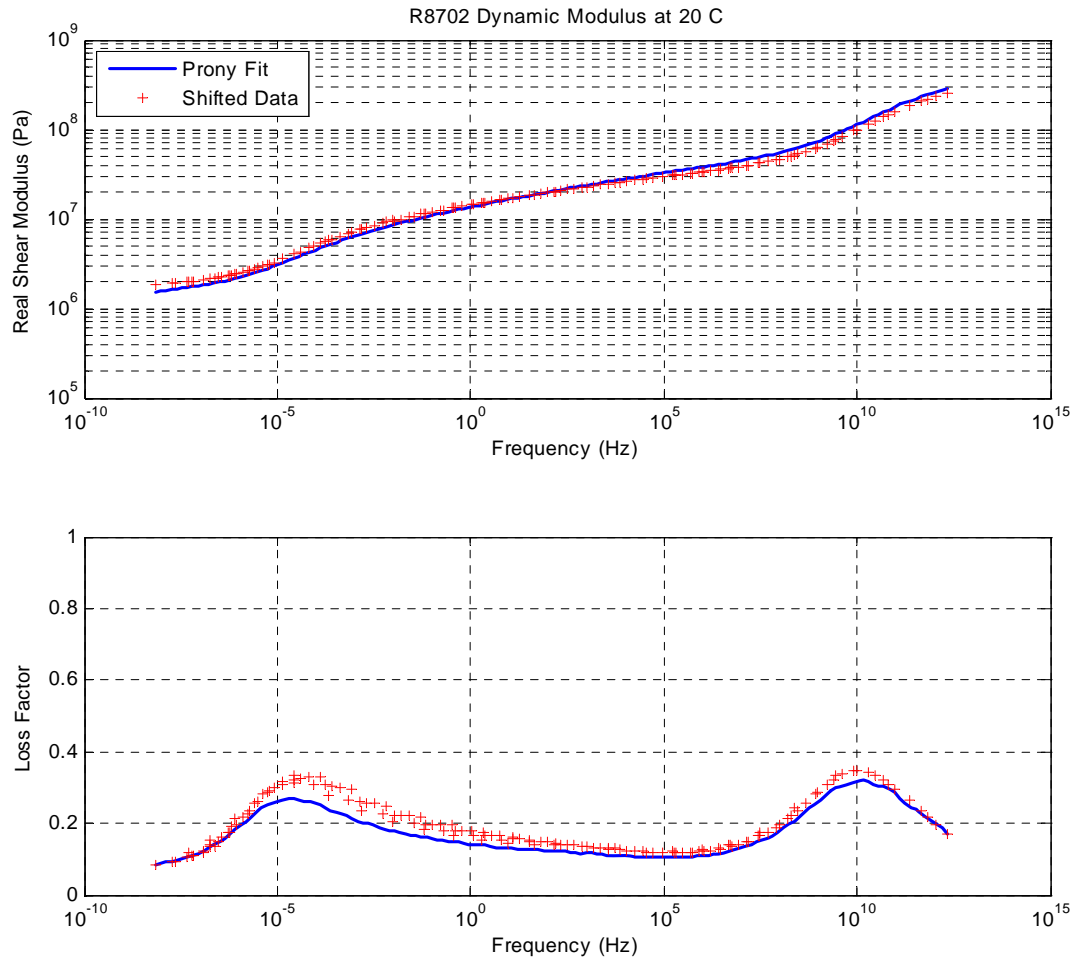


**Figure 3-4 Mastercurve for the dynamic shear modulus and loss factor for RUBATEX R8702 at 20 C**

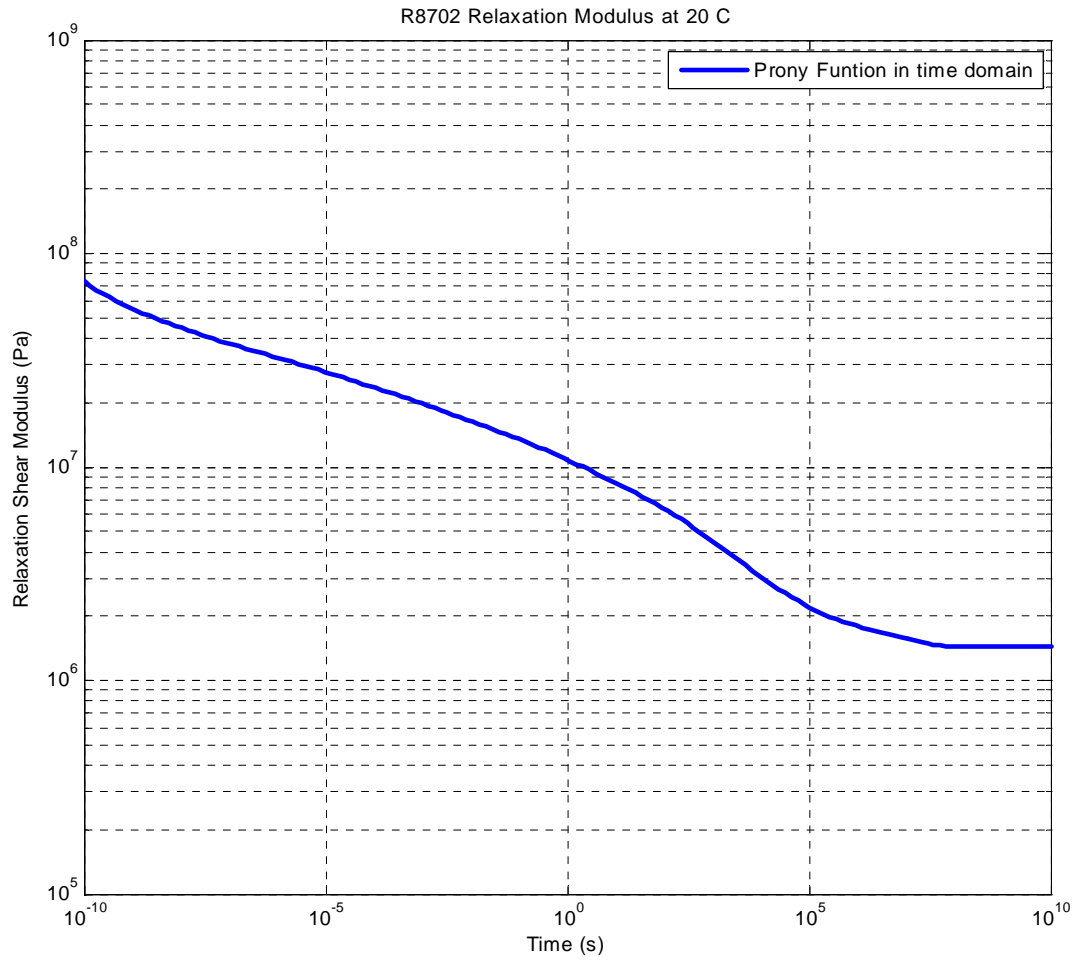


**Figure 3-5 Relaxation shear modulus of RUBATEX R8702 at 20 C**

tau (s)	g (Pa)	g/g0
7.13E-14	7.30E+07	5.07E+01
3.63E-13	5.26E+07	3.65E+01
1.85E-12	5.77E+07	4.01E+01
9.42E-12	4.17E+07	2.90E+01
4.80E-11	2.75E+07	1.91E+01
2.44E-10	1.54E+07	1.07E+01
1.24E-09	9.48E+06	6.59E+00
6.34E-09	6.72E+06	4.67E+00
3.23E-08	5.01E+06	3.48E+00
1.64E-07	4.12E+06	2.86E+00
8.37E-07	3.61E+06	2.51E+00
4.26E-06	3.31E+06	2.30E+00
2.17E-05	3.14E+06	2.18E+00
1.11E-04	2.92E+06	2.03E+00
5.63E-04	2.67E+06	1.86E+00
2.87E-03	2.47E+06	1.71E+00
1.46E-02	2.24E+06	1.55E+00
7.43E-02	2.07E+06	1.44E+00
3.79E-01	1.90E+06	1.32E+00
1.93E+00	1.78E+06	1.24E+00
9.82E+00	1.60E+06	1.11E+00
5.00E+01	1.50E+06	1.04E+00
2.55E+02	1.37E+06	9.53E-01
1.30E+03	1.28E+06	8.87E-01
6.60E+03	1.03E+06	7.14E-01
3.36E+04	6.79E+05	4.72E-01
1.71E+05	3.72E+05	2.58E-01
8.72E+05	2.22E+05	1.54E-01
4.44E+06	1.51E+05	1.05E-01
2.26E+07	1.75E+05	1.21E-01
inf	1.44E+06	1

**Table 3-4 Optimized Prony Coefficients for RUBATEX R8702**

### 3.2.1.3. Prony Series Optimization for RUBATEX R451

The DMTA mastercurve for RUBATEX R451 and its Prony optimization is shown in Figure 3-6. The upper plot is the real part of the dynamic shear modulus and the lower curve gives the dynamic loss factor. The objective function used for optimization was an equal, 50/50, weighting of the difference in predicted and measured  $\log_{10}(\text{Re}(G))$  and  $\log_{10}(\eta)$ . Optimized R451 Prony coefficients are provided in Table 3-5 for this weighting. R451 exhibits a more typical dynamic modulus for a soft rubber with a glass transition frequency just above 1 MHz at the reference temperature of 20C. Like many rubbers, R451 shows a significant creep character, which is characterized by the non-zero low-frequency loss factor.

As we mentioned earlier, the DMTA mastercurve for R451 violates Kramers-Kronig's causality relations. Guillot and Trivett have described a similar difficulty developing mastercurves for R451 from dynamic Young's modulus data [51]. They observed inconsistent time-temperature (horizontal) shift factors for the real and imaginary components of the modulus. Although there is no direct connection between this problem and causality, a possible link exists. In their paper they assert that the imaginary modulus is the more reliable modulus component for establishing the horizontal shift factors. They also make use of 'vertical' shift factors, which are applied to the real part of the modulus to correct the remaining discrepancies that exist after shifting the data set horizontally. The link is that vertical shifting factors applied to the real modulus would also be remedial to the causality problem. This can be seen in Figure

3-6 where one may recognize that the ability of the Prony series to describe both the real and imaginary components of the complex modulus would be improved by vertically shifting the rubbery modulus downward and the glassy region upward. The Prony fit shown in Figure 3-6 is a compromise. The choice of an equally weighted objective function has provided a fairly good overall fit to the real part, but has resulted in a loss factor fit that is significantly biased on the low side of the measurements.

That vertical shifting would improve the causality of the mastercurve is even more evident in Figure 3-8 where we have now changed the weighting of the objective function from 50/50 to 90/10 in favor of the loss factor. Optimized R451 Prony coefficients for this weighting are provided in Table 3-6. The real part of the Prony fit is now representative of the causal counterpart to the loss factor. One might attribute this difference between the shifted data and the Prony fit as a missing vertical shift of the real modulus data.

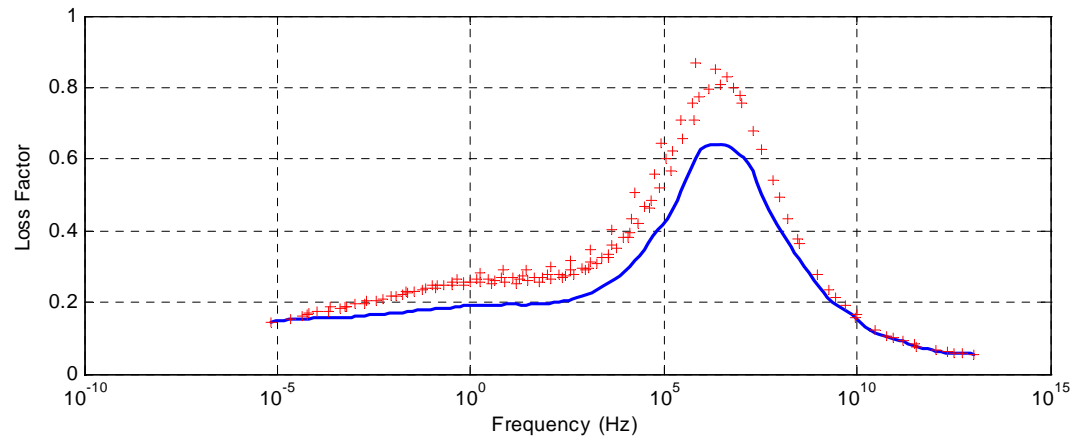
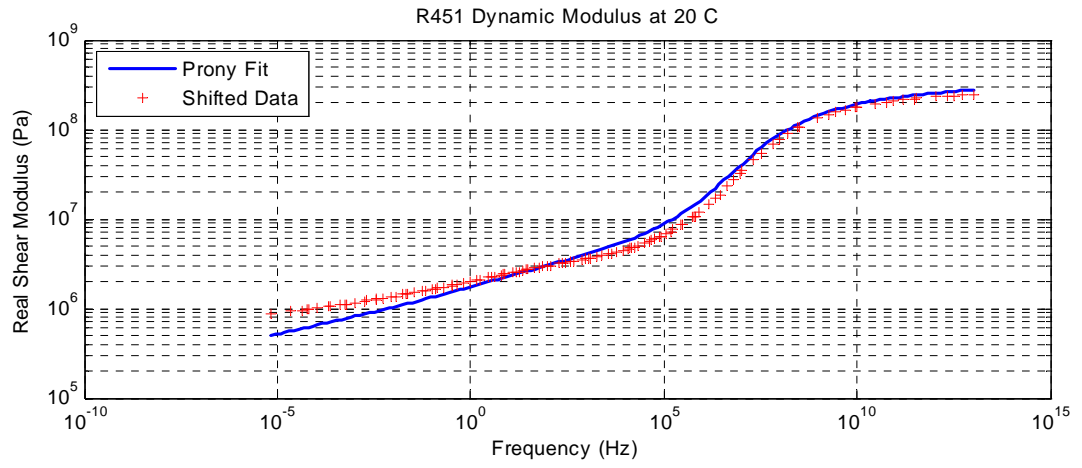


**Figure 3-6 Mastercurve for the real part of the shear modulus – RUBATEX R451**

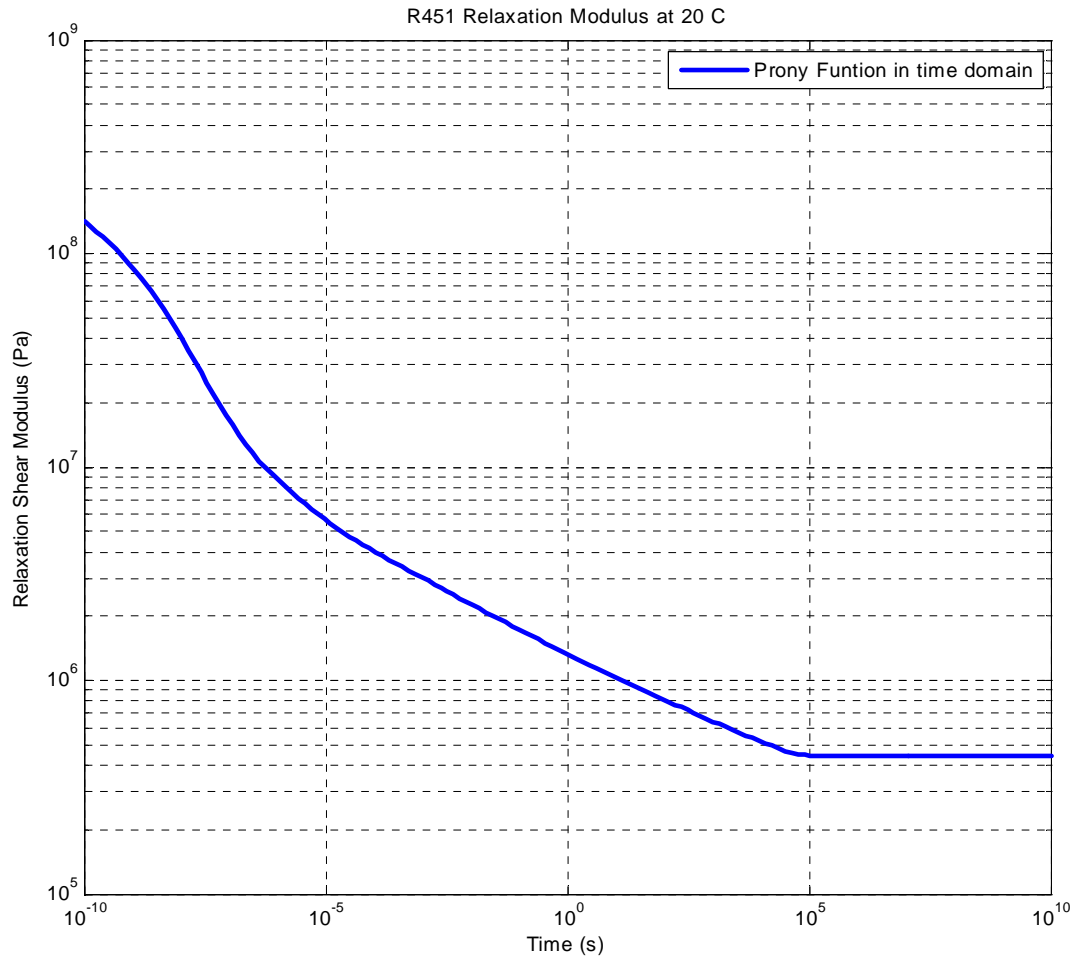


**Figure 3-7 Relaxation shear modulus of RUBATEX R451 at 20 C**

tau (s)	g (Pa)	g/g0
1.46E-14	2.31E+07	5.22E+01
6.19E-14	1.14E+07	2.58E+01
2.63E-13	1.48E+07	3.33E+01
1.12E-12	2.24E+07	5.05E+01
4.74E-12	1.66E+07	3.74E+01
2.01E-11	3.22E+07	7.26E+01
8.55E-11	2.76E+07	6.22E+01
3.63E-10	3.96E+07	8.94E+01
1.54E-09	3.25E+07	7.33E+01
6.55E-09	3.34E+07	7.52E+01
2.78E-08	1.60E+07	3.60E+01
1.18E-07	1.01E+07	2.27E+01
5.02E-07	3.37E+06	7.59E+00
2.13E-06	2.66E+06	6.00E+00
9.05E-06	1.39E+06	3.12E+00
3.84E-05	1.05E+06	2.36E+00
1.63E-04	7.25E+05	1.63E+00
6.93E-04	5.98E+05	1.35E+00
2.94E-03	4.89E+05	1.10E+00
1.25E-02	4.17E+05	9.41E-01
5.31E-02	3.51E+05	7.92E-01
2.25E-01	2.84E+05	6.40E-01
9.58E-01	2.34E+05	5.27E-01
4.07E+00	1.92E+05	4.32E-01
1.73E+01	1.54E+05	3.47E-01
7.34E+01	1.30E+05	2.94E-01
3.12E+02	1.06E+05	2.40E-01
1.32E+03	9.93E+04	2.24E-01
5.62E+03	7.12E+04	1.60E-01
2.39E+04	9.49E+04	2.14E-01
inf	4.44E+05	1

**Table 3-5 Optimized Prony Coefficients for RUBATEX R451**

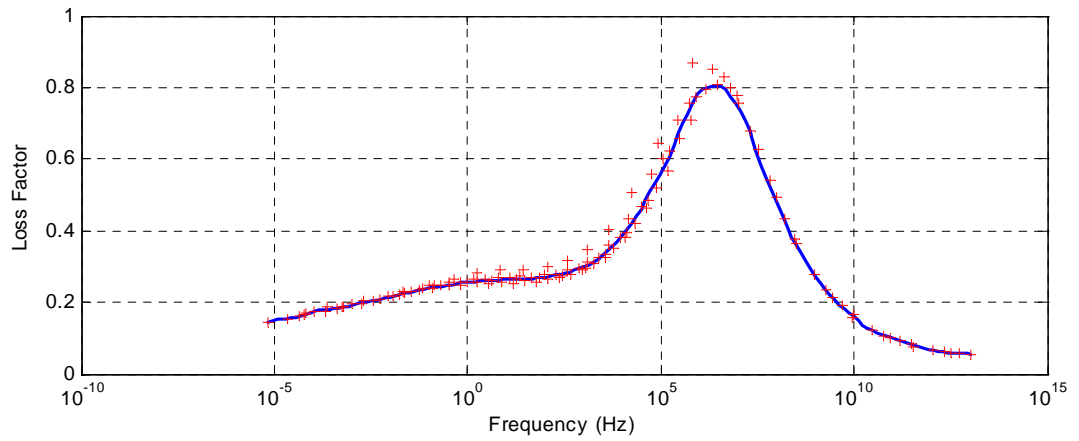
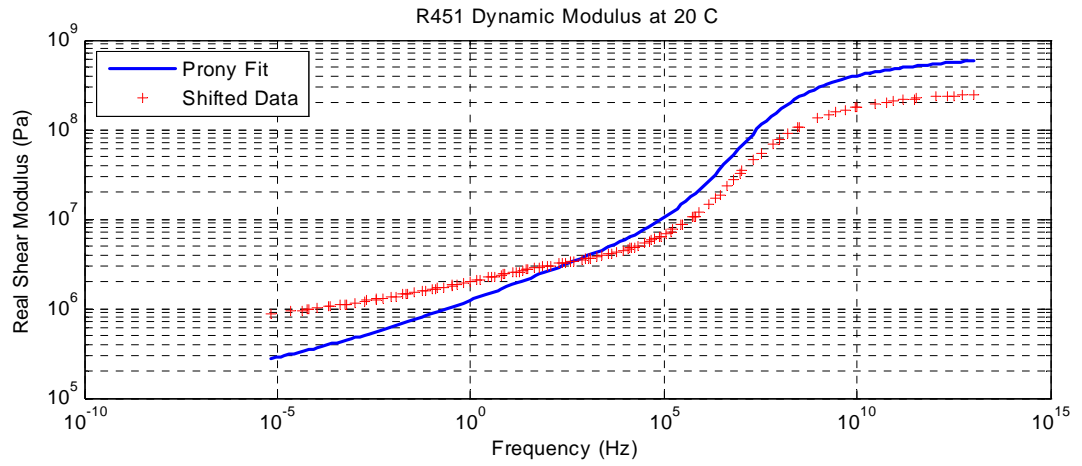


**Figure 3-8 Mastercurve for the real part of the shear modulus – RUBATEX R451 – [High Loss Factor Weighting for Prony Coefficients]**

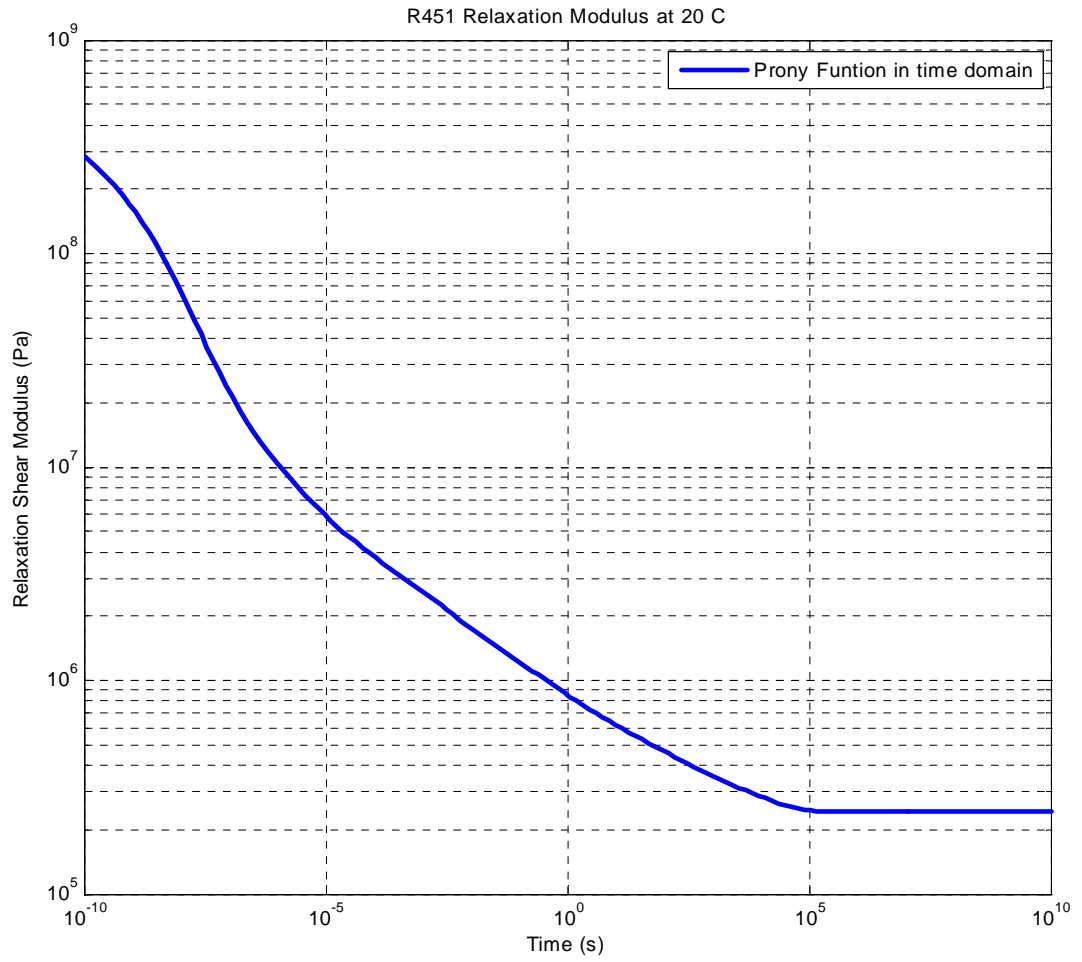


**Figure 3-9 Relaxation shear modulus of RUBATEX R451 at 20 C R451 – [High Loss Factor Weighting for Prony Coefficients]**

tau (s)	g (Pa)	g/g0
1.46E-14	4.89E+07	1.99E+02
6.19E-14	2.33E+07	9.52E+01
2.63E-13	3.45E+07	1.41E+02
1.12E-12	4.33E+07	1.77E+02
4.74E-12	4.30E+07	1.76E+02
2.01E-11	6.27E+07	2.56E+02
8.55E-11	7.10E+07	2.90E+02
3.63E-10	8.35E+07	3.41E+02
1.54E-09	8.02E+07	3.28E+02
6.55E-09	6.45E+07	2.63E+02
2.78E-08	3.09E+07	1.26E+02
1.18E-07	1.48E+07	6.04E+01
5.02E-07	5.94E+06	2.43E+01
2.13E-06	3.62E+06	1.48E+01
9.05E-06	1.99E+06	8.11E+00
3.84E-05	1.31E+06	5.33E+00
1.63E-04	9.32E+05	3.81E+00
6.93E-04	7.10E+05	2.90E+00
2.94E-03	5.47E+05	2.23E+00
1.25E-02	4.41E+05	1.80E+00
5.31E-02	3.44E+05	1.40E+00
2.25E-01	2.64E+05	1.08E+00
9.58E-01	1.99E+05	8.13E-01
4.07E+00	1.55E+05	6.32E-01
1.73E+01	1.13E+05	4.60E-01
7.34E+01	9.42E+04	3.85E-01
3.12E+02	6.70E+04	2.74E-01
1.32E+03	6.34E+04	2.59E-01
5.62E+03	3.64E+04	1.49E-01
2.39E+04	5.34E+04	2.18E-01
inf	2.45E+05	1

**Table 3-6 Optimized Prony Coefficients for RUBATEX R451 [High Loss Factor Weighting]**

### ***3.2.2. APP Dilatometer 1000 Compression Test***

An automated dilatometer system manufactured by Advanced Pressure Products (APP) was used to measure the specimens under hydrostatic pressure. A schematic of the apparatus is shown in Figure 3-10. The system is water-filled. A specimen is placed in the pressure vessel and a computer controls the piston action that generates the system pressure. An encoder monitors the piston displacement, which can be related to the volume change of the system. Alternatively, volume change can be obtained with a level meter mounted in a standpipe on the non-pressurized side of the pressure generator (not shown in the schematic). The level meter system is also referred to as a “leak recovery system” since it provides volume data that is uncorrupted by possible water leaks past the piston seals. Calibrations are performed with no specimen to characterize the system compliance for calibration.

#### ***3.2.2.1. Determining Three-Phase Parameters***

The modified three-phase parameters and the plastic parameters are determined by optimizing the predicted response of a dilatometer experiment. In the case of viscoelastic foams, the Prony coefficients must be established *a priori* of this optimization so that the viscoelastic creep can be separated from the nonlinear, static behavior. This is clearly the case for the foams under investigation as can be seen in from their relaxation moduli in Figure 3-5 and Figure 3-7. Significant relaxation phenomena occur at time scales on the order of days and even weeks. In fact, the equilibrium moduli (where the curve plateaus at long times) as determined from these figures are only apparent. Indeed, they are

simply artifacts of the low-frequency data cut-off of the source dynamic mastercurves. Fortunately, it is unnecessary to identify the “true” equilibrium shear modulus and it is sufficient to work with its apparent value, provided that the relaxation curve at least spans the time scale of the quasi-static experiment.

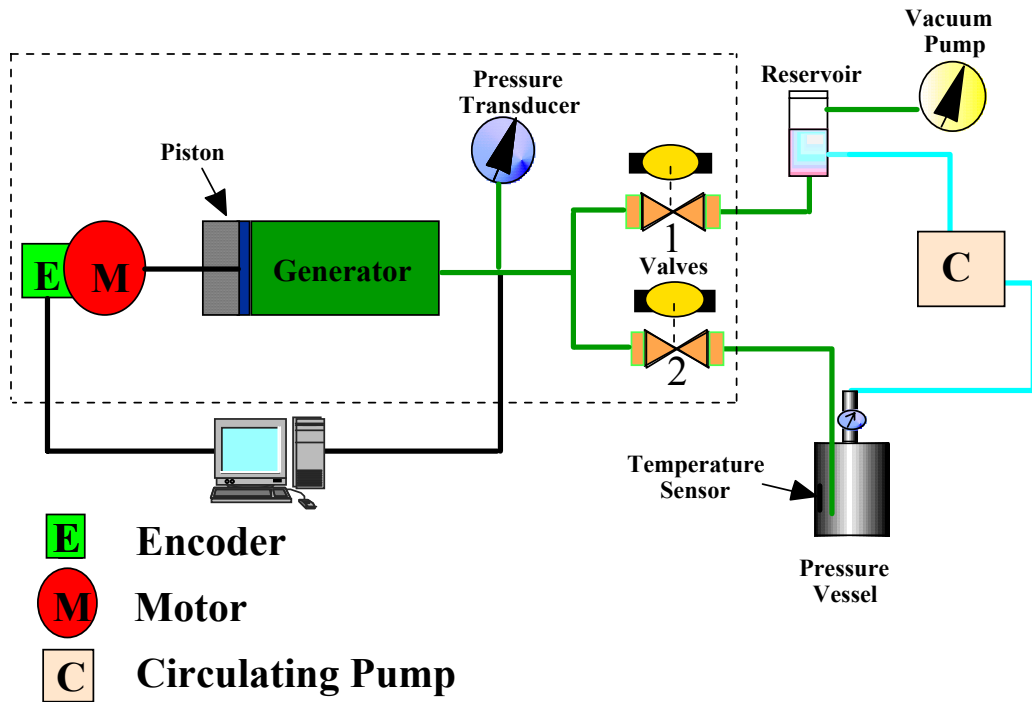
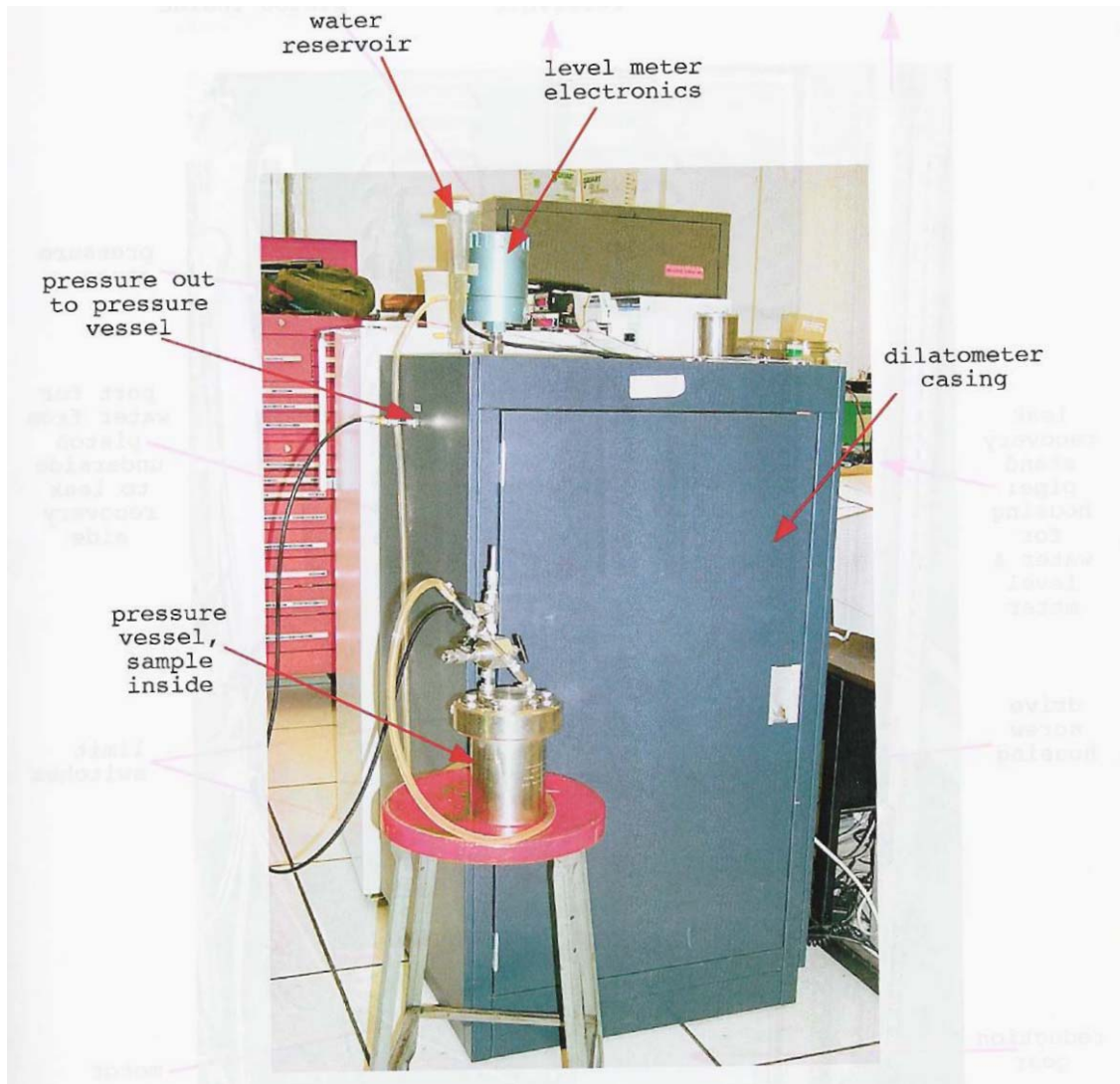
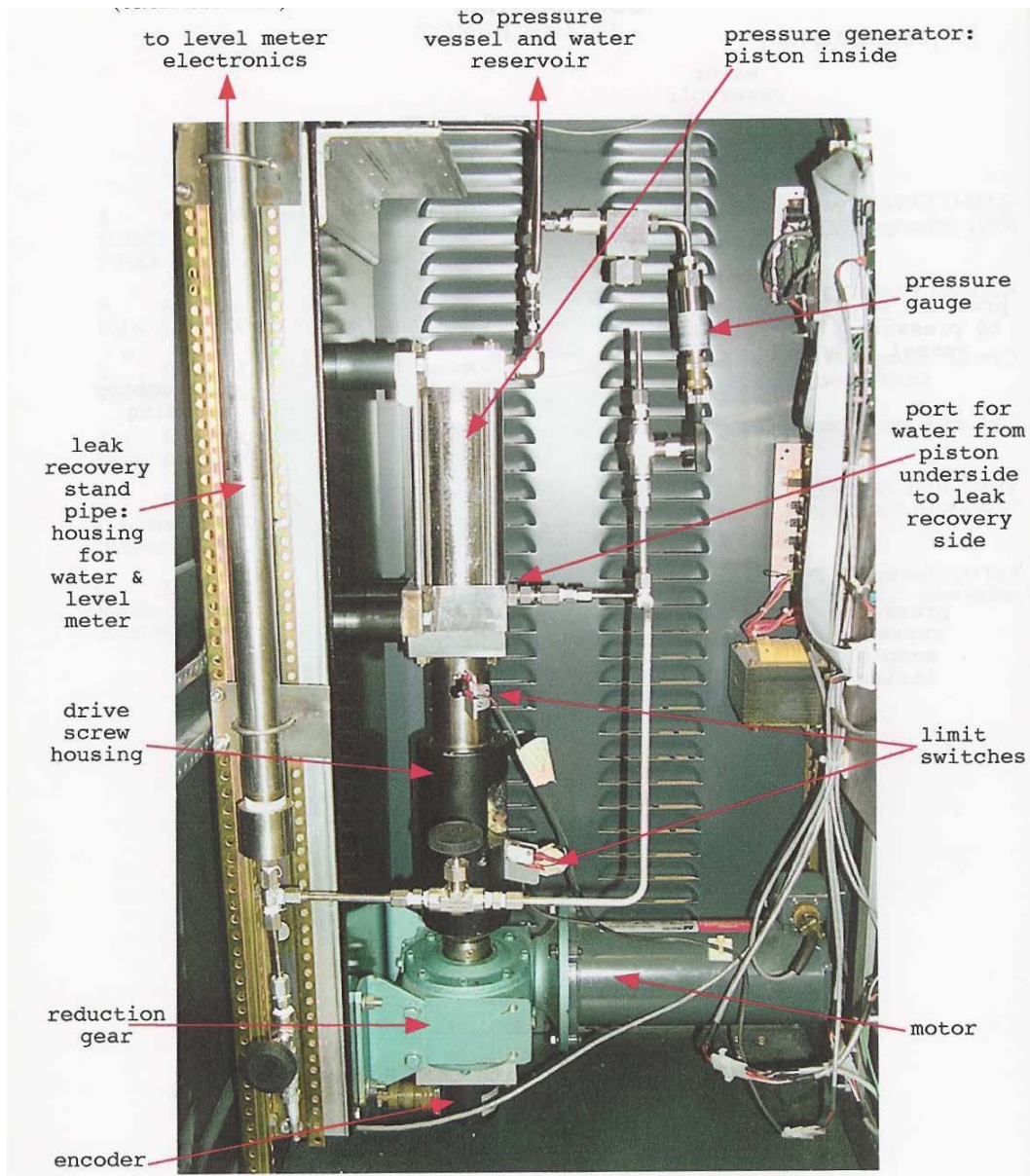


Figure 3-10 Schematic of APP Dilatometer 1000 with Pressure Vessel



**Figure 3-11 APP Dilatometer 1000 with Level Meter for Volume Metering - Exterior**



**Figure 3-12 APP Dilatometer 1000 with Level Meter for Volume Metering - Interior**

A special type of pressure loading history is used to facilitate the separation of plastic and elastic behavior. The sample is subjected to pressure intervals that grow in amplitude and which are separated by a relaxation period. This allows for an examination of the plastic set accumulation - although it remains difficult to distinguish viscoelastic and plastic effects.

#### 3.2.2.2. Three-Phase and Plastic Parameters Optimization for R451

Dilatometer data and the optimization results for R451 are shown in Figure 3-13. The predicted response of the material to the hydrostatic stress-history is developed at a material point (no inertia) with the constitutive model. Inertial effects are negligible because the experiment is conducted at very low strain-rates. Stress relaxation is incorporated in the constitutive model using the Prony coefficients given in Table 3-5. The optimization parameters are the three-phase coefficients, the plastic yield, the plastic set, and the plastic spring. The Prony parameters are fixed during the optimization.

The optimized three-phase and plastic parameters for R451 are given in Table 3-7. With these parameters established, the corresponding hydrostatic moduli can be developed for examination. Figure 3-14 shows the hydrostatic bulk (red) and shear (magenta) moduli for R451. Also, the contributions to the effective bulk modulus from the material (green) and gas (blue) phases are shown. The black, vertical line indicates the densification limit of the foam. Interestingly, the plot shows that the bulk modulus of the foam is dominated by the gas phase, even in its initial state. Hence, the foam is essentially like a rubber balloon, which helps explain its resiliency under repeated

pressure cycles. The optimization did not make use of the parameters describing a bending transition and softening effect in the material phase. Hence, the material is described fully with the three-phase theory using an elevated initial gas pressure in the cells. But considering the dominant effect of the gas phase, it is quite possible that bending effects do occur, but are simply undetectable in the data set.

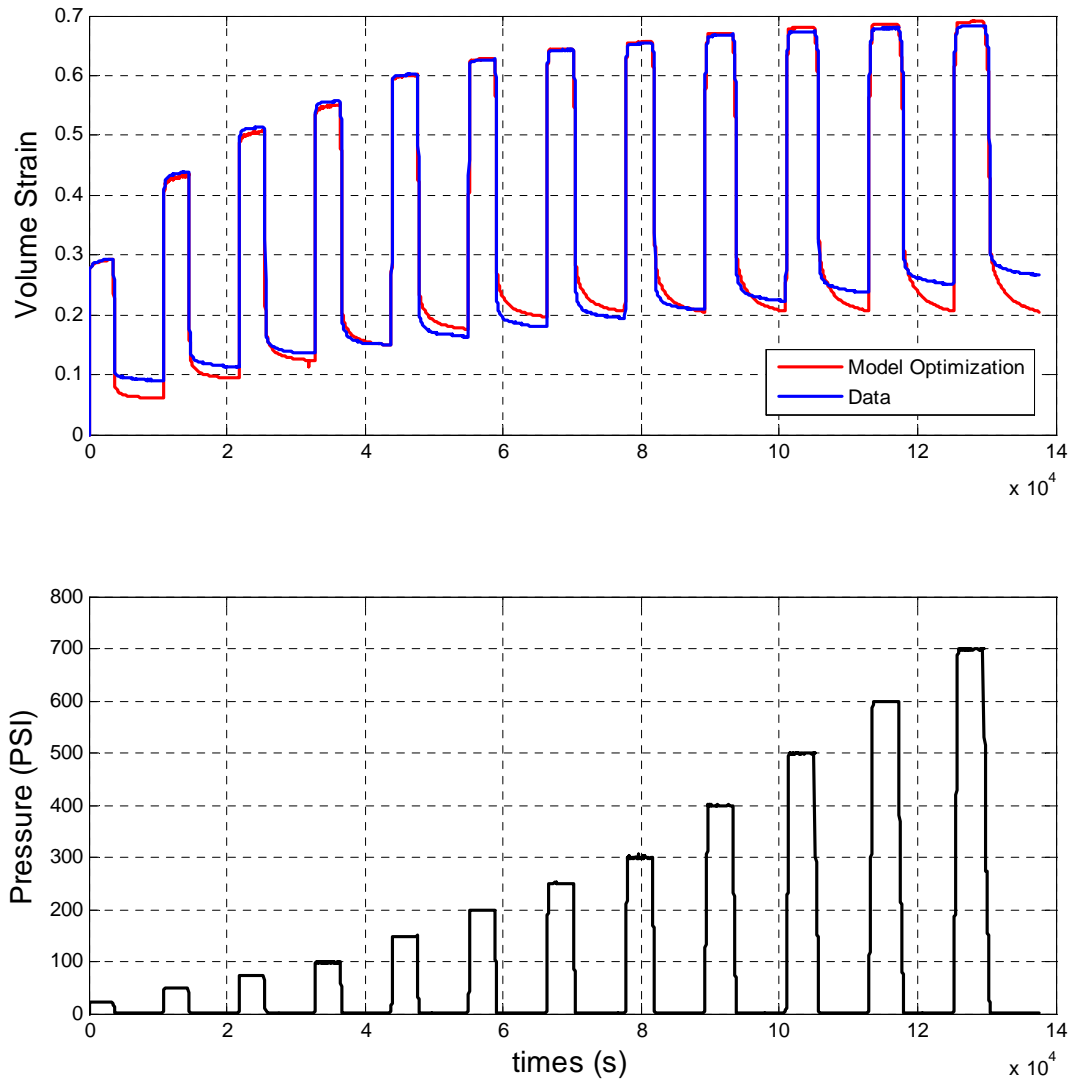


**Figure 3-13 R451 Hyperbaric chamber test data and model optimization results – (fixed relaxation spectrum)**

**Table 3-7. Optimized Three-Phase and Plastic Parameters for R451**

Parameter	Value
$D_1$	$2.2 \times 10^5$ Pa
$D_2$	Not used
$C_1$	Not used
$C_2$	Not used
$P_0$	$1.5 \times 10^5$ Pa (22 psi)
$S_0$	0.28
$p$	0.30
$QLIM$	0.04
$QSET$	0.35

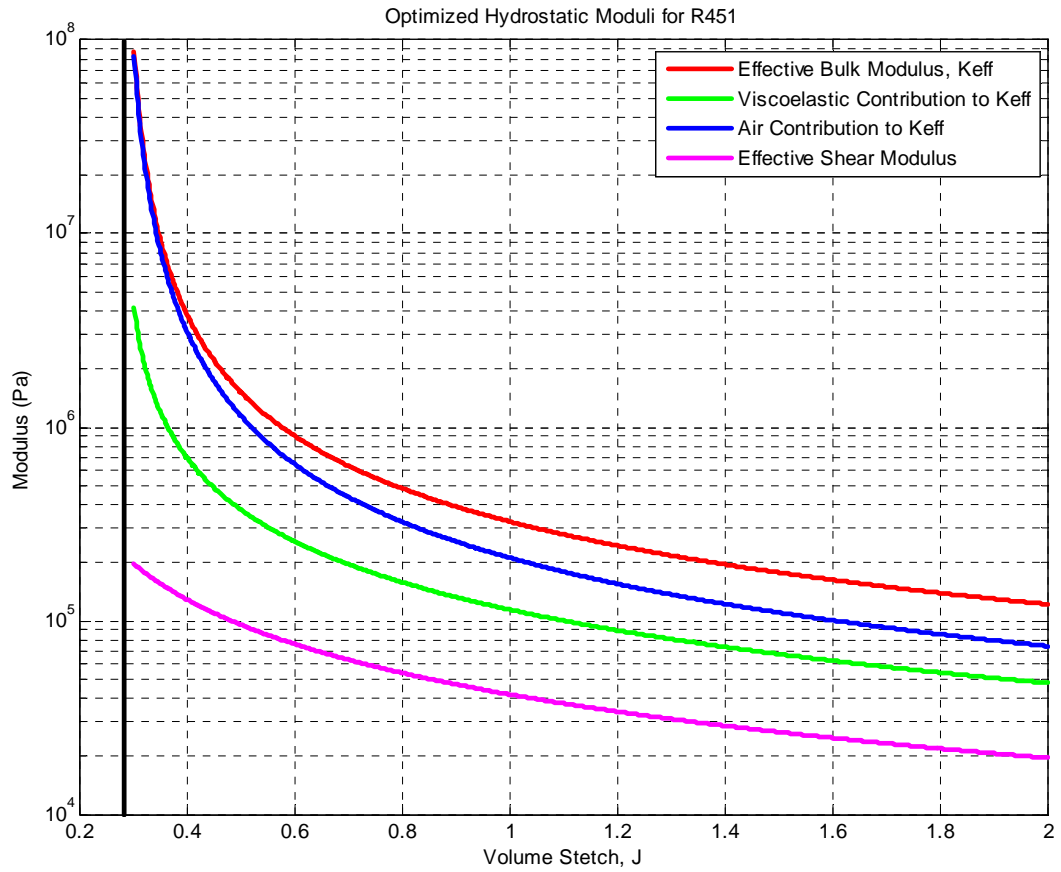


**Figure 3-14 Optimized Static Hydrostatic Moduli for R451 versus Volumetric Stretch**

### 3.2.2.3. Three-Phase and Plastic Parameters Optimization for R8702

Dilatometer data and the optimization results for R8702 are shown Figure 3-15. Stress relaxation is accounted for using the Prony coefficients given Table 3-4.

The optimized three-phase and plastic parameters for R8702 are given in Table 3-8. The corresponding hydrostatic moduli are shown in Figure 3-16, which shows the hydrostatic bulk (red) and shear (magenta) moduli for R8702. Also, the contributions to the effective bulk modulus from the material (green) and gas (blue) phases are shown. The relatively high stiffness of R8702 during the first pressure cycle, seen in Figure 3-15, gives a parameter optimization showing a strong bending transition centered at a volume stretch of 0.88. Before the transition the material phase is the dominant player in the effective bulk modulus. Afterwards the material behavior becomes dominated by the air term similar to the R451 foam.

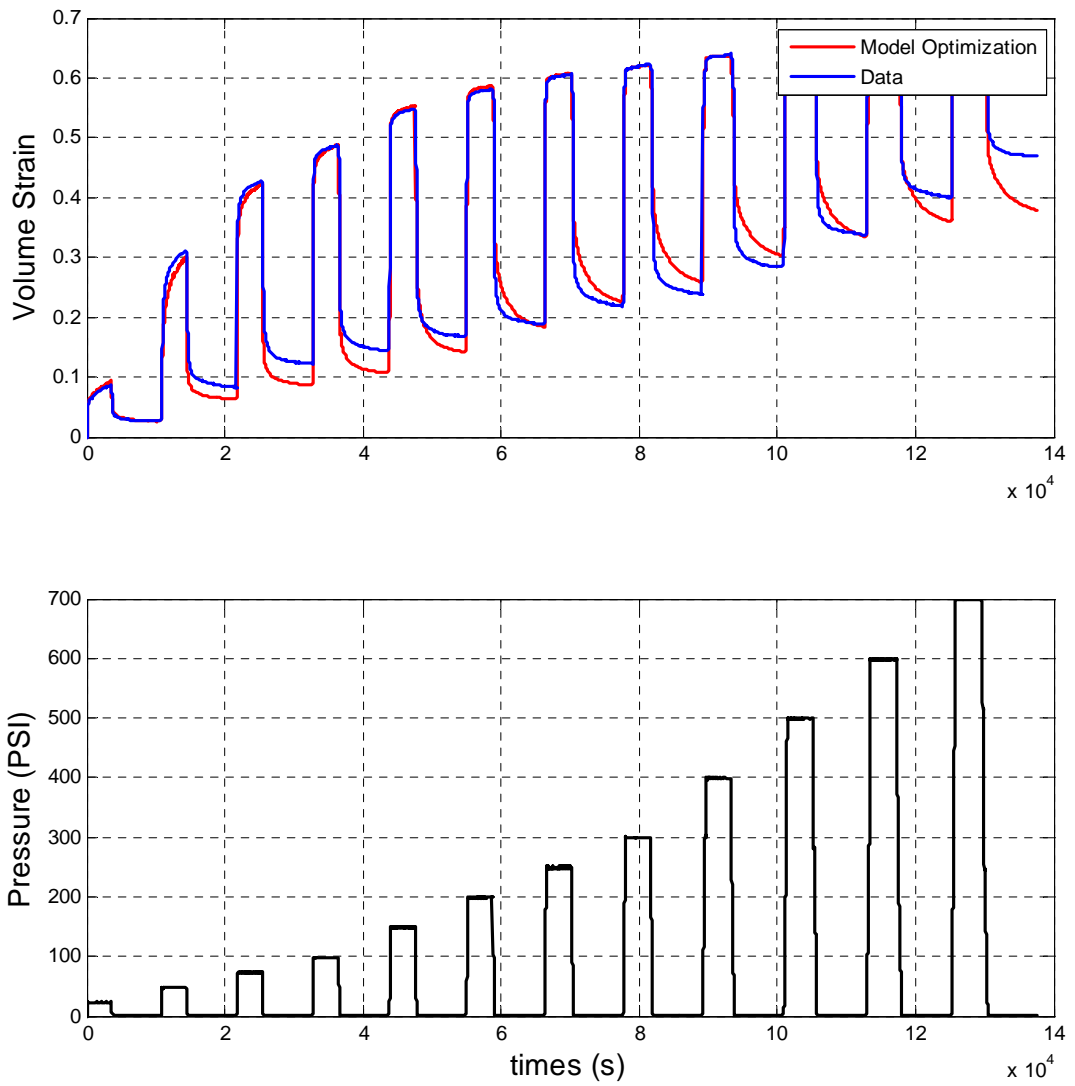


**Figure 3-15 R8702 Hyperbaric chamber test data and model optimization results – (fixed relaxation spectrum)**

**Table 3-8. Optimized Three-Phase and Plastic Parameters for R8702**

Parameter	Value
$D_1$	$1.0 \times 10^6$ Pa
$D_2$	0.86
$C_1$	0.88
$C_2$	20
$P_0$	$1.8 \times 10^5$ Pa (26.5 psi)
$S_0$	0.31
$p$	60
$QLIM$	0.04
$QSET$	0.30

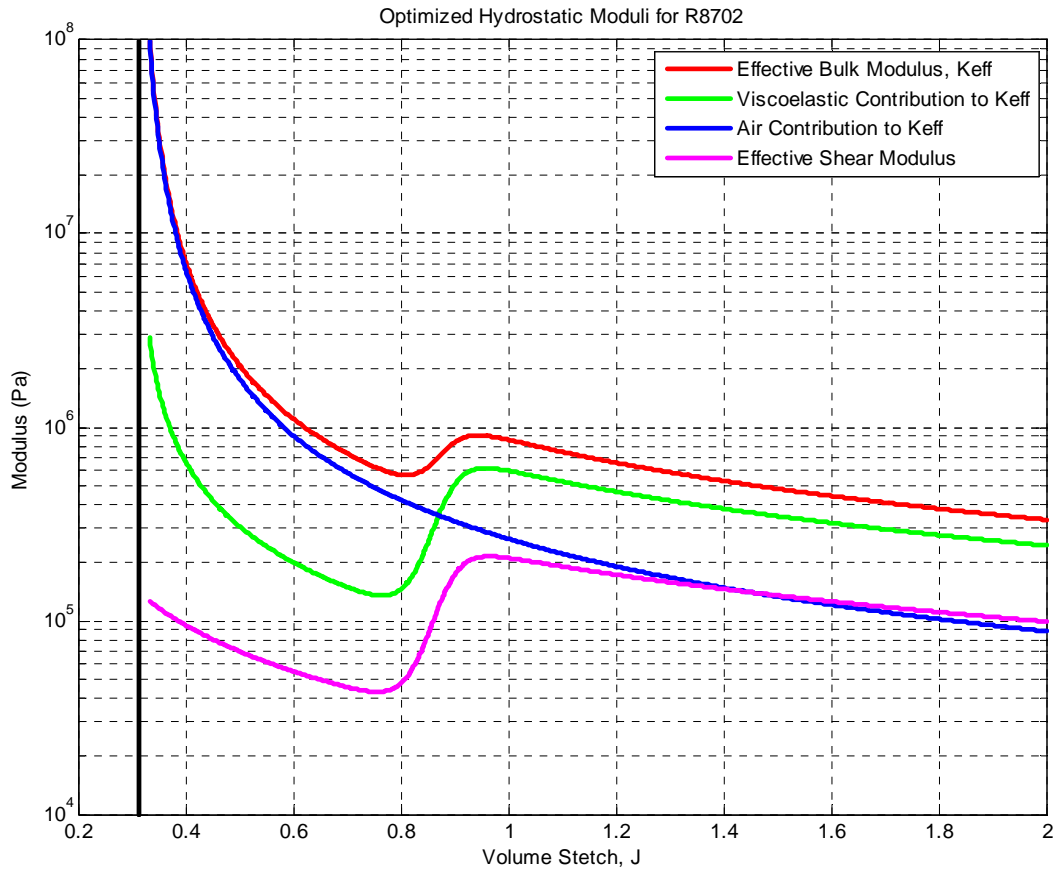


**Figure 3-16 Optimized Static Hydrostatic Moduli for R8702 versus Volumetric Stretch**

### 3.3. Summary

The three-phase and plastic parameters have been determined using a dilatometer apparatus that subjects a specimen to hydrostatic pressure and monitors its volume change. The pressure-history involved periodic pressurization and relaxation. Peak

pressure levels were increased with each cycle with a ramped peak pressure level. Parameters were developed by optimizing the description of the experiment using the constitutive model. Prony parameters, which control relaxation behavior, were established *a priori* using DMTA measurements.

Foam specimen R451 exhibited no detectable bending transition and the data could be described using three-phase theory without the bending modification. The optimized initial gas pressure within the foam was nearly twice atmospheric pressure. This provides the resiliency seen in the data and prevents the model from exhibiting a large amount of viscoelastic set over the pressure cycles. The effective bulk modulus of the material was found to be dominated by the gas phase.

Foam specimen R8702 exhibited a strong bending transition that occurs quickly with volumetric strain. In its initial state the effective bulk modulus is dominated by the material phase. A rapid drop in the material phase contribution occurs through the bending transition and the effective bulk becomes dominated by the gas phase. Like R451, an elevated gas pressure is found to improve optimization with the data set.

## CHAPTER 4

### 4. Shock Experiments

Two types of shock experiments were conducted on the foam specimens. UMD's Split Hopkinson Pressure Bar (SHPB) was used to test  $\frac{3}{4}$ " diameter specimens under high strain rate compression. In this test the specimens are sandwiched within two slender,  $\frac{3}{4}$ " diameter pressure bars of polycarbonate. An impact on one the "incident bar" sends a shock pulse to the specimen section. Specimen behavior is measured by monitoring strains are monitored on the incident bar and on the "receive bar", which accepts transmitted energy passing through the specimen. Larger specimens were tested in a Conical Shock Tube (CST) at the Naval Underwater Warfare Center. The CST is essentially a water-filled, thick walled cylinder with a conical bore. The wide end accepts a test specimen up to about 9.5" diameter. At the narrow end an explosive charge is detonated sending a water-borne shock wave to the specimen. A pressure gauge near the specimen monitors the shock pressures in the water. Specimens are prepared with a pressure sensor embedded behind the specimen to monitor transmitted pressure. Specimens are also fitted with a neutrally buoyant accelerometer on their outward surface to monitor surface motion during the shock event.

#### 4.1. Split Hopkinson Pressure Bar Experiments

A conventional SHPB experimental setup was used as shown in the photograph in Figure 4-1 and the schematic in Figure 4-2. A polycarbonate pressure bar was used

rather than steel or aluminum to provide better impedance matching with the foam specimens. Two BAM-1 bridge amplifiers were used to measure strain in full bridge configuration. Strain gauge pairs, axially aligned, were located at the middle of the incident bar and on the receive bar near the specimen. These were monitored with a digital oscilloscope for data capture. Specimens were sandwiched between the bars and held with a light pressure supported by the frictional contact within the support collars. Samples were otherwise unattached to the bars. Each foam sample was tested in a 1" and 1/2" sample height. Diameters of all specimens were about 3/4" to match the pressure bar.

Since the striker bar is matched to the incident bar in both material and diameter, a nearly perfect square compression pulse results from the impact of the striker bar. Immediately after impact, a compressive strain pulse begins to spread out from the contact interface in both directions equally. The pulse width is exactly twice the striker length since it terminates when the travelling compressive strain in the striker bar reaches its free end. This is why the striker bar is typically less than 1/2 the length of the incident bar: it keeps a small separation in time from the end of a passing pulse and the arrival its reflection.

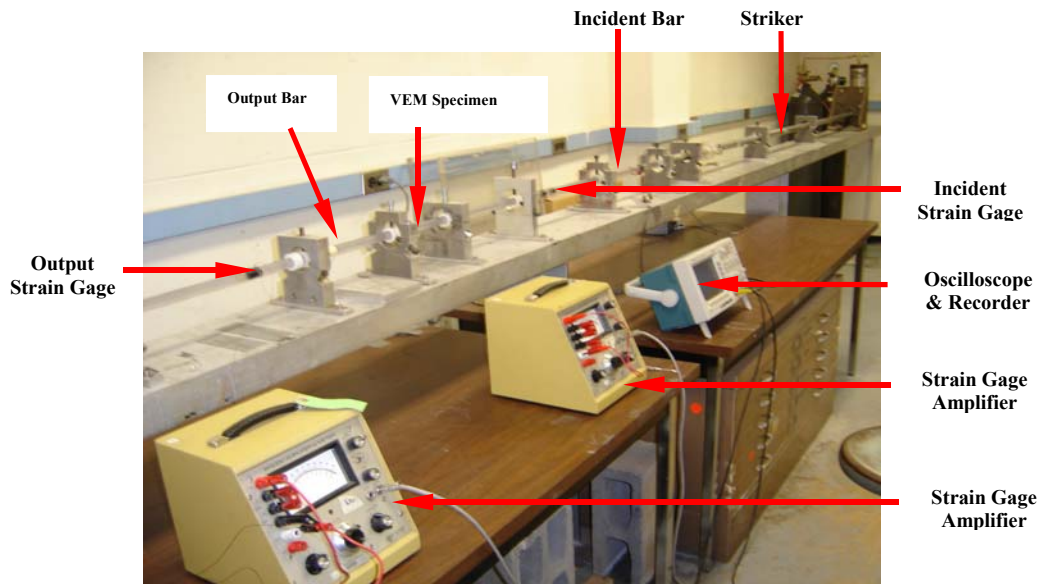


Figure 4-1 Photo of UMD SHPB with Polycarbonate Pressure Bar

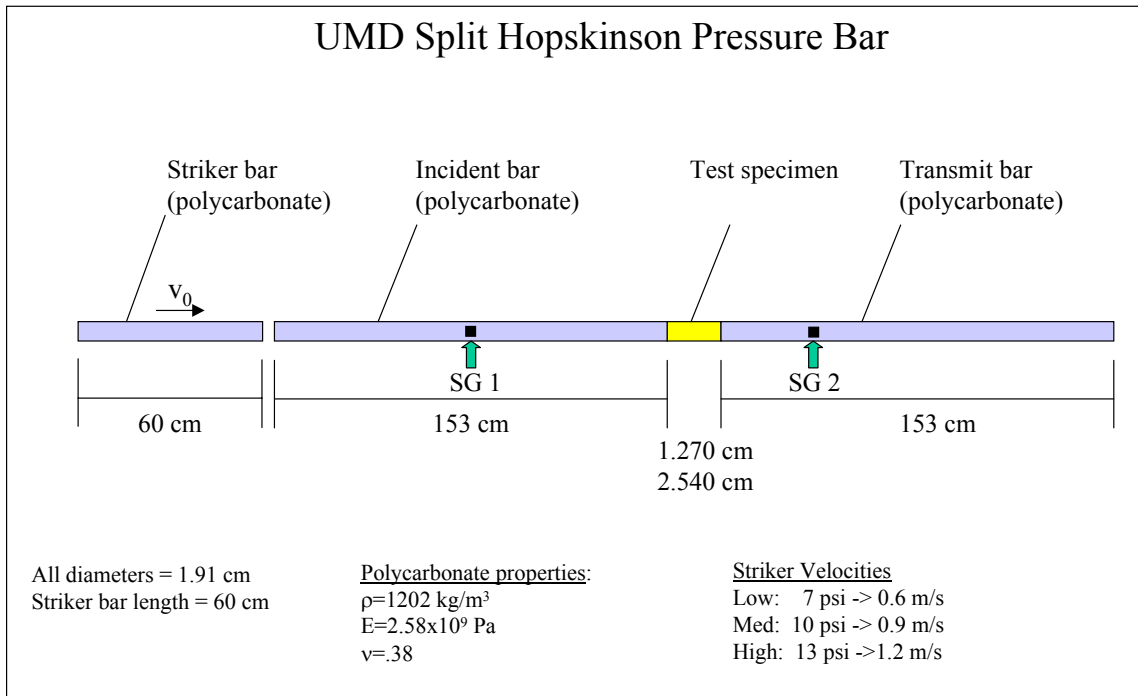


Figure 4-2 Schematic of the UMD SHPB with Polycarbonate Pressure Bar

#### ***4.1.1. SHPB Results for RUBATEX R451***

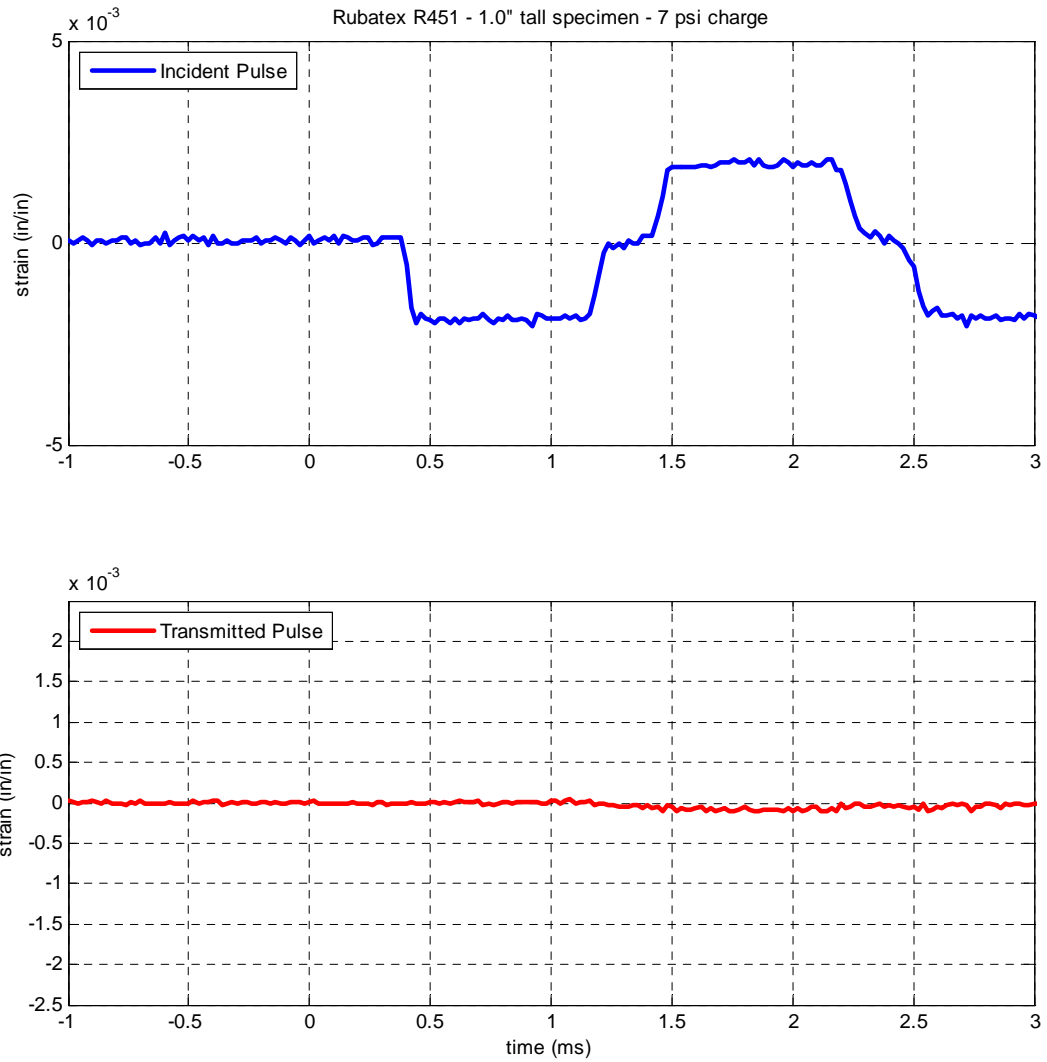
This section provides the SHPB results for R451. Specimens were tested using three different impact velocities and two specimen thicknesses.

Figure 4-3 shows the response of a 1” thick R451 specimen at the lowest striker charge of 7 psi. The upper curve (blue) is the time-history of strain gauge located at the middle of the striker bar. This gauge first detects the compression pulse caused by the striker. Shortly thereafter it detects a reflected tensile wave from the specimen interface. The reflection of the tensile wave from the free end of the incident bar can be seen near the end of the time history. The reflected pulse is nearly the mirror image of the incident pulse, meaning that nearly all the energy was reflected at the specimen interface. This is also evident in the receive bar. The lower curve (red) shows the transmitted strain. In this case it is clear that the foam specimen is nearly 100% effective in blocking the strain pulse.

Figure 4-4 and Figure 4-5 show the 1” R451 responses to the 10-psi and 13 psi striker levels, respectively. As one would expect, the pulse amplitude in the incident bar grows in proportion with the striker velocity. The sample continues to function as a shock isolator, although there is a small but noticeable increase in the amount of transmitted energy.

More interesting results are obtained with the ½” thick specimens. Figure 4-6 shows the response with a 7-psi striker charge. The sample is still blocking a majority of the incident energy, but now a clear transmitted pulse is observed. The pulse arrives at about

1.2 ms and keeps a nearly flat amplitude until about 2 ms where it drops back near zero, giving a pulse width that closely matches the incident wave. After 2 ms the pulse exponentially returns to zero. Results for the 10 psi striker charge on the ½” R451 specimen are shown in Figure 4-7. Now the material begins to transmit a more significant portion of the incident energy and there is a hint of densification effects near the end of the transmitted pulse. The reflected tensile wave is also beginning to show signs of lost energy. This is characterized by a loss of amplitude and rounding near the end of the pulse. Also, the slow decay of the pulse after the nominal pulse width is more evident. Figure 4-8 shows the response to the 13-psi charge. The densification effect is highly pronounced. The peak transmitted strain is slightly more than 50% of the incident strain level. However, from an energy standpoint, it still represents a small fraction of the incident pulse. The decay of the transmitted pulse is now such that the nominal pulse width is no longer discernable. A significant portion of the energy is being trapped in the foam specimen and slowly transmits to the higher impedance bar.



**Figure 4-3 SHPB Strain Gauge Data - 1" RUBATEX R451 specimen with 7psi charge**

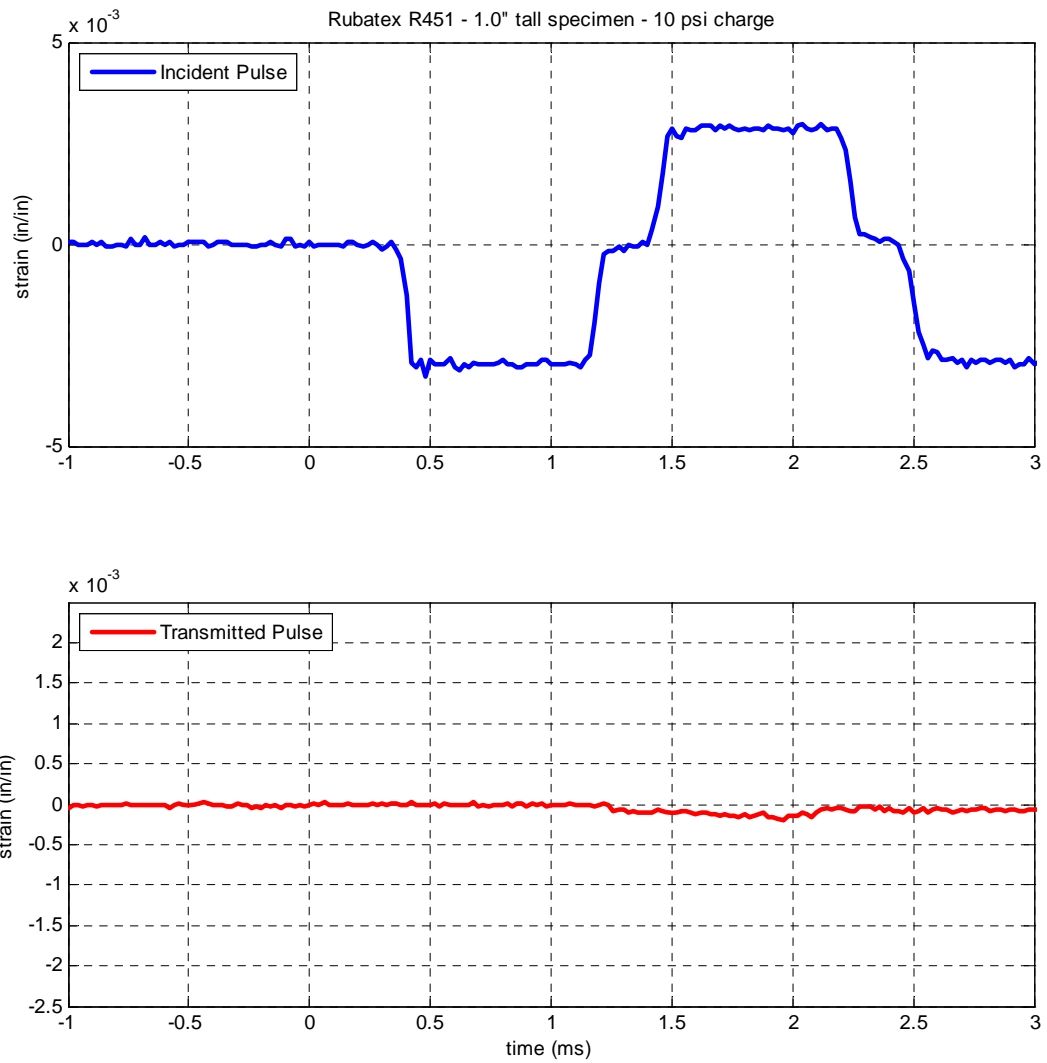


**Figure 4-4 SHPB Strain Gauge Data - 1" RUBATEX R451 specimen with 10 psi charge**

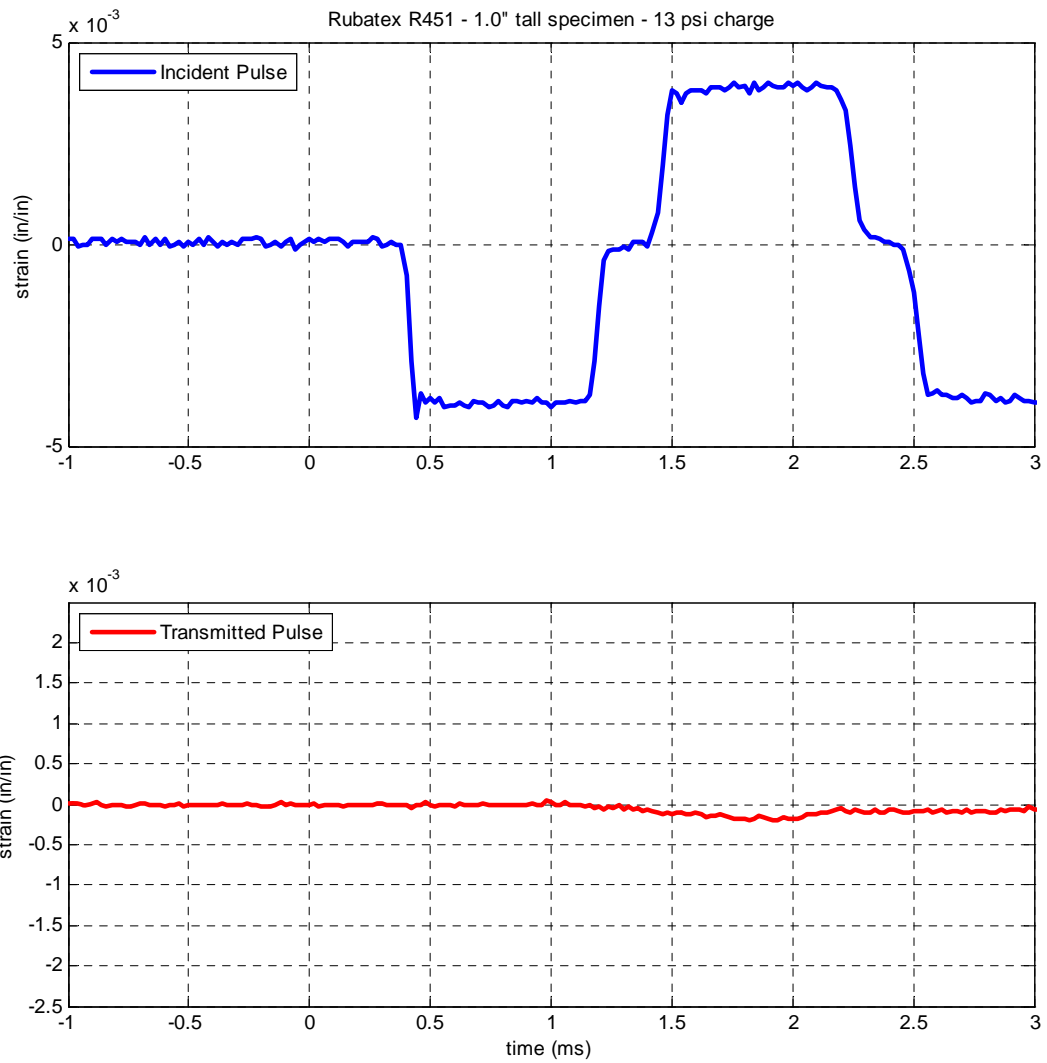


**Figure 4-5 SHPB Strain Gauge Data - 1" RUBATEX R451 specimen with 13 psi charge**

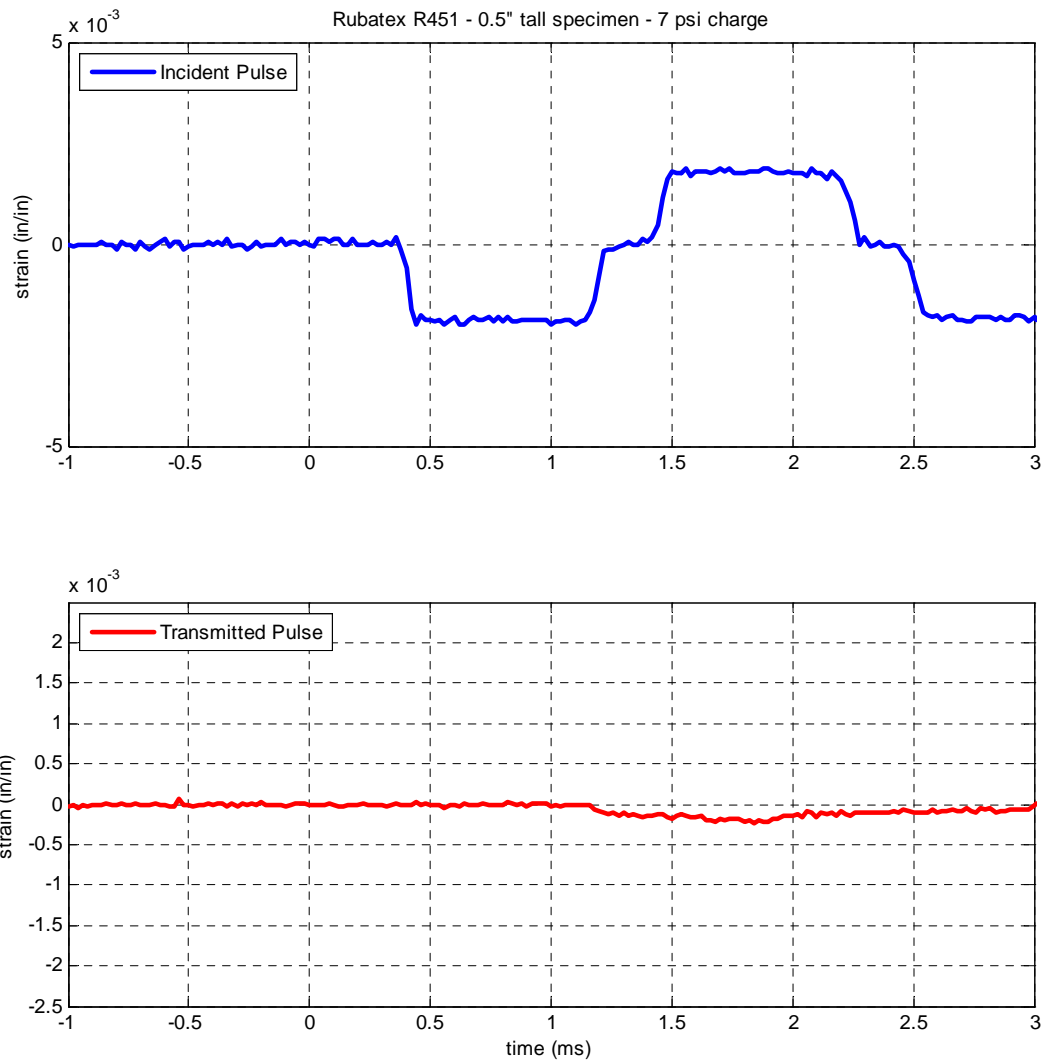


**Figure 4-6 SHPB Strain Gauge Data - 1/2" RUBATEX R451 specimen with 7psi charge**

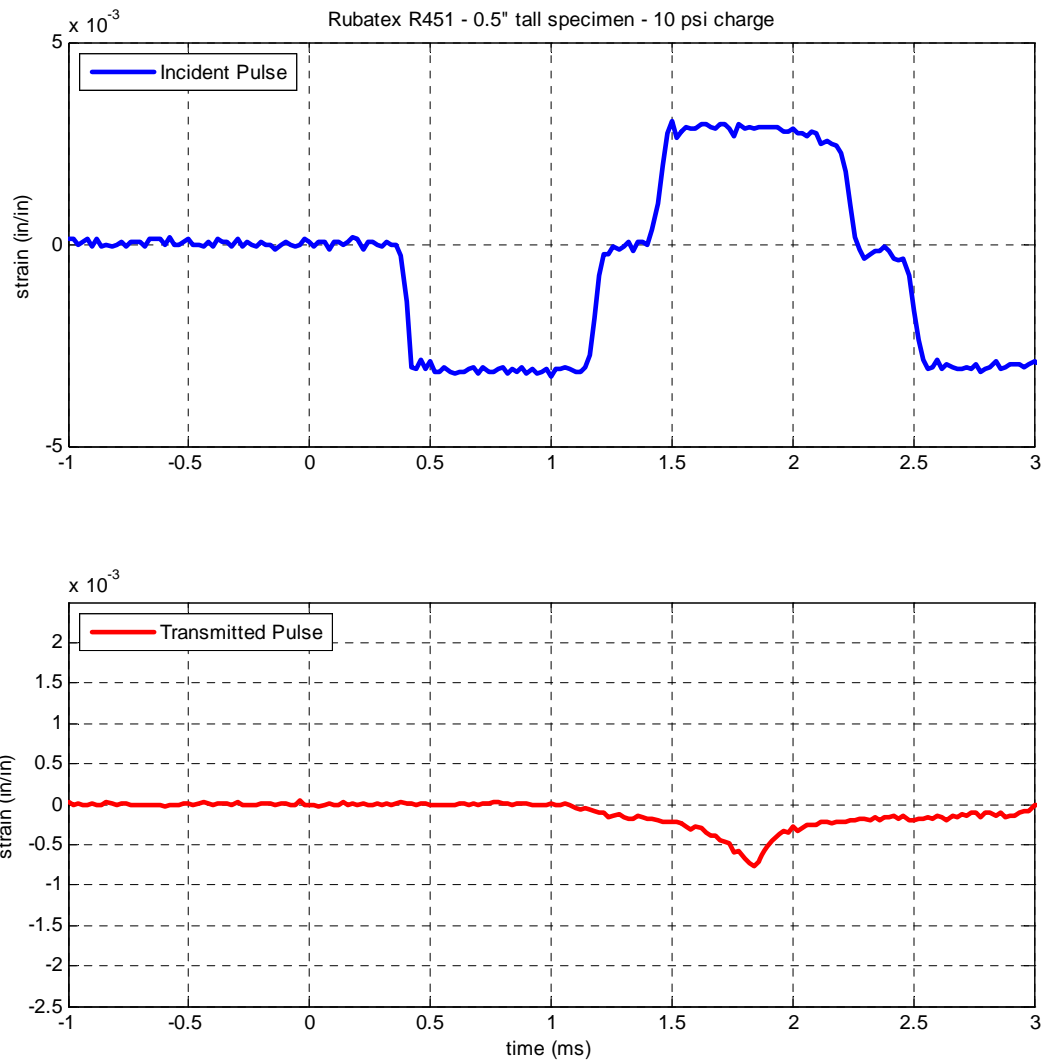


**Figure 4-7 SHPB Strain Gauge Data - 1/2" RUBATEX R451 specimen with 10 psi charge**

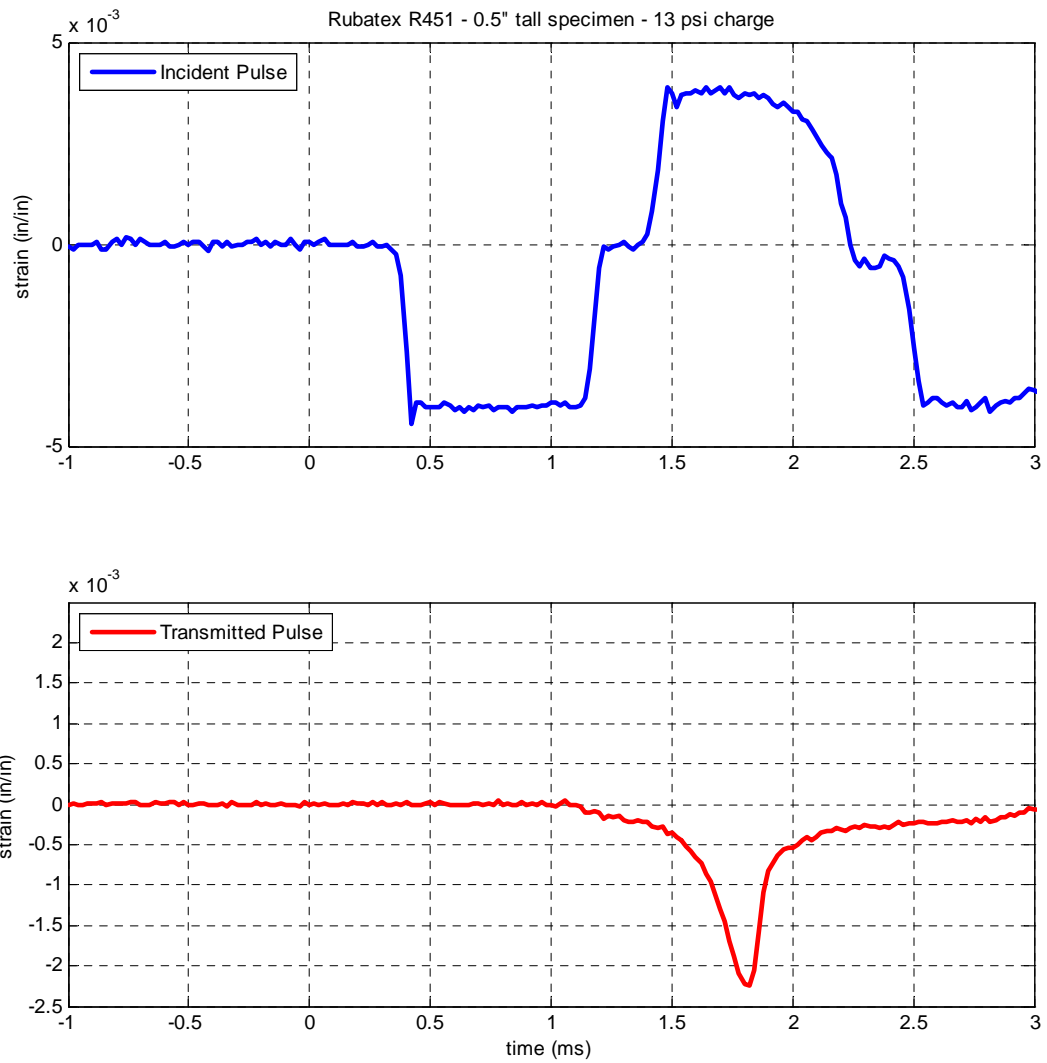


**Figure 4-8 SHPB Strain Gauge Data - 1/2" RUBATEX R451 specimen with 13 psi charge**

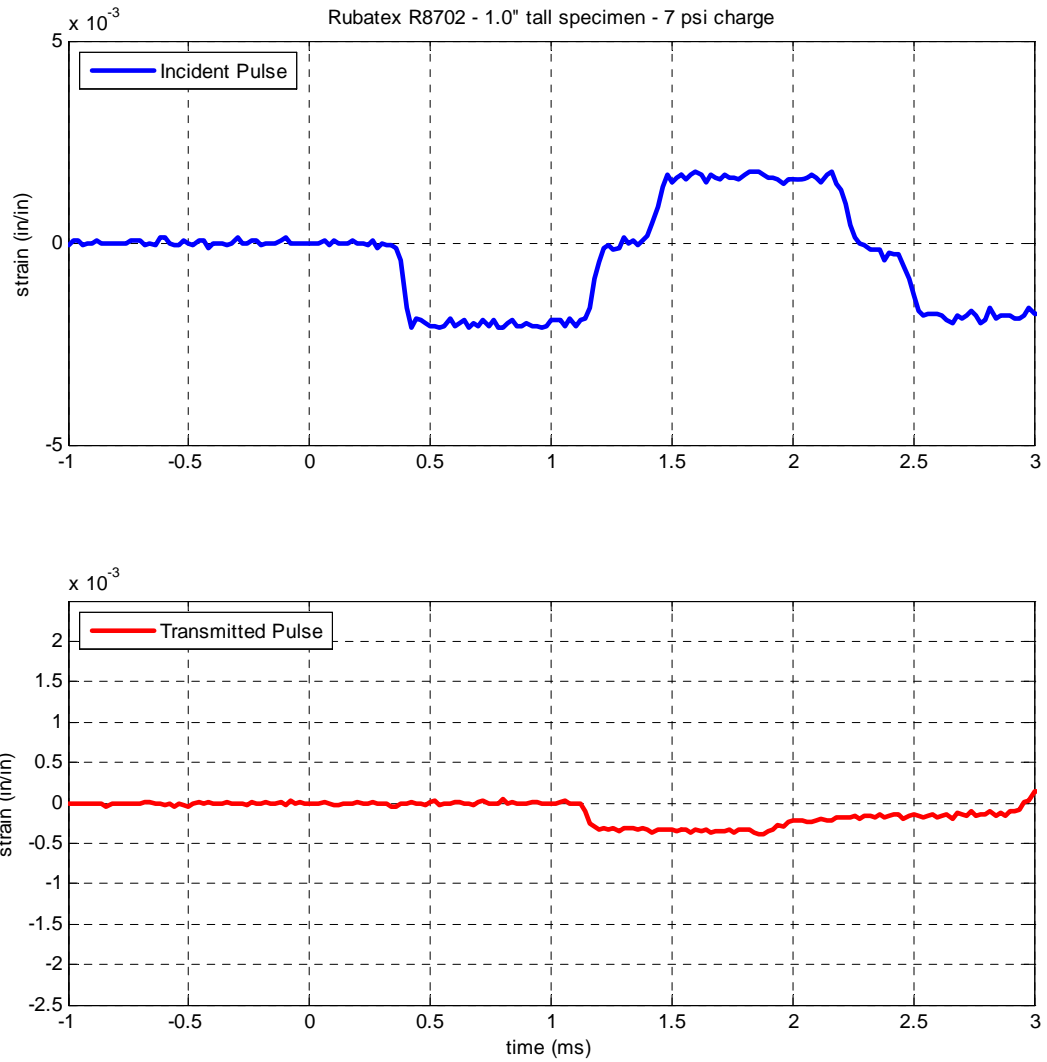
#### ***4.1.2. SHPB Results for RUBATEX R8702***

This section provides the SHPB results for R8702. Specimens were tested using three different impact velocities and two specimen thicknesses.

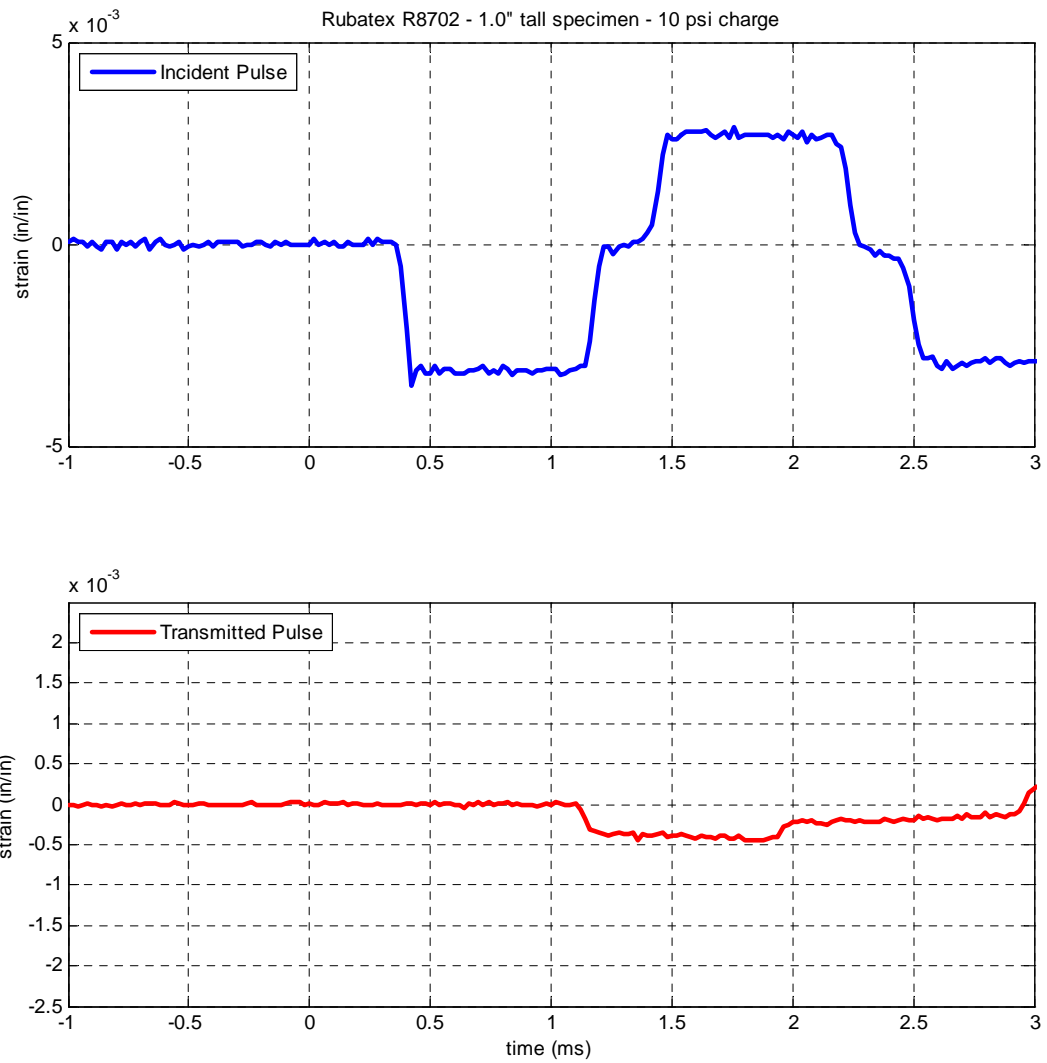
Figure 4-9 shows the response of a 1” thick R8702 specimen at the lowest striker charge of 7 psi. The upper curve (blue) is the time-history of strain gauge located at the middle of the striker bar. This gauge first detects the compression pulse caused by the striker. Shortly thereafter it detects a reflected tensile wave from the specimen interface. The reflection of the tensile wave from the free end of the incident bar can be seen near the end of the time history. The reflected pulse is nearly the mirror image of the incident pulse, except for a small and uniform reduction in amplitude across the entire pulse width. This missing strain energy in the reflected pulse incident bar appears in the receive bar as a low pulse of uniform amplitude (red curve). Hence, the material response is as one might expect for a linear material with a relatively low modulus. Like the R451 specimens, the process of a slow release of trapped strain energy is evident after 2 ms.

Figure 4-10 and Figure 4-11 show the 1” R8702 response to the 10-psi and 13 psi striker levels, respectively. The character of the sample response is mostly unchanged, except for a small increase in the amplitude over the pulse width. It is interesting that the initial pulse amplitude is somewhat insensitive to the incident strain level, which is likely due to the specimen reaching its stress plateau.

Figure 4-12 shows the response of a ½” R8720 specimen with a 7 psi striker charge. The behavior is pretty much unchanged from what is seen in the 1” specimens. Figure 4-13 and Figure 4-14 show the response at the 10-psi and 13 psi striker charge levels, respectively. The figures show that the initial portion of the transmitted pulse remains unchanged, but the densification effects that occur later becomes pronounced.



**Figure 4-9 SHPB Strain Gauge Data - 1" RUBATEX R8702 specimen with 7psi charge**



**Figure 4-10 SHPB Strain Gauge Data - 1" RUBATEX R8702 specimen with 10psi charge**

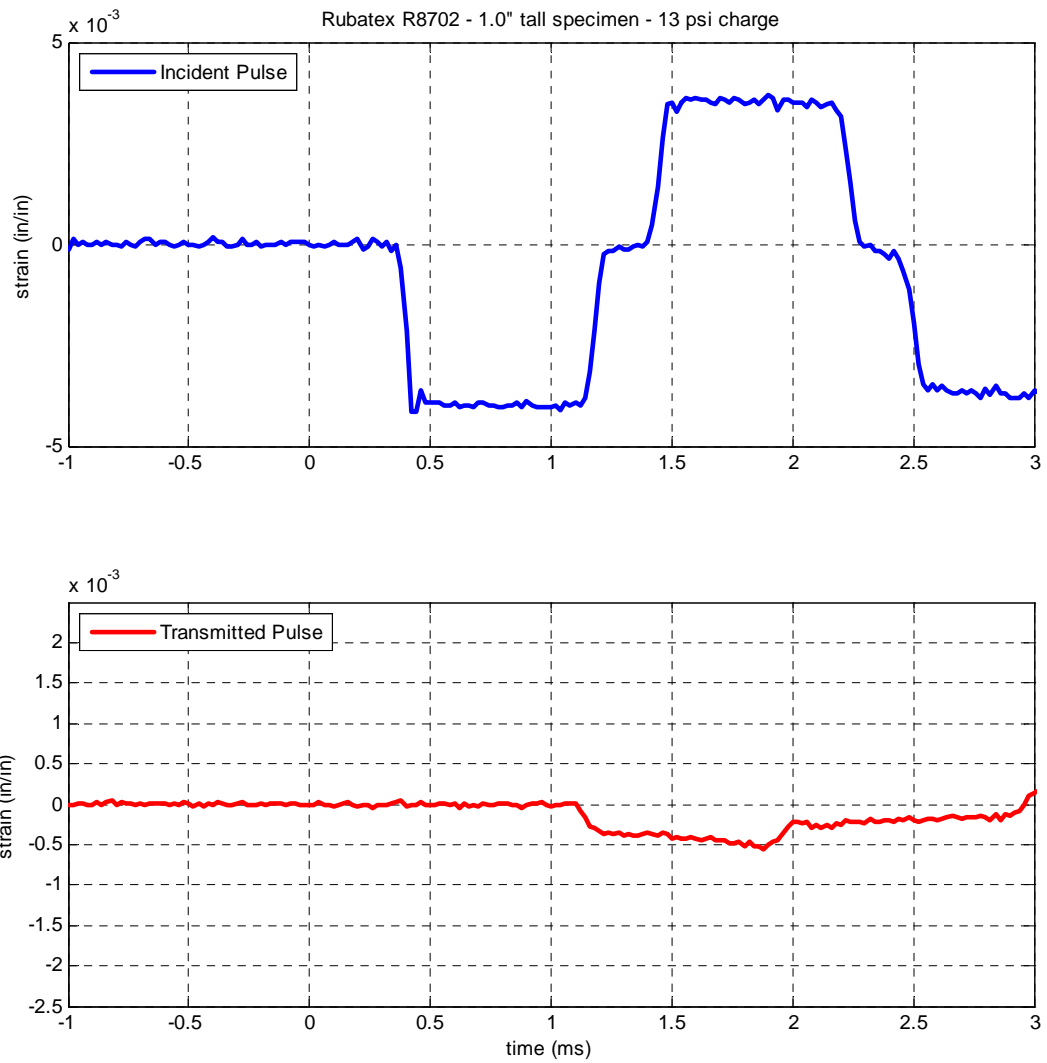


**Figure 4-11 SHPB Strain Gauge Data - 1" RUBATEX R8702 specimen with 13psi charge**

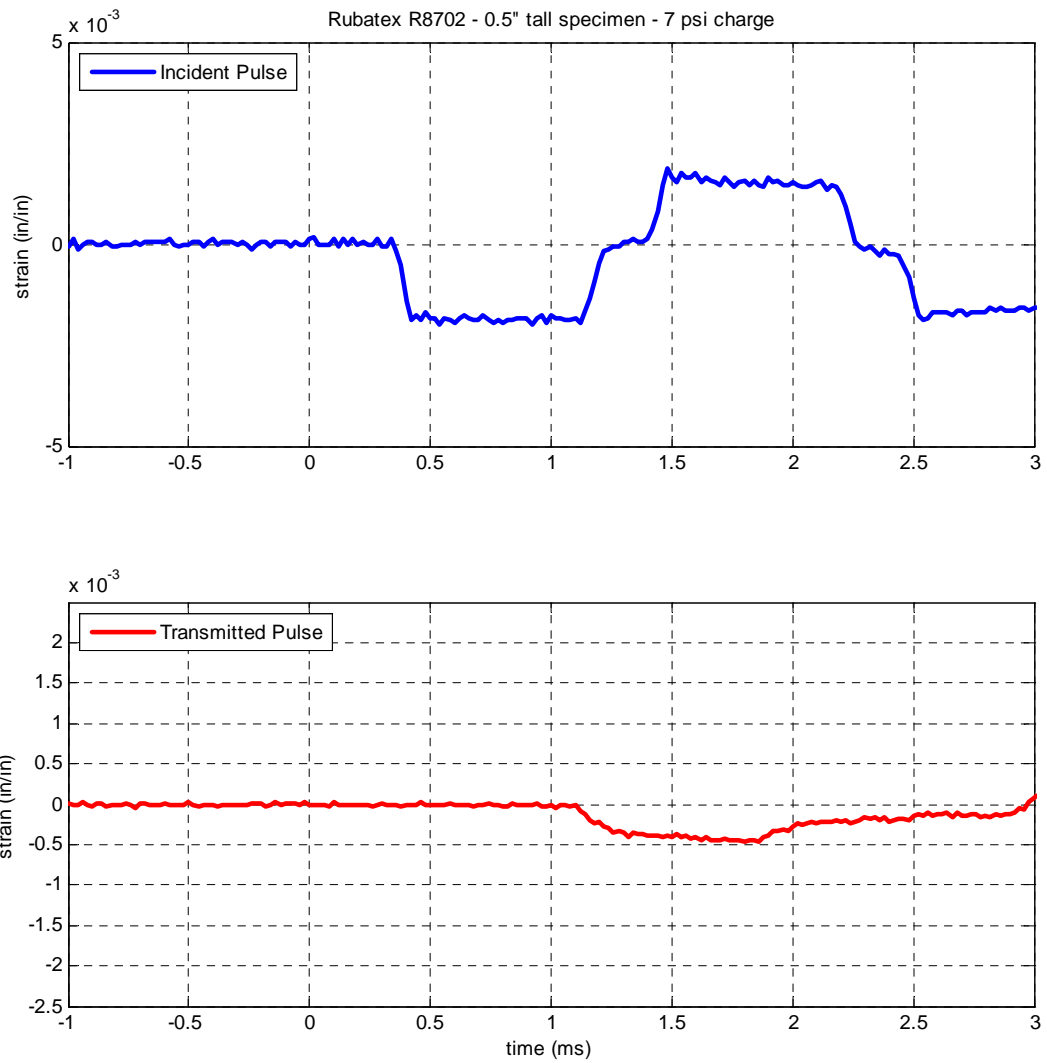


**Figure 4-12 SHPB Strain Gauge Data - 1/2" RUBATEX R8702 specimen with 7psi charge**

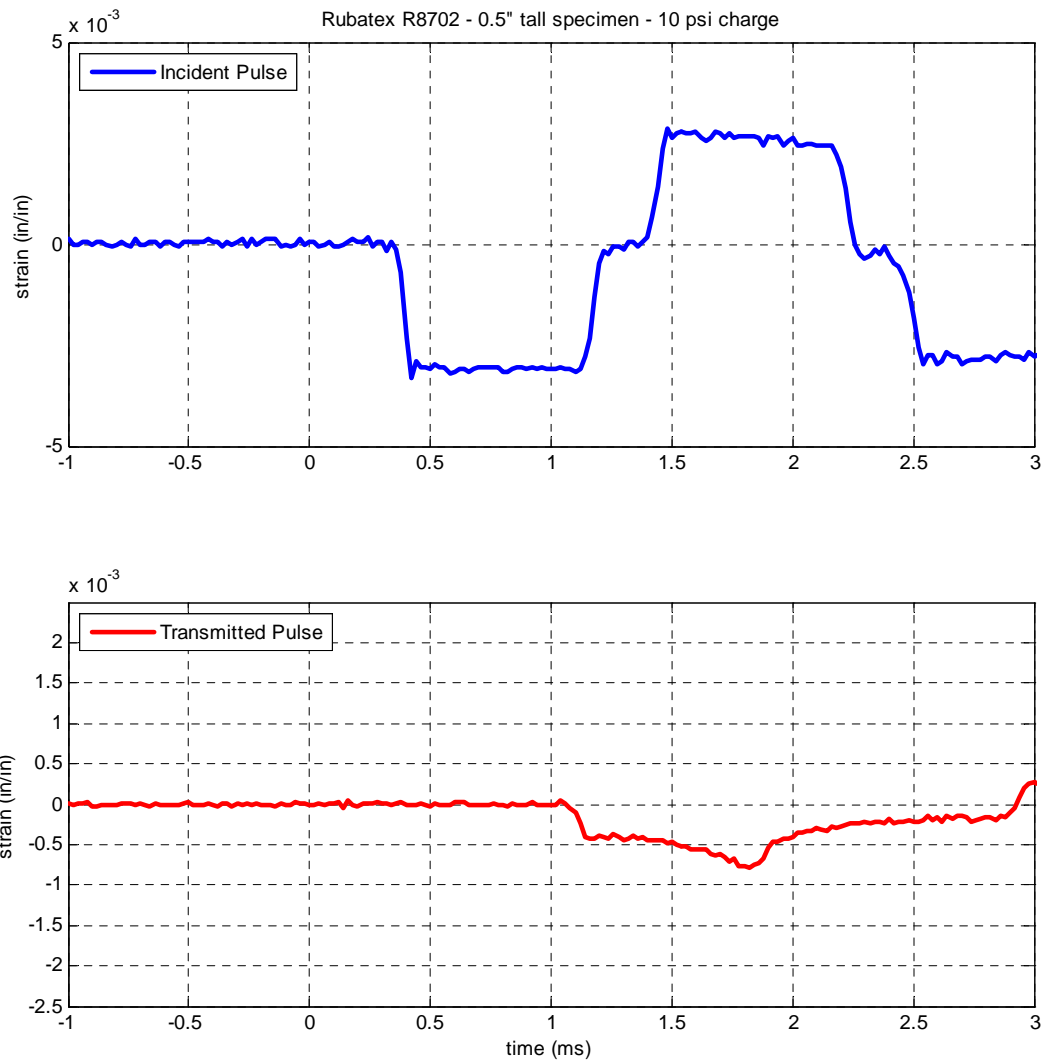


**Figure 4-13 SHPB Strain Gauge Data - 1/2" RUBATEX R8702 specimen with 10 psi charge**

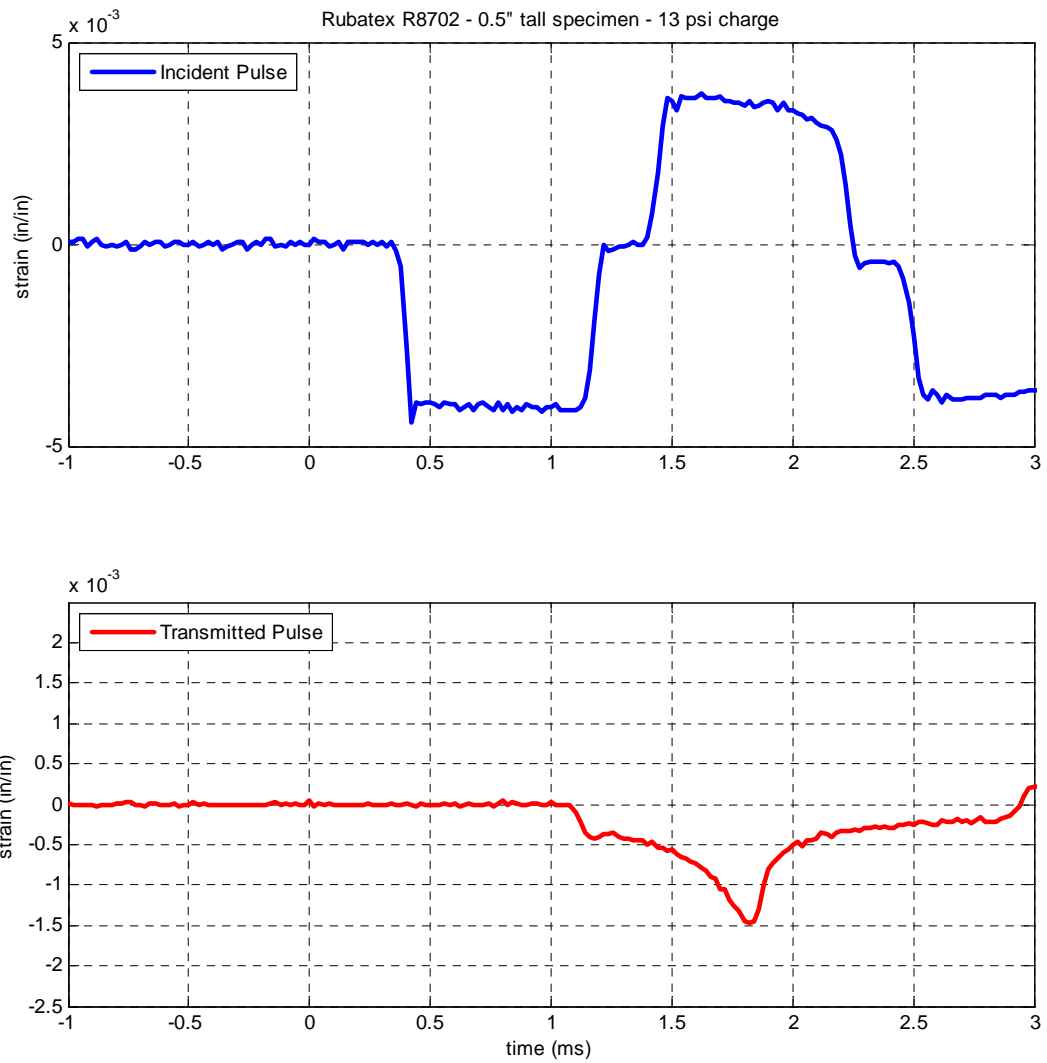


**Figure 4-14 SHPB Strain Gauge Data - 1/2" RUBATEX R8702 specimen with 13 psi charge**

## **4.2. Conical Shock Tube Experiments**

The NUWC Conical Shock Facility, shown in Figure 4-15, is designed to simulate a small conical sector of a full-scale, spherical underwater charge. Test specimens can be mounted on a blocked witness plate or a slider mass can be used to simulate the mass impedance of the floating shock platform used in the Navy standard Heavyweight Shock Test (MIL-S-901D). A blocked witness plate was selected for specimen testing. In each test the data were collected from three sensors. The slider shown in the schematic was not used.

The wall thickness of the tube sections increases along the length of the tube. This ensures a rigid boundary condition for the travelling shock wave and prevents dispersion of the shock pulse due to radial wall compliance.

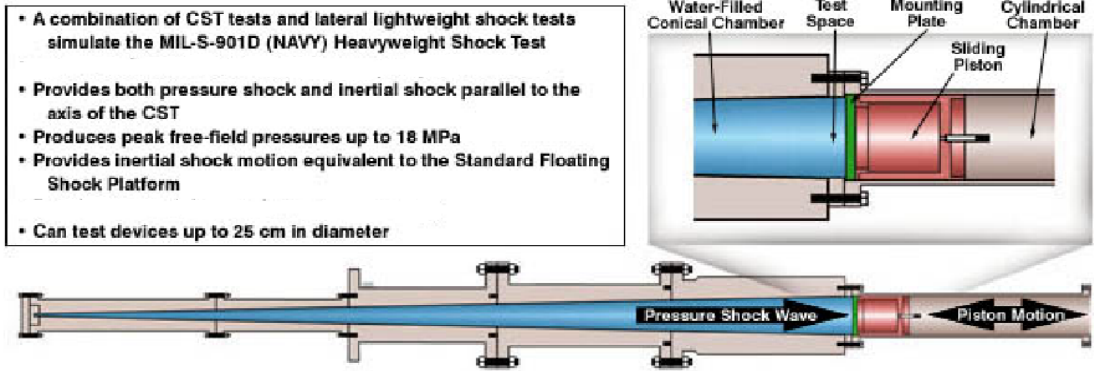


**Figure 4-15 Conical Shock Tube Schematic (top). Photo of rigged test specimen (bottom)**

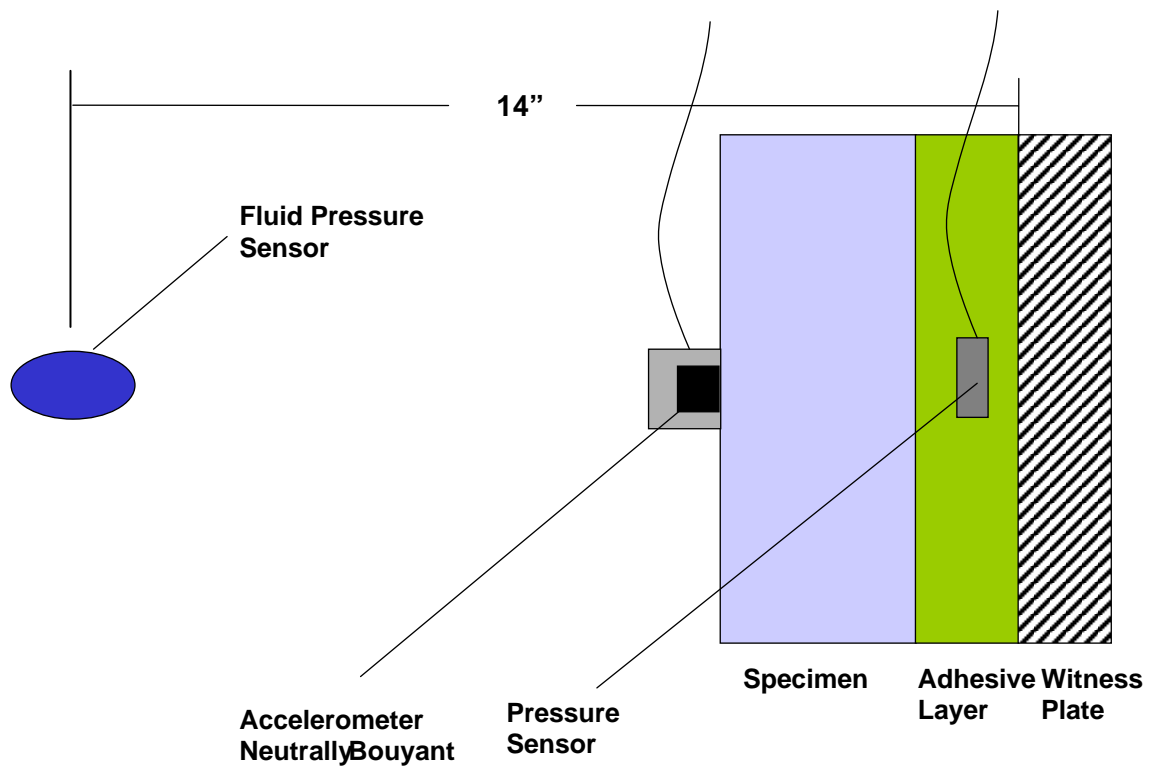
Figure 4-16 shows how the specimen is configured in the test section. The CST facility provides a pressure sensor to monitor the shock pressure at a location near the test specimen. This sensor was rigged at a location nominally 14” in front of the specimens. This sensor shows the incident shock wave and its exponential decay as it passes towards the specimen. Since the RUBATEX test specimens are low-impedance relative to water, a strong inverted shock pulse is reflected from the specimen back towards the sensor. Upon arrival at the sensor, there is sudden cancellation of the incident pressure. The inverted pulse is not fully developed however because water cavitation occurred at very low negative pressure in most cases. Instead, a period of near zero pressure is observed during the cancellation period. Later in time, an extended period of positive pressure occurs due to the relatively slow process of compressive strain energy release from the specimen. At even longer times, there is a gradual rise in pressure, which is an artifact of the CST measurement. The propagation impedance of the reflected wave increases due to the diminishing cross section, thereby trapping the energy.

Figure 4-18 shows the specimen the 1.875” thick R451 specimen being prepared for the test. Motion of the specimen’s outer surface is measured with an Endevco Instron<sup>®</sup> accelerometer, Model 2255B-01, mounted on the face of the specimens. To reduce local inertia effects, the accelerometers are encased in a collar of syntactic foam to zero their net buoyancy. Time integration of the accelerometer response provides the surface velocity. A second integration provides the surface displacement. As the shock wave reaches the sample, which has a low characteristic impedance relative to water, an

acceleration profile is developed at the interface that is qualitatively resembles the time derivative of the incident pressure wave. The accelerometer does have a low-frequency roll-off shown in Figure 4-17. Hence, velocities and displacements established via integration of the accelerometer data will accumulate error as the integration is extended in time.

The sensor behind the specimen provides a measure of shock energy that is transmitted through the specimen and to the structure. The sensor used is a PCB Underwater ICP Blast Pressure Sensor, model #138M176. In the CST experiments conducted for this report, the tube was terminated with a rigid witness plate, rather than the sliding piston, so the data are most representative of the foam behavior on a high-impedance structure. Finite-impedance structures would likely experience lower transmitted pressures.

To make this measurement, a pressure sensor was imbedded in a 1/2" thick adhesive layer joining the specimen to the metal attachment plate. The greenish adhesive layer can be seen in the photograph shown in Figure 4-18 between the specimen and the witness plate. The sensor cable can be seen on the far side of the photo. The transmitted pressure at the sample/blocked interface also provides information that is complementary to the accelerometer to isolate material response from the fluid effects. This could be very useful because the fluid behavior, which is complicated by cavitation effects as well as tube dynamics, is difficult to model properly.



**Figure 4-16 Test specimen setup in the CST**

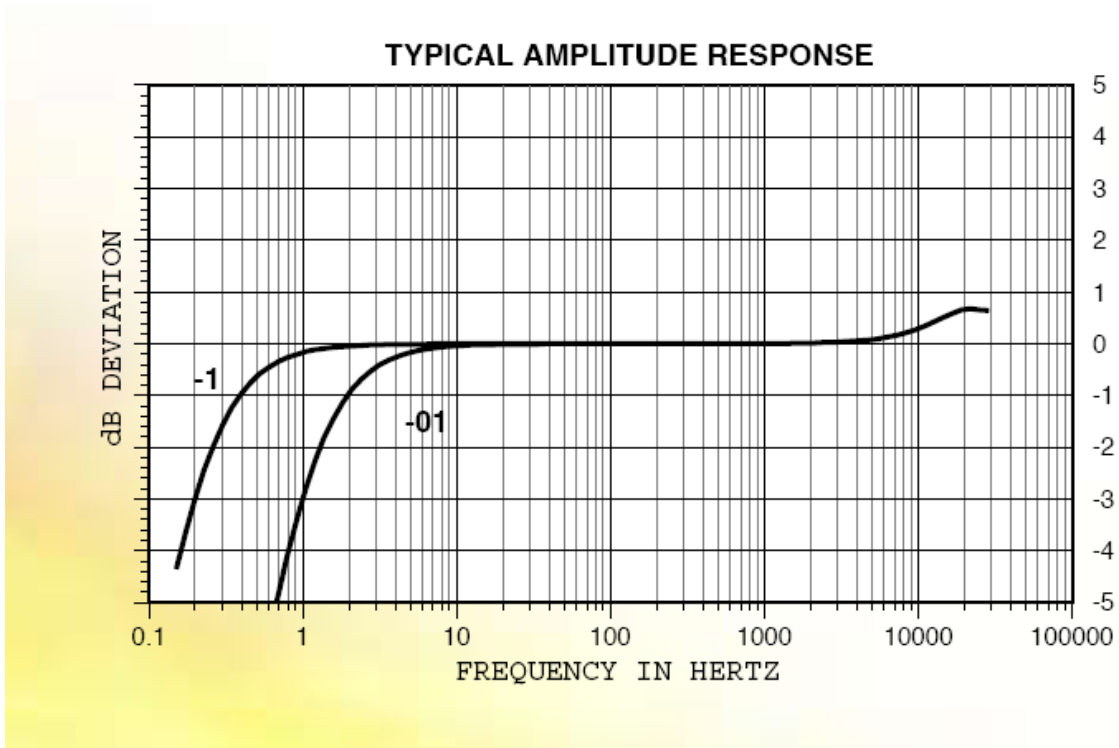


**Figure 4-17 Frequency Response of Endeveco Model 2255B Shock Accelerometer (Type -01 Used in CST)**



**Figure 4-18 RUBATEX R451 sample ready for Concial Shock Tube Testing**

***4.2.1. CST Results for RUBATEX R451***

Figure 4-19 shows the CST results for a 1.875” thick R451 specimen using the lower shock level (no booster). The blue curve shows the pressure at an offset of 14” from the specimen surface. The shock wave passes with a peak pressure of about 1600-psi and rapidly decays thereafter. The reflection from the specimen surface arrives at the pressure sensor at about 5.1 ms and cancels the incident pressure. Cavitation of the water prevents a negative pressure from forming, which would be analogous to the tensile reflection in the SHPB experiment. The thick, soft specimen causes an extended period of cavitation and no pressure is seen for over the time scale reported. The pressure

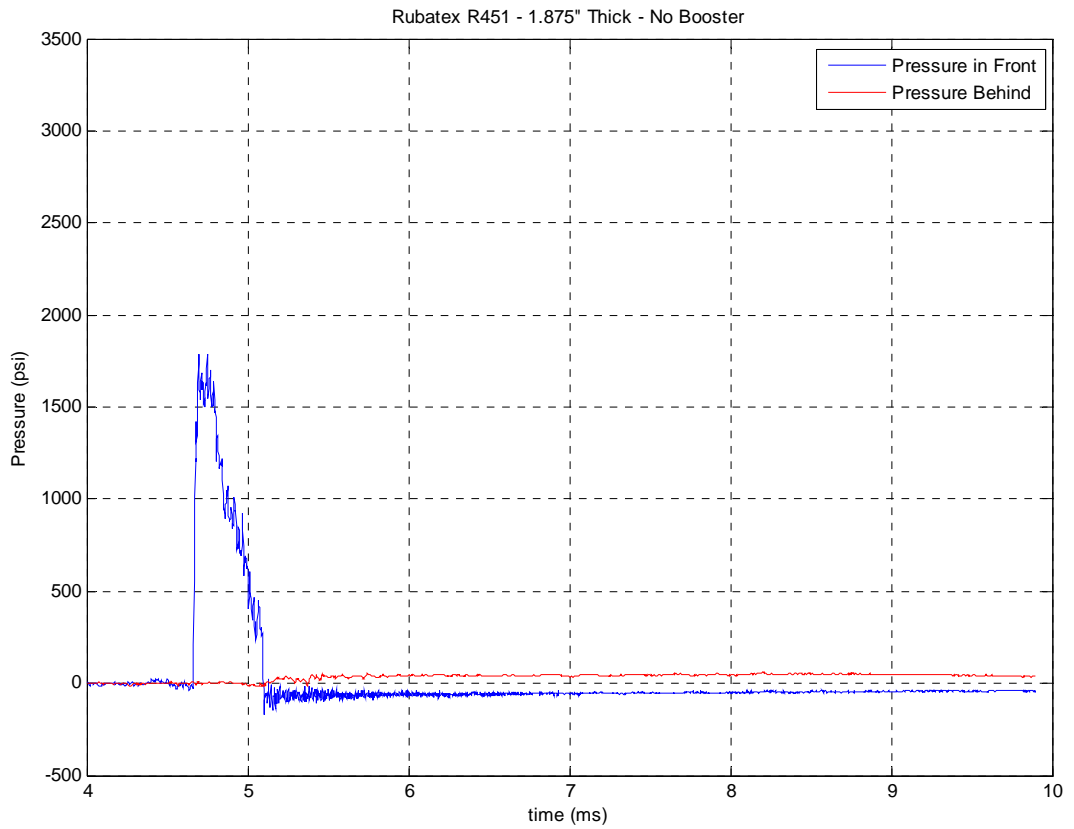
behind the specimen is very small indicating that the material has effectively blocked the majority of the shock energy from reaching the witness plate. Note however that the transmitted pressure, although small, lingers at the witness plate for the extended period shown in the figure.

The accelerometer data for this test are shown in Figure 4-20. The acceleration is shown in the top plot. Velocity and displacements were developed by integration the accelerometer data as shown in the center and bottom plots, respectively. The displacement peak of about 1" is believable for this specimen, but it should be noted that due to the low-frequency roll-off of the accelerometer used, significant error accumulation can be expected after about 2 ms.

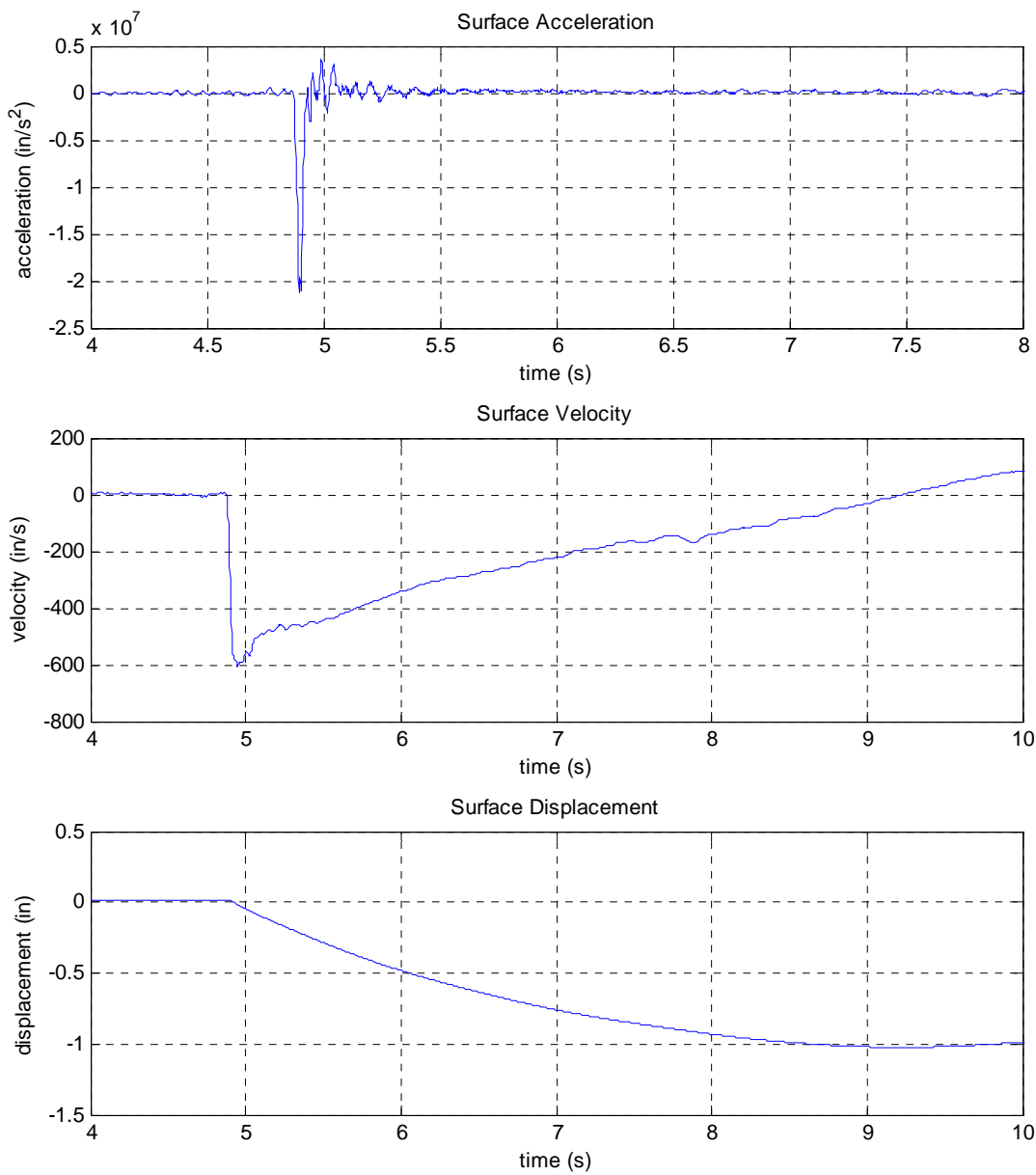
Figure 4-21 shows the CST results for a 1.875" thick R451 specimen using the higher shock level (with booster). The blue curve shows the pressure at an offset of 12" from the specimen surface. The shock wave passes with a peak pressure of about 3200-psi and rapidly decays thereafter. The reflection from the specimen surface arrives at the pressure sensor at about 4.9 ms and cancels the incident pressure. The pressure behind the specimen (red curve) shows a significant densification as a small portion of energy gets through the material. As this trapped stress is slowly released back to the water it helps to collapse the cavitation bubble which is seen at about 9 ms in the offset pressure sensor.

Figure 4-22 shows the accelerometer results for this test. The peak acceleration and velocity levels are nearly double compared to the low level shot, which is consistent with

the relative peak pressure levels. In this case however, the problem with integration of the accelerometer level is evident in the displacement plot, which shows the specimen surface reaching a peak displacement of 2.1 inches, which is in excess of the specimen thickness of 1.875”.



**Figure 4-19 CST Pressure Sensors Data - 1.875” RUBATEX R451 specimen – no booster**



**Figure 4-20 CST Accelerometer Data - 1.875" RUBATEX R451 specimen – no booster**

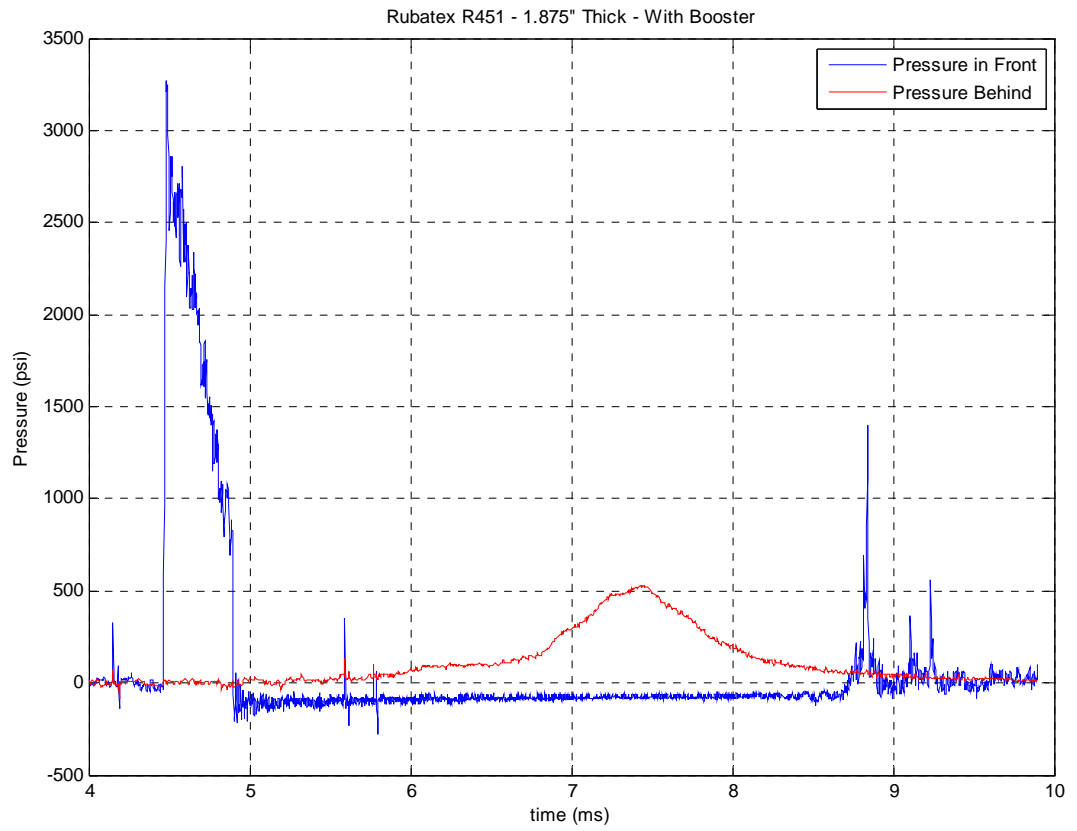


**Figure 4-21 CST Pressure Sensors Data - 1.875" RUBATEX R451 specimen – with booster**

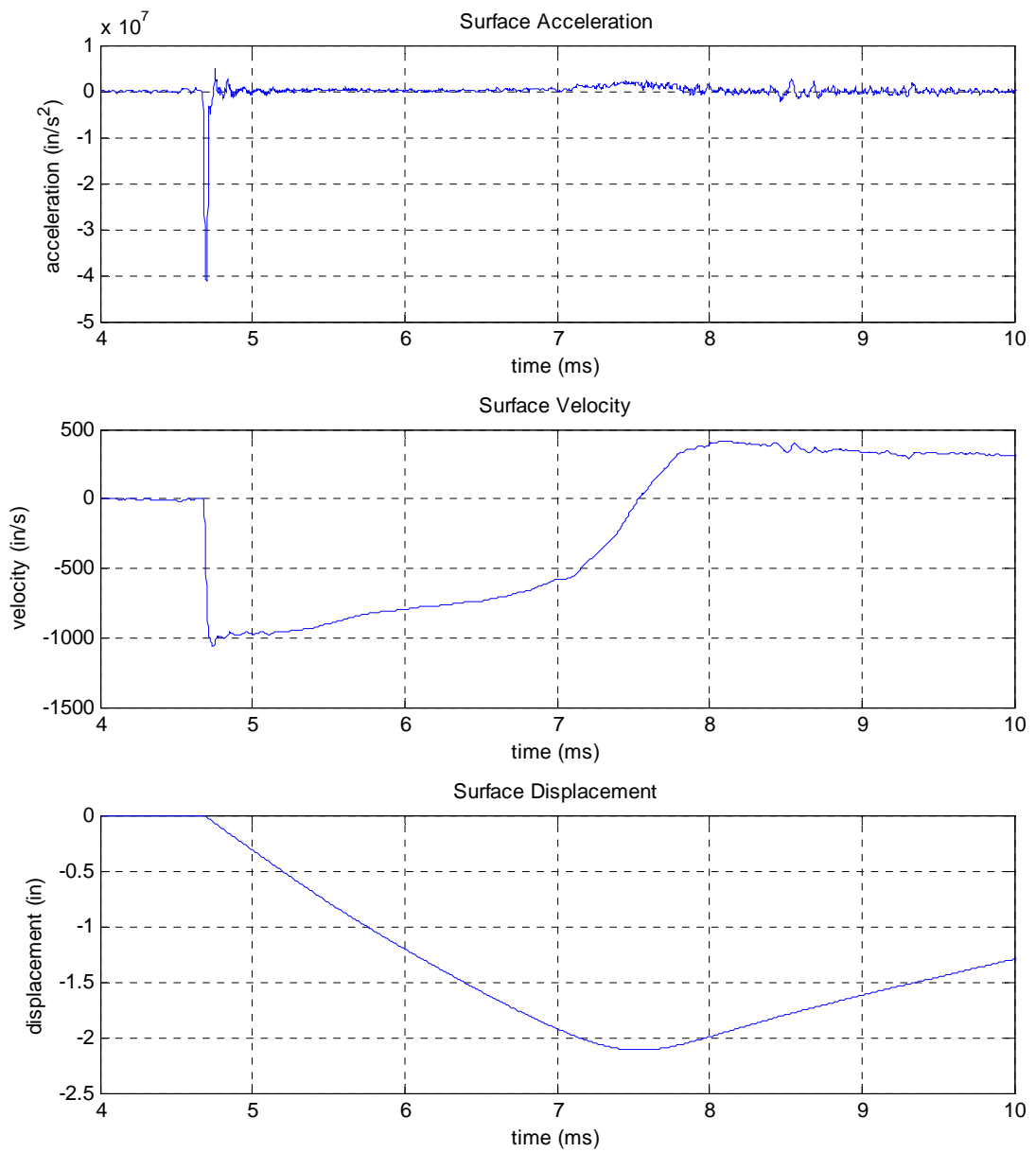


**Figure 4-22 CST Accelerometer Data - 1.875" RUBATEX R451 specimen – with booster**

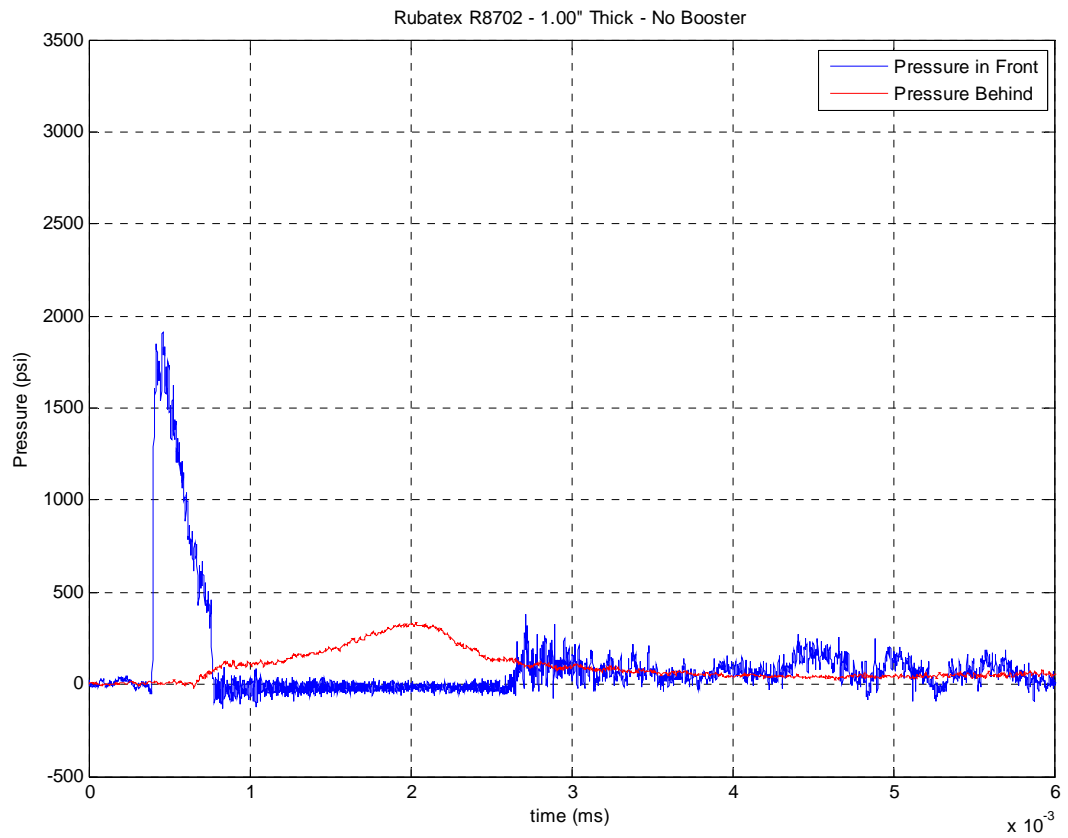
#### ***4.2.2. CST Results for RUBATEX R8702***

Figure 4-23 shows the CST results for a 1.875” thick R8702 specimen using the lower shock level (no booster). The blue curve shows the pressure at an offset of 14” from the specimen surface. The shock wave passes with a peak pressure of about 1800-psi and rapidly decays thereafter. The reflection from the specimen surface arrives at the pressure sensor at about 0.7 ms and cancels the incident pressure. Cavitation of the water prevents a negative pressure from forming, which would be analogous to the tensile reflection in the SHPB experiment. The soft specimen causes an extended period lasting about 2 ms. Unlike the R451 specimen, a small but significant portion of the pressure transmits through the specimen. Some of this energy arrives quickly and has the same character as was seen in the SHPB experiments (see Figure 4-14 for example). As has been seen throughout the experiments, there is an extended of elevated stress that decays in exponential fashion.

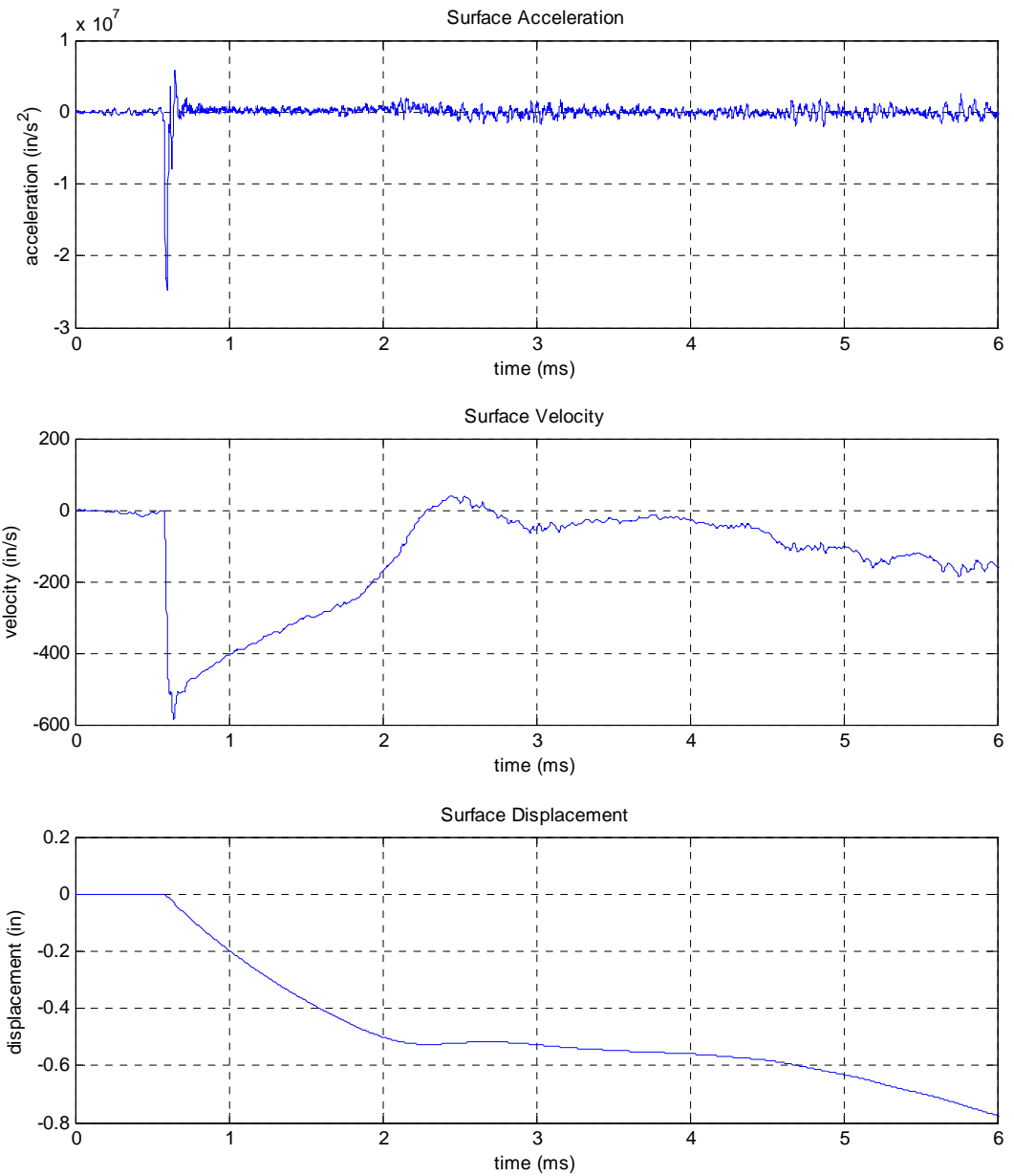
The accelerometer data for this test are shown in Figure 4-20. The acceleration is shown in the top plot. Velocity and displacements were developed by integration the accelerometer data as shown in the center and bottom plots, respectively. The shorter specimen improves the situation with the integration of the accelerometer data since the peak displacement occurs sooner. The displacement peak of about 0.55” seen at 2.2 ms is believable for this specimen, but the data beyond this point is obviously suspect for the reasons mentioned earlier.

Figure 4-25 shows the CST results for a 1.0” thick R8702 specimen using the higher shock level (with booster). The blue curve shows the pressure at an offset of 14” from the specimen surface. The shock wave passes with a peak pressure of about 3300-psi and rapidly decays thereafter. The reflection from the specimen surface arrives at the pressure sensor at about 4.9 ms and cancels the incident pressure. The pressure behind the specimen (red curve) shows a significant densification as a significant portion of energy gets through the material. Note that the quick arriving stress (red curve at about 4.9 ms) has lost its sharp ascent as was seen in the previous low level shock experiment and all of the SHPB tests. This is most likely due to the fact that this is the first experiment conducted on a non-virgin specimen. Judging by the ratio of the densification peak in this test with the quick-arriving energy seen in the previous test, it is clear that this experiment has caused the greatest densification of R8702 in the experimental data set.

Figure 4-26 shows the accelerometer data for this test. Again, the faster response of the R8702 specimen gives us a better chance of measuring the displacement peak. The peak of about 0.85” occurs at 6 ms. This exceeds the 0.69” peak expected at full densification.



**Figure 4-23 CST Pressure Sensors Data - 1.00\" RUBATEX R8702 specimen – no booster**



**Figure 4-24 CST Accelerometer Data - 1.00" RUBATEX R8702 specimen – no booster**

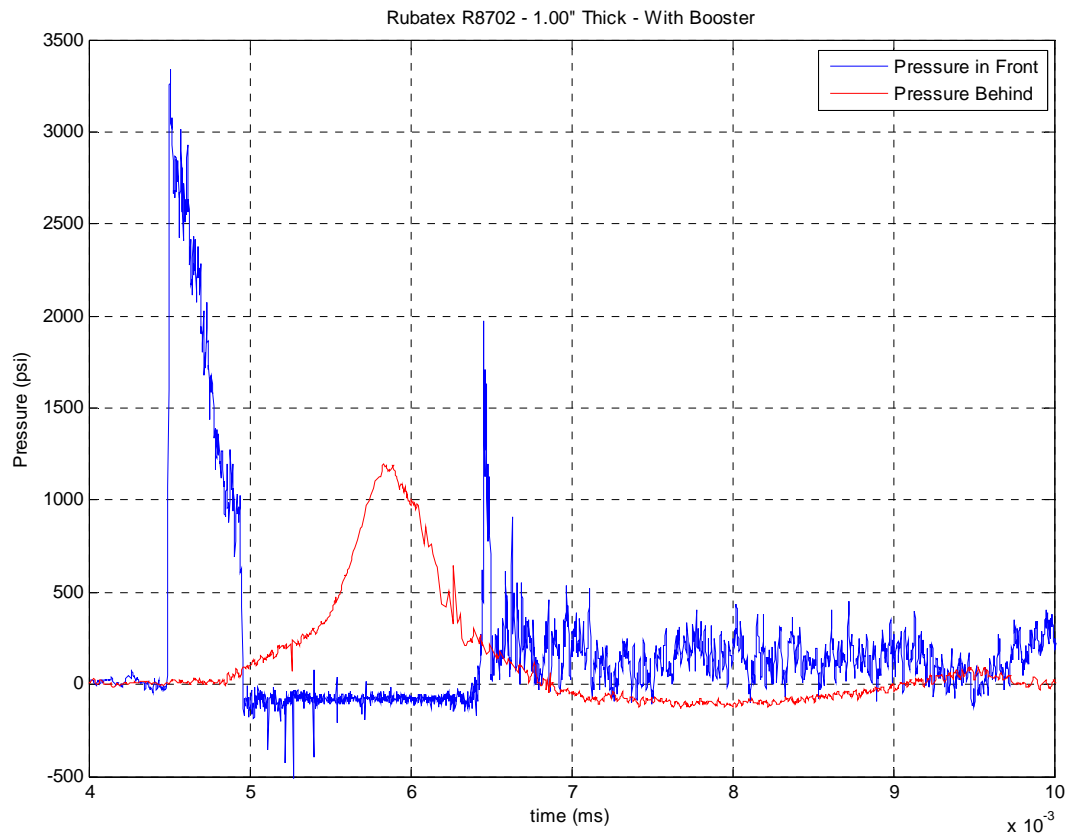


**Figure 4-25 CST Pressure Sensors Data - 1.00" RUBATEX R8702 specimen – with booster**

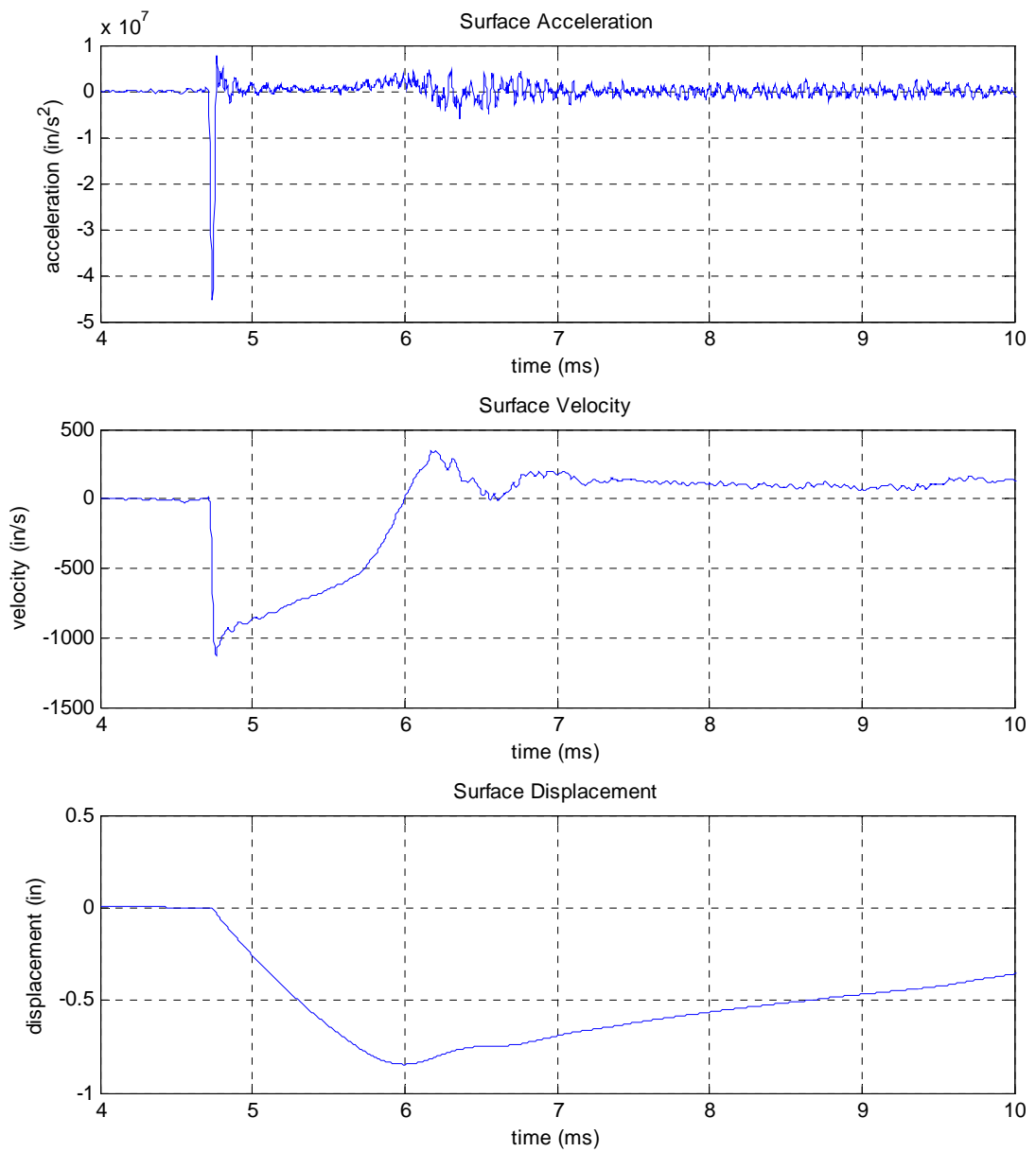


**Figure 4-26 CST Accelerometer Sensors Data - 1.00" RUBATEX R8702 specimen – with booster**

### 4.3. Summary

A Split Hopkinson Pressure Bar (SHPB) and a Conical Shock Tube (CST) were used to investigate the shock response of RUBATEX R451 and RUBATEX R8702 closed-cell foams.

The SHPB was used to test small  $\frac{3}{4}$ " diameter button specimens under high compression-rate loading. Specimens were tested in two thicknesses;  $\frac{1}{2}$ " and 1". Three striker charge levels of 7 psi, 10 psi and 13 psi were used to generate the shock pulse. These were found to correspond to striker velocities of 600, 900 and 1200 cm/s. The SHPB experiments captured the range of foam performance: from nearly perfect shock isolation to densification and energy transmission. The two foams exhibited distinct characters in their response. R8702 showed a small amount of energy transmission at all striker levels and specimen thicknesses. This was characterized by a level strain response, except at the highest two striker levels on the  $\frac{1}{2}$ " specimen where densification effects were significant. The R451 specimen exhibited nearly perfect isolation in the 1" thickness and in the  $\frac{1}{2}$ " thickness at the 7 psi striker level. When densification effects could be seen in the  $\frac{1}{2}$ " specimens at the 10 and 13-psi striker levels, the transmitted levels exceeded those seen in the R8702 foam.

The CST experiment was used to test larger 9.5" diameter specimens of the foams in their full slab thickness, which is 1.875" for R451 and 1" for R8702. The larger aspect ratio of the CST specimens provides more of a plane wave response from the material than is obtained in the SHPB. In a sense, the CST is quite similar to the SHPB

experiment. Both have a transmission velocity of about 1500 m/s and both can be used to measure a transfer function across the specimen. A major difference is the cavitation effect that occurs in the water, which prevents any significant “tensile” wave from being formed. Nonetheless, the experiments were in good agreement qualitatively in what they reveal about the foam specimens. The CST data for R8702 in its first test exhibited the same type of transmission as was seen in the higher level SHPB tests. This is characterized by a relatively fast arrival of transmitted pressure followed by a stress plateau and ultimately densification. It was interesting that the second shot on the R8702 specimen did not have the pronounced arrival of the fast energy as was seen in all other experiments. This could be explained by the fact that it was the only experiment on a non-virgin specimen. Likewise, the behavior of R451 in the CST resembles its behavior in the SHPB experiment. At the lower blast level, the R451 was nearly 100% effective in isolating the shock wave from reaching the witness plate. At the higher blast level, a densification peak that exceeded the R8702 specimen was measured.

## CHAPTER 5

### 5. Finite Element Implementation

In this section implementation of the constitutive theory is developed in two finite element approaches.

#### 5.1. Dedicated MATLAB Model

MATLAB was used to implement the constitutive theory for material parameter optimization with the hydrostatic chamber data. An axisymmetric finite element model was also developed for the specific purpose of supporting the development of the constitutive theory. The efficiency of MATLAB's built-in matrix functions makes it feasible to also use this model for the SHPB simulations. The MATLAB model is not the intended focus of this work, but it is worthwhile to provide a brief description of the finite element derivation to illustrate in detail how the constitutive model can be incorporated in an implicit finite element approach.

##### *5.1.1. Axisymmetric Element Derivation*

A displacement based quad element was used as shown in Figure 5-1.

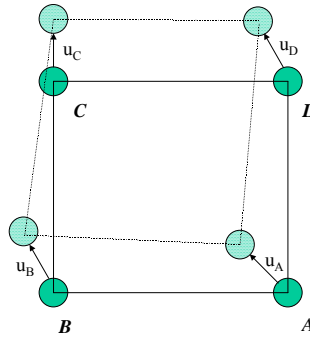


**Figure 5-1 Quad Element**

Shape functions are used to map the displacement field within the element.

$$u_r(z, r) = c_1 + c_2 r + c_3 z + c_4 z r, \quad (5-1)$$

$$u_z(z, r) = d_1 + d_2 r + d_3 z + d_4 z r. \quad (5-2)$$

Nodal displacement are related to the shape function coefficients by the shape matrix, N:

$$\begin{bmatrix} u_{rA} \\ u_{rB} \\ u_{rC} \\ u_{rD} \end{bmatrix} = \begin{bmatrix} 1 & z_A & r_A & z_A r_A \\ 1 & z_B & r_B & z_B r_B \\ 1 & z_C & r_C & z_C r_C \\ 1 & z_D & r_D & z_D r_D \end{bmatrix} \begin{bmatrix} c_1 \\ c_2 \\ c_3 \\ c_4 \end{bmatrix} \quad \begin{bmatrix} u_{zA} \\ u_{zB} \\ u_{zC} \\ u_{zD} \end{bmatrix} = \begin{bmatrix} 1 & z_A & r_A & z_A r_A \\ 1 & z_B & r_B & z_B r_B \\ 1 & z_C & r_C & z_C r_C \\ 1 & z_D & r_D & z_D r_D \end{bmatrix} \begin{bmatrix} d_1 \\ d_2 \\ d_3 \\ d_4 \end{bmatrix}$$

$$\mathbf{u}_r = \mathbf{Nc}$$

$$\mathbf{u}_z = \mathbf{Nd}$$

$$\mathbf{c} = \mathbf{N}^{-1} \mathbf{u}_r$$

$$\mathbf{d} = \mathbf{N}^{-1} \mathbf{u}_z$$

The incremental change in Hencky strain is derived in terms of the shape function coefficients as follows:

$$\varepsilon_{rr}(z, r) = \frac{\partial u_r}{\partial r} = c_3 + c_4 z \quad (5-3)$$

$$\varepsilon_{zz}(z, r) = \frac{\partial u_z}{\partial z} = d_3 + d_4 r \quad (5-4)$$

$$\varepsilon_{rz}(z, r) = \frac{1}{2} \left( \frac{\partial u_r}{\partial z} + \frac{\partial u_z}{\partial r} \right) = \frac{1}{2} (c_3 + c_4 r + d_2 + d_4 z) \quad (5-5)$$

$$\varepsilon_{\theta\theta}(z, r) = \frac{u_r}{r} = (c_1/r + c_2 + c_3 z/r + c_4 z). \quad (5-6)$$

The corresponding incremental change in the finite strain tensor is then developed with current value of the deformation gradient:

$$\Delta \mathbf{E} = \mathbf{F}^T (\boldsymbol{\varepsilon}) \mathbf{F}. \quad (5-7)$$

We proceed to develop the nodal forces by consideration of the internal work. The finite strain is energy conjugate with the second Piola-Kirchhoff stress such that,

$$W = \int \mathbf{S} : \mathbf{dE}. \quad (5-8)$$

Hence, the change in internal energy over a small time increment is given by:

$$\Delta W = \left( \mathbf{S} + \frac{\Delta \mathbf{S}}{2} \right) : \Delta \mathbf{E}, \quad (5-9)$$

$$\Delta W = \left( \mathbf{S} + \frac{1}{2} \left( \frac{\partial \Delta \mathbf{S}}{\partial \Delta \mathbf{E}} \right) \Delta \mathbf{E} + \frac{1}{2} \left( \frac{\partial \Delta \mathbf{S}}{\partial t} \right) \Delta t \right) : \Delta \mathbf{E}, \quad (5-10)$$

$$\Delta W = \left( \mathbf{S} + \frac{1}{2} \mathbf{\Lambda} \Delta \mathbf{E} + \frac{1}{2} \mathbf{\Theta} \Delta t \right) : \Delta \mathbf{E}. \quad (5-11)$$

The incremental stress Jacobian and the time derivative were developed in section 2.8.

The existing stress is updated throughout the analysis, and the finite strain tensor will be related to the nodal displacements. Before proceeding further, it is convenient to vectorize the following quantities as follows,

$$\mathbf{u} = [u_{rA} \quad u_{rB} \quad u_{rC} \quad u_{rD} \quad u_{zA} \quad u_{zB} \quad u_{zC} \quad u_{zD}]^T, \quad (5-12)$$

$$\mathbf{c} = [c_1 \quad c_2 \quad c_3 \quad c_4 \quad d_1 \quad d_2 \quad d_3 \quad d_4]^T. \quad (5-13)$$

Also we introduce the nodal forces,

$$\mathbf{f} = [f_{rA} \quad f_{rB} \quad f_{rC} \quad f_{rD} \quad f_{zA} \quad f_{zB} \quad f_{zC} \quad f_{zD}]^T, \quad (5-14)$$

Now the vectorized shape coefficients are related to the vectorized displacements by,

$$\mathbf{c} = \bar{\mathbf{N}}^{-1} \mathbf{u} \quad (5-15)$$

$$c_k = \bar{N}_{km}^{-1} u_m \quad (5-16)$$

where,

$$\bar{\mathbf{N}}^{-1} = \begin{bmatrix} \mathbf{N}^{-1} & \mathbf{0} \\ \mathbf{0} & \mathbf{N}^{-1} \end{bmatrix} \quad (5-17)$$

The nodal forces are derived by equating the change in internal energy caused by each displacement with the work done at the node. Using the chain rule we can write this incremental forces as,

$$f_i = 2\pi\hat{r}_0 A_0 \left( \frac{\partial \Delta W}{\partial c_j} \right) \left( \frac{\partial c_j}{\partial u_i} \right) \quad (5-18)$$

where  $r_0$  and  $A_0$  are the mean radius and the area of the element in original reference configuration, respectively. The force represents is given as the average over the time increment. The first bracketed term on the right side, the partial derivative of the incremental energy with respect to the shape coefficients, has the form,

$$\frac{\partial \Delta W}{\partial c_j} = \beta_{jk} c_k + \chi_j, \quad (5-19)$$

where  $\beta$  is a 6x6 matrix containing the first order derivative coefficients and  $\chi$  is a 6x1 column vector containing the zero order terms from the differentiation. The second term, the partial derivative of the shape coefficients with respect to the nodal displacements, is simply related to the shape matrices as follows:

$$\frac{\partial c_j}{\partial u_i} = \bar{N}_{ji}^{-1}. \quad (5-20)$$

Substituting equations (5-19) and (5-20) into (5-18) we have:

$$f_i = 2\pi\hat{r}_0 A_0 \left( \beta_{jk} c_k \bar{N}_{ji}^{-1} + \chi_j \bar{N}_{ji}^{-1} \right). \quad (5-21)$$

The left-hand side of the equation represents the average nodal force over the time increment using the midpoint rule. Finally, substituting equation (5-16) and rearranging we obtain:

$$f_i = 2\pi r_0 A_0 \left( \bar{N}_{ji}^{-1} \beta_{jk} \bar{N}_{km}^{-1} u_m + \chi_j \bar{N}_{ji}^{-1} \right), \quad (5-22)$$

or in matrix form,

$$\mathbf{f} = 2\pi r_0 A_0 \left( \bar{\mathbf{N}}^{-T} \boldsymbol{\beta} \bar{\mathbf{N}}^{-1} \mathbf{u} + \bar{\mathbf{N}}^{-T} \boldsymbol{\chi} \right). \quad (5-23)$$

Equation (5-22) represents the incremental force contributions from the element to the attached nodes. In general, each nodal location will receive incremental force contributions from 1,2 or 4 elements, depending on its location in the mesh.

The matrix  $\beta$  and the vector  $\chi$  contain lengthy algebraic expressions involving the tangent moduli, the stress, and the stress relaxation. The algebraic expressions are developed with symbolic equation manipulator.

#### 5.1.1.1. Element Stabilization and the Prevention of Hour Glassing

Hour glassing is a well-known phenomenon that can occur in finite element analysis. It is caused by the propagation of zero energy modes that can exist in certain element formulations. The effect of hour glassing can be negligible in small strain analysis, but the accumulative effect in finite strain problems can lead to erroneous results and eventually element instabilities. Consider the element illustrated on the left in Figure 5-2. In this case, the nodal forces are derived from an evaluation of the change in internal

energy as evaluated at the center point of the element. Now consider the deformation mode illustrated on the right in Figure 5-2. By inspection it is obvious that this mode causes neither volumetric nor deviatoric strain when evaluated at the center point. It follows that there is no incremental energy change associated with this mode and hence there are no nodal forces. This mode can propagate throughout a finite element mesh in an alternating pattern which gives rise to the hour glass appearance.

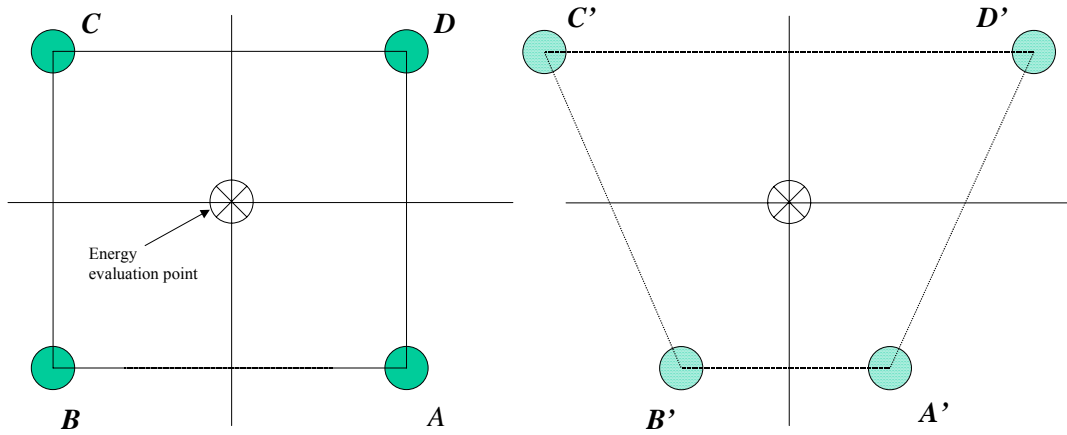


**Figure 5-2 Hour Glassing Mode in an Element with a Single Energy Evaluation Point**

Hour glassing can be effectively suppressed by increasing the number of energy evaluation points. In the present formulation four evaluation points are used as shown in Figure 5-3. Clearly, the hour glassing mode shown on the right in Figure 5-3 will now generate a significant volumetric and deviatoric response at the centroid of each quadrant

and hence the mode will no longer be tolerated energetically. Since the constitutive model is highly nonlinear, further stabilization and accuracy of the element under large deformation is obtained by tracking inhomogeneity within the element by monitoring the properties within each quadrant. This requires tracking each quadrant's internal displacement, stress state and constitutive internal variables throughout the analysis.

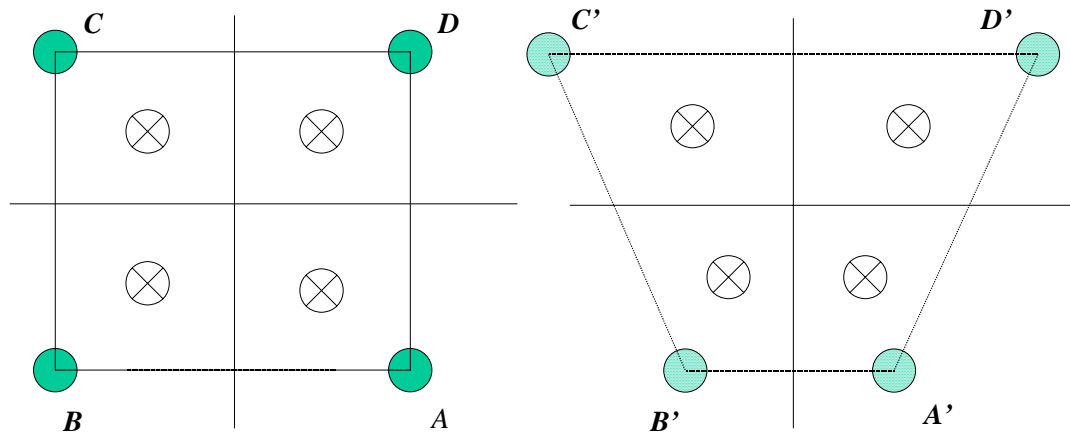


**Figure 5-3 Multiple Energy Evaluation Points to Suppress Hour Glassing**

#### *5.1.1.2. Mass Matrix*

A simple lumped-mass approach is used. Each element quadrant is assigned a mass at the beginning of the analysis is assumed to remain unchanged under deformation.

Vectorizing the elemental mass matrix we have,

$$\mathbf{m} = [m_A \quad m_B \quad m_C \quad m_D]^T \quad (5-24)$$

### 5.1.2. The Equation of Motion

The average acceleration method is used to develop the equation of motion. We begin by considering the change in velocity at a node,

$$\dot{x}_i(t + \Delta t) = \dot{x}_i(t) + a_i \Delta t \quad (5-25)$$

where  $x$  can represent either the current  $r$  or  $z$  position, and  $a_i$  represents the corresponding average acceleration over the time increment. The acceleration is also related to the nodal force and mass,

$$a_i = \frac{-\sum f_i}{\sum m_i}. \quad (5-26)$$

The summation refers to the multiple element contributions to the node and does not refer to the nodal position subscript,  $i$ . A negative sign is used with the force terms because they represent the internal forces of the element. Substituting (5-26) into (5-25) we have:

$$u_i = \dot{x}_i(t) \Delta t - \frac{\sum f_i}{2 \sum m_i} \Delta t^2 \quad (5-27)$$

Substitution of equations (5-22) and (5-24) into equation (5-27) lead directly to the final equation of motion for the node:

$$A u_i = B \quad (5-28)$$

where,

$$A = \left( \sum m \right)_i + \left( \pi \hat{r}_0 A_0 \frac{\Delta t^2}{2} \right) \bar{N}_{ji}^{-1} \left( \sum \beta \right)_{jk} \bar{N}_{km}^{-1} \quad (5-29)$$

$$B = \left( \sum m \right)_i \dot{u}_i \Delta t - \left( \pi \hat{r}_0 A_0 \frac{\Delta t^2}{2} \right) \left( \sum \chi \right)_j \bar{N}_{ji}^{-1} \quad (5-30)$$

Construction of sparse system matrices accomplished with the built-in MATLAB function SPARSE.

SHPB simulations are compared with the experiments in section 6.

### 5.1.3. Mesh Transition

A special boundary condition was developed to link non-matching element meshes. This allows the mesh density in the specimen region to be increased without changing the mesh of the region occupied by the pressure bar. The technique exploits the large modulus mismatch between the test specimen and the pressure bar. Consider the figure below. Elements 1 through 4 represent foam in the test section and element 5 represents the pressure bar. Node locations 1C, 2D, 2C, 3D, 3C, and 4D are not connected to the coarse region. To correct the situation, the displacement equation coefficients  $A$  and  $B$  of equation (5-28) are transferred from each of the non-matching nodes to nodes 5B and 5A in proportion to their distance. This effectively transfers the reaction stresses at the non-connected nodes to the coarse region. Afterwards these displacement equations are eliminated and the nodes are forced to move with the edge of the coarse element (5). This is accomplished by introducing displacement equations for the non-connected nodes via linear interpolation of displacements 5B and 5A.

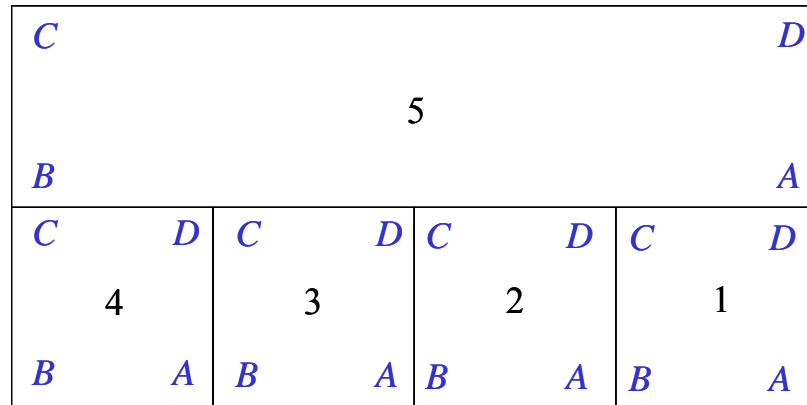


**Figure 5-4 Interface between dissimilar mesh densities**

## **5.2. ABAQUS/EXPLICIT User Defined Material Subroutine (VUMAT)**

A VUMAT subroutine was written so that the constitutive theory would be available with the commercial FEA software, ABAQUS/EXPLICIT. The implementation has been made only for the explicit solver, but a UMAT for the implicit solver, ABAQUS/STANDARD, could readily be developed since the stress Jacobian has been fully derived for the implicit-based MATLAB model. The basic difference between an explicit and an implicit analysis is that the former requires no information regarding the state variables at the end of the increment. Rather it relies on sufficiently small time increments such that system's future state can be extrapolated from the current state. The state variables are updated after the increment. An implicit approach accounts for the change in state variables that occur over the step. Hence, they require that the stress

Jacobian be available. Implicit solutions tend to be more time consuming, but much larger time increments are possible. The MATLAB analysis derived in the previous section is an example of an implicit solution method. We will not attempt to here to provide a detailed review of the ABAQUS theories or their implementation. The reader is referred to the ABAQUS theory manual for more detail.

The VUMAT was adapted from the constitutive algorithm developed for the MATLAB analysis following the instruction provided with the ABAQUS documentation. The FORTRAN code for the VUMAT is provided in Appendix A.

ABAQUS models were used to duplicate one of the SHPB simulations made with the MATLAB software as a redundancy check. It also provided the only means of simulating the Conical Shock Tube experiments since it provides the needed fluid elements and cavitation effects. Results from these models are discussed in the following section.

### **5.3. Summary**

An axisymmetric finite element program was written to develop the constitutive theory and to simulate the SHPB experiments. An axisymmetric quad element was developed. This element has four energy evaluation points (also known as “fully integrated”). An implicit-based analysis is used. The incremental change in internal energy is formed in terms of the second Piola-Kirchhoff stress and finite strain increment. The incremental stress Jacobian and time-derivative are needed to form the equation of

motion and were developed. A special interface boundary condition was developed to join dissimilar mesh densities. The displacement equations for nodes at the interface in the finer mesh are forced to move with element edge in the coarser mesh. The forces associated with these nodes are transferred to the nodes of the coarse element.

## **CHAPTER 6**

### **6. Comparisons of FE Simulations and Experimental Data**

In this section finite element simulations of the SHPB and CST experiments are compared with the experimental results. Other investigators have pursued finite element simulations and have proposed an inverse analysis to develop constitutive material parameters [46]. Here, finite element analysis serves as a validation of the underlying premise of this dissertation, which is that behavior in the shock region can be predicted from characterizations made in other regions of strain/strain-rate space.

#### **6.1. MATLAB SHPB Model Compared with Experimental Data**

A model of the SHPB was meshed in MATLAB. The overall geometry is illustrated in Figure 6-1. Several locations were selected for results and are indicated in the figure. The analysis described in section 5 is implemented with the incremental constitutive model developed in section 2. The properties of the polycarbonate striker bar are given a small loss factor of 0.05 by using the viscoelastic portion of the constitutive model. Otherwise the elastic moduli match those given in the figure. The strain in the z-direction is written to a results file at the specified locations. The strain quantity is actually the finite strain, but in the polycarbonate, this quantity is equivalent to the Hencky strain, which is measured in the experiments.

The striker bar and incident bar are modeled as a single piece. To excite the model into motion, an initial velocity is assigned to the striker bar. This simulates the condition

at impact. At later time a tensile wave returns to the impact interface. In reality the striker bar separates from the incident bar. The model does not account for the separation, but this discrepancy affects the simulations at a time that lies outside the period of interest.

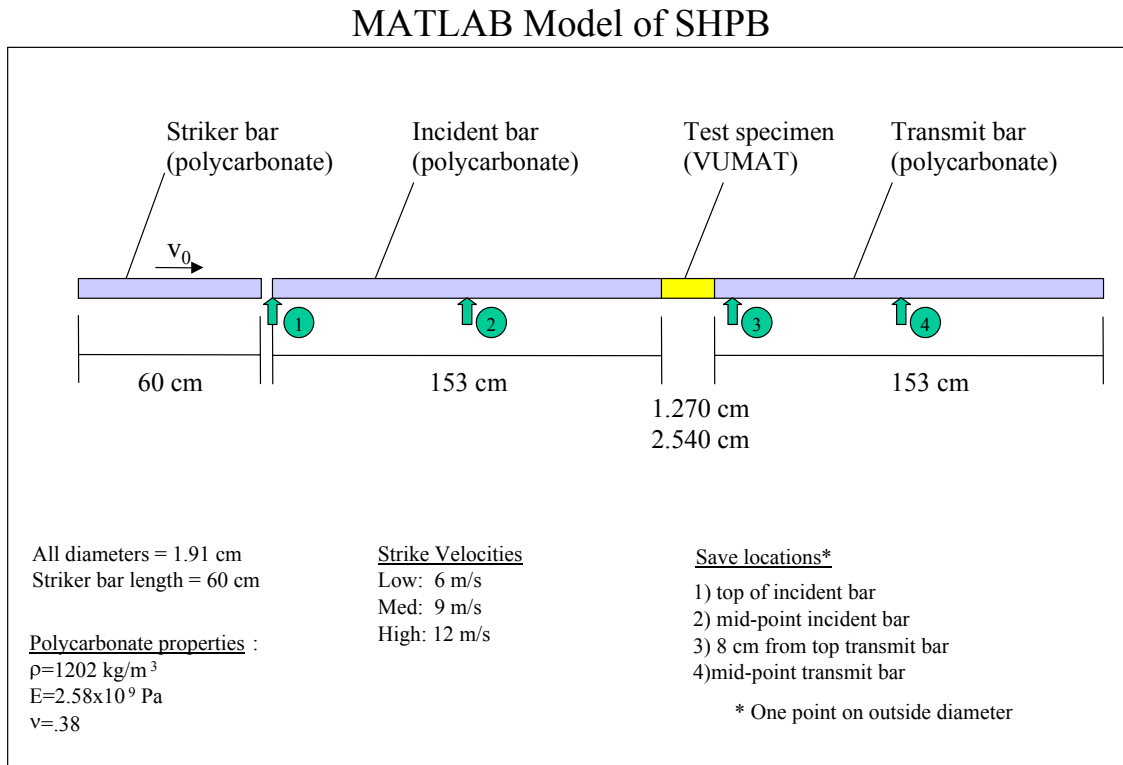


**Figure 6-1 SHPB geometry and MATLAB model configuration**

**6.1.1. Still Images from SHPB Simulations of R8702**

Sample images from the simulations of 1/2" R8702 at the highest striker velocity are shown in the series of figures from Figure 6-2 to Figure 6-12. Each figure gives an overall view of the SHPB on the left and a close-up of the specimen section on the right.

The blue end of the color spectrum indicates compressive strain. Strains shown for the overall view are magnified by a factor of 1000. Figure 6-2 shows the simulation early on at 0.10 ms when the striker bar has just begun to impinge on the incident bar at a location of about 311 cm. Figure 6-3 shows the simulation just 0.2 ms later when the pulse is still fanning out in both directions in symmetric fashion, but has not yet reached the free boundary. Figure 6-4 shows the simulation at 1.0 ms when the pulse has been fully formed and its arrival at the interface is imminent. Figure 6-5 through Figure 6-10 show the simulation in 0.2 ms increments from this point as the sample reacts to the compressive pulse. Some interesting behavior of the specimen is seen at 1.4 ms (Figure 6-6) where there is a distinct plane of a large strain gradient develops from the upper-center down towards the middle-right. This behavior is not seen in simulations of R451, which indicates that it is most likely associated with the bending transition in the material. At 1.8 ms (Figure 6-8) the specimen has just passed its densification peak and a compressive pulse is launched into the receive bar, which is visible in the overall view. The remaining figures show the progression of the material's rebound at 2.0 ms, 2.2 ms, 2.5 ms, and finally, much later at 3.5 ms.

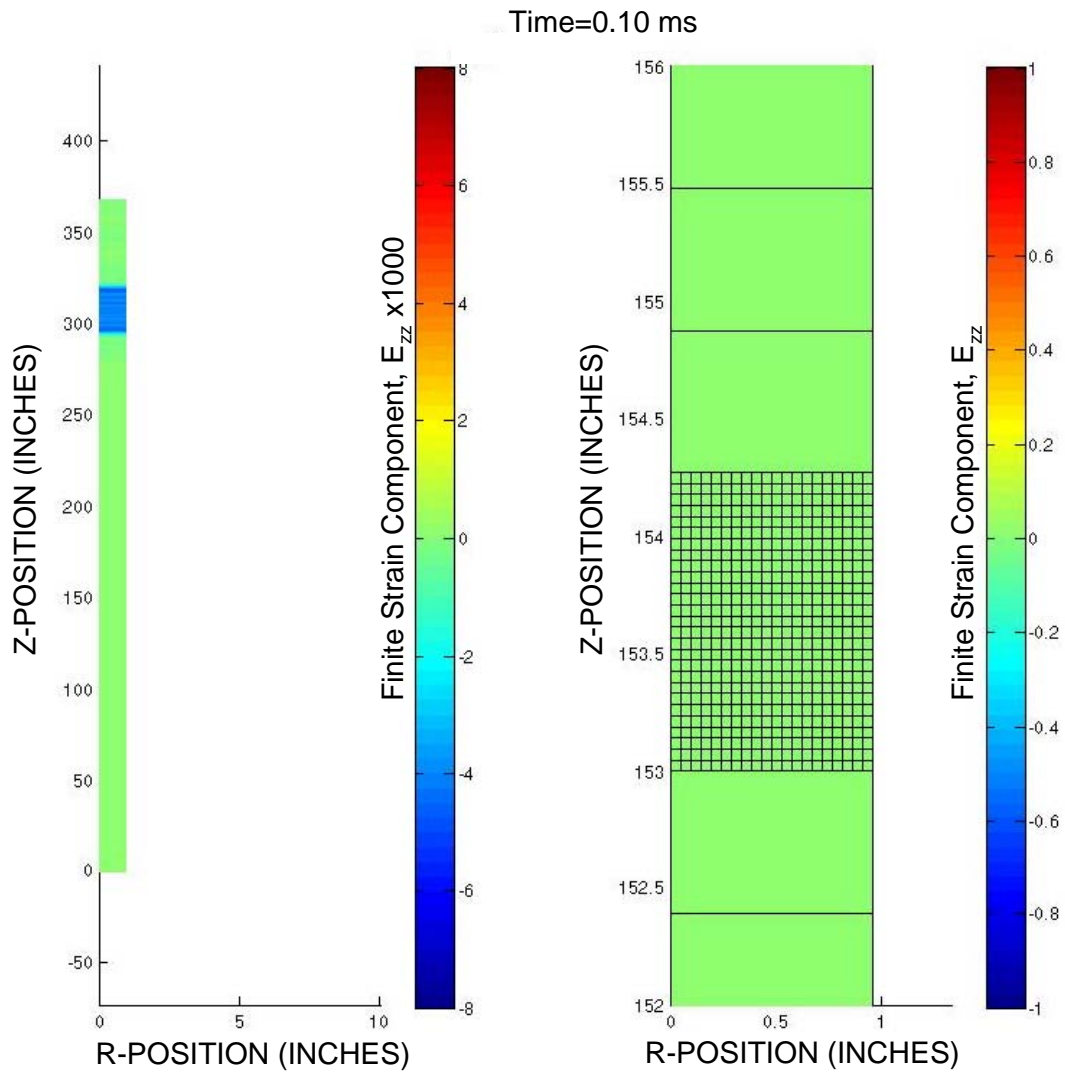


**Figure 6-2 SHPB Simulation at 0.10 ms– 1/2” R8702 Specimen with 13 psi charge. Overall view (left). Specimen area (right).**

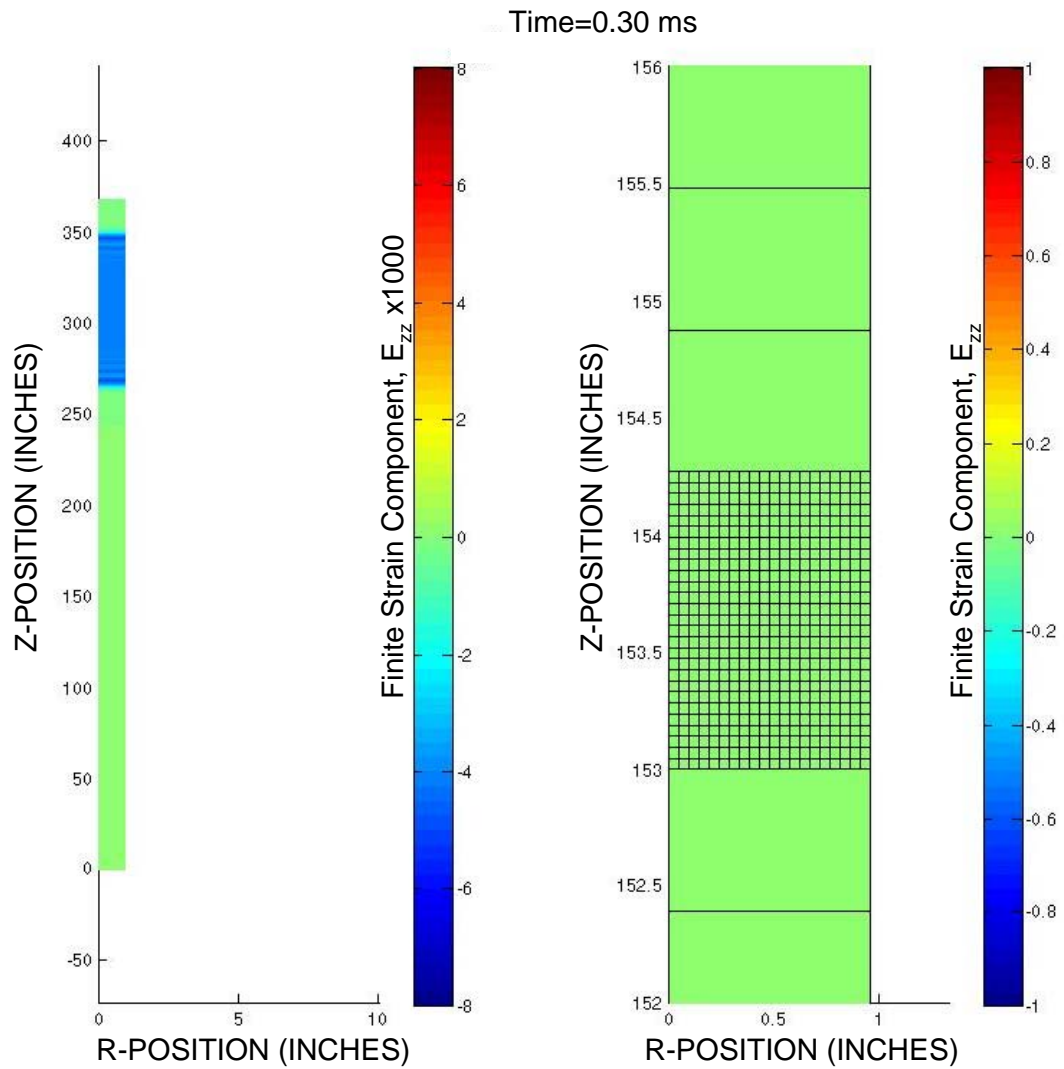


**Figure 6-3 SHPB Simulation at 0.30 ms— ½” R8702 Specimen with 13 psi charge. Overall view (left). Specimen area (right).**

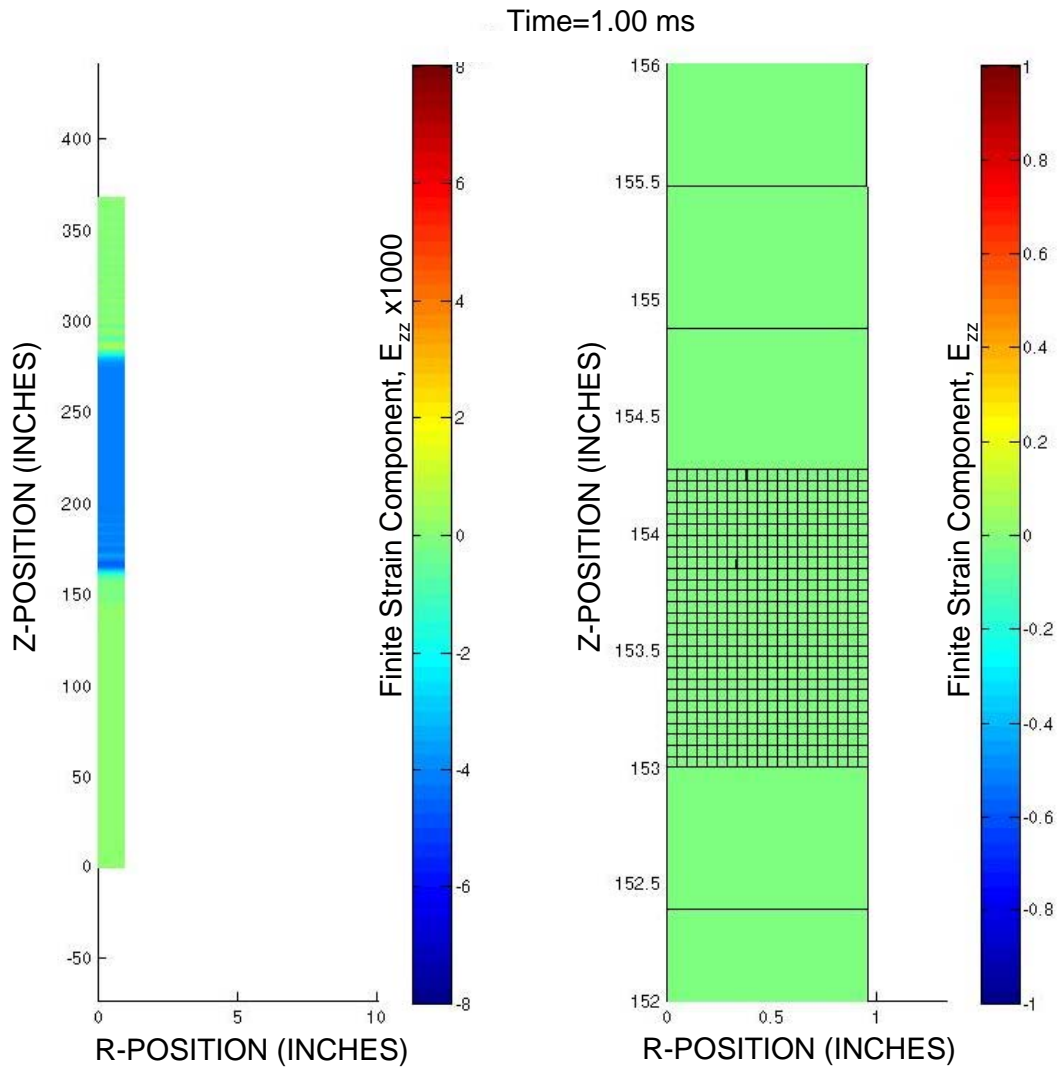


**Figure 6-4 SHPB Simulation at 1.00 ms— ½” R8702 Specimen with 13 psi charge. Overall view (left). Specimen area (right).**

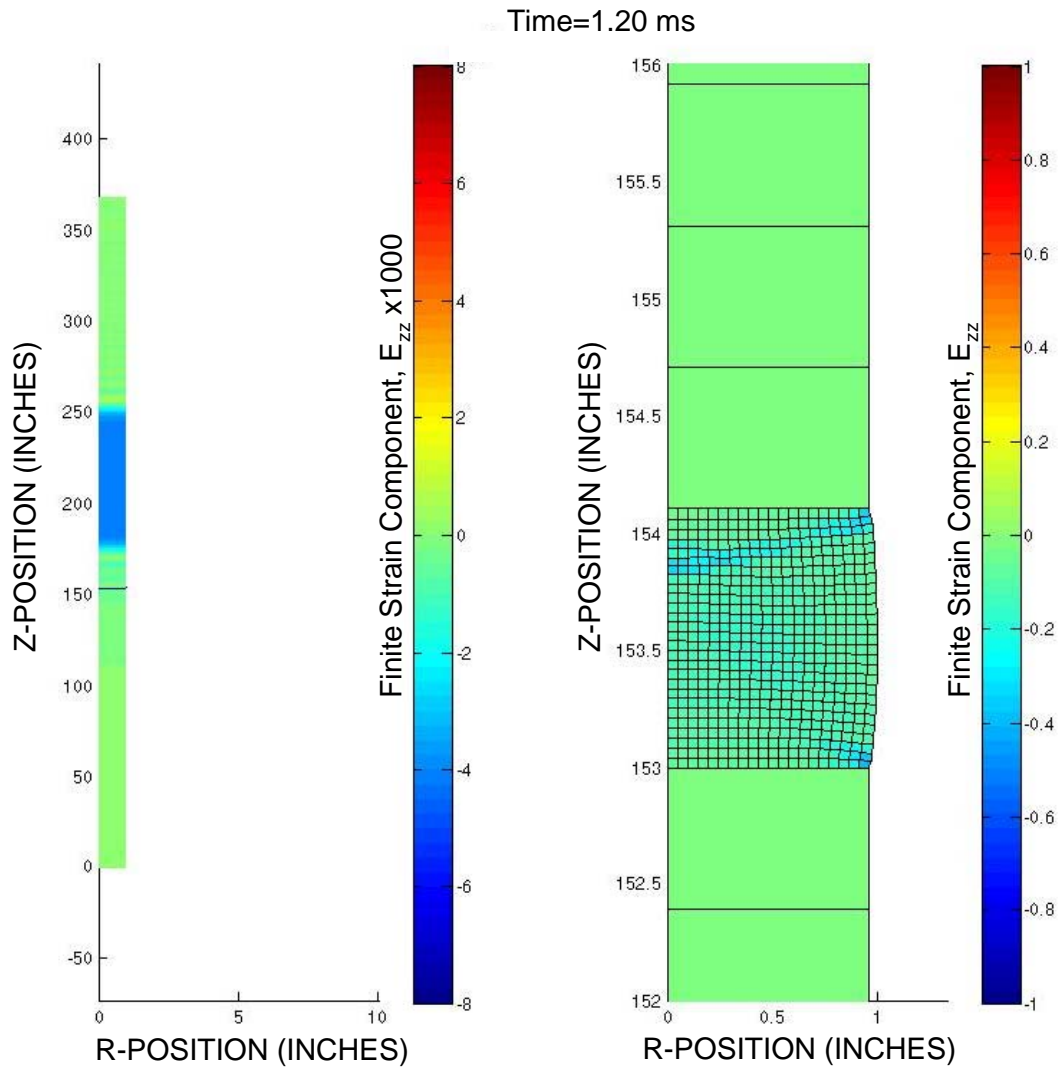


**Figure 6-5 SHPB Simulation at 1.20 ms— ½” R8702 Specimen with 13 psi charge. Overall view (left). Specimen area (right).**

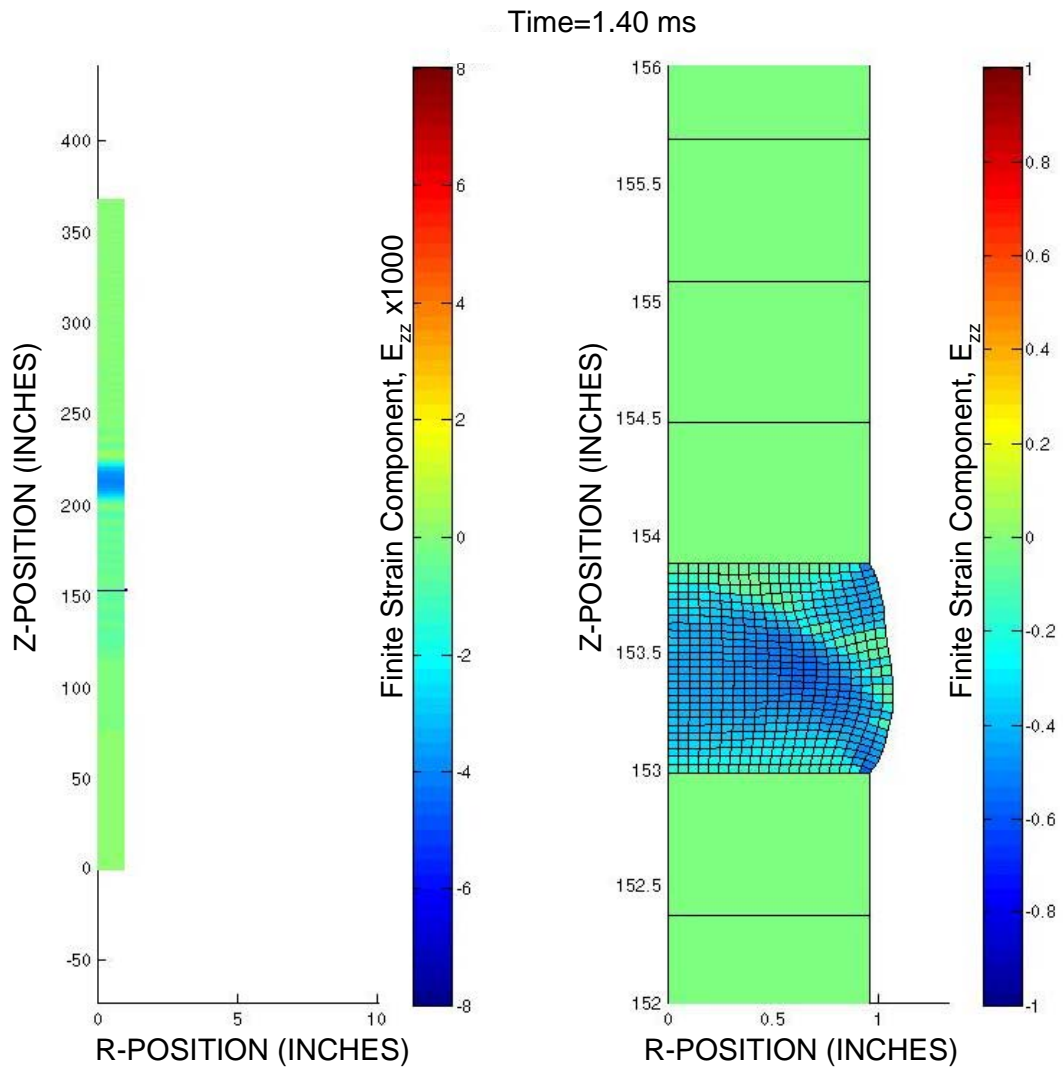


**Figure 6-6 SHPB Simulation at 1.40 ms— ½” R8702 Specimen with 13 psi charge. Overall view (left). Specimen area (right).**

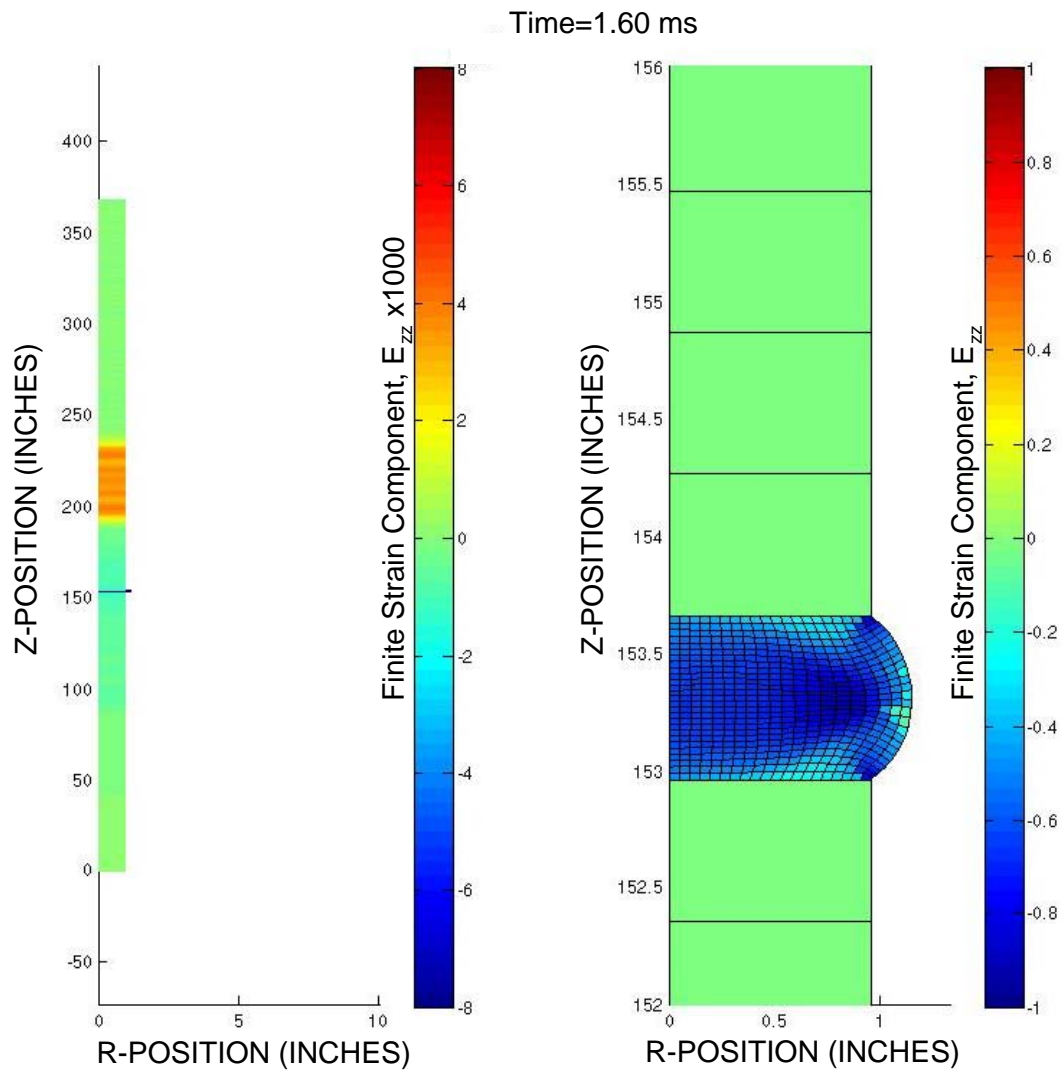


**Figure 6-7 SHPB Simulation at 1.60 ms— ½” R8702 Specimen with 13 psi charge. Overall view (left). Specimen area (right).**

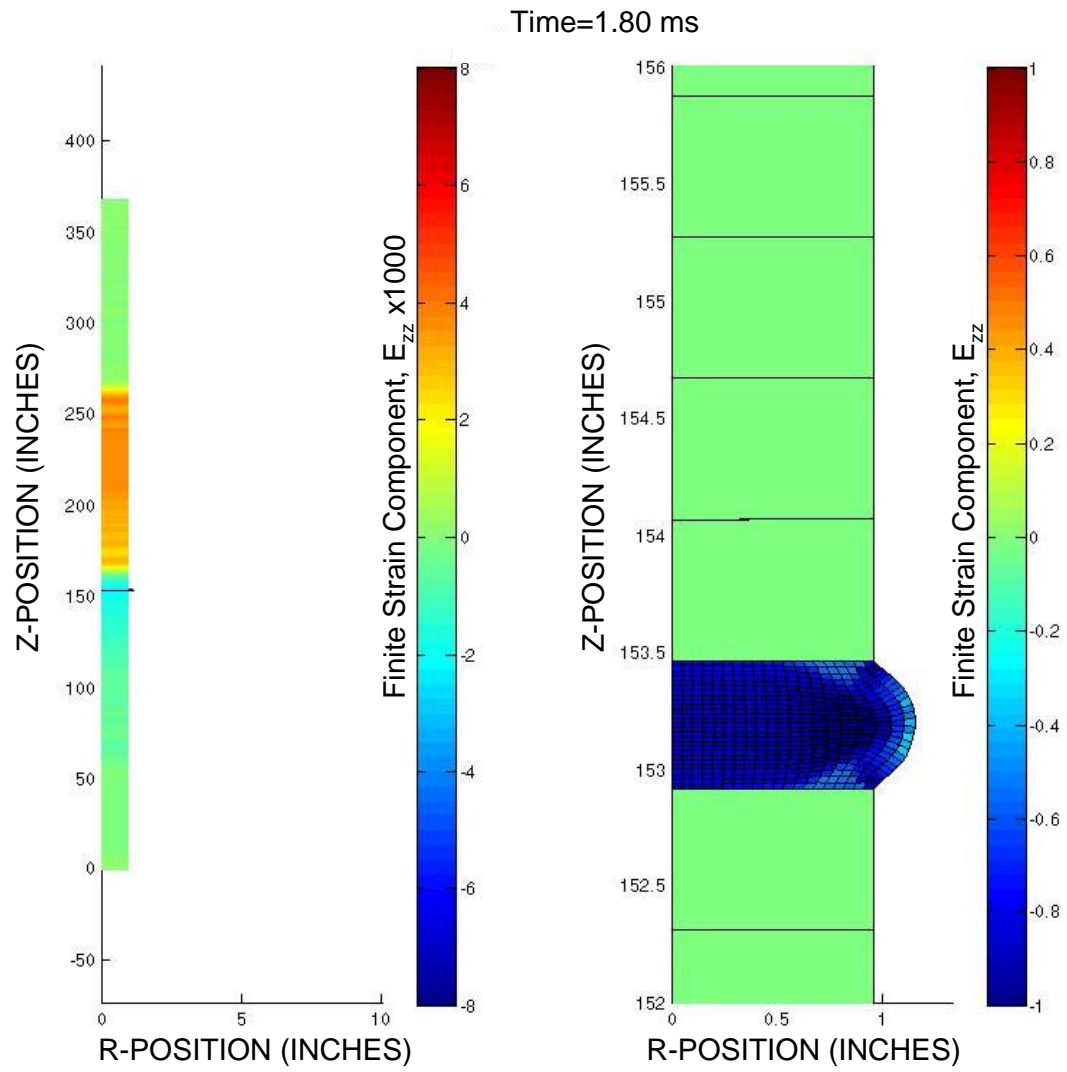


**Figure 6-8 SHPB Simulation at 1.80 ms— ½” R8702 Specimen with 13 psi charge. Overall view (left). Specimen area (right).**

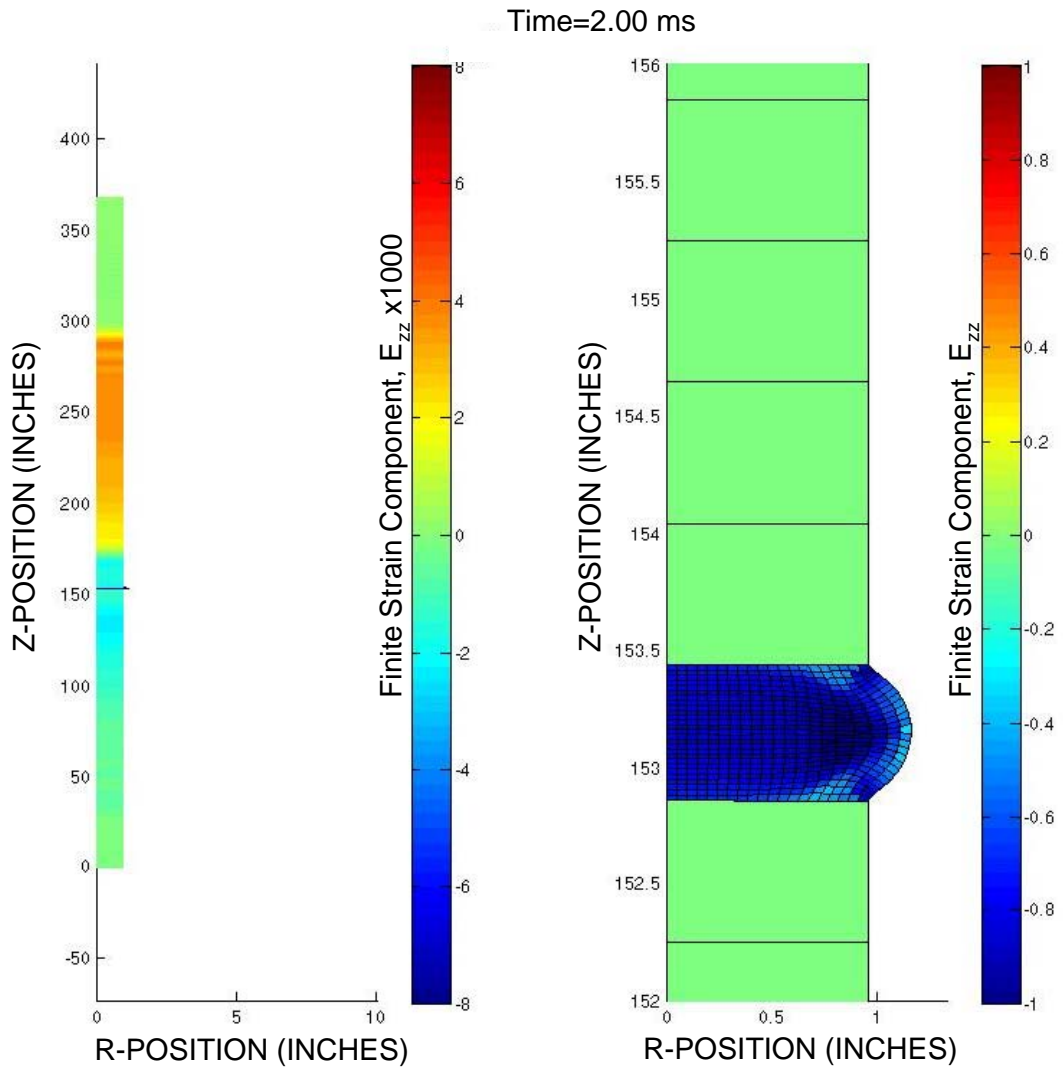


**Figure 6-9 SHPB Simulation at 2.00 ms— ½” R8702 Specimen with 13 psi charge. Overall view (left). Specimen area (right).**

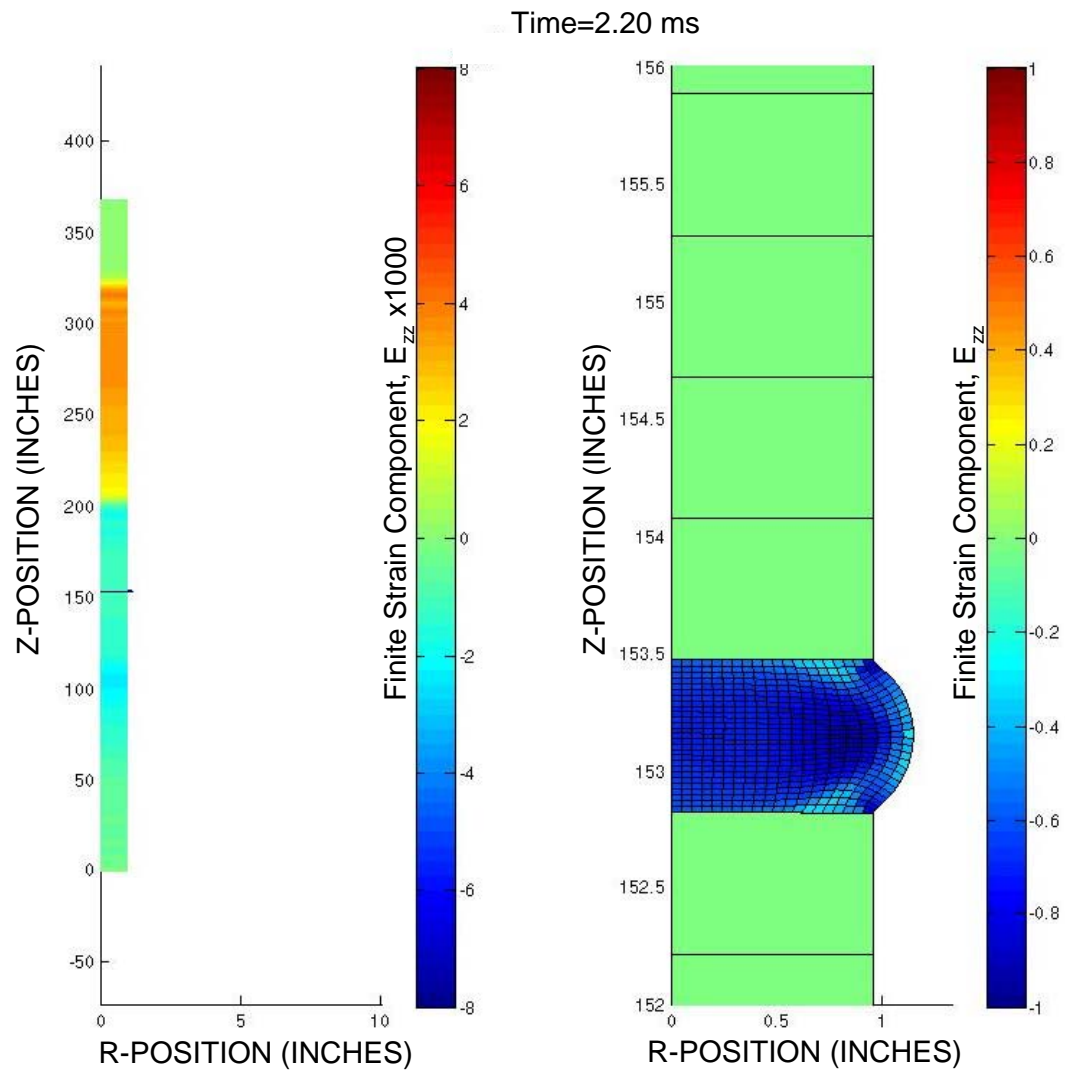


**Figure 6-10 SHPB Simulation at 2.20 ms– ½” R8702 Specimen with 13 psi charge. Overall view (left). Specimen area (right).**

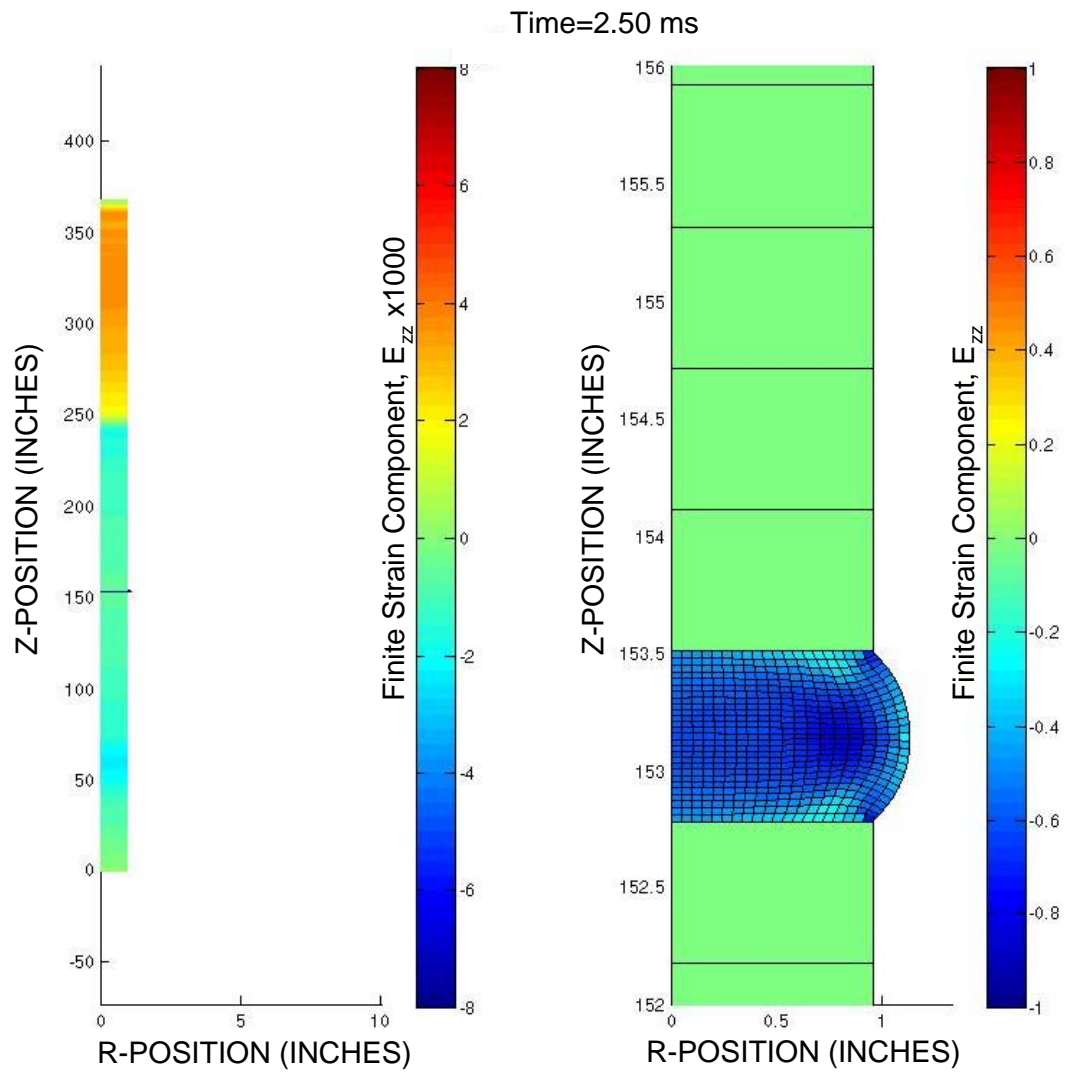


**Figure 6-11 SHPB Simulation at 2.50 ms– ½” R8702 Specimen with 13 psi charge. Overall view (left). Specimen area (right).**

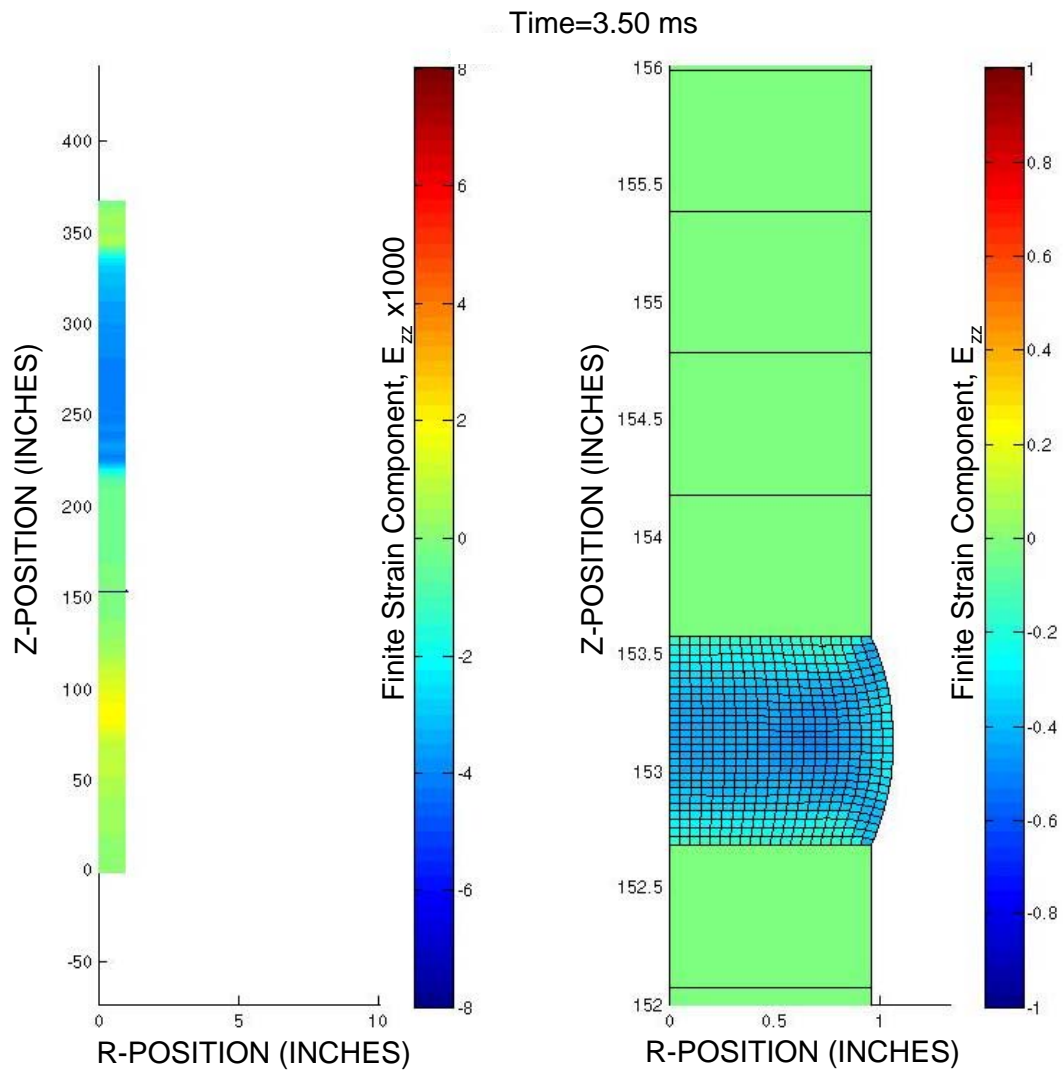


**Figure 6-12 SHPB Simulation at 3.50 ms– ½” R8702 Specimen with 13 psi charge. Overall view (left). Specimen area (right).**

### ***6.1.2. SHPB Simulations for R8702 Compared with Measurements***

SHPB strain levels for a 1.0” thick R8702 samples are shown in Figure 6-13, Figure 6-14, and Figure 6-15 for a 7-psi, 10 psi and 13 psi striker charge, respectively. The model agrees well with the 1” R8702 experiments. It captures both the level and character of the measurement. However, at times beyond 2 ms there is a distinct and interesting discrepancy in the rate at which the strain levels return to zero.

SHPB strain levels for 0.5” thick R8702 samples are shown in Figure 6-16, Figure 6-17, and Figure 6-18 for a 7-psi, 10 psi and 13 psi striker charge, respectively. The model agrees fairly well with the 0.5” experiments. It captures both character of the measurement, but the densification peak levels is overstated in the simulations for the 10 and 13 psi striker charges. Also, the discrepancy in the stress decay at times beyond 2 is more prominent. A second discrepancy also becomes more apparent with the shorter specimen. There is a brief period between about 2.2 and 2.5 ms where we have valid data/theory comparison of the strain in the incident bar immediately after the passing of the tensile wave. At the highest striker charge level, Figure 6-18, there is a noticeable disagreement. The model shows a compression wave trailing the tensile wave, which must be due to the reaction of the specimen. The two discrepancies combined hint at an unaccounted loss mechanism either in the material or in the experiment.

### 6.1.2.1. Use of Christensen's shear equation

A special simulation was made where Kerner's approximate shear equation was replaced with the exact equation developed by Christensen. R8702 was selected to make this comparison since it was found that the material phase plays a greater role in its overall behavior. The 0.5" specimen thickness with the highest striker charge was selected since it involves the greatest deformation of the specimen.

Figure 6-19 shows the comparison of the simulations with Kerner and Christensen's shear equations, compared with the data set. The incident bar results have been omitted, and an expanded scale is used to examine the differences. We find that Christensen's equation makes only a very small difference in the results. It makes a slight improvement on the initial rise of strain, but has no significant effect on the behavior near densification. This finding is welcomed since the use of Christensen's shear equation was found to slow the execution of the computation by more than a factor of 2. It also supports the underlying assumption that deviatoric response is of secondary importance in compressive load scenarios. An unexpected consequence of using Christensen's equation was the triggering of a Drucker instability that occurred in the computation at 1.6 ms. This does not imply that there is a general stability issue associated with his equation. Rather it demonstrates how near the R8702 model is to unstable behavior for this load condition. Reduction of the sharpness parameter,  $C_2$ , for the deviatoric response by a factor of 2 allowed the computation to proceed beyond the densification peak

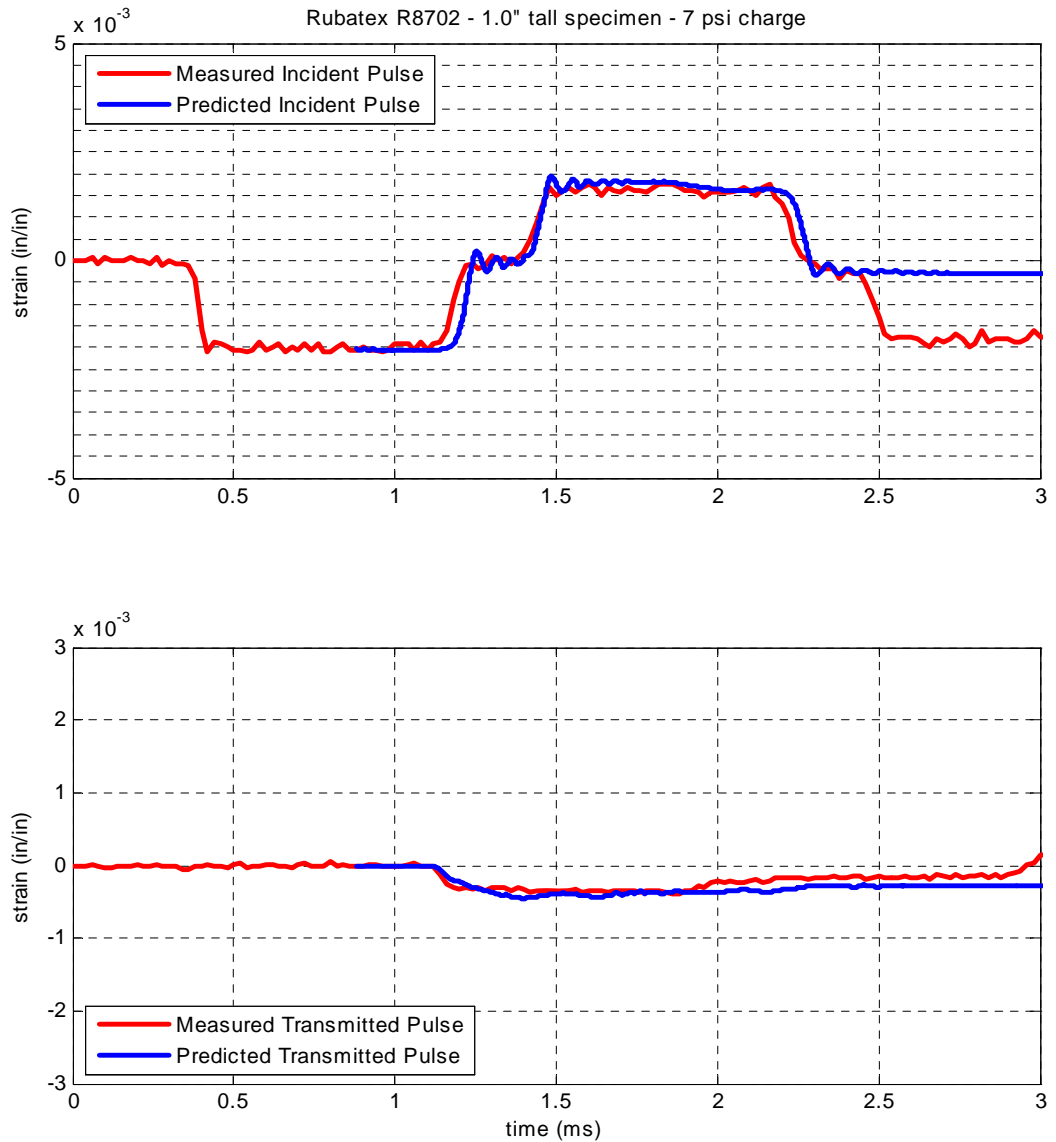


**Figure 6-13 SHPB Data Theory Comparison - MATLAB model – 1.00” R8702 Specimen with 7 psi charge**

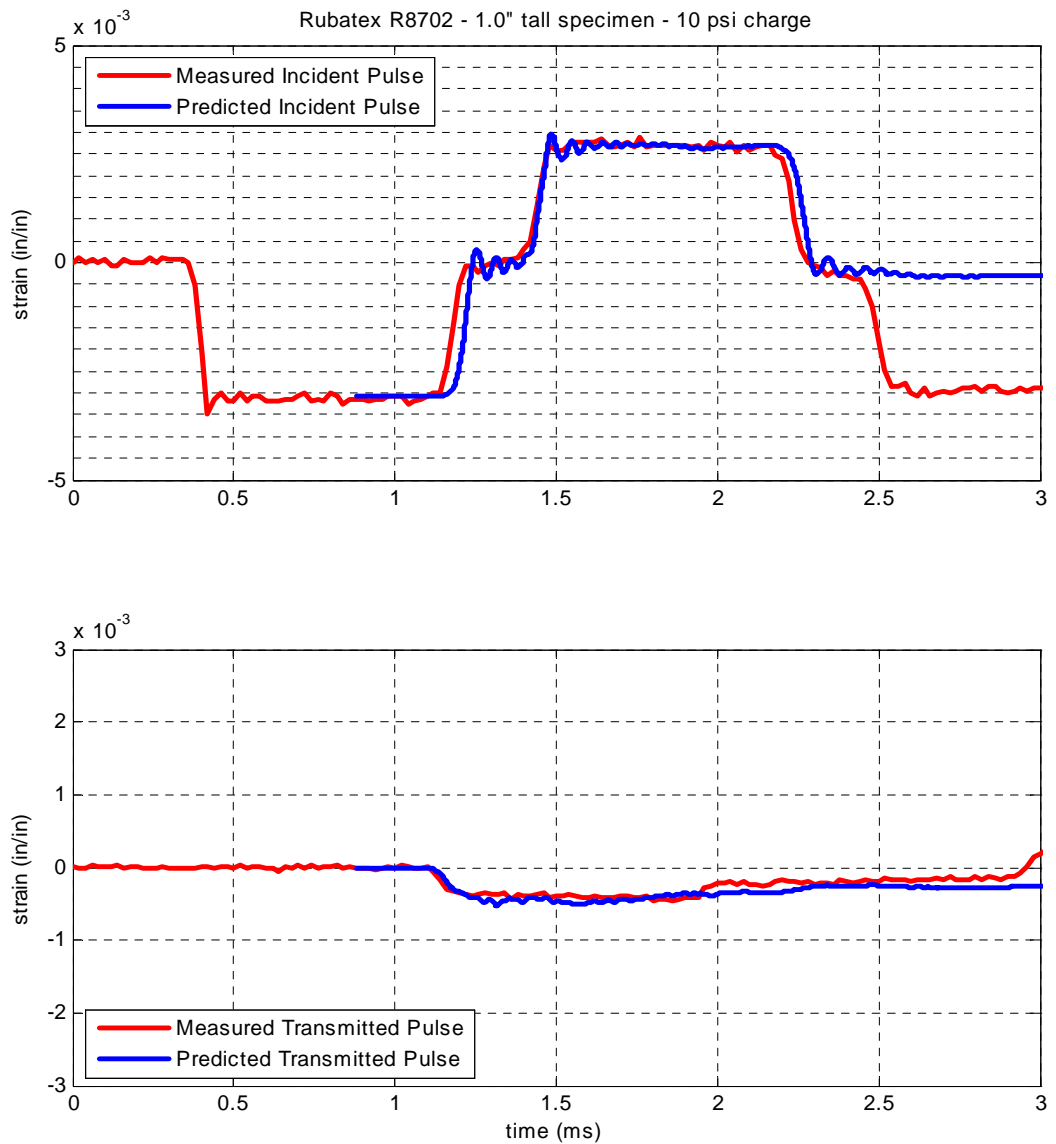


**Figure 6-14 SHPB Data Theory Comparison - MATLAB model – 1.00” R8702 Specimen with 10 psi charge**

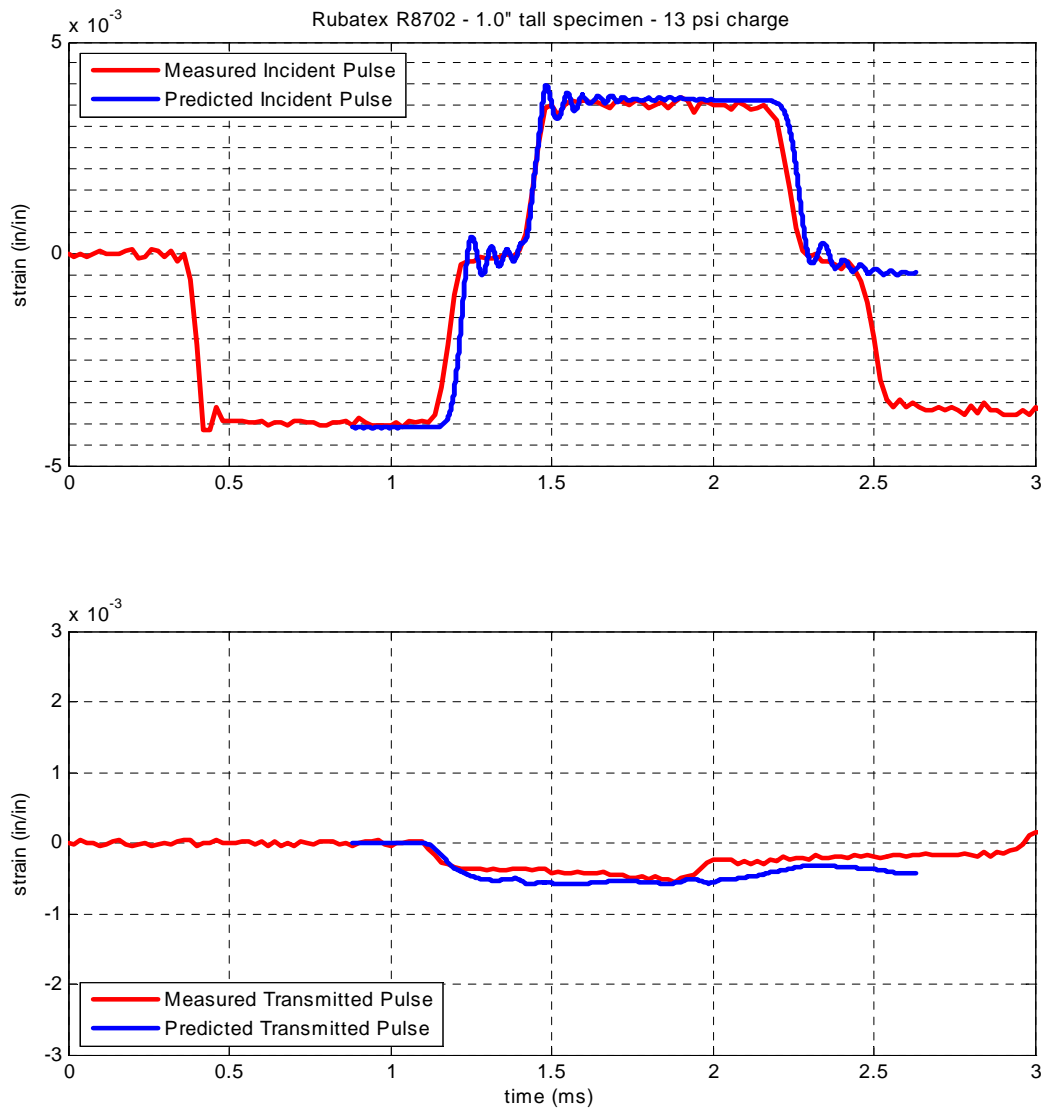


**Figure 6-15 SHPB Data Theory Comparison - MATLAB model – 1.00” R8702 Specimen with 13 psi charge**

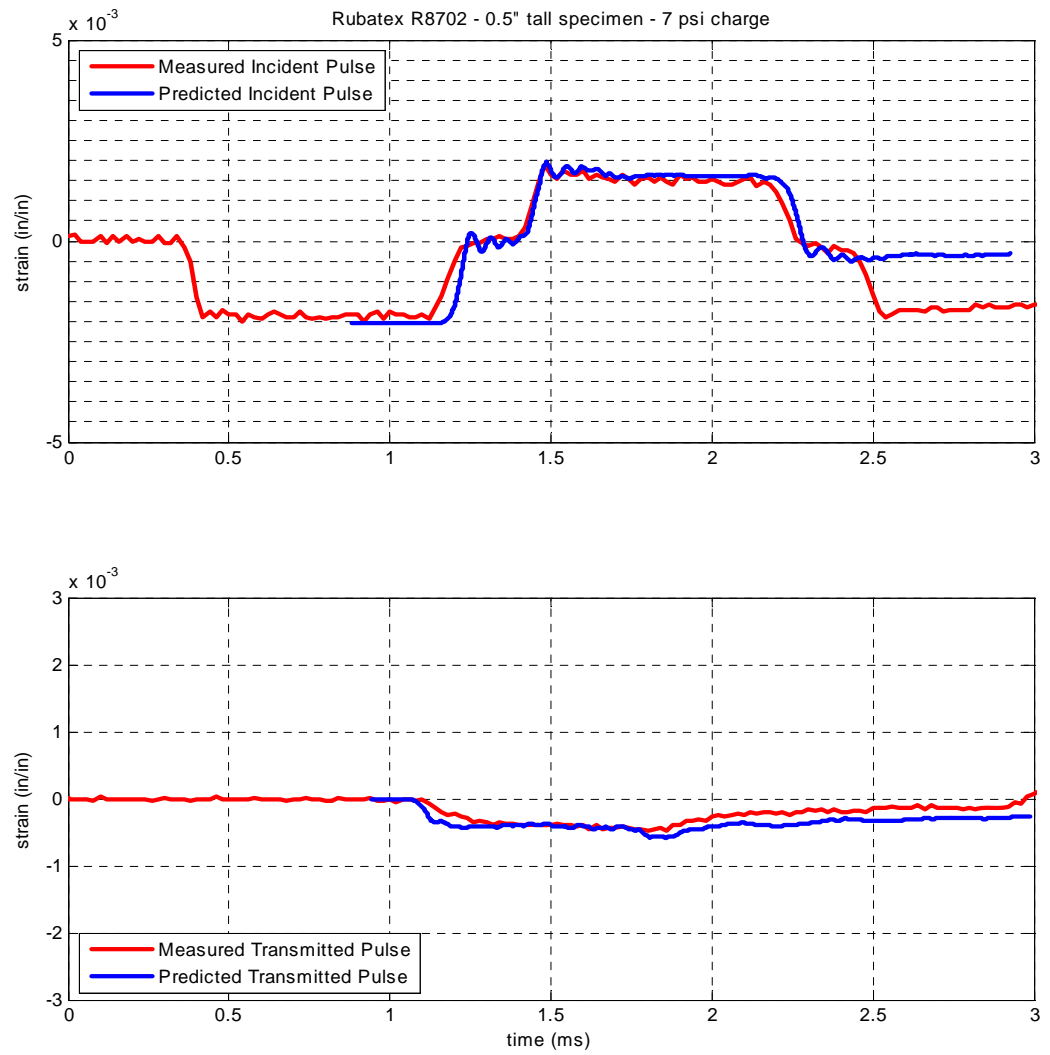


**Figure 6-16 SHPB Data Theory Comparison - MATLAB model – 0.50” R8702 Specimen with 7 psi charge**

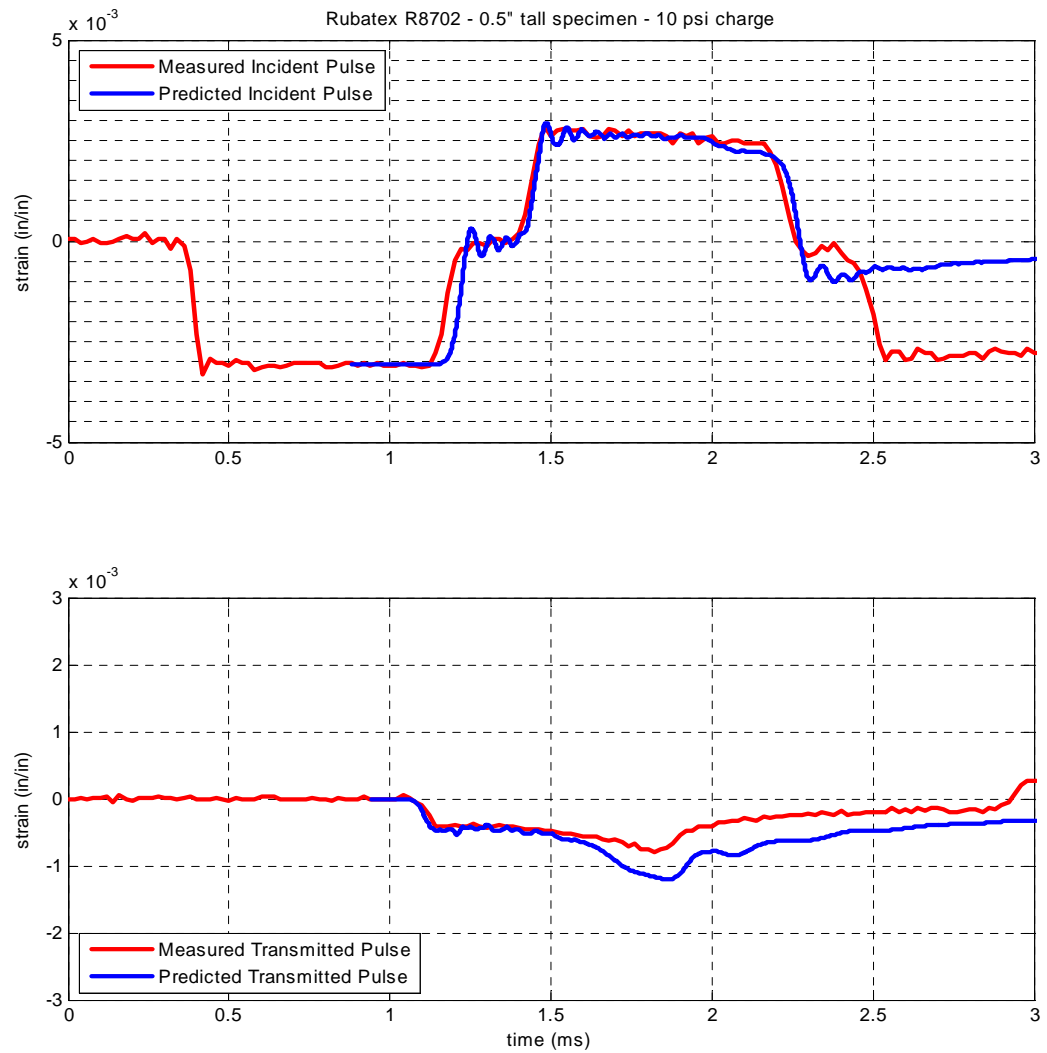


**Figure 6-17 SHPB Data Theory Comparison - MATLAB model – 0.50” R8702 Specimen with 10 psi charge**

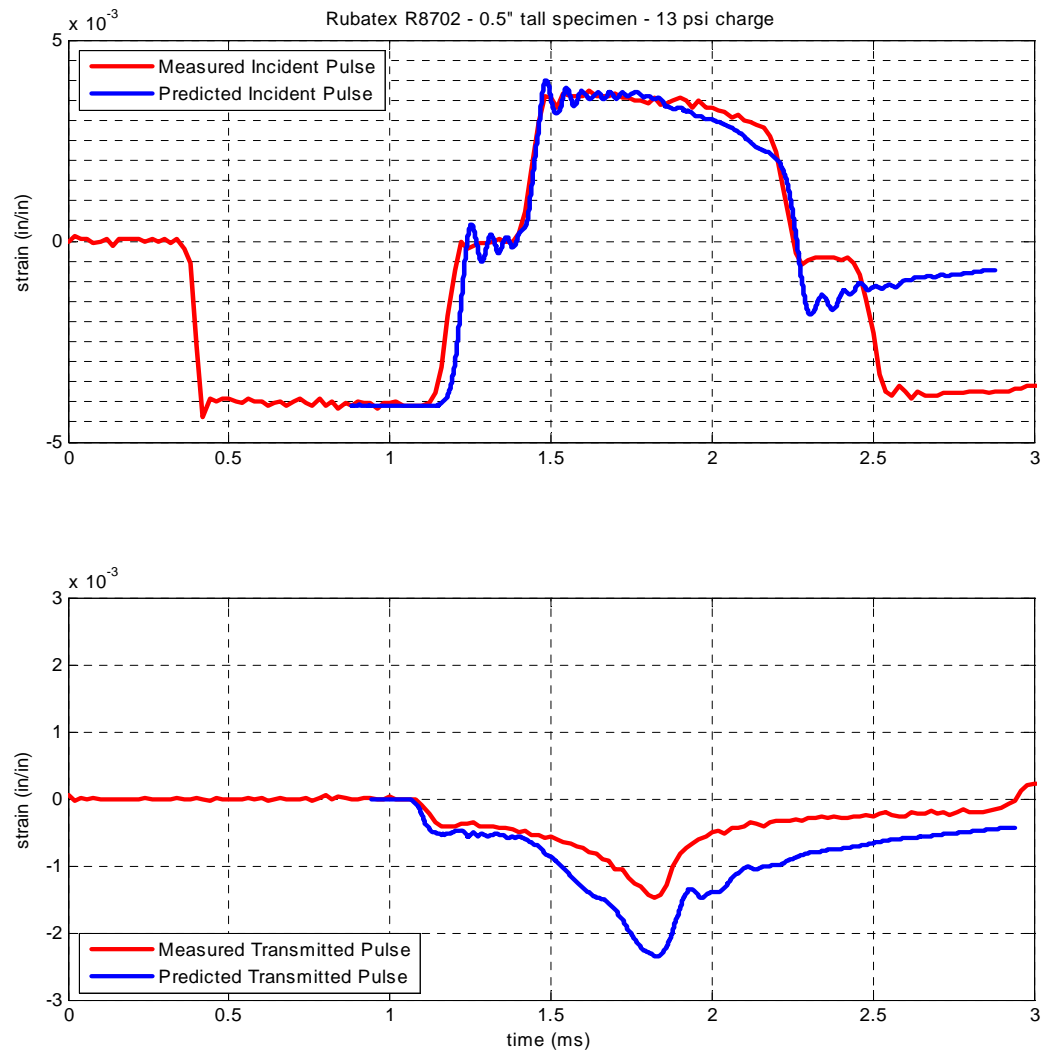


**Figure 6-18 SHPB Data Theory Comparison - MATLAB model – 0.50” R8702 Specimen with 13 psi charge**

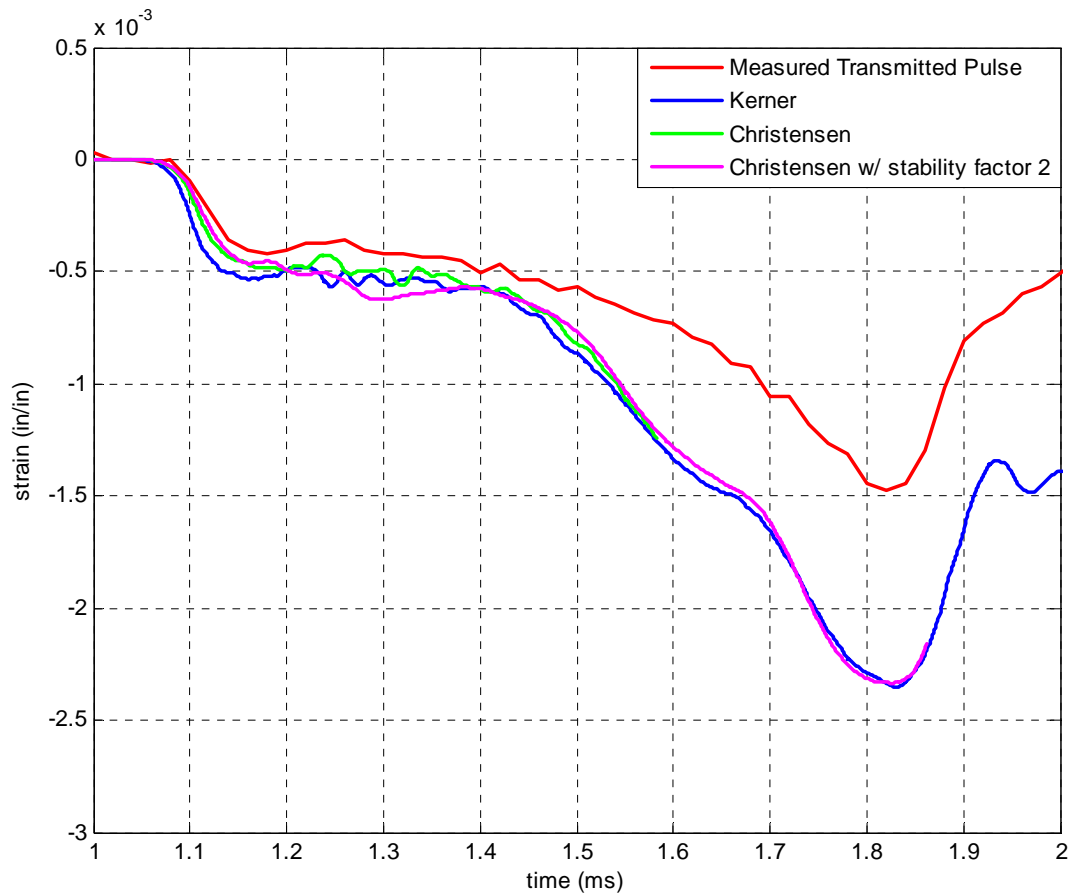


**Figure 6-19 Effect of Christensen’s Shear Equation – 0.5” R8702 Specimen with 13 psi charge**

**6.1.3. SHPB Simulations for R451 Compared with Measurements**

Figure 6-20 through Figure 6-22 show data-model comparisons for the 1.0” thick R451 using the 7-psi, 10 psi and 13 psi striker charges, respectively. The model agrees with the data set fairly well, which is not entirely impressive since the energy is being

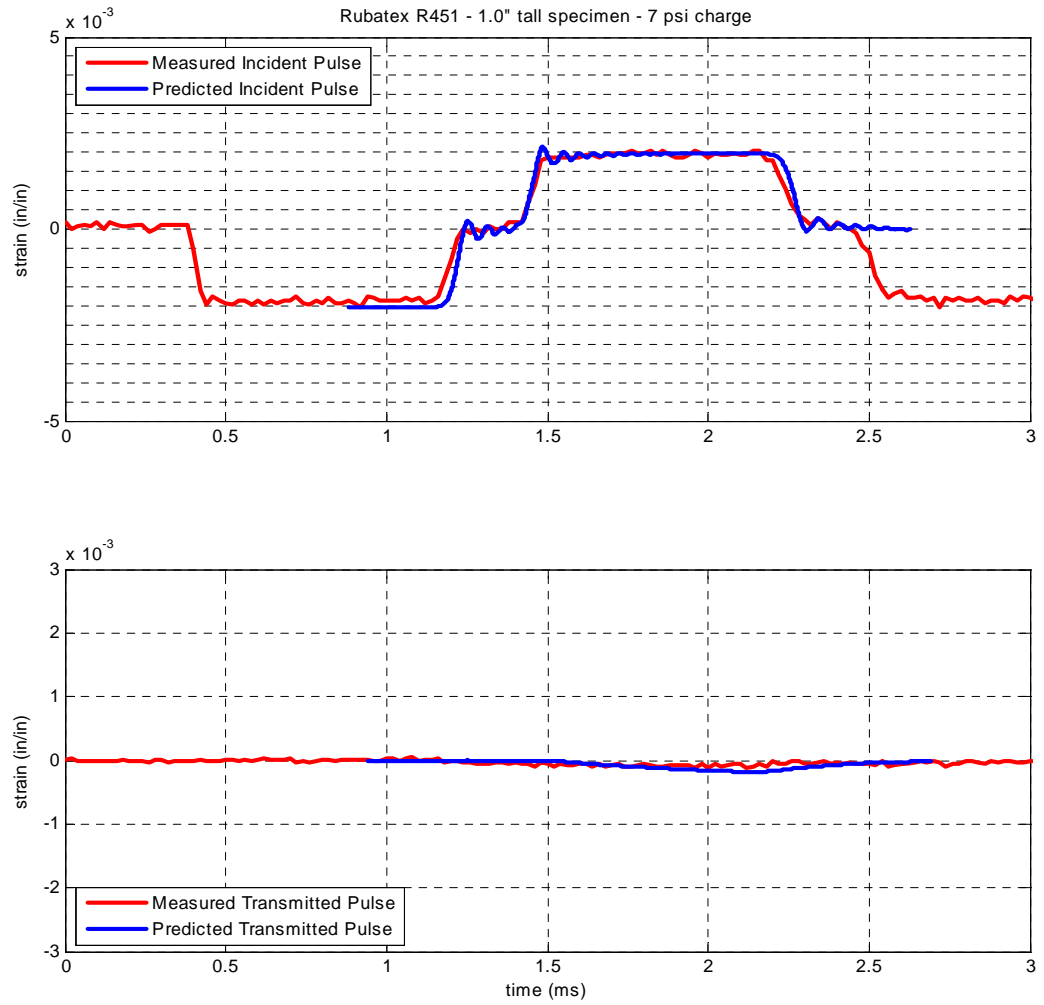
almost completely reflected. At the highest striker levels, a small but noticeable discrepancy develops. The model shows a small amount of late-arriving transmitted energy not seen in the data.

Figure 6-23 through Figure 6-25 show the data-model agreement for the 0.5” thick R451 specimens with the 7-psi, 10 psi and 13 psi striker charges, respectively. The model does a good job tracking the densification peak with this specimen. Note that there is now a clear discrepancy on the arrival time of the transmitted energy likely due to a missing pre-bending stiffness in the R451 model. Fortunately, the missing feature is not significant to the overall response.

#### 6.1.3.1. Use of High Loss Factor Weighting for R451

A special simulation was made where the relaxation moduli for R451 was changed from the even, 50/50, weighting of real modulus and loss factor, to the one shown in Figure 3-9 where the loss factor was favored in the weighting by 90/10.

Figure 6-26 shows the comparison of the simulations, with the 90/10 weighting function on the real and loss factor components of the mastercurve. We find that the 50/50 weighting provides better overall agreement to the data set. However, the higher loss did help smooth the response, and in that sense, improved the agreement to the data character.



**Figure 6-20 SHPB Data Theory Comparison - MATLAB model – 1.00” R451 Specimen with 7 psi charge**

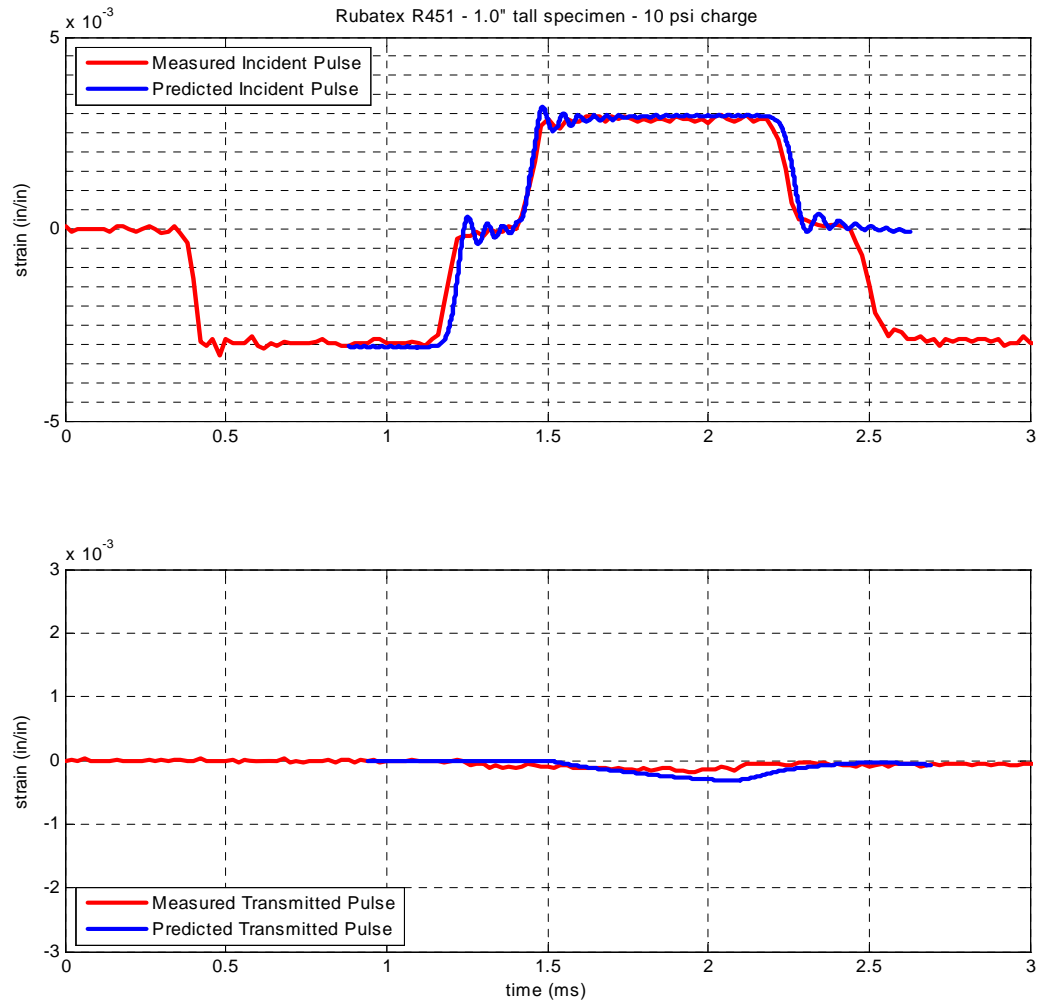


**Figure 6-21 SHPB Data Theory Comparison - MATLAB model – 1.00” R451 Specimen with 10 psi charge**

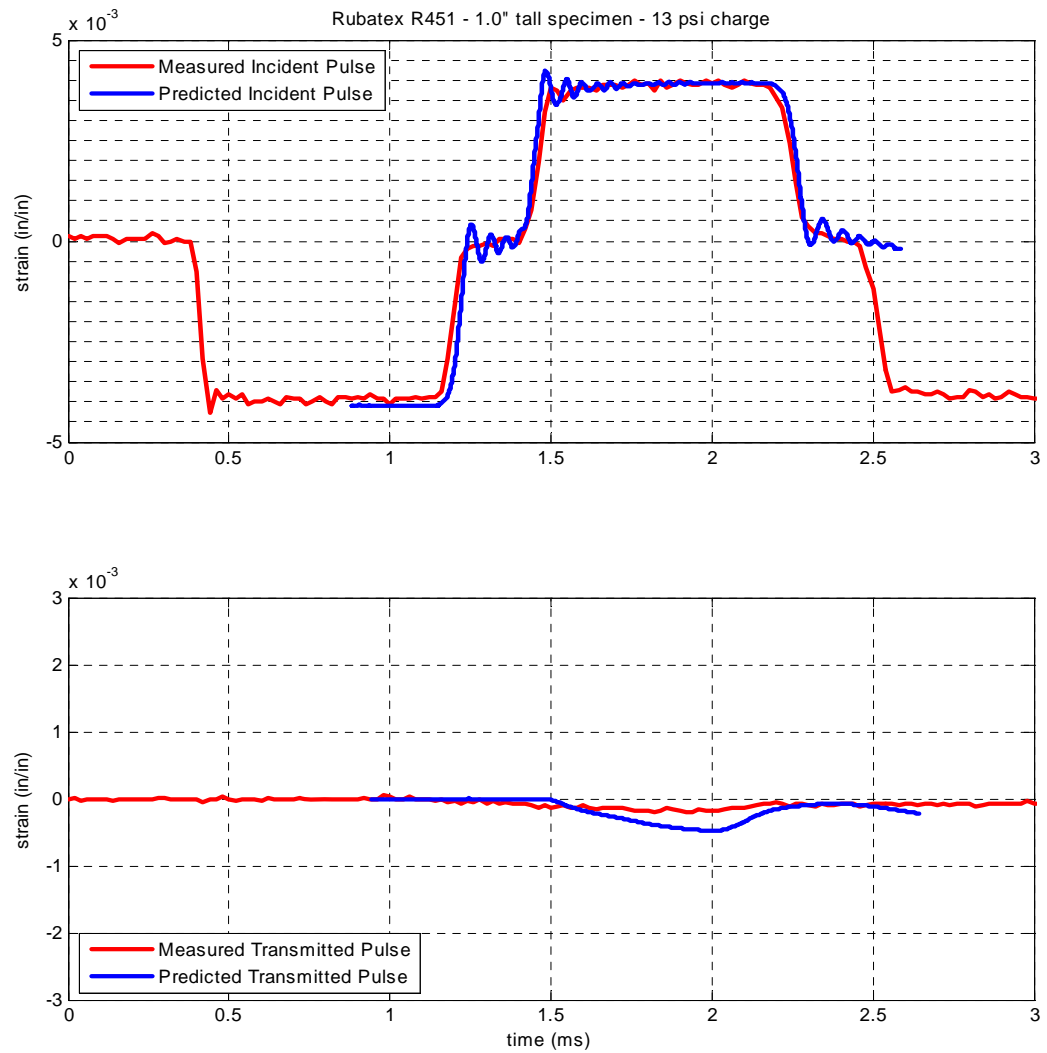


**Figure 6-22 SHPB Data Theory Comparison - MATLAB model – 1.00” R451 Specimen with 13 psi charge**

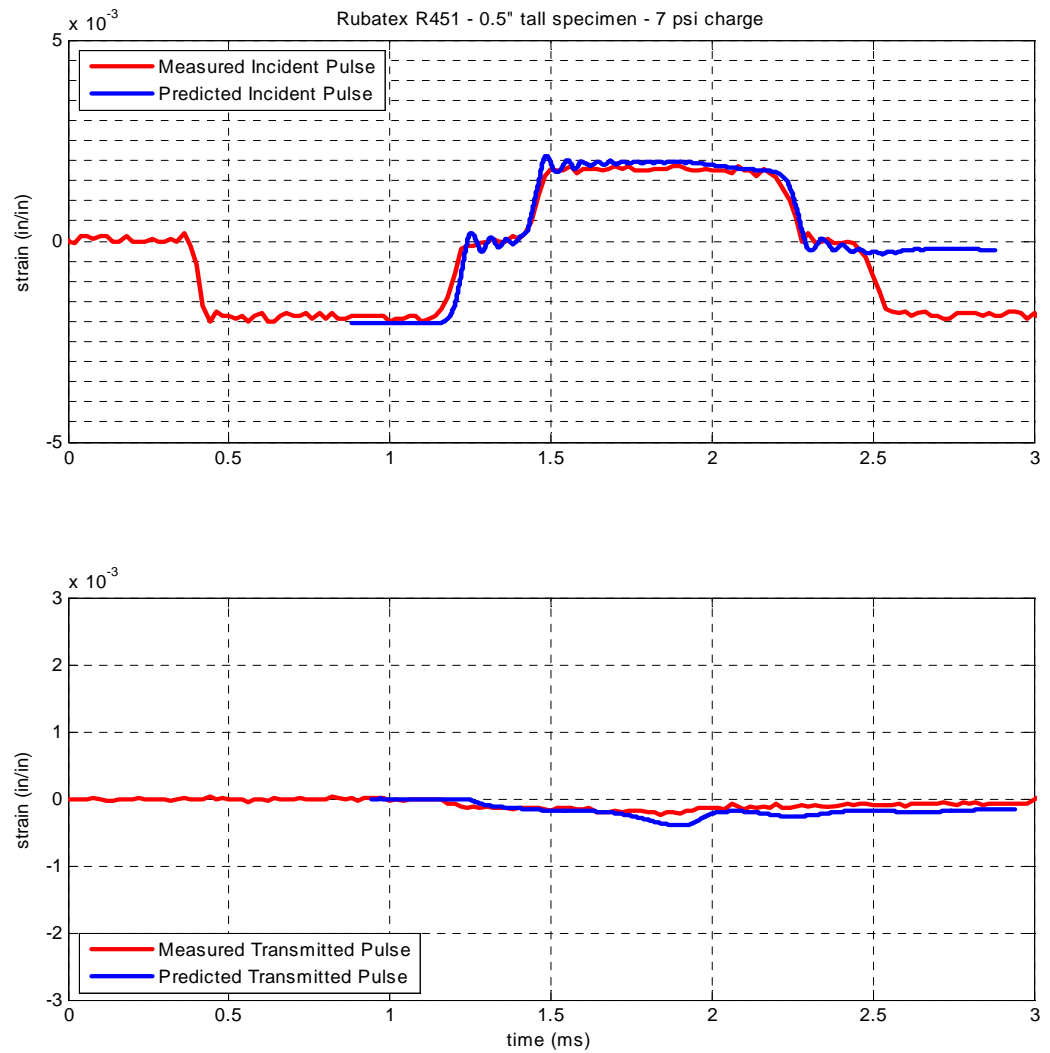


**Figure 6-23 SHPB Data Theory Comparison - MATLAB model – 0.50” R451 Specimen with 7 psi charge**

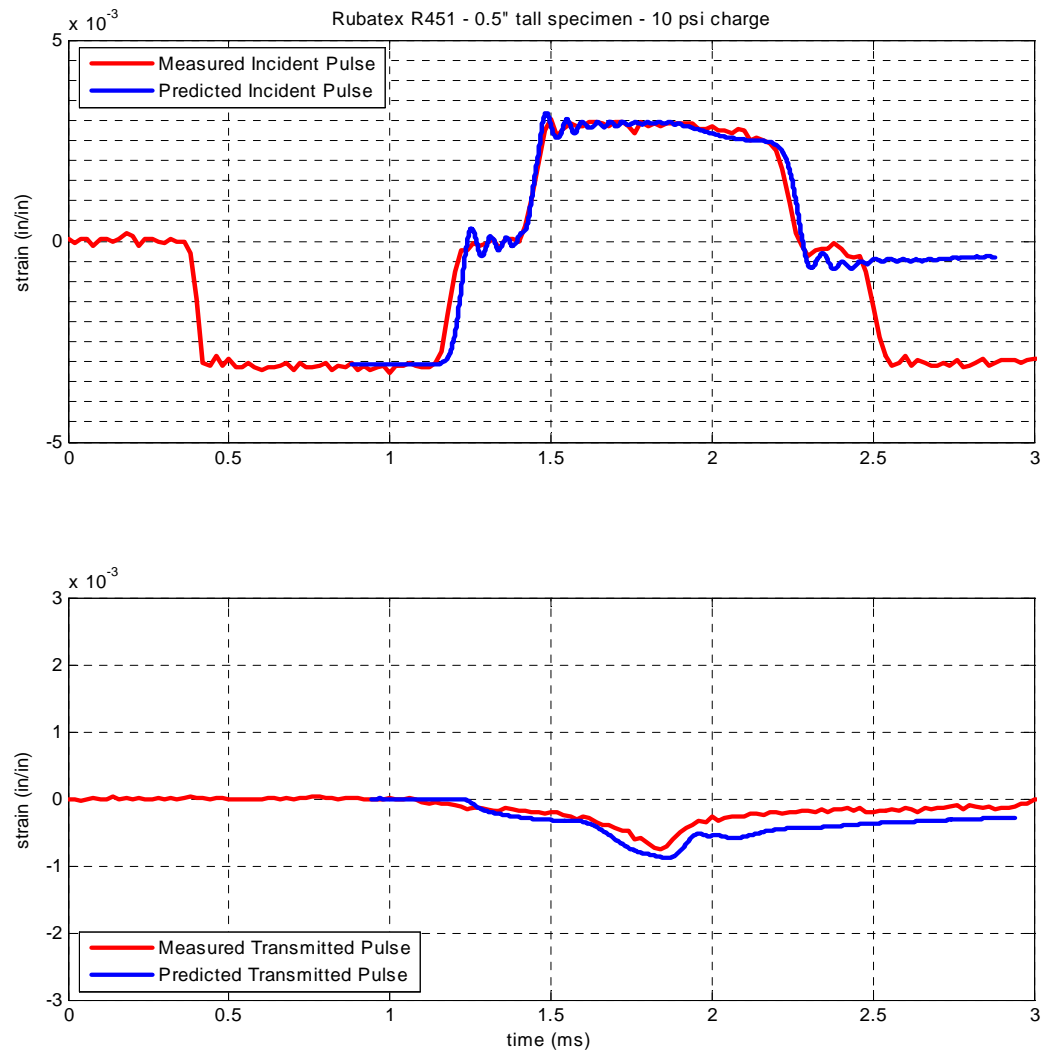


**Figure 6-24 SHPB Data Theory Comparison - MATLAB model – 0.50" R451 Specimen with 10 psi charge**

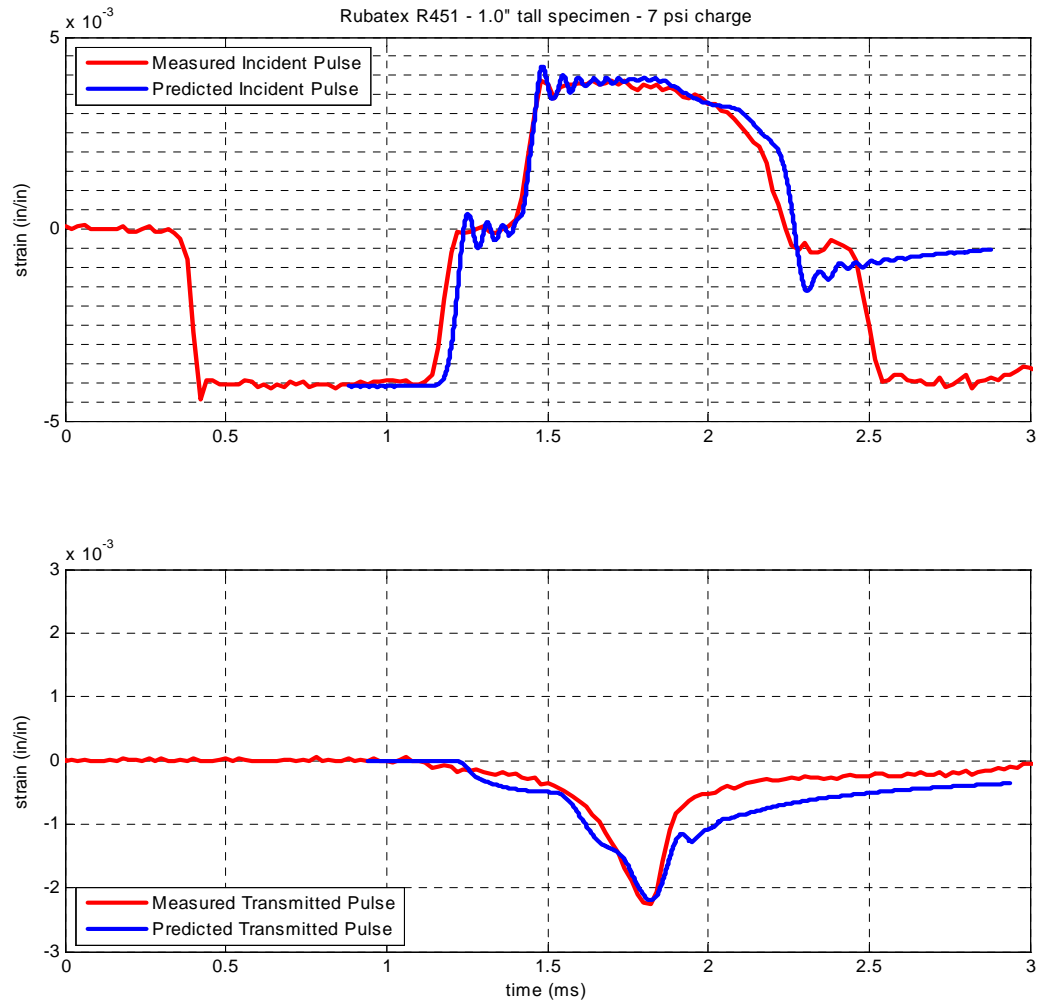


**Figure 6-25 SHPB Data Theory Comparison - MATLAB model – 0.50” R451 Specimen with 13 psi charge**

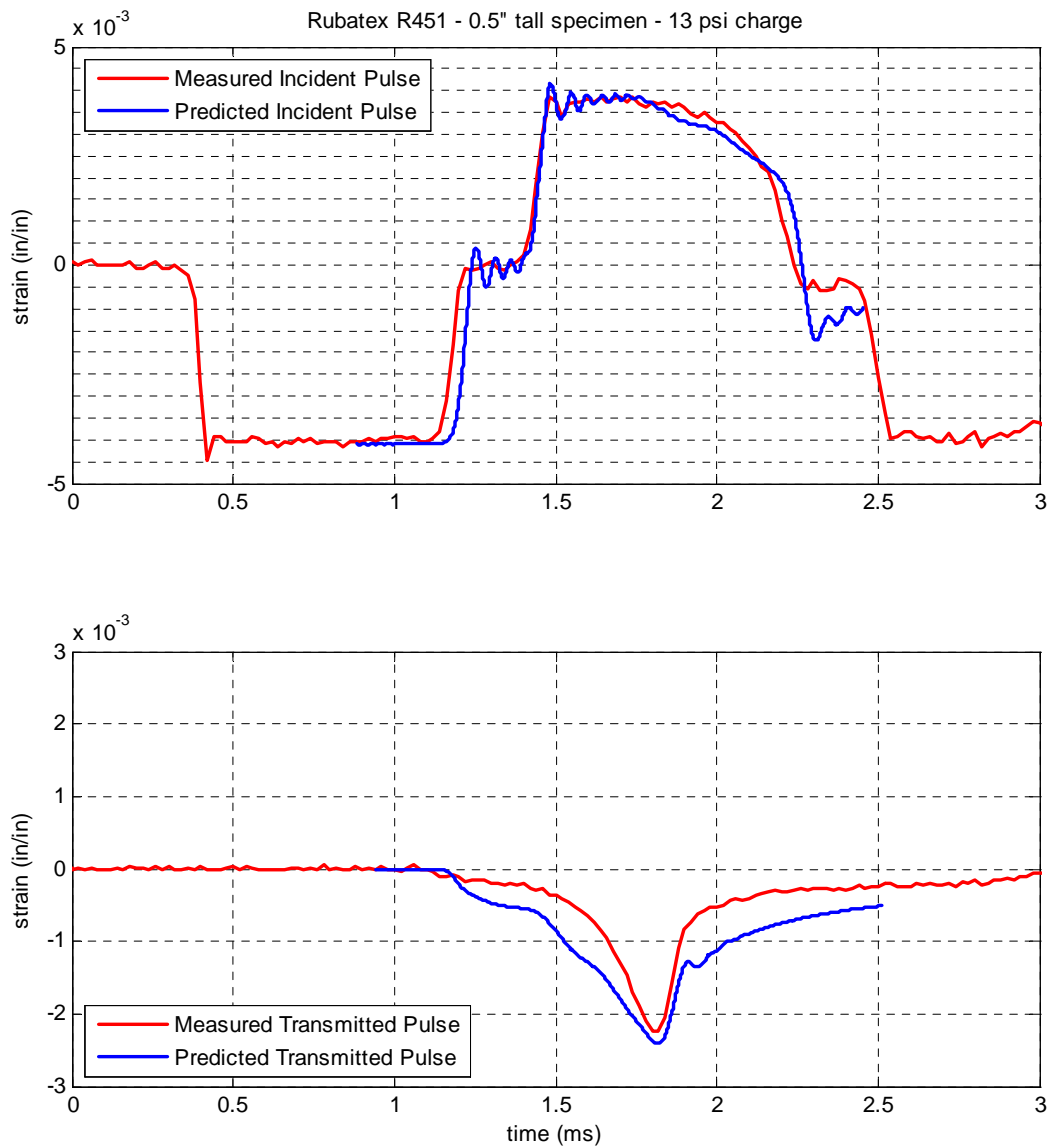


**Figure 6-26 SHPB Data Theory Comparison - MATLAB model – 0.50” R451 Specimen with 13 psi charge – [High Loss Factor Weighting for Prony Coefficients]**

## 6.2. Comparison of ABAQUS and MATLAB Models for SHPB Cases

Figure 6-27 ABAQUS Mesh of the SHPB experiment near the specimen region. Comparisons were made at the highest striker level on the ½” thick specimens since those cases involve the greatest split between the reflected and transmitted pulses. The VUMAT provided in Appendix A was used to execute the constitutive theory for the foams in ABAQUS using the same model parameters used with MATLAB.

It should be noted that the ABAQUS and MATLAB models differ in several ways that could be significant to the interpretation of the comparisons. In the ABAQUS model, the striker bar is modeled as separate piece and the impact is modeled using a contact analysis. A frictionless surface is assumed between the striker bar and the incident bar. The MATLAB simulation models the striker and incident bars as one piece, which would be equivalent to the contact surface having an *infinite* friction coefficient in the ABAQUS model.. The models also differ significantly in their mesh densities. A much finer mesh was used with the ABAQUS model in both the specimen region and the bar. Finally, the solution approach is different as was previously discussed in section 5.

The agreement between the ABAQUS and MATLAB simulations is shown in Figure 6-32 for the R451 specimen. We find that the models agree quite well, but there is an interesting discrepancy. The ABAQUS model shows greater strain oscillation throughout the simulation. These oscillations are associated with a ringing of the radial mode in the bar as the strain pulse travels. It was initially believed that the use of a small loss factor for the polycarbonate bar in the MATLAB modeling was the source of the discrepancy,

but running the MATLAB case without the loss factor yielded an indistinguishable result. The difference in the mesh densities of the polycarbonate bar was also ruled out as the source of the discrepancy. Remaining possibilities include the difference in the way the collision between the striker and incident bar, and numerical damping effects in one or both solution methods.

The agreement between the ABAQUS and MATLAB simulations is shown in Figure 6-32 for the R8702 specimen. Again, we find that the models agree quite well, but the ABAQUS model suffered numerical problems at about 1.6 ms preventing the run from reaching completion. This may be a Drucker instability that is aggravated by the finer mesh used in the ABAQUS analysis. Another possible factor is the additional stability built into the axisymmetric elements used with the MATLAB simulation, which may be helping to control excessive deformation of elements. The latter explanation is likely: ABAQUS only provides single point integration elements with EXPLICIT and artificial hour glass control needed to stabilize the elements.

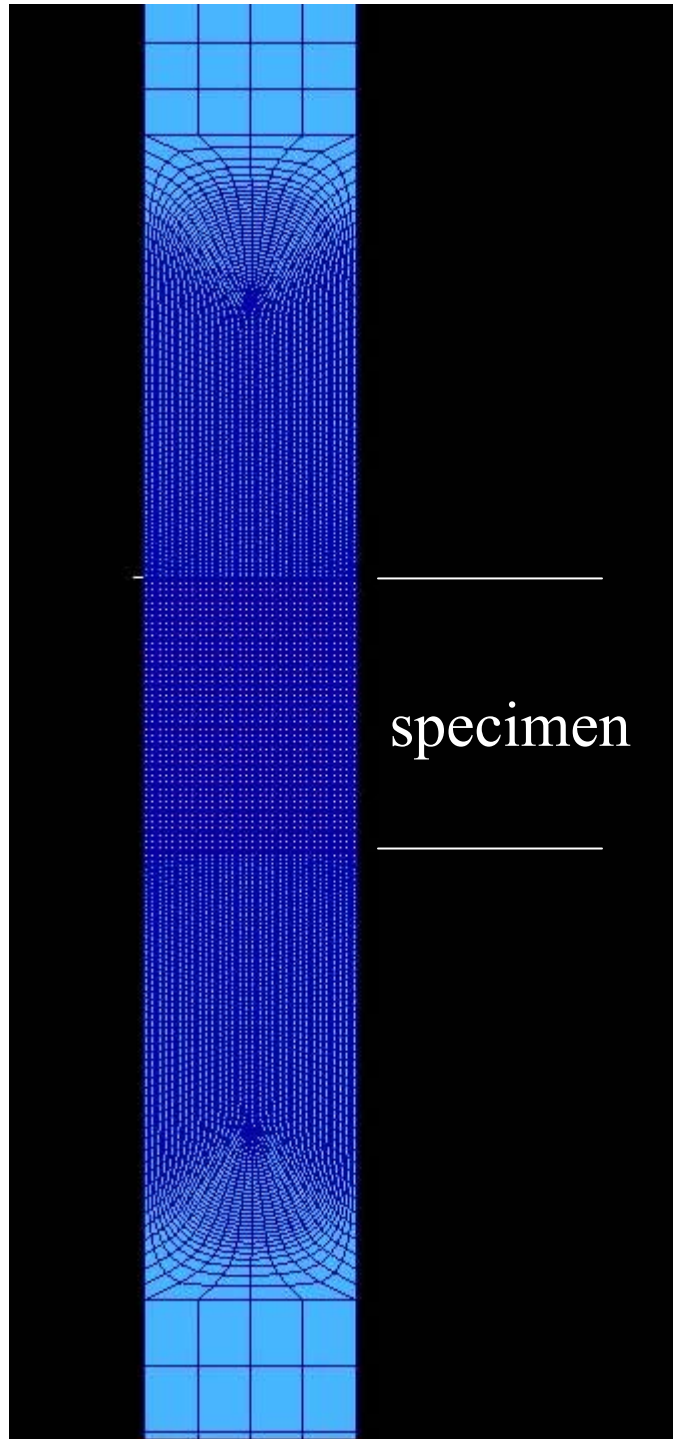


**Figure 6-27 ABAQUS Mesh of the SHPB experiment near the specimen**

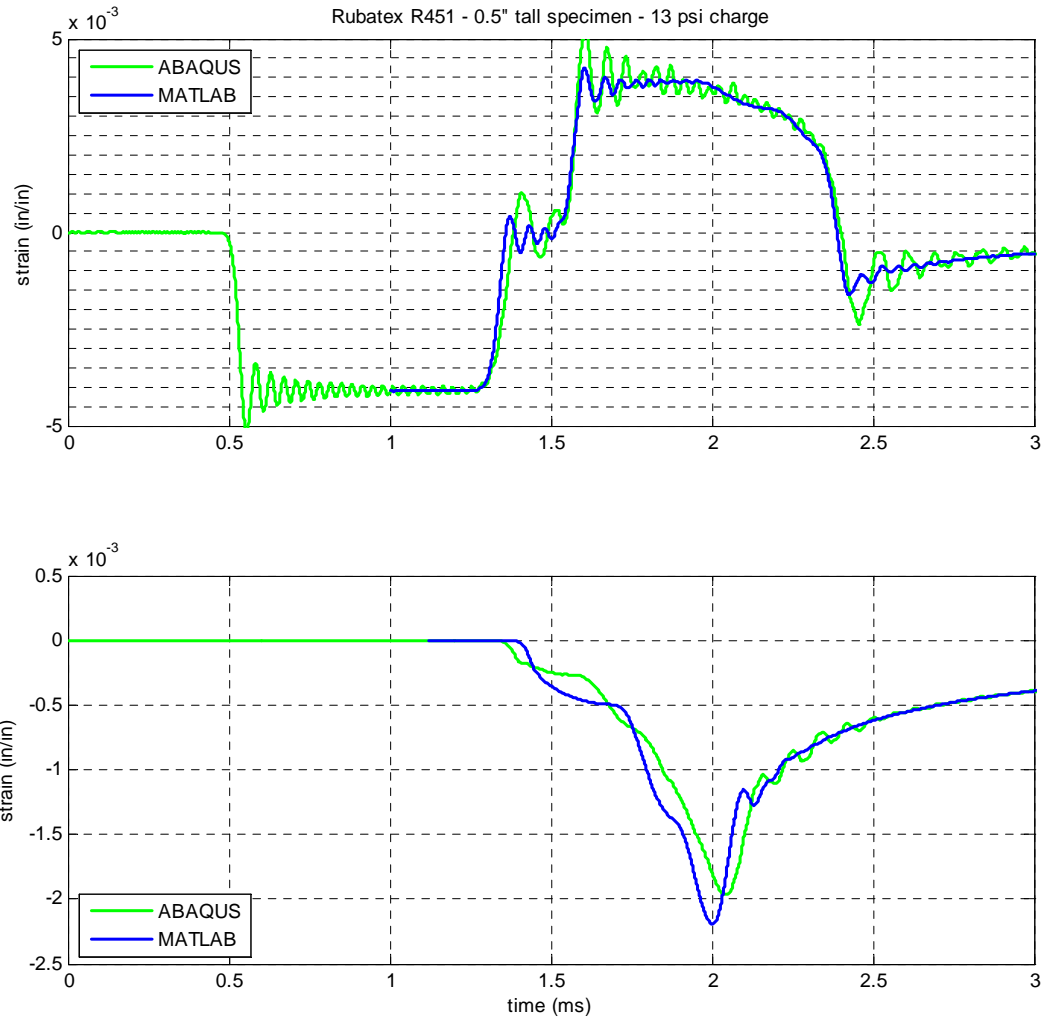


**Figure 6-28** A comparison of ABAQUS and MATLAB simulations of the SHPB experiment for 1/2" R451 with a 13 psi striker charge.

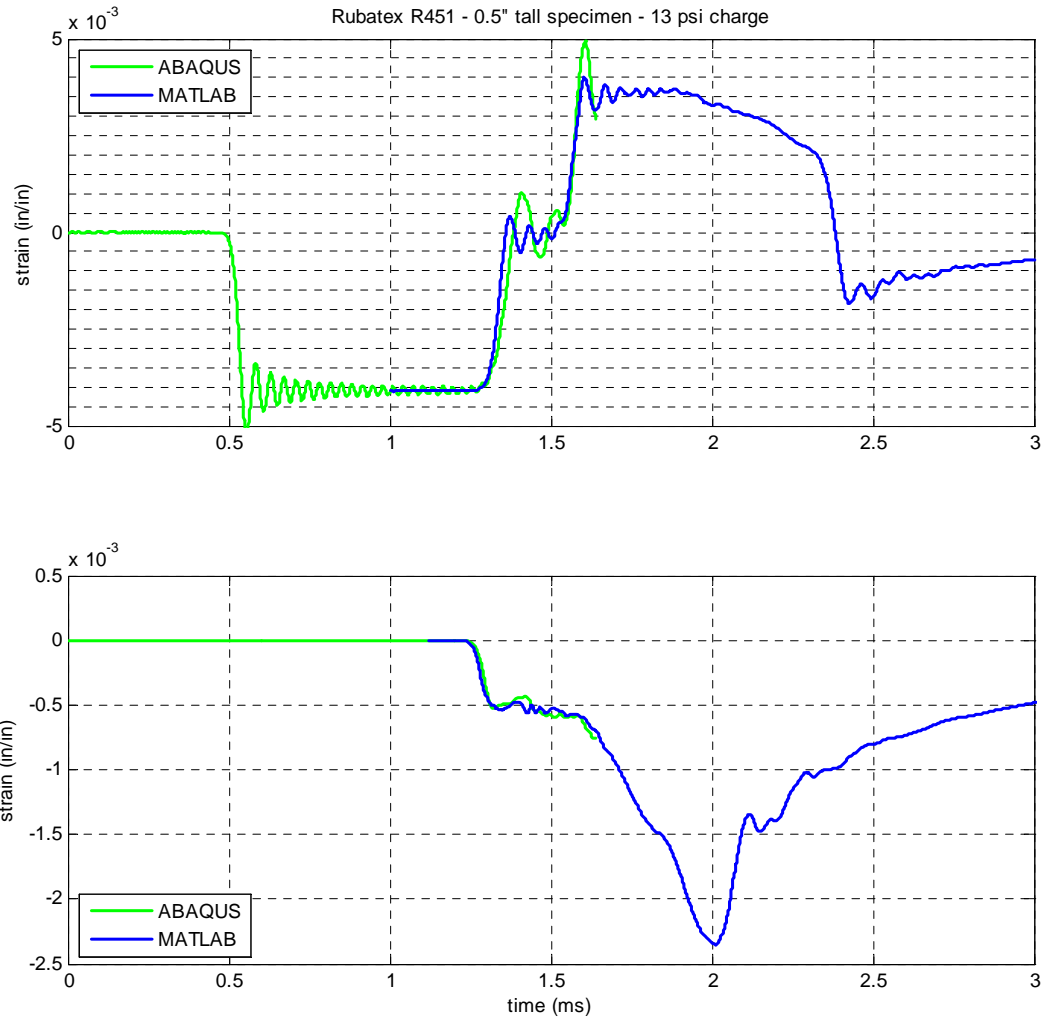


**Figure 6-29** A comparison of ABAQUS and MATLAB simulations of the SHPB experiment for  $\frac{1}{2}$ " R8702 with a 13 psi striker charge.

### **6.3. ABAQUS CST Model Compared with Experimental Data**

ABAQUS models of the CST experiments were made for additional validation of the constitutive model. Modeling the CST experiment is a far more difficult task than the SHPB experiment mainly because of cavitation, which occurs when tensile stress tries to develop in the water medium causing bubble formation. An idealized description of the model was used to facilitate the analysis, so the model details and assumptions should be considered before interpreting the comparisons. The ABAQUS mesh for the CST analysis is shown in Figure 6-30 for the R451 specimen. The fluid region extends 10” from the specimen face. A reflection-free boundary condition is applied at the top of the model to permit the reflected pressure to propagate away. The conical geometry was simplified to be cylindrical at the specimen end. A rigid boundary condition was applied along the sides of the water. A roller boundary condition was applied to the specimens. This is a reasonable assumption for the R451 specimen, which has an aspect ratio (diameter-to-thickness) of 5. The assumption is much better for the R8702 specimen, which has an aspect ratio of 10. With a roller boundary condition, the specimen response is insensitive to diameter for normally incident plane wave excitation. This motivated the choice of a 2” diameter for the simulation, rather than the 9.5” specimen diameter, since model size could be reduced. However, the assumption of model insensitivity to diameter is not perfectly valid considering that we are also modeling the cavitation effects. Some impact on the simulation due to our choice of diameter must be expected, but since cavitation inception is chaotic and strongly influenced by the fluid mesh, we did

not expect to gain greater accuracy by growing the model to match the diameter of the experiment.

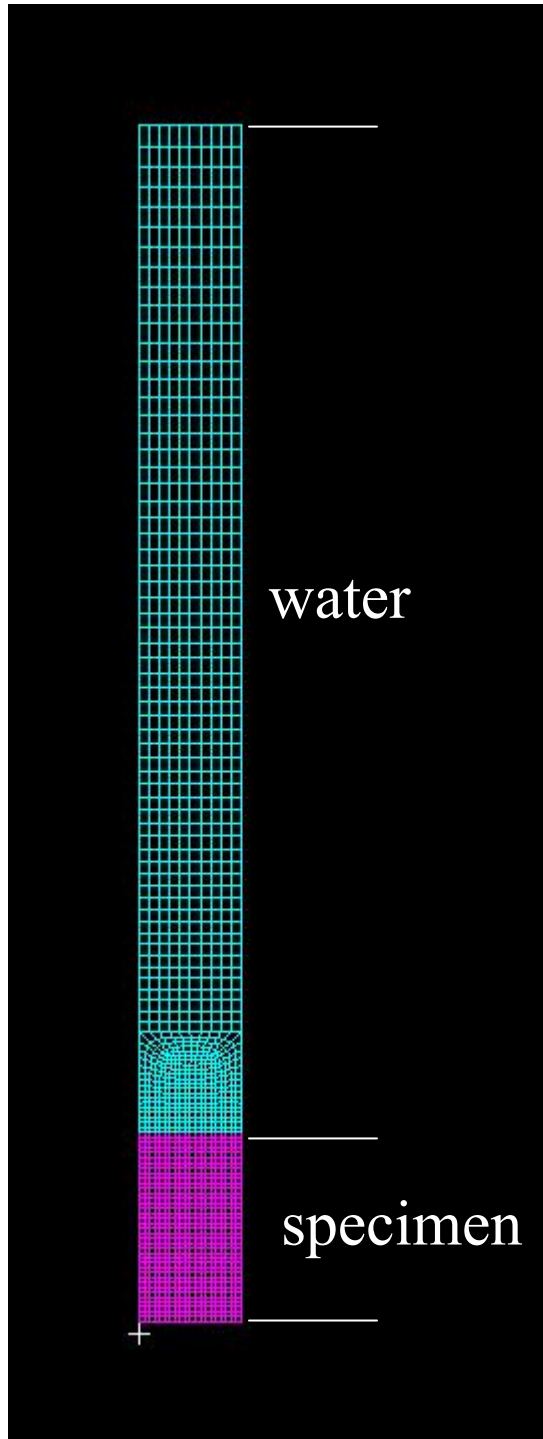


**Figure 6-30 ABAQUS Mesh for the CST experiment**

ABAQUS allows the incident shock pressures from a remotely located source to be prescribed at a specific location. Shock pressure profiles from earlier CST measurements were used as the prescribed incident pressures for the CST models. Figure 6-31 shows the incident shock pressure profile used to model the higher shock level. Cavitation due to reflection from a specimen caused the incident pressure profile to be lost after 0.44 ms. The missing information is replaced with an exponential curve fit [left figure, red curve], which is extrapolated out in time to provide a complete incident profile for the simulation [right figure].

Cavitation pressure was set at 15 psi for all CST simulations.

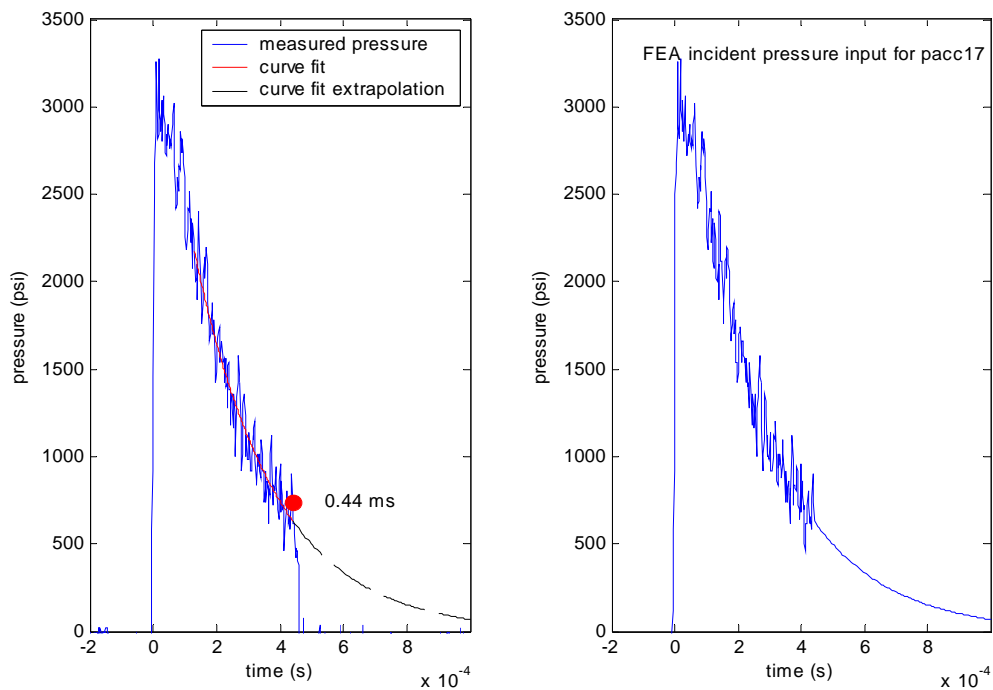


**Figure 6-31 Incident Shock Pressure Profile used for CST model – with booster**



### ***6.3.1. CST Simulations for R8702 Compared with Measurements***

CST pressure levels for a 1.0” thick R8702 specimen at the lower shock level (no booster used with the charge) are shown in Figure 6-32.

The lower figure shows output from the pressure sensor imbedded between the specimen and the witness plate compared with the predicted pressure for this location. We find that the model predicts slightly higher transmitted pressure levels. Also, like was seen with the SHPB model, a much slower decay back to zero pressure is predicted.

The upper figure shows output from the pressure sensor, which is located 14” in front of the witness plate. This is compared with the predicted pressure at 11” from the witness plate. The slight discrepancy in position would cause about a small 0.10 ms discrepancy in the arrival of reflected energy from the specimen. The model prediction of the passing shock waves differs from the experiment only because a different measurement was used to establish the incident pulse in the simulation. At about 0.8 ms the reflected energy cancels the incident pulse and there is a subsequent period of cavitation that lasts until 2.2 ms in the simulation and until 2.7 ms in the experiment. After the cavitation bubble is closed the simulation shows the decay of pressure consistent with the transmit sensor as the pressure equilibrates throughout the model. The equilibrium of pressure beyond about 3 ms is evident from the convergence of the pressure in the fluid and the pressure behind the specimen. The experimental data also shows this equilibration, but at lower pressure levels.

CST pressure levels for a 1.0” thick R8702 specimen at the higher shock level (using the booster) are shown in Figure 6-32. From the fluid pressure sensor, we find that the cavitation pressure was slightly higher than the 15 psi used in the simulation. The model tracks the increase in transmitted pressure [lower figure] fairly well, but the simulation shows a broader pressure pulse and shows more oscillation. Again we find a discrepancy in the decay of the pressures at longer times. The simulation shows equilibration of pressure beyond 3 ms. The experimental results do not show equilibration as there is a discrepancy in the fluid and transmitted pressure levels

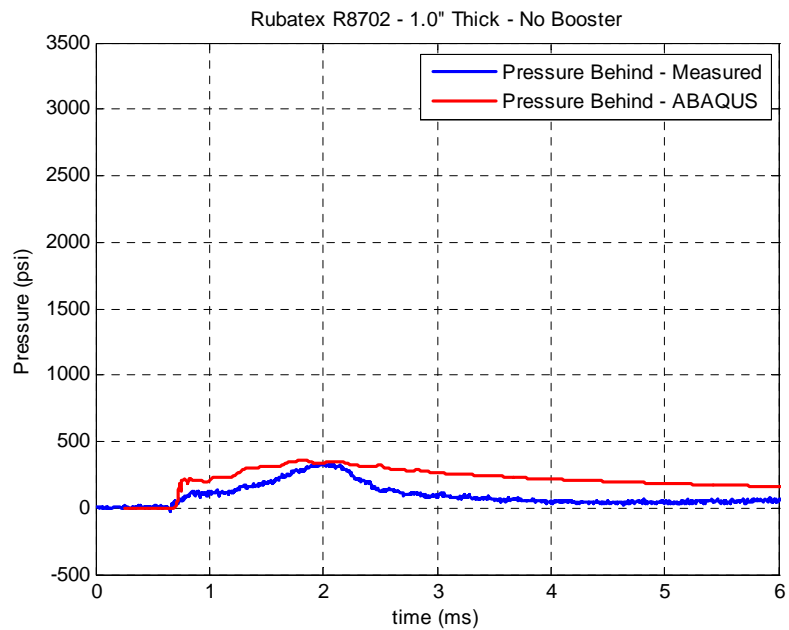
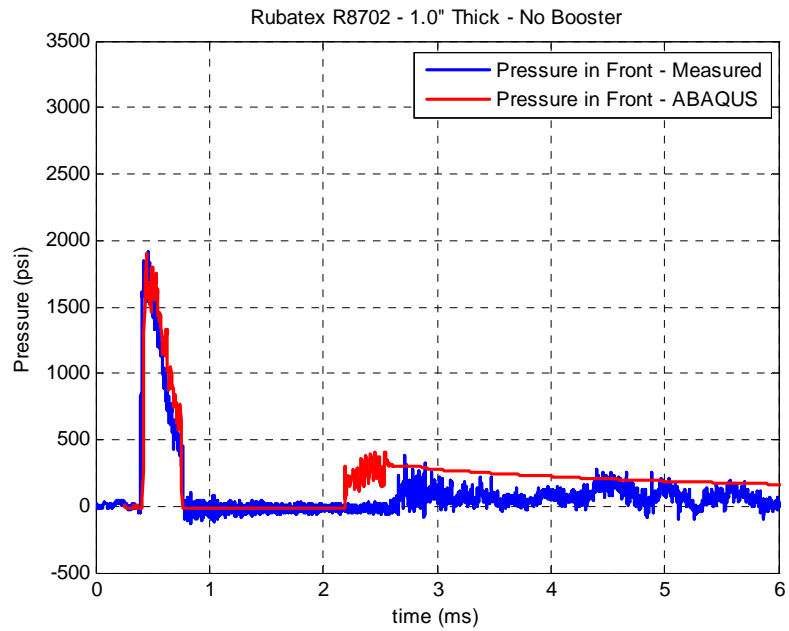


**Figure 6-32 Comparison of data with ABAQUS simulation of the CST experiment for 1.0” R8702. No booster used.**

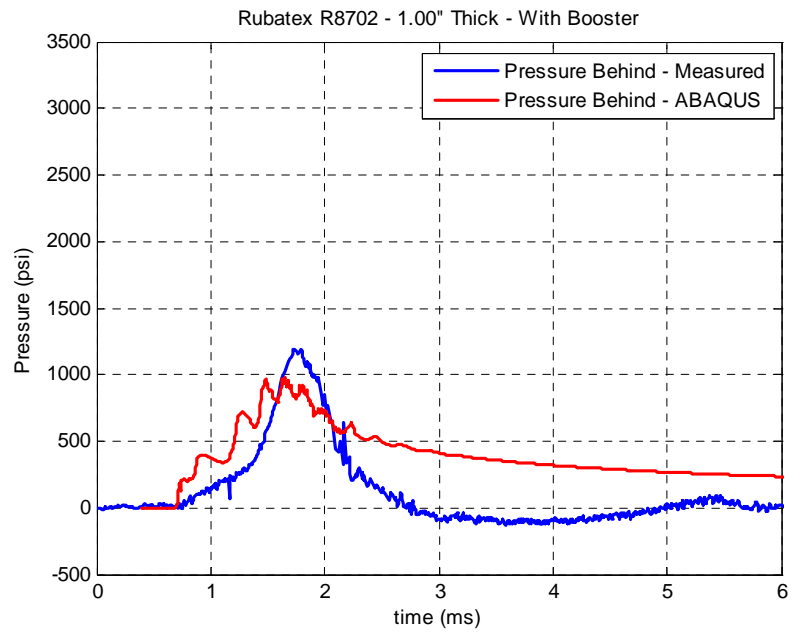
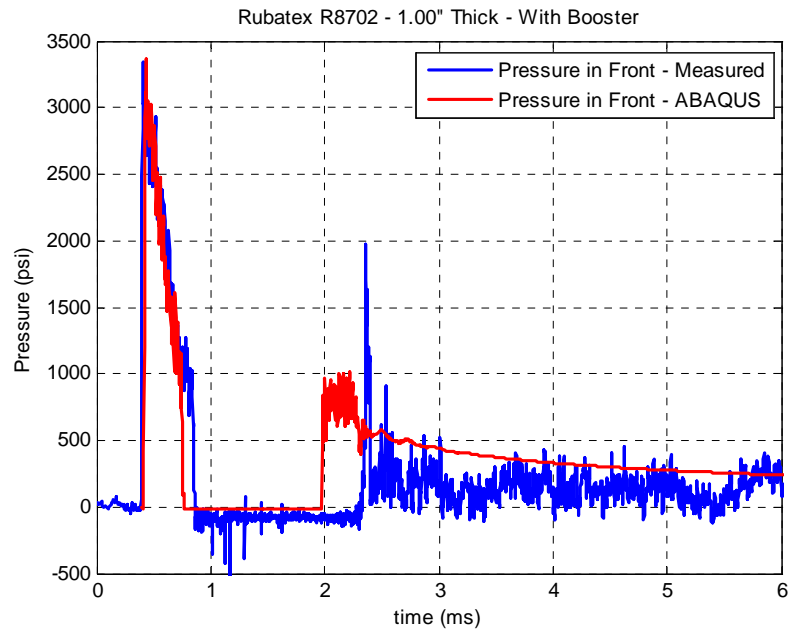


**Figure 6-33 Comparison of data with ABAQUS simulation of the CST experiment for 1.0" R8702. Booster used.**

### ***6.3.2. CST Simulations for R451 Compared with Measurements***

CST pressure levels for a 1.875” thick R451 specimen at the lower shock level (no booster used with the cap) are shown in Figure 6-34.

The lower figure shows output from the pressure sensor imbedded between the specimen and the witness plate compared with the predicted pressure for this location. The experiment shows very little energy making its way through the specimen, whereas the model predicts a small but significant transmitted pressure level. A similar comparison was seen on the 1” SHPB simulation of R451 at the highest striker levels [see Figure 6-22].

The upper figure shows output from the pressure sensor, which is located 14” in front of the witness plate. This is compared with the predicted pressure at about 11.9” from the witness plate. The slight discrepancy in position would cause about a small 0.07 ms discrepancy in the arrival of reflected energy from the specimen. The model prediction of the passing shock waves differs from the experiment only because a different measurement was used to establish the incident pulse in the simulation. At about 1.0 ms the reflected energy cancels the incident pulse and there is a subsequent period of cavitation that lasts until 4 ms in the simulation. The closing of the cavitation bubble in the experiment is not seen over the entire period reported.

CST pressure levels for a 1.0” thick R451 specimen at the higher shock level (using the booster) are shown in Figure 6-32. The model tracks the increase in transmitted pressure fairly well, but there is a significant discrepancy in the arrival time of

transmitted pressure and once again, the simulation shows a broader pressure pulse. Also, we again find a discrepancy in the decay rate of the pressures after the main shock event, which has appeared consistently throughout the data-model comparisons.

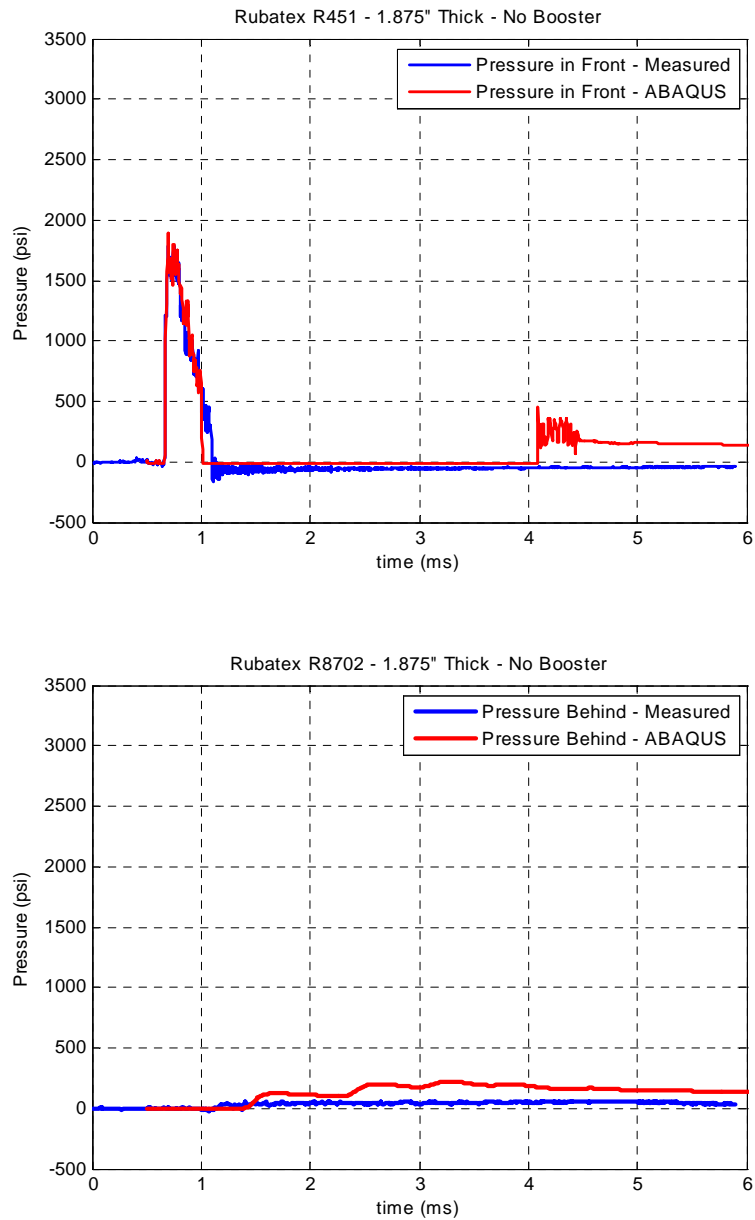


**Figure 6-34 Comparison of data with ABAQUS simulation of the CST experiment for 1.0" R8702. No booster used.**

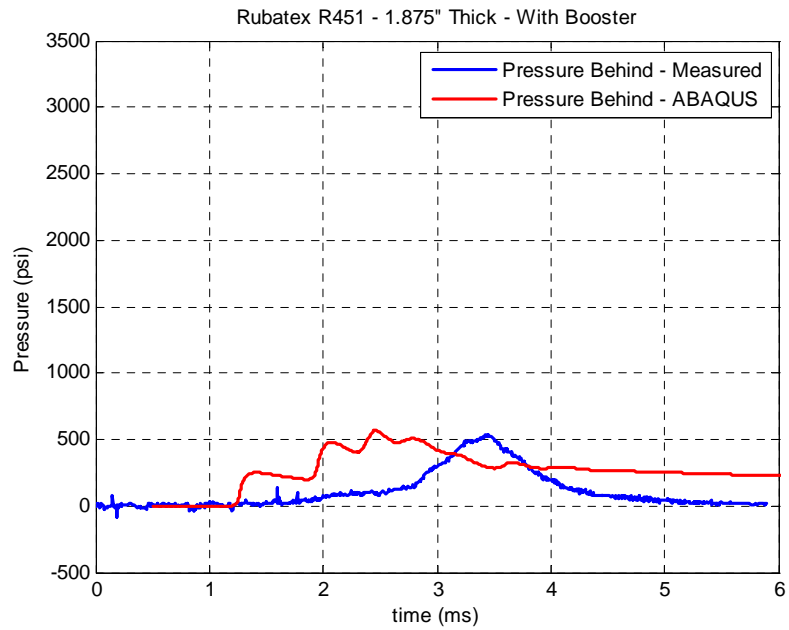
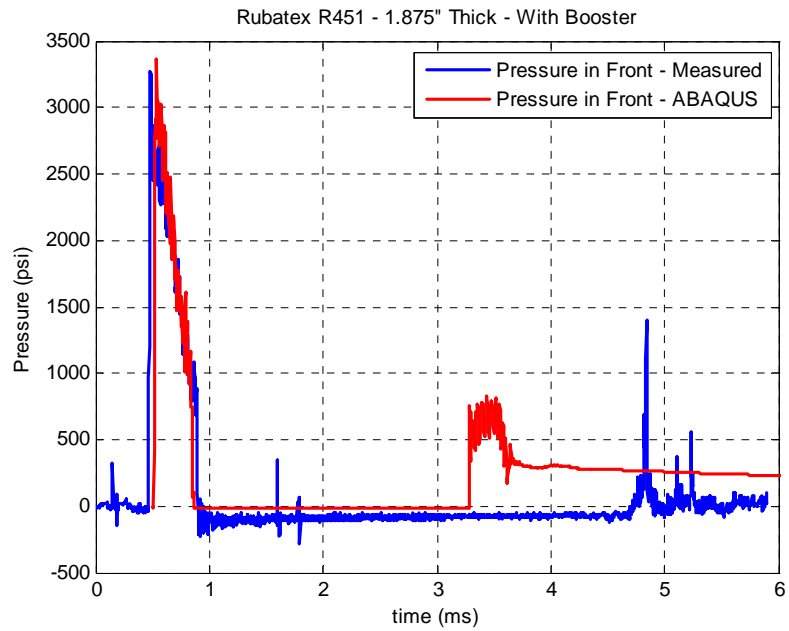


**Figure 6-35 Comparison of data with ABAQUS simulation of the CST experiment for 1.0" R8702. Booster used.**

## 6.4. Summary

Simulations of the Split Hopkinson Pressure Bar experiments correlate well with the measurements. The model did exceptionally well at capturing the transmitted and reflected strain levels with increasing striker charge levels, especially for the R451 specimen. The model tended to over predict the transmitted pressure level in the R8702 specimen, but it tracked the character of the data well.

The use of Christensen's equation made a slight improvement to the model-data comparison of the R8702 specimen. This slight improvement comes at the price of increased computation time. It also triggered a Drucker instability, which revealed that the R8702 model is very near the instability condition.

Simulations of the Conical Shock Tube experiments showed fair correlation with the measurements. In most cases, the model did fairly good job of predicting the peak amplitudes of the transmitted pressure. However, significant discrepancies were noted in arrival times of the transmitted pressure with the R451 specimen, as well as the time at which the cavitation bubble closed. Also, the character of the transmitted pressure pulse differed significantly from the measured pulse.

A consistent discrepancy between the model and the data for both the SHPB and CST experiments was the difference in the decay rate of the transmitted strain and pressure, respectively. The discrepancy indicates that there is an unaccounted loss

mechanism at work. An unknown loss mechanism could also explain other discrepancies in data character seen in the experiments.

## CHAPTER 7

### 7. Summary and Conclusions

In this dissertation a fully isotropic constitutive model was developed for closed-cell foams such that it is specialized towards shock loads that are predominantly compressive in nature. The hyperelastic free energy was written in a special form so that it could be fully defined with the hydrostatic bulk and shear moduli, which in turn are functions of the volumetric stretch. This permitted the use of three-phase composite theory to fully define the hyperelastic free energy. Use of the three-phase model had three major advantages:

- 1) Identification of the hyperelastic free energy contributions of the gas and material phases.
- 2) Elimination of deviatoric experiments for parameter determination.
- 3) Proper behavior at the densification limit

Separation of the gas and material phase contributions was critical in properly establishing the proper relaxation behavior of the foam. The three-phase theory provided a link between the deviatoric response of the foam and its volumetric response, thereby eliminating the need for deviatoric experiments altogether. It also ensures that the material will reach a state of incompressibility when the densification limit is approached under high compressive strains. The Elastic-Viscoelastic Correspondence Principle was used to create a hyperviscoelastic description from the hyperelastic framework.

Nonlinear strain functions were developed from the stress equation, which serve as analogs to the infinitesimal strain in linear viscoelasticity. Since three-phase composite theory lacks a description of cell wall bending, a phenomenological correction to the composite theory was developed to include this behavior.

A characterization approach was developed for closed-cell foams. This involves just two experiments and optimization of model parameters. A Dynamic Mechanical Thermal Analyzer (DMTA) was used to develop mastercurves of the specimen's dynamic complex shear modulus from which the Prony coefficients are developed. A dilatometer experiment was used to measure specimen volumetric compression in a controlled hydrostatic pressure-history. This was used to establish three-phase parameters and the plastic terms.

Difficulty was encountered with the determination of the Prony coefficients for RUBATEX R451. The DMTA mastercurve was clearly in violation of Kramers-Kronig's causality relations, making the Prony model was unable to describe both the real and imaginary components of modulus. This caused weighting factors used in the optimization to play a significant role in the final Prony fit. Favoring the loss factor worsened the predictions of the SHPB experiment, but considering the other uncertainties in the modeling approach it is difficult to draw firm conclusions for this finding.

The behavior of closed-cell elastomeric foams under shock loading conditions was investigated experimentally. Split Hopkinson Pressure Bar (SHPB) and a Conical Shock Tube (CST) experiments were conducted. The data show that a layer of soft elastomeric

foam can be used as a treatment to effectively isolate an underlying structure from the shock loading. It was also shown that the isolation performance degrades dramatically once the foam nears its densification point. The conditions leading to degradation were shown to involve multiple parameters. The experiments revealed that the amplitude of the shock event and the layer thickness are among these parameters. The experimental data also provided verification for the constitutive model. For this purpose, finite element models of the shock experiments were made. It was demonstrated that the constitutive description and foam characterization were sufficient to provide good correlation to the high strain-rate experiments. The SHPB and CST experiments revealed consistent attributes for the two foam specimens. Both tests showed that R8702 specimen passes some energy regardless of the shock level whereas the R451 was nearly 100% effective until densification levels were reached.

SHPB data agreed favorably with model simulations. The model was able to predict with reasonable accuracy the transmitted strain levels and their dependence on specimen thickness and shock amplitude. CST data agreed less favorably with simulations, but in most cases, the model was able to predict peak amplitudes of the transmitted pressure. Generally, there were discrepancies in the decay rate of the transmitted stress and also with the strength of the compressive reflection from the specimen that follows the tensile reflection. Both of these discrepancies point toward an unaccounted loss mechanism.

One of the major theses of this work was that high strain-rate experiments could be predicted from low strain-rate experiments. From an engineering perspective, this was

successfully demonstrated to the extent that good qualitative agreement was achieved with many of the experimental results, and by the fact the model was largely successful at predicting peak transmitted energy levels. However, the persistent discrepancy in system energy between experimental and model results, suggesting an unaccounted loss mechanism, raises the question as to whether the missing mechanism might be due to a coupling between the rubber relaxation behavior and the finite strain. If so, the separability assumption, which is key to the model development, may be introducing a significant under-accounting of the foams capacity to absorb energy. This unaccounted loss mechanism is an area well worth further study in both the experiments and the constitutive theory.

The model provided additional insight into the shock isolation performance of foams. It was shown that, in addition to layer thickness and shock amplitude, the duration of the shock event is a key parameter in determining whether the foam will effectively isolate an underlying structure. The model also provided insight into the material physics. The foam exhibited a drastic loss of moduli in the stress plateau region, and it was shown that the only significant source of elastic response in this region is due to the gas contained within the closed cells of the foam. Modeling also indicated that, although plasticity was an insignificant player in shock events, it does play an important role in the interpretation of low strain-rate characterization experiments. An interesting observation is that the constitutive model provides a description of behavior resembling

Mullen's effect, which was found to arise from a combination of viscoelastic creep, plastic set, and strain dependent moduli.

An important aspect of the description of closed cell foams is the contribution of the gas phase to the constitutive response. There is still more work to be done on this aspect of the problem. If the contribution of the gas phase relative to the material phase is not described well, there could be significant errors in the predicted viscoelastic behavior. The optimization results for the RUBATEX foams proved to be interesting in this regard. Based on the hydrostatic chamber experiments, the effective bulk modulus of R451 at low strain rates was seen to be dominated by the gas phase whereas R8702 was dominated by the material phase initially, and then became gas-dominated upon compression. Since there was no rigorous treatment of the gas thermodynamics and its interaction with the material phase, the initial gas pressure in the foam was left as a parameter for optimization. Both foams showed improved dilatometer optimizations with an internal gas pressure above atmospheric pressure. For R451 the parameter was  $1.5x P_{\text{atm}}$  and for R8702 the parameter was  $1.8x P_{\text{atm}}$ . This could be due in part to an adiabatic response of the gas in the dilatometer experiment, but considering the low strain rate of this experiment one may be inclined to assume isothermal behavior. It is also possible that some of the elevated pressure is real. Based on discussions with RUBATEX regarding the manufacturing process, this finding seems plausible. The foams are formed by pressurizing the resins under nitrogen gas during the vulcanization process. The slabs are then rolled out to atmospheric conditions while they are partially

cured. At that time the slab rises as the dissolved nitrogen expands and the rubber completes its curing process.

The general applicability of three-phase composite theory for these types of foams remains an open issue. While we were fairly successful in predicting material behavior with this model, a number of caveats must be noted. First, we did not enforce a consistency between the DMTA static shear modulus value with that derived from the optimization of the dilatometer data. DMTA was used only to establish the relaxation moduli *relative* to the static shear modulus, whereas the dilatometer optimization was used to establish the actual static value. Furthermore, in the case of R8702, a strong bending correction was applied to the three-phase theory. However, the general hyperelastic form that has been developed in this dissertation is adaptable to any composite theory, phenomenological or not, as long as it is capable of describing the hydrostatic moduli as continuous functions of volume strain. It could also accommodate experimentally determined hydrostatic moduli, provided that they cover the range of expected volumetric deformation. This is another major advantage that this approach offers over other hyperelastic models.

## Appendix A: VUMAT

```
subroutine vumat(  
  C Read only (unmodifiable)variables -  
    1 nblock, ndir, nshr, nstatev, nfieldv, nprops, lanneal,  
    2 stepTime, totalTime, dt, cmname, coordMp, charLength,  
    3 props, density, strainInc, relSpinInc,  
    4 tempOld, stretchOld, defgradOld, fieldOld,  
    5 stressOld, stateOld, enerInternOld, enerInelasOld,  
    6 tempNew, stretchNew, defgradNew, fieldNew,  
  C Write only (modifiable) variables -  
    7 stressNew, stateNew, enerInternNew, enerInelasNew )  
  C  
    include 'vaba_param.inc'  
  C  
    dimension props(nprops), density(nblock), coordMp(nblock,*),  
    1 charLength(nblock), strainInc(nblock,ndir+nshr),  
    2 relSpinInc(nblock,nshr), tempOld(nblock),  
    3 stretchOld(nblock,ndir+nshr),  
    4 defgradOld(nblock,ndir+nshr+nshr),  
    5 fieldOld(nblock,nfieldv), stressOld(nblock,ndir+nshr),  
    6 stateOld(nblock,nstatev), enerInternOld(nblock),  
    7 enerInelasOld(nblock), tempNew(nblock),  
    8 stretchNew(nblock,ndir+nshr),  
    8 defgradNew(nblock,ndir+nshr+nshr),  
    9 fieldNew(nblock,nfieldv),  
    1 stressNew(nblock,ndir+nshr), stateNew(nblock,nstatev),  
    2 enerInternNew(nblock), enerInelasNew(nblock),  
  
    1 eye3(3,3), kdelta(3,3), Voigt1(6), Voigt2(6),  
    2 DSTATEV(nstatev),FSTRAN(6), DFSTRAN(6),DFSTRANA(6), DSTRAN(6), DSTRES(6), G(6),  
    3 DDSDD(6,6),STRESS(3,3),S2PK_OLD(6),S2PK_NEW(6),  
    4 CAUCH0(3,3),CAUCH1(3,3),CAUCHM(3,3),CAUCH(3,3),  
    5 CB0(3,3),CB1(3,3),CBM(3,3),CB(3,3),  
    5 CI0(3,3),CI1(3,3),CIM(3,3),CI(3,3),  
    5 CDI0(3,3),CDI1(3,3),CDIM(3,3),CDI(3,3),  
    5 U0(3,3),U1(3,3),UM(3,3),U(3,3),U0I(3,3), U1I(3,3), UMI(3,3), UI(3,3),  
    6 DE(3,3),DEA(3,3), cid0(3,3), cid1(3,3), cidm(3,3), cid(3,3),  
    7 STRAN_NLIN0(3,3), STRAN_NLINA0(3,3), STRAN_NLIN1(3,3), STRAN_NLINA1(3,3),  
    8 STRAN_NLIN(3,3), STRAN_NLINA(3,3), FINITE_STRAIN(3,3)  
  
  C  
    character*80 cmname  
  C  
  
    NELS=(nprops-10)/2  
  
    NTENS=ndir+nshr  
  
    nstatev2=3*ntens+(ntens*ntens)*nels+1  
  
  C Identity Matrix  
    eye3(1,1)=1  
    eye3(2,2)=1  
    eye3(3,3)=1  
    eye3(1,2)=0  
    eye3(2,1)=0  
    eye3(1,3)=0  
    eye3(3,1)=0  
    eye3(2,3)=0
```

```

        eye3(3,2)=0

        kdelta=eye3
C   Voigt Notation
        Voigt1(1)=1
        Voigt1(2)=2
        Voigt1(3)=3
        Voigt1(4)=1
        Voigt1(5)=1
        Voigt1(6)=2

        Voigt2(1)=1
        Voigt2(2)=2
        Voigt2(3)=3
        Voigt2(4)=2
        Voigt2(5)=3
        Voigt2(6)=3

c       print*, stepTime, totalTime, dt, nels, ntens, nblock, nstatev
C
C
C
C ----- MAIN BLOCK LOOP -----
        DO 100 km=1,nblock
C
C
C
C   Get the current properties
C
        J1=2*NELS
        PHI0 = PROPS(J1+1)
        BN   = PROPS(J1+2)
        C1   = PROPS(J1+3)
        C2   = PROPS(J1+4)
        D1   = PROPS(J1+5)
        D2   = PROPS(J1+6)
        PR   = PROPS(J1+7)
        ELIMIT = PROPS(J1+8)
        ESET  = PROPS(J1+9)
        p0=PROPS(J1+10)
C
        s0=1.-phi0
C
C   Set the Drucker Stability parameter here.  DS=1 (no control)  DS>1 (control)
        DS=1.
        C2G=C2/DS
C
C ----- conditions at begining of time step -----
C
        U0(1,1)=stretchOld(km,1)
        U0(2,2)=stretchOld(km,2)
        U0(3,3)=stretchOld(km,3)
        U0(1,2)=stretchOld(km,4)
        U0(2,1)=stretchOld(km,4)
        U0(1,3)=0
        U0(3,1)=0
        U0(2,3)=0
        U0(3,2)=0

        X11=U0(1,1)
        X12=U0(1,2)
        X13=U0(1,3)
        X21=U0(2,1)

```

```

X22=U0(2,2)
X23=U0(2,3)
X31=U0(3,1)
X32=U0(3,2)
X33=U0(3,3)

U0I(1,1)=(X22*X33-X23*X32)/(X11*X22*X33-X11*X23*X32-
X21*X12*X33+X21*X13*X32+X31*X12*X23-X31*X13*X22)
U0I(1,2)=-(X12*X33-X13*X32)/(X11*X22*X33-X11*X23*X32-
X21*X12*X33+X21*X13*X32+X31*X12*X23-X31*X13*X22)
U0I(1,3)=(X12*X23-X13*X22)/(X11*X22*X33-X11*X23*X32-
X21*X12*X33+X21*X13*X32+X31*X12*X23-X31*X13*X22)
U0I(2,1)=-(X21*X33-X23*X31)/(X11*X22*X33-X11*X23*X32-
X21*X12*X33+X21*X13*X32+X31*X12*X23-X31*X13*X22)
U0I(2,2)=(X11*X33-X13*X31)/(X11*X22*X33-X11*X23*X32-
X21*X12*X33+X21*X13*X32+X31*X12*X23-X31*X13*X22)
U0I(2,3)=-(X11*X23-X13*X21)/(X11*X22*X33-X11*X23*X32-
X21*X12*X33+X21*X13*X32+X31*X12*X23-X31*X13*X22)
U0I(3,1)=(X21*X32-X22*X31)/(X11*X22*X33-X11*X23*X32-
X21*X12*X33+X21*X13*X32+X31*X12*X23-X31*X13*X22)
U0I(3,2)=-(X11*X32-X12*X31)/(X11*X22*X33-X11*X23*X32-
X21*X12*X33+X21*X13*X32+X31*X12*X23-X31*X13*X22)
U0I(3,3)=(X11*X22-X12*X21)/(X11*X22*X33-X11*X23*X32-
X21*X12*X33+X21*X13*X32+X31*X12*X23-X31*X13*X22)
C
VS0=X11*X22*X33-X11*X23*X32-X21*X12*X33+X21*X13*X32+X31*X12*X23-X31*X13*X22
C
CAUCH0=MATMUL(U0,U0)
X11=CAUCH0(1,1)
X12=CAUCH0(1,2)
X13=CAUCH0(1,3)
X21=CAUCH0(2,1)
X22=CAUCH0(2,2)
X23=CAUCH0(2,3)
X31=CAUCH0(3,1)
X32=CAUCH0(3,2)
X33=CAUCH0(3,3)

CI0(1,1)=(X22*X33-X23*X32)/(X11*X22*X33-X11*X23*X32-
X21*X12*X33+X21*X13*X32+X31*X12*X23-X31*X13*X22)
CI0(1,2)=-(X12*X33-X13*X32)/(X11*X22*X33-X11*X23*X32-
X21*X12*X33+X21*X13*X32+X31*X12*X23-X31*X13*X22)
CI0(1,3)=(X12*X23-X13*X22)/(X11*X22*X33-X11*X23*X32-
X21*X12*X33+X21*X13*X32+X31*X12*X23-X31*X13*X22)
CI0(2,1)=-(X21*X33-X23*X31)/(X11*X22*X33-X11*X23*X32-
X21*X12*X33+X21*X13*X32+X31*X12*X23-X31*X13*X22)
CI0(2,2)=(X11*X33-X13*X31)/(X11*X22*X33-X11*X23*X32-
X21*X12*X33+X21*X13*X32+X31*X12*X23-X31*X13*X22)
CI0(2,3)=-(X11*X23-X13*X21)/(X11*X22*X33-X11*X23*X32-
X21*X12*X33+X21*X13*X32+X31*X12*X23-X31*X13*X22)
CI0(3,1)=(X21*X32-X22*X31)/(X11*X22*X33-X11*X23*X32-
X21*X12*X33+X21*X13*X32+X31*X12*X23-X31*X13*X22)
CI0(3,2)=-(X11*X32-X12*X31)/(X11*X22*X33-X11*X23*X32-
X21*X12*X33+X21*X13*X32+X31*X12*X23-X31*X13*X22)
CI0(3,3)=(X11*X22-X12*X21)/(X11*X22*X33-X11*X23*X32-
X21*X12*X33+X21*X13*X32+X31*X12*X23-X31*X13*X22)

SINV0=VS0**(-2./3.)*(CAUCH0(1,1)+CAUCH0(2,2)+CAUCH0(3,3))
CID0=kdelta
CID0(1,1)=CI0(1,1)
CID0(2,2)=CI0(2,2)
CID0(3,3)=CI0(3,3)

CB0=CAUCH0*VS0**(-2./3.)

```

```

C
C ----- conditions at end of time step -----
C
      U1(1,1)=stretchNew(km,1)
      U1(2,2)=stretchNew(km,2)
      U1(3,3)=stretchNew(km,3)
      U1(1,2)=stretchNew(km,4)
      U1(2,1)=stretchNew(km,4)
      U1(1,3)=0
      U1(3,1)=0
      U1(2,3)=0
      U1(3,2)=0

      X11=U1(1,1)
      X12=U1(1,2)
      X13=U1(1,3)
      X21=U1(2,1)
      X22=U1(2,2)
      X23=U1(2,3)
      X31=U1(3,1)
      X32=U1(3,2)
      X33=U1(3,3)
C
      U1I(1,1)=(X22*X33-X23*X32)/(X11*X22*X33-X11*X23*X32-
X21*X12*X33+X21*X13*X32+X31*X12*X23-X31*X13*X22)
      U1I(1,2)=-(X12*X33-X13*X32)/(X11*X22*X33-X11*X23*X32-
X21*X12*X33+X21*X13*X32+X31*X12*X23-X31*X13*X22)
      U1I(1,3)=(X12*X23-X13*X22)/(X11*X22*X33-X11*X23*X32-
X21*X12*X33+X21*X13*X32+X31*X12*X23-X31*X13*X22)
      U1I(2,1)=-(X21*X33-X23*X31)/(X11*X22*X33-X11*X23*X32-
X21*X12*X33+X21*X13*X32+X31*X12*X23-X31*X13*X22)
      U1I(2,2)=(X11*X33-X13*X31)/(X11*X22*X33-X11*X23*X32-
X21*X12*X33+X21*X13*X32+X31*X12*X23-X31*X13*X22)
      U1I(2,3)=
      -(X11*X23-X13*X21)/(X11*X22*X33-X11*X23*X32-
X21*X12*X33+X21*X13*X32+X31*X12*X23-X31*X13*X22)
      U1I(3,1)=(X21*X32-X22*X31)/(X11*X22*X33-X11*X23*X32-
X21*X12*X33+X21*X13*X32+X31*X12*X23-X31*X13*X22)
      U1I(3,2)=
      -(X11*X32-X12*X31)/(X11*X22*X33-X11*X23*X32-
X21*X12*X33+X21*X13*X32+X31*X12*X23-X31*X13*X22)
      U1I(3,3)=(X11*X22-X12*X21)/(X11*X22*X33-X11*X23*X32-
X21*X12*X33+X21*X13*X32+X31*X12*X23-X31*X13*X22)
C
      VS1=X11*X22*X33-X11*X23*X32-X21*X12*X33+X21*X13*X32+X31*X12*X23-X31*X13*X22
C
      CAUCH1=MATMUL(U1,U1)
      X11=CAUCH1(1,1)
      X12=CAUCH1(1,2)
      X13=CAUCH1(1,3)
      X21=CAUCH1(2,1)
      X22=CAUCH1(2,2)
      X23=CAUCH1(2,3)
      X31=CAUCH1(3,1)
      X32=CAUCH1(3,2)
      X33=CAUCH1(3,3)

      CI1(1,1)=(X22*X33-X23*X32)/(X11*X22*X33-X11*X23*X32-
X21*X12*X33+X21*X13*X32+X31*X12*X23-X31*X13*X22)
      CI1(1,2)=-(X12*X33-X13*X32)/(X11*X22*X33-X11*X23*X32-
X21*X12*X33+X21*X13*X32+X31*X12*X23-X31*X13*X22)
      CI1(1,3)=(X12*X23-X13*X22)/(X11*X22*X33-X11*X23*X32-
X21*X12*X33+X21*X13*X32+X31*X12*X23-X31*X13*X22)
      CI1(2,1)=-(X21*X33-X23*X31)/(X11*X22*X33-X11*X23*X32-
X21*X12*X33+X21*X13*X32+X31*X12*X23-X31*X13*X22)
      CI1(2,2)=(X11*X33-X13*X31)/(X11*X22*X33-X11*X23*X32-
X21*X12*X33+X21*X13*X32+X31*X12*X23-X31*X13*X22)

```

```

      CI1(2,3)=
X21*X12*X33+X21*X13*X32+X31*X12*X23-X31*X13*X22)
      CI1(3,1)=(X21*X32-X22*X31)/(X11*X22*X33-X11*X23*X32-
X21*X12*X33+X21*X13*X32+X31*X12*X23-X31*X13*X22)
      CI1(3,2)=
X21*X12*X33+X21*X13*X32+X31*X12*X23-X31*X13*X22)
      CI1(3,3)=(X11*X22-X12*X21)/(X11*X22*X33-X11*X23*X32-
X21*X12*X33+X21*X13*X32+X31*X12*X23-X31*X13*X22)

      SINVB1=VS1**(-2./3.)*(CAUCH1(1,1)+CAUCH1(2,2)+CAUCH1(3,3))
      CID1=kdelta
      CID1(1,1)=CI1(1,1)
      CID1(2,2)=CI1(2,2)
      CID1(3,3)=CI1(3,3)

      CB1=CAUCH1*VS1**(-2./3.)
c      print*, 2
C
C
C ----- conditions at mid point -----
C
      UM=(U0+U1)/2.

      X11=UM(1,1)
      X12=UM(1,2)
      X13=UM(1,3)
      X21=UM(2,1)
      X22=UM(2,2)
      X23=UM(2,3)
      X31=UM(3,1)
      X32=UM(3,2)
      X33=UM(3,3)

      UMI(1,1)=(X22*X33-X23*X32)/(X11*X22*X33-X11*X23*X32-
X21*X12*X33+X21*X13*X32+X31*X12*X23-X31*X13*X22)
      UMI(1,2)=-(X12*X33-X13*X32)/(X11*X22*X33-X11*X23*X32-
X21*X12*X33+X21*X13*X32+X31*X12*X23-X31*X13*X22)
      UMI(1,3)=(X12*X23-X13*X22)/(X11*X22*X33-X11*X23*X32-
X21*X12*X33+X21*X13*X32+X31*X12*X23-X31*X13*X22)
      UMI(2,1)=-(X21*X33-X23*X31)/(X11*X22*X33-X11*X23*X32-
X21*X12*X33+X21*X13*X32+X31*X12*X23-X31*X13*X22)
      UMI(2,2)=(X11*X33-X13*X31)/(X11*X22*X33-X11*X23*X32-
X21*X12*X33+X21*X13*X32+X31*X12*X23-X31*X13*X22)
      UMI(2,3)=
X21*X12*X33+X21*X13*X32+X31*X12*X23-X31*X13*X22)
      UMI(3,1)=(X21*X32-X22*X31)/(X11*X22*X33-X11*X23*X32-
X21*X12*X33+X21*X13*X32+X31*X12*X23-X31*X13*X22)
      UMI(3,2)=
X21*X12*X33+X21*X13*X32+X31*X12*X23-X31*X13*X22)
      UMI(3,3)=(X11*X22-X12*X21)/(X11*X22*X33-X11*X23*X32-
X21*X12*X33+X21*X13*X32+X31*X12*X23-X31*X13*X22)

      VSM=X11*X22*X33-X11*X23*X32-X21*X12*X33+X21*X13*X32+X31*X12*X23-X31*X13*X22

      CAUCHM=MATMUL(UM,UM)
      X11=CAUCHM(1,1)
      X12=CAUCHM(1,2)
      X13=CAUCHM(1,3)
      X21=CAUCHM(2,1)
      X22=CAUCHM(2,2)
      X23=CAUCHM(2,3)
      X31=CAUCHM(3,1)
      X32=CAUCHM(3,2)
      X33=CAUCHM(3,3)

```

```

      CIM(1,1)=(X22*X33-X23*X32)/(X11*X22*X33-X11*X23*X32-
X21*X12*X33+X21*X13*X32+X31*X12*X23-X31*X13*X22)
      CIM(1,2)=-(X12*X33-X13*X32)/(X11*X22*X33-X11*X23*X32-
X21*X12*X33+X21*X13*X32+X31*X12*X23-X31*X13*X22)
      CIM(1,3)=(X12*X23-X13*X22)/(X11*X22*X33-X11*X23*X32-
X21*X12*X33+X21*X13*X32+X31*X12*X23-X31*X13*X22)
      CIM(2,1)=-(X21*X33-X23*X31)/(X11*X22*X33-X11*X23*X32-
X21*X12*X33+X21*X13*X32+X31*X12*X23-X31*X13*X22)
      CIM(2,2)=(X11*X33-X13*X31)/(X11*X22*X33-X11*X23*X32-
X21*X12*X33+X21*X13*X32+X31*X12*X23-X31*X13*X22)
      CIM(2,3)=-(X11*X23-X13*X21)/(X11*X22*X33-X11*X23*X32-
X21*X12*X33+X21*X13*X32+X31*X12*X23-X31*X13*X22)
      CIM(3,1)=(X21*X32-X22*X31)/(X11*X22*X33-X11*X23*X32-
X21*X12*X33+X21*X13*X32+X31*X12*X23-X31*X13*X22)
      CIM(3,2)=-(X11*X32-X12*X31)/(X11*X22*X33-X11*X23*X32-
X21*X12*X33+X21*X13*X32+X31*X12*X23-X31*X13*X22)
      CIM(3,3)=(X11*X22-X12*X21)/(X11*X22*X33-X11*X23*X32-
X21*X12*X33+X21*X13*X32+X31*X12*X23-X31*X13*X22)

      SINVBM=VSM**(-2./3.)*(CAUCHM(1,1)+CAUCHM(2,2)+CAUCHM(3,3))
      CIDM=kdelta
      CIDM(1,1)=CIM(1,1)
      CIDM(2,2)=CIM(2,2)
      CIDM(3,3)=CIM(3,3)

      CBM=CAUCHM*VSM**(-2./3.)
c      print*, 3

C GET THE STARTING NONLINEAR STRAIN FUNCTION
      VS=VS0
      SINVB=SINVB0
      CI=CI0
      CID=CID0

      fb=(tanh(C2*(C1-VS))+1.)/2.
      SFR=D2
      Bv=(4.*S0/(3.*(VS-S0)))*(1.-fb*SFR)
C      Gv=(3.*S0/(5.*VS-2.*S0))
C      PHI =3./2.*VS*S0/(5.*VS-2.*S0)
C      PHIJ =3./2.*S0/(5.*VS-2.*S0)-15./2.*VS*S0/(5.*VS-2.*S0)**2
C      PHIJJ =-15.*S0/(5.*VS-2.*S0)**2+75.*VS*S0/(5.*VS-2.*S0)**3
      Gv =3./2.*S0*(2.+D2*tanh(C2G*(-C1+VS))-D2)/(5.*VS-2.*S0)
      PHI =3./4.*VS*S0*(2.+D2*tanh(C2G*(-C1+VS))-D2)/(5.*VS-2.*S0)
      PHIJ =3./4.*S0*(2.+D2*tanh(C2G*(-C1+VS))-D2)/(5.*VS-2.*S0)+3./4.*VS*S0*D2*(1.-
tanh(C2G*(-C1+VS))**2)*C2G/(5.*VS-2.*S0)-15./4.*VS*S0*(2.+D2*tanh(C2G*(-C1+VS))-
D2)/(5.*VS-2.*S0)**2
      PHIJJ =3./2.*S0*D2*(1.-tanh(C2G*(-C1+VS))**2)*C2G/(5.*VS-2.*S0)-
15./2.*S0*(2.+D2*tanh(C2G*(-C1+VS))-D2)/(5.*VS-2.*S0)**2-3./2.*VS*S0*D2*tanh(C2G*(-
C1+VS))*(1.-tanh(C2G*(-C1+VS))**2)*C2G**2/(5.*VS-2.*S0)-15./2.*VS*S0*D2*(1.-tanh(C2G*(-
C1+VS))**2)*C2G/(5.*VS-2.*S0)**2+75./2.*VS*S0*(2.+D2*tanh(C2G*(-C1+VS))-D2)/(5.*VS-
2.*S0)**3

      Ba=P0*VS*(1.-S0)/(VS-S0)**2
      BAINT =P0*(VS-1.)/(VS-S0)
      BVINT=stateold(km,NSTATEV)

      TSIJJ=Bv/VS
      TSIJ=BVINT

      TSIJJA=Ba/VS
      TSIJA=BAINT

```

```

STRAN_NLIN0=(VS*TSIJ+VS*PHIJ*(SINVB-3.)-2./3.*PHI*SINVB)*(2.*CI-CID)+2.*PHI*VS**(-
2./3.)*kdelta
STRAN_NLINA0=VS*TSIJA*(2.*CI-CID)

c      print*, 4

C  GET THE ENDING NONLINEAR STRAIN FUNCTION
VS=VS1
SINVB=SINVB1
CI=CI1
CID=CID1

fb=(tanh(C2*(C1-VS))+1.)/2.
SFR=D2
Bv=(4.*S0/(3.*(VS-S0)))*(1.-fb*SFR)
Gv =3./2.*S0*(2.+D2*tanh(C2G*(-C1+VS))-D2)/(5.*VS-2.*S0)
PHI =3./4.*VS*S0*(2.+D2*tanh(C2G*(-C1+VS))-D2)/(5.*VS-2.*S0)
PHIJ =3./4.*S0*(2.+D2*tanh(C2G*(-C1+VS))-D2)/(5.*VS-2.*S0)+3./4.*VS*S0*D2*(1.-
tanh(C2G*(-C1+VS)))**2*C2G/(5.*VS-2.*S0)-15./4.*VS*S0*(2.+D2*tanh(C2G*(-C1+VS))-
D2)/(5.*VS-2.*S0)**2
PHIJJ =3./2.*S0*D2*(1.-tanh(C2G*(-C1+VS)))**2*C2G/(5.*VS-2.*S0)-
15./2.*S0*(2.+D2*tanh(C2G*(-C1+VS))-D2)/(5.*VS-2.*S0)**2-3./2.*VS*S0*D2*tanh(C2G*(-
C1+VS))*(1.-tanh(C2G*(-C1+VS)))**2*C2G**2/(5.*VS-2.*S0)-15./2.*VS*S0*D2*(1.-tanh(C2G*(-
C1+VS)))**2*C2G/(5.*VS-2.*S0)**2+75./2.*VS*S0*(2.+D2*tanh(C2G*(-C1+VS))-D2)/(5.*VS-
2.*S0)**3

Ba=P0*VS*(1.-S0)/(VS-S0)**2
BAINT =P0*(VS-1.)/(VS-S0)
BVINT=stateold(km,NSTATEV) + ( Bv/VSM*(VS1-VS0))

TSIJJ=Bv/VS
TSIJ=BVINT

TSIJJA=Ba/VS
TSIJA=BAINT

STRAN_NLIN1=(VS*TSIJ+VS*PHIJ*(SINVB-3.)-2./3.*PHI*SINVB)*(2.*CI-CID)+2.*PHI*VS**(-
2./3.)*kdelta
STRAN_NLINA1=VS*TSIJA*(2.*CI-CID)

c      print*, 5

C  GET THE MIDPOINT NONLINEAR STRAIN FUNCTION
VS=VSM
SINVB=SINVBM
CI=CIM
CID=CIDM

fb=(tanh(C2*(C1-VS))+1.)/2.
SFR=D2
Bv=(4.*S0/(3.*(VS-S0)))*(1.-fb*SFR)
Gv =3./2.*S0*(2.+D2*tanh(C2G*(-C1+VS))-D2)/(5.*VS-2.*S0)
PHI =3./4.*VS*S0*(2.+D2*tanh(C2G*(-C1+VS))-D2)/(5.*VS-2.*S0)
PHIJ =3./4.*S0*(2.+D2*tanh(C2G*(-C1+VS))-D2)/(5.*VS-2.*S0)+3./4.*VS*S0*D2*(1.-
tanh(C2G*(-C1+VS)))**2*C2G/(5.*VS-2.*S0)-15./4.*VS*S0*(2.+D2*tanh(C2G*(-C1+VS))-
D2)/(5.*VS-2.*S0)**2
PHIJJ =3./2.*S0*D2*(1.-tanh(C2G*(-C1+VS)))**2*C2G/(5.*VS-2.*S0)-
15./2.*S0*(2.+D2*tanh(C2G*(-C1+VS))-D2)/(5.*VS-2.*S0)**2-3./2.*VS*S0*D2*tanh(C2G*(-
C1+VS))*(1.-tanh(C2G*(-C1+VS)))**2*C2G**2/(5.*VS-2.*S0)-15./2.*VS*S0*D2*(1.-tanh(C2G*(-
C1+VS)))**2*C2G/(5.*VS-2.*S0)**2+75./2.*VS*S0*(2.+D2*tanh(C2G*(-C1+VS))-D2)/(5.*VS-
2.*S0)**3

```

```

Ba=P0*VS*(1.-S0)/(VS-S0)**2
BAINT =P0*(VS-1.)/(VS-S0)
BVINT=stateold(km,NSTATEV)+1./2.*( Bv/VSM*(VS1-VS0))
DSTATEV(NSTATEV)=Bv/VSM*(VS1-VS0)

TSIJJ=Bv/VS
TSIJ=BVINT

TSIJJA=Ba/VS
TSIJA=BAINT

STRAN_NLIN=(VS*TSIJ+VS*PHIJ*(SINVB-3.)-2./3.*PHI*SINVB)*(2.*CI-CID)+2.*PHI*VS**(-
2./3.)*kdelta
STRAN_NLINA=VS*TSIJA*(2.*CI-CID)

```

C DE will represent the change in the nonlinear strain function

```

DE=(STRAN_NLIN1-STRAN_NLIN0)
DEA=(STRAN_NLINA1-STRAN_NLINA0)

```

```

DFSTRAN(1)=DE(1,1)
DFSTRAN(2)=DE(2,2)
DFSTRAN(3)=DE(3,3)
DFSTRAN(4)=DE(1,2)
DFSTRAN(5)=DE(1,3)
DFSTRAN(6)=DE(2,3)

```

```

DFSTRANA(1)=DEA(1,1)
DFSTRANA(2)=DEA(2,2)
DFSTRANA(3)=DEA(3,3)
DFSTRANA(4)=DEA(1,2)
DFSTRANA(5)=DEA(1,3)
DFSTRANA(6)=DEA(2,3)

```

```

FINITE_STRAIN=STRAN_NLIN

```

```

FSTRAN(1)=FINITE_STRAIN(1,1)
FSTRAN(2)=FINITE_STRAIN(2,2)
FSTRAN(3)=FINITE_STRAIN(3,3)
FSTRAN(4)=FINITE_STRAIN(1,2)
FSTRAN(5)=FINITE_STRAIN(1,3)
FSTRAN(6)=FINITE_STRAIN(2,3)

```

C ----- CONVERT THE OLD CAUCHY STRESS TO THE OLD 2PK STRESS -----

```

STRESS(1,1)=stressOld(km,1)
STRESS(2,2)=stressOld(km,2)
STRESS(3,3)=stressOld(km,3)
STRESS(1,2)=stressOld(km,4)
STRESS(2,1)=stressOld(km,4)
STRESS(1,3)=0
STRESS(3,1)=0
STRESS(2,3)=0
STRESS(3,2)=0

```

```

STRESS=VS0*(matmul(U0I,STRESS))
STRESS=matmul(STRESS,U0I)

```

```

S2PK_OLD(1)=STRESS(1,1)
S2PK_OLD(2)=STRESS(2,2)
S2PK_OLD(3)=STRESS(3,3)
S2PK_OLD(4)=STRESS(1,2)

```

c print\*, 6

```

C ----- GET PLASTIC STATE -----
C Update the MAXIMUM strains (Note volume strain is negative in compression)
C Also compute new plastic strains
C
  DO K1=1,NTENS
    IF (FSTRAN(K1)+DFSTRAN(K1).GT.stateold(km,3*K1-2)) THEN

      STRAN_TEST=FSTRAN(K1)-stateold(km,3*K1)+DFSTRAN(K1)

      IF ((STRAN_TEST.GT.+1.*ELIMIT).AND.(stateold(km,3*K1).LT.+1.*ESET)) THEN
        g(K1)=PR
      ELSE
        g(K1)=0
      END IF
      DSTATEV(3*K1-2)=FSTRAN(K1)+DFSTRAN(K1)-stateold(km,3*K1-2)
      DSTATEV(3*K1-1)=0
      DSTATEV(3*K1)=DFSTRAN(K1)*g(K1)/(g(K1)+1.)

    ELSE IF ((FSTRAN(K1)+DFSTRAN(K1)).LT.stateold(km,3*K1-1)) THEN

      STRAN_TEST=FSTRAN(K1)-stateold(km,3*K1)+DFSTRAN(K1)

      IF ((STRAN_TEST.LT.-1.*ELIMIT).AND.(stateold(km,3*K1)>-1.*ESET)) THEN
        g(K1)=PR
      ELSE
        g(K1)=0
      END IF
      DSTATEV(3*K1-2)=0
      DSTATEV(3*K1-1)=FSTRAN(K1)+DFSTRAN(K1)-stateold(km,3*K1-1)
      DSTATEV(3*K1)=DFSTRAN(K1)*g(K1)/(g(K1)+1.)

    ELSE
      DSTATEV(3*K1-2)=0
      DSTATEV(3*K1-1)=0
      DSTATEV(3*K1)=0
      g(K1)=0
    END IF

  END DO
c   print*, 61, at

C *****
C CHANGE IN 2PK STRESS COMPONENT (PRONY SYSTEM)
C *****
  SKIP=3*NTENS
C
  icnt=0
  DO K1=1,NTENS
    vM0=D1*DFSTRAN(K1)/(1.+g(K1))+DFSTRANA(K1)
    vNUM=vM0
    DO J1=1,NELS
      icnt=icnt+1
      ISTATV=SKIP+icnt
      TAU=PROPS(J1+NELS)
      vME=D1*PROPS(J1)
      vNUM=vNUM + vME*DFSTRAN(K1)/(1.+DTIME/2./TAU)
stateold(km,ISTATV)*DTIME/(TAU+DTIME/2.) = (vME*(DFSTRAN(K1))-
      DSTATEV(ISTATV)
DTIME*stateold(km,ISTATV)/TAU)/(1.+DTIME/2./TAU)
    END DO
    DSTRES(K1)=vNUM
  END DO
C

```

```

C
c   print*, 7

C   GET THE NEW SECOND PIOLA KIRCHOFF STRESS

      DO K1=1,NTENS
          S2PK_NEW(K1)=S2PK_OLD(K1)+DSTRES(K1)
      END DO

C   UPDATE THE CAUCHY STRESS

      STRESS(1,1)=S2PK_NEW(1)
      STRESS(2,2)=S2PK_NEW(2)
      STRESS(3,3)=S2PK_NEW(3)
      STRESS(1,2)=S2PK_NEW(4)
      STRESS(2,1)=S2PK_NEW(4)
      STRESS(1,3)=0
      STRESS(3,1)=0
      STRESS(2,3)=0
      STRESS(3,2)=0

      STRESS=(matmul(U1,STRESS))
      STRESS=matmul(STRESS,U1)/VS1

      stressNew(km,1)=STRESS(1,1)
      stressNew(km,2)=STRESS(2,2)
      stressNew(km,3)=STRESS(3,3)
      stressNew(km,4)=STRESS(1,2)

C
C   UPDATE THE STATE VARIABLES
C
      do K1=1,NSTATEV
          stateNew(km,K1)=StateOld(km,K1)+DSTATEV(K1)
      end do
c   print*, 8

C
100  continue
C
      RETURN
      END

```

## Bibliography

- [1] Ferry, J.D. , *Viscoelastic Properties of Polymers*; John Wiley & Sons, New York, 1980
- [2] Rosen, S.L. *Fundamental Principles of Polymeric Materials*, 2<sup>nd</sup> ed., John Wiley & Sons, New York, 1993
- [3] Christensen, R.M., *Theory of Viscoelasticity, An Introduction*, Academic Press, New York, 1982
- [4] Christensen, R.M., *Mechanics of Composite Materials*, John Wiley & Sons, New York, 1979
- [5] Findley, W. N.; Lai, J. S.; Onaran, K. *Creep Relaxation of Nonlinear Viscoelastic Materials – with an Introduction to Linear Viscoelasticity*, Dover Publications, Inc, New York, 1989
- [6] Park, S.W.; Schapery, R.A., “Methods of Interconversion Between Linear Viscoelastic Material Functions. Part I - a Numerical Method Based on Prony Series”, *International Journal of Solids and Structures*, v 36, no. 11, Apr 1999, pp 1653-1675
- [7] Sherwood, J. A.; “Constitutive Modeling and Simulation of Energy Absorbing Polyurethane Foam Under Impact Loading”, *Polymer Engineering and Science*, v 32, no. 16, Aug 1992, pp. 1138-1146

- [8] Shim, V.P.W.; Yang, L. M.; et al., “A Visco-Hyperelastic Constitutive Model to Characterize Both Tensile and Compressive Behavior of Rubber”, *Journal of Applied Polymer Science*, v 92, no. 1, Apr 5, 2004, pp. 523-531
- [9] Jung, G.; Youn, S.; and Kim, B; “Development of a three-dimensional nonlinear viscoelastic constitutive model of solid propellant”, *J. Braz. Soc. Mech. Sci.*, 2000, v.22, no.3, pp.457-476.
- [10] Farber, J. N.; Farris, R. J. “Model for prediction of the elastic response of reinforced materials over wide ranges of concentration”, *Journal of Applied Polymer Science* v 34, no. 6, 1987. pp. 2093-2104
- [11] Shim, V.P.W.; Yang, L. M.; et al., “A Visco-Hyperelastic Constitutive Model to Characterize Both Tensile and Compressive Behavior of Rubber”, *Journal of Applied Polymer Science*, v 92, no. 1, Apr 5, 2004, pp. 523-531
- [12] Hibbit, Karlsson and Sorenson Inc., 2004, “ABAQUS theory manual”, Version 6.4.
- [13] Livermore Software Technology Corp.; Hallquist, J. O. (ed.), *LS-DYNA Theoretical Manual*, May 1998
- [14] Peyraut, F.; “Loading Restrictions for the Blatz-Ko Hyperelastic Model – Application to a Finite Element Analysis”, *International Journal of Non-Linear Mechanics*, v. 39 2004, pp. 969-976

- [15] Farber, J. N.; Farris, R. J. “Model for prediction of the elastic response of reinforced materials over wide ranges of concentration”, *Journal of Applied Polymer Science* v 34, no. 6, 1987. pp. 2093-2104
- [16] Feng W.W.; Hallquist J.O.; “On Constitutive Equations for Elastomers and Elastomeric Foams”, *4<sup>th</sup> European LS-DYNA Users Conference*, 2003
- [17] Pan, E.; Sassolas, B.; and Pfeffer, W. T. “A 3-D boundary Element Formulation of Viscoelastic Media with Gravity”, *Computational Mechanics*, v. 19, 1997, pp. 308-316
- [18] Lubliner, J; “A Model of Rubber Viscoelasticity”, *Mechanics Research Communications*, v.12, no. 2, 1985, pp. 93-99
- [19] Holzappel, G. A.; “On Large Strain Viscoelasticity: Continuum Formulation and Finite Element Applications to Elastomeric Structures”, *International Journal for Numerical Methods in Engineering*”, v. 39, 1996 pp. 3903-3926
- [20] Holzappel, G. A.; Simo, J.C.; “A New Viscoelastic Constitutive Model for Continuous Media at Finite Thermomechanical Changes”, *International Journal of Solid Structures*”, v. 33, no. 20-22 1996 pp. 3019-3034
- [21] Simo, J. C.; “On a Fully Three-Dimensional Finite-Strain Viscoelastic Damage Model: Formulation and Computational Aspects”, *Computer Methods in Applied Mechanics and Engineering*, v. 60, 1987, pp. 153-173

- [22] Amin, A. F. M. S.; Alam, M. S.; Okui, Y.; “An Improved Hyperelasticity Relation in Modeling Viscoelasticity Response of Natural and High Damping Rubbers in Compression: Experiments, Parameter Identification and Numerical Verification”, *Mechanics of Materials*, v. 34 (2002) pp. 75-95
- [23] Nedjar, B.; “Frameworks for Finite Strain Viscoelastic-Plasticity Based on Multiplicative Decomposition. Part 1: Continuum Formulations”, *Computer Methods in Applied Mechanics and Engineering*, v. 191 (2002), pp. 1541-1562
- [24] Yang, L. M. ; “Visco-hyperelastic Approach to Modelling the Constitutive Behavior of Rubber” , *International Journal of Impact Engineering*, v. 24 no. 6, Jun 2000, pp. 545-560
- [25] Yang, L. M.; “A Visco-Hyperelastic Constitutive Description of Elastomeric Foam” *International Journal of Impact Engineering*, v. 30 no. 8-9, Sep-Oct 2004, pp. 1099-1110
- [26] Bilkard, J.; “Finite Viscoelasticity, Plasticity and Damage of a Class of Filled Elastomers: Constitutive Model”, *Mechanics Research Communications*, v. 28, no. 6, Nov-Dec, 2001, pp. 693-702
- [27] Chiyokura, K; Wantanabe, O.; “Constitutive Equation of Dynamic Plasticity Using Internal Time Theory (Uniaxial Response and Determination of Material Constants)”, *Transactions of the Japan Society of Engineers*, Part Am v. 59, no. 567, Nov 1993, pp. 2626-2634

- [28] Tsakmakis, C.; Haupt, P; “On The Hypoelastic-Idealplastic Constitutive Model”, *Acta Mechanica*, v 80, no. 3-4, Dec 1989, pp. 273-285
- [29] Richardson, M. O. W.; Nandra, D. S.; “Load Deflection Analyses of Shock Mitigating Polyurethane-Silicon Foams”, *Cellular Polymers*, v 4, no. 6, 1985, pp. 445-462
- [30] Zhang, X.; Liu, L.; Zhang, J; Chen, Q; Zhang, L.; “Study on Mircostructure and Mechanical properties Relationship of Short Fibers/Rubber Foam Composites”, *European Polymer Journal*, v. 40, no. 8, Aug 2004, pp.1733-1742
- [31] Siegmann, A.; “Mechanical Behavior of Reinforced Polyurethane Foams”, *Polymer Composites*, v. 4, no. 2, Apr 1983, pp. 113-119
- [32] Gibson, L. J.; Ashby, M. F.; “Mechanics of Three-Dimensional Cellular Materials”, *Proceeding of the Royal Society of London, Series A: Mathematical and Physical Sciences*, v. 382, no. 1782, Jul 1982, pp. 43-59
- [33] Farber, J. N.; “Model for Prediction of Elastic Response of Reinforced Materials over Wide Ranges of Concentration”, *Journal of Applied Polymer Science*, v 34, no. 6 Nov 1987, pp. 2093-2104
- [34] Fish, J; Shek, K.; “Finite Deformation Plasticity Based on the Additive Split of the Rate of Deformation And Hyperelasticity”, *Computational Methods in Applied Mechanical Engineering*, v. 190, 2000, pp. 75-93

- [35] Bardenhagen, S. G.; Stout, M. G.; Gray, G. T.; “Three-dimensional, finite deformation, viscoplastic constitutive models for polymeric materials”, *Mechanics of Materials*, v 25, 1997, pp. 235-253
- [36] Du Bois, P. A.; Kolling, S.; Koesters, M; Frank, T.; “Material Behaviour of Polymers Under Impact Loading”, *International Journal of Impact Engineering*, v 32, 2006, pp. 725-740
- [37] Kakavas, P. A.; Anifantis, K; “Effective Moduli of Hyperelastic Porous Media at Large Deformation”, *Acta Mechanica*, v. 160, 2003, pp. 127-147
- [38] Bikard, J.; Désoyer, T.; “Finite Viscoelasticity, Plasticity and Damage of a Class of Filled Elastomers: Constitutive Model”, *Mechanics Research Communications*, v 28, no. 6, 2001, pp. 693-702
- [39] Lopez-Pamies, O.; Castañeda, P. P.; “Second-Order Estimates for the Macroscopic Response and Loss of Ellipticity in Porous Rubbers at Large Deformations”, *Journal of Elasticity*, v. 76, 2004, pp. 247-287
- [40] Mettupalayam, V.; Sivaselvan, V; Reinhorn, A; “Hysteretic Models for Deteriorating Inelastic Structures”, *Journal of Engineering Mechanics*, June 2000, pp. 633-640
- [41] Browning R. V.; Gurtin, M. E.; Williams, W. O.; “A One-Dimensional Viscoplastic Constitutive Theory for Filled Polymers”, *International Journal of Solids and Structures*, v 20, no. 11/12, 1984, pp. 921-934

- [42] Danielsson, M.; Parks, D.M.; Boyce, M.C; “Constitutive Modeling of Porous Hyperelastic Materials”, *Mechanics of Materials*, v. 36, 2004, pp. 347-358
- [43] Blatz, P. J.; Ko, W. L; “Application of Finite Elastic Theory to the Deformation of Rubbery Materials”, *Transactions of the Society of Rheology*, v. 6, 1962, pp. 223-251
- [44] Casem, D. T.; Fournay, W. L; Chang, P; “A Polymeric Split Hopkinson Pressure Bar Instrumented with a Velocity Gauge”, *Society for Experimental Mechanics*, v. 43, no. 4, 4 Dec 2003, pp. 420-427
- [45] Frew, D. J.; Forrestal, M. J; Chen, W; “Pulse Shaping Techniques for Testing Elastic-plastic Materials with a Split Hopkinson Pressure Bar”, *Society for Experimental Mechanics*, v 45, no. 2, April 2005, pp. 186-195
- [46] Gavrus, A.; Caestecker, E; Ragneau, E; Davoodi, B; “Analysis of the Dynamic SHPB Test Using the Finite Element Simulation”, *Society for Experimental Mechanics*, v 45, no. 2, April 2005, pp. 186-195
- [47] Liu, Q. L.; Subhash, G.; “A Phenomenological Constitutive Model for Foams Under Large Deformations”, *Polymer Engineering and Science*, v 44, no. 3, March 2004, pp. 463-473
- [48] Fish, J; Shek, K.; “Finite Deformation Plasticity Based on the Additive Split of the Rate of Deformation and Hyperelasticity”, *Comp. Meth. Appl. Mech. Engng.*, v 190, 2000, pp. 75-93

- [49] Zhou X.; Sha D.; Tamma, K.; “A Novel Nonlinearly Explicit Second-Order Accurate L-Stable Methodology for Finite Deformation Hypo/Hypoelasto-Plastic Structural Dynamics Problems with Total/Updated Lagrangian Formulations”, *AIAA-2002-1304.*, 43rd AIAA/ASME/ASCE/AHS/ASC Structures, Structural Dynamics, and Materials Conference, 2002
- [50] Drucker, D.C.; “A Definition of Stable Inelastic Material”, *J. Appl. Mech.*, v 26, 1959, pp. 101-106
- [51] Guillot, F. M.; Trivett, D. H.; “A Dynamic Young’s Modulus Measurement System for Highly Compliant Polymers”, *J. Acoust. Soc. Am.*, v 114 (3), Sep 2003, pp. 1334-1345
- [52] Ramesh, K. T.; Narasimham, S.; “Finite Deformations and the Dynamic Measurement of Radial Strains in Compression Kolsky Bar Experiments”, *Intl. J. of Solids and Structures*, v 33, 1996, pp. 3723-3738
- [53] Scott, N. H.; “The Incremental Bulk Modulus, Young’s Modulus and Poisson’s Ratio in Nonlinear Isotropic Elasticity: Physically Reasonable Response”, *Mathematics and Mechanics of Solids OnlineFirst*, April 7, 2006
- [54] Ogden, R. W.; “Large Deformation Isotropic Elasticity: On the Correlation of Theory and Experiment for Compressible Rubberlike Solids”, *Proc. R. Soc. London*, 1972

- [55] Jemiolo, S; Turteltaub, S.; “A Parametric Model for a Class of Foam-Like Isotropic Hyperelastic Materials”, *Trans. of the ASME*, v 67, June, 2000, pp. 248-254
- [56] Kramers, H. A; *Nature*, v 117, 1925, pp. 775
- [57] Kronig, R. de L.; *Journal of the Optical Society of America*, v 12, 1926, pp. 547
- [58] Beda, T.; “Reconciling the Fundamental Phenomenological Expression of the Strain Energy of Rubber with Established Experimental Facts”, *Wiley InterScience*, 21 Aug 2004
- [59] Wijeyewickrema, A. C.; “Prediction of Interphase Properties of a Three-Phase Composite Using Three-Phase and Four-Phase Composite Models”, *16<sup>th</sup> ASCE Engineering Mechanics Conference*, July 16-18, 2003